ASME
SETTING THE STANDARD

Transactions of the ASME, Journal of Fluids Engineering (ISSN 0098-2202) is published monthly by The American Society of Mechanical Engineers, Three Park Avenue, New York, NY 10016. Periodicals postage paid at New York, NY and additional mailing offices.
POSTMASTER: Send address changes to Transactions of the ASME, Journal of Fluids Engineering, c/o THE AMERICAN SOCIETY OF MECHANICAL ENGINEERS, 22 Law Drive, Box 2300, Fairfield, NJ 07007-2300.
CHANGES OF ADDRESS must be received at Society headquarters seven weeks before they are to be effective. Please send old label and new address.
STATEMENT from By-Laws. The Society shall not be responsible for statements or opinions advanced in papers or ... printed in its publications (B7.1, Par. 3).

Journal of Fluids Engineering

Published Monthly by ASME

VOLUME 132 • NUMBER 4 • APRIL 2010

RESEARCH PAPERS

Flows in Complex Systems

041101 Performance Improvement of Weis-Fogh Type Ship's Propulsion Mechanism Using a Wing Restrained by an Elastic Spring
Kideok Ro

041102 Experimental Analysis of Microchannel Entrance Length Characteristics Using Microparticle Image Velocimetry
Tariq Ahmad and Ibrahim Hassan

041103 Combined Effect of Surface Roughness and Heterogeneity of Wall Potential on Electroosmosis in Microfluidic/Nanofuidic Channels
S. Bhattacharyya and A. K. Nayak

041104 Application of Realizability and Shock Unsteadiness to $k-\varepsilon$ Simulations of Under-Expanded Axisymmetric Supersonic Free Jets
Babak Emami, Markus Bussmann, and Honghi Tran

041105 Analysis of Unsteady Confined Viscous Flows With Variable Inflow Velocity and Oscillating Walls
Dan Mateescu, Manuel Muñoz, and Olivier Scholz

Fundamental Issues and Canonical Flows

041201 Eddy Heat Transfer by Secondary Görtler Instability
L. Momayez, G. Delacourt, P. Dupont, and H. Peerhossaini

041202 On Self-Similarity in the Inner Wall Layer of a Turbulent Channel Flow
Bérengère Podvin, Yann Fraigneau, Julien Jouanguy, and J.-P. Laval

041203 Review of Hydraulic Roughness Scales in the Fully Rough Regime
Karen A. Flack and Michael P. Schultz

Multiphase Flows

041301 CFD Simulation of the Bubbling and Slugging Gas-Solid Fluidized Beds
Seyyed Hossein Hosseini, Wenqi Zhong, Mohsen Nasr Esfahany, Leila Pourjafar, and Salar Azizi

041302 Implicit LES Predictions of the Cavitating Flow on a Propeller
Rickard E. Bensow and Göran Bark

041303 An Examination of Trapped Bubbles for Viscous Drag Reduction on Submerged Surfaces
Kelly A. Stephani and David B. Goldstein

TECHNICAL BRIEFS

044501 On the Suppression of Vortex Shedding From Circular Cylinders Using Detached Short Splitter-Plates
Behzad Ghadiri Dehkordi and Hamed Houri Jafari

(Contents continued on inside back cover)

This journal is printed on acid-free paper, which exceeds the ANSI Z39.48-1992 specification for permanence of paper and library materials. ♾™
♻ 85% recycled content, including 10% post-consumer fibers.

044502 Buoyancy Effects on Thermal Boundary Layer Over a Vertical Plate With a Convective Surface Boundary Condition
O. D. Makinde and P. O. Olanrewaju

The ASME Journal of Fluids Engineering is abstracted and indexed in the following:

Applied Science & Technology Index, Chemical Abstracts, Chemical Engineering and Biotechnology Abstracts (Electronic equivalent of Process and Chemical Engineering), Civil Engineering Abstracts, Computer & Information Systems Abstracts, Corrosion Abstracts, Current Contents, Ei EncompassLit, Electronics & Communications Abstracts, Engineered Materials Abstracts, Engineering Index, Environmental Engineering Abstracts, Environmental Science and Pollution Management, Excerpta Medica, Fluidex, Index to Scientific Reviews, INSPEC, International Building Services Abstracts, Mechanical & Transportation Engineering Abstracts, Mechanical Engineering Abstracts, METADEX (The electronic equivalent of Metals Abstracts and Alloys Index), Petroleum Abstracts, Process and Chemical Engineering, Referativnyi Zhurnal, Science Citation Index, SciSearch (The electronic equivalent of Science Citation Index), Shock and Vibration Digest, Solid State and Superconductivity Abstracts, Theoretical Chemical Engineering

Performance Improvement of Weis-Fogh Type Ship's Propulsion Mechanism Using a Wing Restrained by an Elastic Spring

Kideok Ro
Professor
Department of Mechanical System Engineering,
Institute of Marine Industry,
Gyeongsang National University,
445 Inpyeong-dong, Tongyeong,
Gyeongnam 650-160, Republic of Korea
e-mail: rokid@gaechuk.gsnu.ac.kr

This study was conducted in an attempt to improve the hydrodynamic performance of a Weis-Fogh type ship propulsion mechanism by installing a spring to the wing so that the opening angle of the wing can be changed automatically. With the prototype design, the average thrust coefficient was almost fixed with all velocity ratios; but with the spring type, the thrust coefficient was increased sharply as the velocity ratio increased. The average propulsive efficiency was higher with a bigger opening angle in the prototype but in the spring type design, the one with a smaller spring coefficient had higher efficiency. In the case of velocity ratios over 1.5 where big thrust can be generated, the spring type had more than twice the increase in propulsion efficiency compared with the prototype.
[DOI: 10.1115/1.4001155]

Keywords: hydraulic machine, propulsion mechanism, fluid force, elastic wing, spring type, performance improvement

1 Introduction

The Weis-Fogh mechanism [1,2], which was developed based on the hovering flight of a small bee, is gathering the attention of many scientists who study hydrodynamics because of its unique and efficient lift generation mechanism [3–7]. Recently, engineering applications of the mechanism have been actively attempted as well [8–12]. Some scientists have proposed a propulsion model that uses the principle of the mechanism [9] and have conducted experiments on the dynamic characteristics with a driving test of a model ship. This showed that this propulsion mechanism worked very effectively as a new ship propulsion system [9]. Also, they visualized the unsteady flow field that was created around the wings when the propulsion mechanism was operating [13] and verified the time variation in the thrust and the drag on the wing [14]. The weakest point of this mechanism is that while the propulsive efficiency is high, the range of the velocity ratio that generates the maximum propulsive efficiency is small, and the velocity ratio is less than 1, which means that the thrust is relatively small. To put this propulsion mechanism to practical use, the low thrust must be improved.

One way to generate high thrust in the high velocity ratio range would be to change the wing of the propulsion mechanism from a hard, flat-plate to an elastic body. In fact, the wings of a small bee and the body of a fish are elastic, and it is likely that the elastic body contributes to the improvement in thrust. Tsutahara et al. [15] reported that by using an elastic wing with a spring, thrust was greatly increased even without increasing drag by automatically controlling the opening angle according to the drag acting on the wing during one stroke. However in that study, the measured values of the average thrust coefficient and average drag coefficient in terms of the velocity ratio covered a wide range, making interpretation uncertain. Also, the range of the velocity ratio was limited to less than 2.0. In the author's opinion, who was the one of the co-authors of that study, the uncertainty of the characteristics is from the errors of the experimental apparatus. Therefore in the current study, the experimental apparatus has been improved and the characteristics of the thrust, drag, and propulsive efficiency of the spring type elastic wing are thoroughly studied over a wide range of the velocity ratio.

2 Experimental Device and Method

2.1 Model of a Propulsion Mechanism. Figure 1 shows the model of the propulsion mechanism that will be used in this experiment. The figure shows the model from the upper perpendicular side; as the wing works in a certain motion in the water channel, thrust is generated toward the left of the figure, which is the same as the direction of the ship. As point p, which corresponds to the center pivot point of the wing, oscillates perpendicular to the uniform flow U and in the velocity of V, the wing first opens from the lower wall (opening stage), then moves translationally, maintaining the opening angle of α (translating stage), and finally rotates and closes on the upper wall (closing stage). Then, the wing repeats the motion: it rotates and opens from the upper wall, moves translationally, and finally rotates and closes on the lower wall.

In the original Weis-Fogh mechanism, circulation in the opposite direction is formed at each wing as a pair of flat-plate wings open while their trailing edges touch. Through the principle of mirror image, the combination of channel walls and a single wing represents the same flow.

2.2 Measurement of the Thrust and Drag Acting on the Wing. The experiment was conducted by making a wing driving system that moves the same as the wing movement of the propulsion mechanism in Fig. 1. It was installed in a circulating water channel with a uniform flow and the thrust and drag acting on the wing were measured. Figure 2 shows the schematic diagram of the driving unit of the wing.

The main structure of the system was made with acrylic boards

Contributed by the Fluids Engineering Division of ASME for publication in the JOURNAL OF FLUIDS ENGINEERING. Manuscript received November 22, 2008; final manuscript received January 30, 2010; published online March 29, 2010. Assoc. Editor: Zvi Rusak.

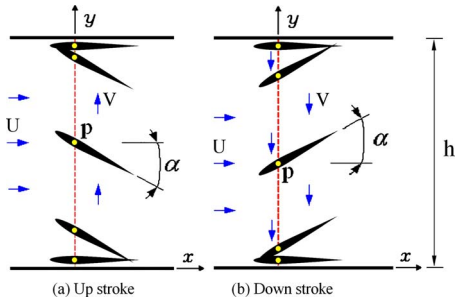

Fig. 1 A model of propulsion mechanism

and aluminum angle bars. The dimensions are 500 mm in length and 650 mm in width to fit into the circulating water channel. In the wing driving system, the shaft was fixed onto the slider and the slider was attached to one side of the belt so that when the motor (dc 30 W) spins forward or backward, the wing moved in an oscillating motion. The front and back spin of the motor was operated by a limit switch and a relay circuit installed at the ends of the slider rail, and the velocity of the wing movement was controlled with adjusting the spin speed of the motor.

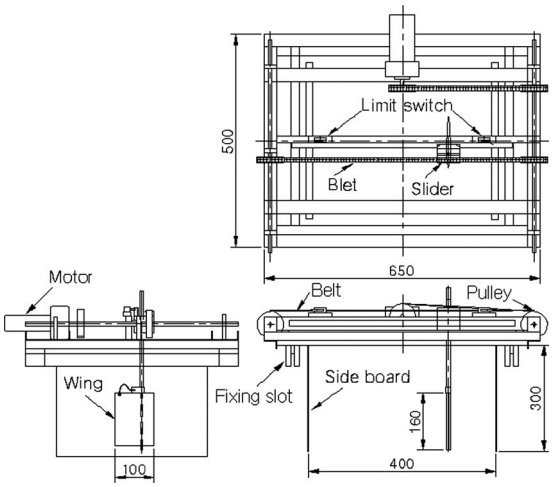

Fig. 2 Driving unit of the wing (unit: mm)

The wing used in this experiment was made in the shape of NACA0010, as shown in Fig. 3. The size of the wing chord is $C=100$ mm and its span 160 mm. The shaft was penetrated at the point 0.75C away from trailing edge of the wing through a hole 3 mm in diameter. The reason for making the wing NACA0010 type, the width of water channel $h=4C$ and the center pivot point 0.75C from the trailing edge was to easily compare the experimental results with the results from previous studies [13–15]. The shaft was made with a titanium bar of 9 mm in diameter and a stainless bar of 3 mm in diameter. The wing was inserted to the shaft of the wing so that when the slider moves in a translating motion, momentum around the shaft works toward the wing to open it; and in the closing stage, the leading edge of the wing collides with the side board, forcing it to close. As shown in Figs. 3(*a*) and 3(*b*), two types of wings were used in this experiment. In Fig. 3(*a*), the V-shaped angle adjustment plate was fixed onto the shaft, and the pin was fixed onto the head of the wing. Therefore, when the wing shaft moves, the wing opens up because of the drag on the wing in the opposite direction as the wing movement. At the same time, the pin hits the inner side of the V-shaped plate, which limits the maximum opening angle α. Two different kinds of angle adjustment plates were made with opening angles $\alpha=15$ deg and 30 deg. These opening angles were used because the maximum propulsive efficiency was relatively high at these angles [9,15]. In Fig. 3(*b*), one spring fixed plate was secured onto the shaft and another spring fixed plate was attached to the trailing edge of the wing. As shown in the figure, two sizes of steel wire with diameters of $\varphi=0.8$ and 1.0 were bent and connected between the two fixed plates to work as a spring. The spring makes the opening angle α change according to the drag acting on the wing when it is in motion. This experimental apparatus is similar to the one Tsutahara et al. [15] used. However, for a more accurate experiment, it was improved as follows. To reduce the vibration acting on the wing shaft, the material of the shaft was changed from a steel bar to a titanium bar. The mechanism for power transmission was changed from a chain to a timing belt. In addition, to precisely control the opening angle, an angle adjustment plate was used instead of a string. Also, as shown in Fig. 3(*b*), the

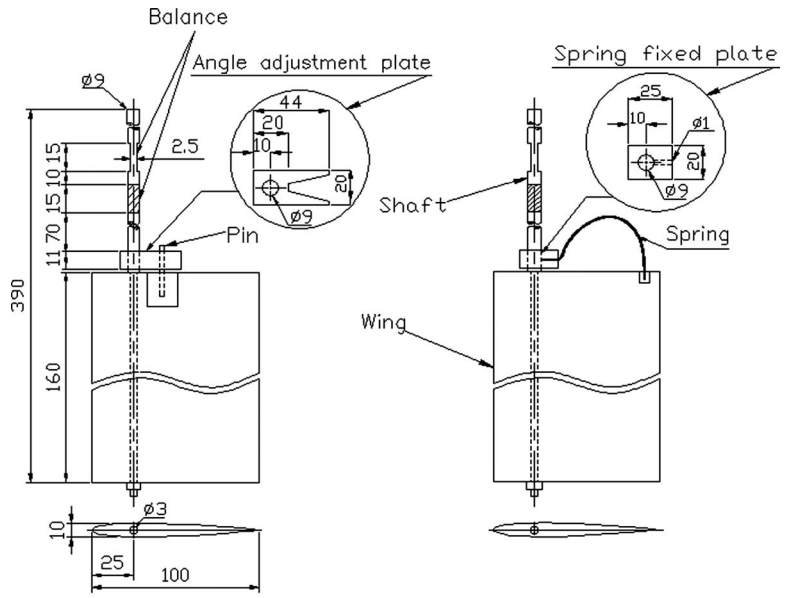

Fig. 3 Structure of the wing and shaft (unit: mm)

Table 1 The spring coefficients of each elastic wing

The diameter of spring (ϕ) (mm)	0.8	1.0
Spring coefficient (N m/rad)	0.0884	0.1185

spring was made from bending a steel wire instead of using the existing coil type. To stabilize the wing driving unit when the wing is in motion, a fixing slot was installed to the support beam so that the unit was held fast at both sides of the circulating water channel, as seen in Fig. 2. The ultimate point of this experiment is to improve the hydrodynamic performance by adjusting the opening angle with water resistance instead of the fixed opening angle in the typical Weis-Fogh type propulsion mechanism. Table 1 shows the measurement of the spring coefficient of each spring.

Balance was achieved by evenly cutting the top of the shaft in front, back, right, and left, as shown in Fig. 3. Thrust and drag were measured by deformation of four attached strain gauges. The voltage waveforms from the strain gauges produced the value of thrust and drag by a precompensated coefficient on a personal computer through a bridge circuit, strain amplifier and A/D converter in each channel (two channels in total).

The experiment was conducted by changing the uniform flow $U(U=0.049-0.349$ m/s) and wing movement velocity $V(V=0.055-0.246$ m/s) at regular intervals while testing the two prototype wings with maximum opening angles α of 15 deg and 30 deg, and the two spring type wings, which automatically adjusted the opening angles. The time variation in thrust and drag was measured, and the average thrust coefficient, average drag coefficient, and average propulsive efficiency were produced by averaging the values in one cycle. The range of Reynolds number was $\mathrm{Re}=7.2\times10^3-3.9\times10^4$ when the wing chord was fixed as unit length and yielded by uniform flow U.

2.3 Definition of the Characteristic Coefficients. Each coefficient that shows the hydrodynamic characteristic of this propulsion mechanism, that is, thrust coefficient C_T and drag coefficient C_D by wing movement velocity V are defined as follows:

$$C_T = \frac{T}{\frac{1}{2}\rho V^2 S} \tag{1}$$

$$C_D = \frac{D}{\frac{1}{2}\rho V^2 S} \tag{2}$$

T represents thrust, D is the drag, ρ is the density of the fluid, and S is the wing area below the water surface. As defined in Fig. 4, thrust T is the component of force in the direction of the progress of the ship, which is the opposite direction of uniform flow U. Drag D is the component of force in the opposite direction of the movement velocity V of the wing axis. Also, the average propulsive efficiency of the mechanism, $\bar{\eta}$ is the power applied to the wing; in other words, the ratio of the net output generated from the wing to the input, and is calculated by

$$\bar{\eta} = \frac{\int_0^{T_c} C_T U dt}{\int_0^{T_c} C_D V dt} \times 100 \tag{3}$$

Here, T_c represents the period of one cycle of the wing movement.

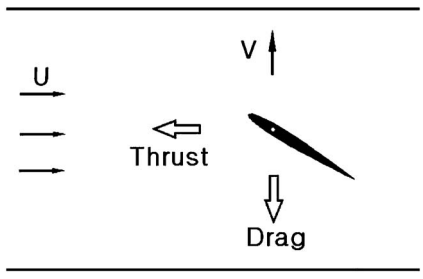

Fig. 4 Definition of thrust and drag

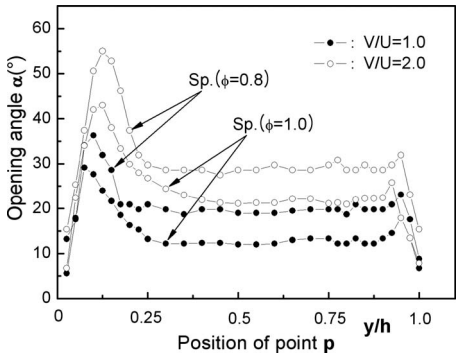

Fig. 5 Variations for opening angle with the position of wing in a stroke for elastic wings of spring type

3 Results and Discussion

Figure 5 shows the change in the opening angle according to the wing position change in one stroke of each spring type elastic wing illustrated in Table 1. Here, the x-axis expresses the dimensionless value of the distance the wing moves y compared with the width of the channel h. Although there were some variations according to the velocity ratio U/V and the spring coefficient, the change in the opening angle compared with the change in wing position in the channel showed a similar tendency. The wing opened up very wide when it left from the channel wall, then the opening angle decreased until it came to a certain angle where it stabilized and moved translationally, and finally, when the wing approached the other side of the channel, it opened up a little bit more before it closed.

Figure 6 shows the calibration results of thrust and drag executed on the measuring shaft in Fig. 3.

The calibration of thrust and drag was executed by installing the propulsion mechanism of Fig. 2 inside an empty water channel and adding dead load at the point 1/2 of the wing span in $\pm$ direction of thrust and drag in Fig. 4. The voltage output that corresponded to each load was obtained by increasing 0.3 N in ±0.9 N range for thrust; drag was increased by 1 N in the range of ±4.0 N. With this data, the load and voltage output relationship was computed by linear least-squares approximation. As illustrated in Fig. 6, the results of the calibration showed that both thrust and drag were on a straight line and the error range of root mean square from the experimental value and the linear relation value of thrust and drag were all under 0.02.

Figure 7 shows the change in thrust coefficient C_T and drag coefficient C_D over two reciprocating movements of the wing at the velocity ratio of $V/U=1.0$.

The dotted line in the figure represents the prototype wing with the maximum opening angle at $\alpha=15$ deg and the solid line represents the elastic spring type wing that adjusts opening angle by using steel line of $\varphi=1.0$ used as a spring. In the figure, the x-axis expresses the traveling distance of wing shaft normalized by the channel width; this value means the number of strokes. First, in the change in thrust coefficient, the value was positive throughout the whole stroke except for the opening stages. This means that regardless of the wing's reciprocating motion, the thrust occurred

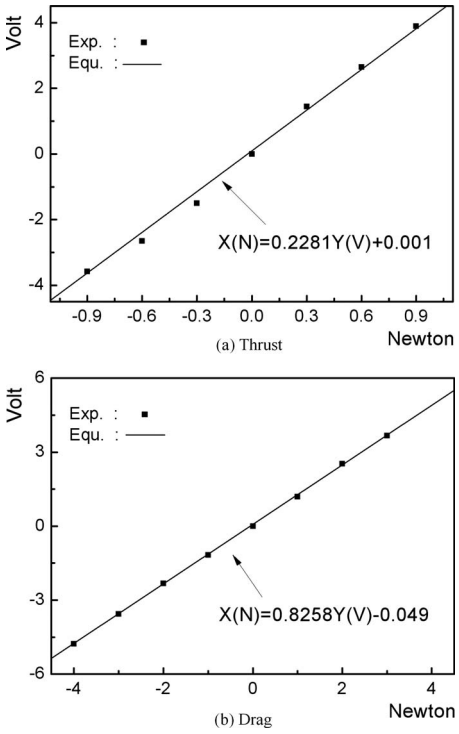

Fig. 6 Calibrations of thrust and drag

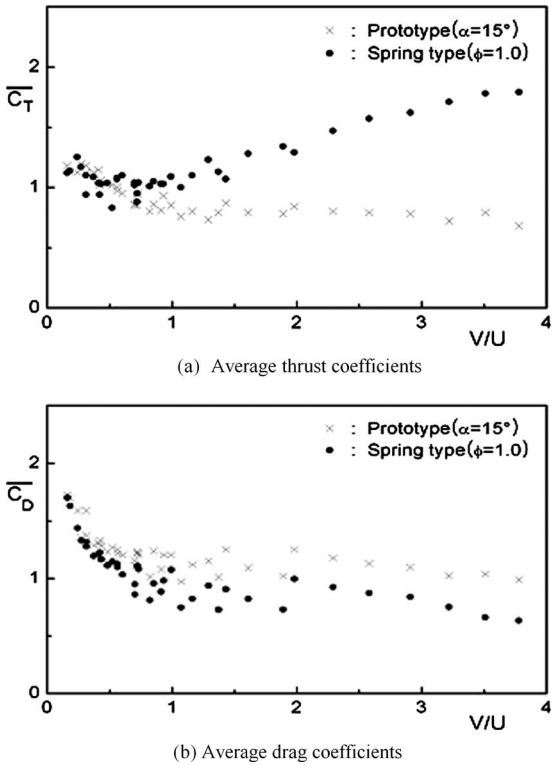

Fig. 8 Average thrust and drag coefficients with velocity ratio

toward the direction of the progress of the ship. When comparing the dotted and solid lines, there were some fluctuations in the dotted line but it had a relatively constant value, whereas the solid line decreased after having a large value at the beginning of the stroke. This is because when the prototype wing moves from the opening stage to the translational stage during opening, a vortex is released from the trailing edge of the wing. This happens because the wing starts off from the wall when there was negative pressure and the pressure between the wing and the channel wall was much lower than the pressure toward the moving direction of the wing.

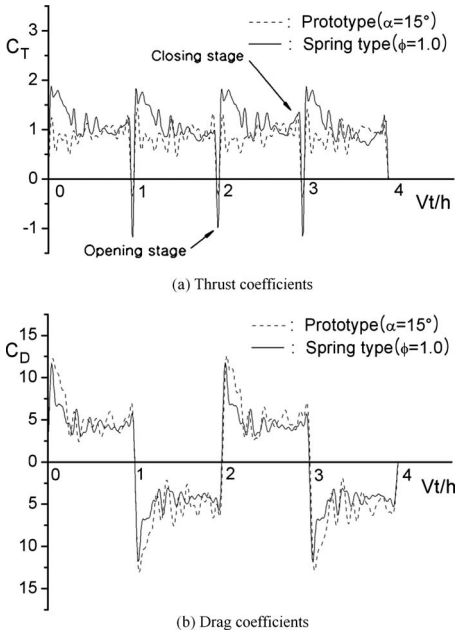

Fig. 7 Time variations for thrust and drag coefficients (V/U =1.0)

In fact with the prototype, during the opening in the visualization experiment [13] of the flow field, fluid was inhaled because of the negative pressure between the wing and the wall and a numerical calculation [14] confirmed that the vortex was released from the trailing edge of the wing in the translational stage. But with the elastic spring wing, it is assumed that right before the start-off, the pressure difference in both sides of the wing would be smaller than the one in the prototype. Because of the spring, momentum is applied to the wing; therefore the wing opens up to a bigger angle as the trailing edge of the wing touches the wall before it starts. Therefore with the spring type, the wing can shift over to the translational stage to become an effective Weis-Fogh mechanism.

Meanwhile, when in the change in drag coefficient (b), in each stroke, the value was reversed by x-axis; this is because each stroke of wing movement was in the opposite direction. The drag coefficient of the elastic wing (solid line) was smaller than the prototype wing (dotted line) but the difference is very small. This is because with the elastic wing, the opening angle increased a little because of water resistance during wing movement. Especially in the closing stage, the water resistance increased but the opening angle was opened up automatically by the spring, which prevented the decrease in propulsive efficiency that occurs with an increase in drag.

Figure 8 shows the average thrust coefficient (a) and the average drag coefficient (b) with the change in velocity ratio U/V of the prototype wing with the maximum opening angle of $\alpha = 15$ deg and the spring type elastic wing with a $\varphi = 1.0$ spring. Each point in (a) and (b) in the figure corresponds to the average values of one cycle in Fig. 7 of (a) and (b).

First, in the distribution of average thrust coefficient with the prototype ($\alpha = 15$ deg), the values were almost constant regardless of the velocity ratio. On the other hand with the spring type ($\varphi = 1.0$), the values increased sharply as the velocity ratio increased. In the former type, the opening angle did not change even though the velocity ratio increased. In the latter, as explained before in Fig. 7, as the velocity ratio increased, the opening angle right before the translational stage increased sharply, as shown in Fig.

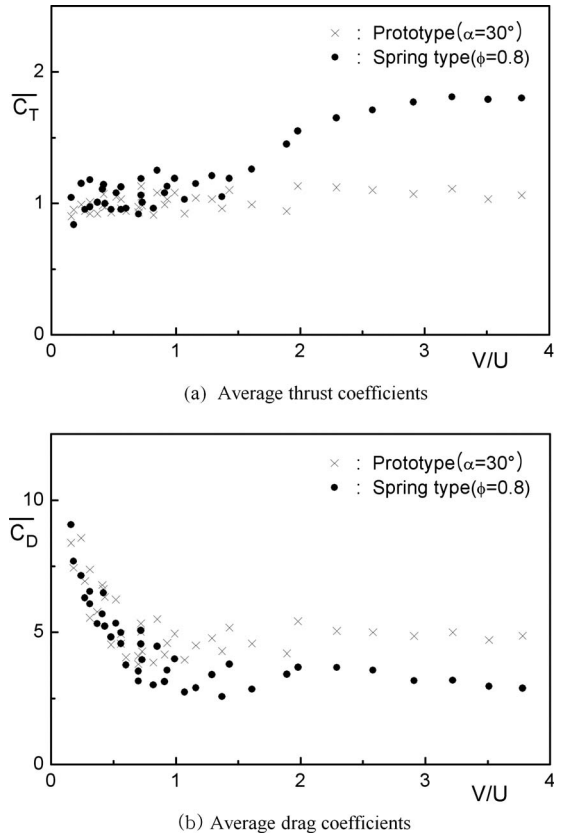

Fig. 9 Average thrust and drag coefficients with velocity ratio

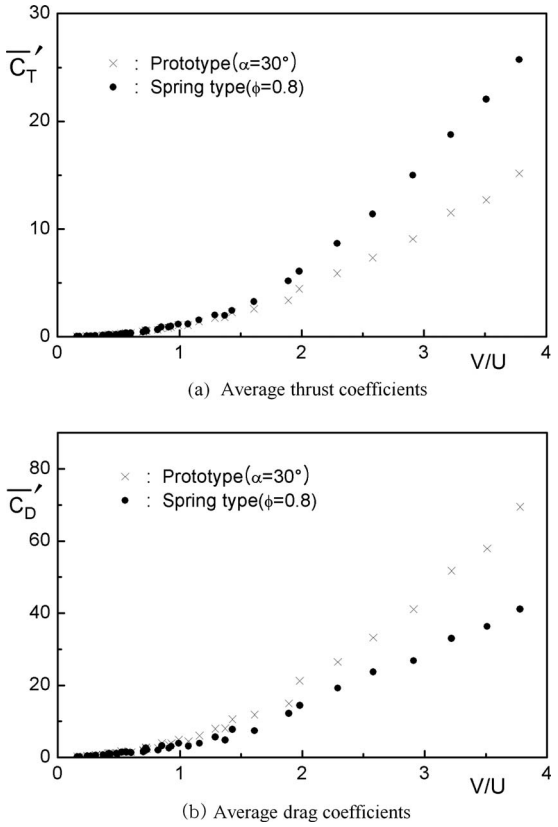

Fig. 10 Average thrust and drag coefficients with velocity ratio

5, to produce an impressive Weis-Fogh effect. Also, in the distribution of average drag coefficient, over velocity ratio of 1, the differences between the values increased a little as the velocity ratio increased; this is because with the spring type (φ=1.0), the opening angle increased as the velocity ratio increased, which led to a decrease in average drag. On the other hand, where the velocity ratio was low, especially under 0.5, as velocity ratio decreased, average thrust coefficient was similar in both types, and the average drag coefficient increased in both. This is because in this range, water resistance is small, which makes the opening angle to be small.

Figure 9 shows the average thrust coefficient (a) and the average drag coefficient (b) with the change in velocity ratio V/U of prototype wing with the maximum opening angle of α=30 deg and spring type elastic wing with φ=0.8 spring.

This spring coefficient was smaller than the one in Fig. 8; therefore at the same velocity ratio even if the opening angle was big, the tendency in the change in the average thrust coefficient and average drag coefficient according to the velocity ratio was the same. The average thrust coefficient of prototype (α=30 deg) was 1.0, and was constant regardless of the velocity ratio. However with the spring type (φ=0.8), the value increased sharply as the velocity ratio increased. It did not increase in a straight line because the spring coefficient was too small, which made the increase in the opening angle with velocity ratio exceed the range of elasticity. Meanwhile, as shown in Fig. 8, the distribution of the average drag coefficient was both similar in tendency with velocity ratio but the absolute value was smaller in the spring type than the prototype. This is because in the spring type, as the velocity ratio increased, the opening angle increased also, which led to a decrease in average drag.

Figure 10 shows the average thrust coefficient $\overline{C_T}'$ (a) and the average drag coefficient $\overline{C_D}'$ (b), which were calculated by average thrust coefficient and average drag coefficient from Fig. 9, yielded by uniform flow U. This value is derived from inserting uniform flow U in the place of wing movement velocity V in each Eq. (1) and Eq. (2) and is converted to a dimensionless form.

When comparing Figs. 9 and 10, especially in the case of the prototype, the values $\overline{C_T}$ and $\overline{C_D}$ turned into a dimensionless form by V^2 both remained constant as velocity ratio V/U increased, whereas the values $\overline{C_T}'$ and $\overline{C_D}'$ turned into a dimensionless form by U^2 increased in a two-dimensional curve. This means that both thrust and drag depend heavily on wing movement velocity V rather than uniform flow U. Also, this result shows that when designing this kind of propulsion mechanism, it is effective to use the former as the applicable thrust and drag coefficient and the latter when the characteristics on thrust and drag are important.

Figure 11 shows the average propulsive efficiency of various types of wings with a change in the velocity ratio V/U.

When the velocity ratio is greater than 1, as shown in Fig. 11, the prototype with a constant maximum opening angle, the prototype with the larger opening angle had higher average propulsive efficiency. For the spring type wings, where the opening angle changes, the one with the smaller spring coefficient had higher efficiency. Especially with a velocity ratio of more than 1.5 where big thrust can be generated, propulsive efficiency can be increased over twice that of the existing fixed angle type. Therefore, practical application of the propulsion mechanism is anticipated, which can greatly complement the weakness of low propulsive efficiency of the prototype in the high velocity ratio range.

4 Conclusions

This study was conducted as an attempt to improve the hydrodynamic performance of the propulsion mechanism by installing a spring to the wing so that the opening angle of the wing in one stroke can be changed automatically compared with the existing method of a fixed maximum opening angle in the Weis-Fogh type

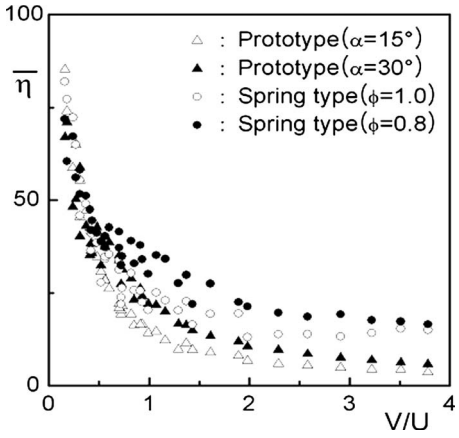

Fig. 11 Average propulsive efficiency with velocity ratio for wings of various types

ship propulsion mechanism. There were two prototypes of fixed wings with maximum opening angles of $\alpha=15$ deg and $\alpha=30$ deg and two types of elastic wings with different spring coefficients. By changing the velocity ratio V/U, thrust, drag, and propulsive efficiency were examined experimentally. The summaries of results are as follows.

(1) With the spring type, the opening angle had a large value when moving from the opening stage to the translational stage and moving from the translational stage to the closing stage.
(2) The average thrust coefficient was constant with the prototype at all velocity ratios but it increased sharply with the spring type as the velocity ratio increased.
(3) The average drag coefficient with velocity ratio was similar for all wings but the absolute values were smaller in the spring type than the prototype.
(4) The average propulsive efficiency was higher with a larger opening angle in the prototype, and with the smaller spring coefficient in the spring type.
(5) With a velocity ratio over 1.5, where big thrust can be generated, the spring type showed more than twice the propulsive efficiency of the prototype.

The profile of the wing section that was used for this experiment was NACA0010. The position of the wing shaft was limited to 1/4 length of the wing chord. For a practical application of this propulsion mechanism, there is a need for finding the optimal location of the wing shaft as well as the shape of the wing section in the future. Also, to understand the effect of the Reynolds numbers, the range should be expanded up to 10^6 in future experiments.

The paper provides an improved contraption that works but it works inefficiently since it was designed ad hoc. The paper proves the main point accurately but provides no fundamental theoretical justification for it. A detailed mathematical analysis is needed to substantiate the work.

Acknowledgment

This work was supported by the Korea Science and Engineering Foundation (KOSEF) grant funded by the Korea government (MEST) (Contract No. R01-2007-000-10038-0). The author wishes to thank Professor Michihisa Tsutahara, Kobe National University, for his valuable comments.

References

[1] Weis-Fogh, T., 1973, "Quick Estimates of Flight Fitness in Hovering Animals, Including Novel Mechanism for Lift Production," J. Exp. Biol., **59**, pp. 169–230.
[2] Lighthill, M. J., 1973, "On the Weis-Fogh Mechanism of Lift Generation," J. Fluid Mech., **60**, pp. 1–17.
[3] Maxworthy, T., 1979, "Experiments on the Weis-Fogh Mechanism of Lift Generation by Insects in Hovering Flight. Part 1. Dynamics of the 'Fling'," J. Fluid Mech., **93**, pp. 47–63.
[4] Edwards, R. H., and Cheng, H. K., 1982, "The Separation Vortex in the WeisFogh Circulation-Generation Mechanism," J. Fluid Mech., **120**, pp. 463–473.
[5] Spedding, G. R., and Maxworthy, T., 1986, "The Generation of Circulation and Lift in a Rigid Two-Dimensional Fling," J. Fluid Mech., **165**, pp. 247–272.
[6] Ro, K. D., and Tsutahara, M., 1997, "Numerical Analysis of Unsteady Flow in the Weis-Fogh Mechanism by the 3D Discrete Vortex Method With GRAPE3A," ASME J. Fluids Eng., **119**, pp. 96–102.
[7] Zhang, S. S., Wu, X. H., and Wang, X. F., 1999, "Research and Progress of Weis-Fogh Mechanism Hydrodynamics," J. Hydrodynam., **3**, pp. 55–60.
[8] Furber, S. B., and Ffowcs Williams, J. E., 1979, "Is the Weis-Fogh Principle Exploitable in Turbomachinary?," J. Fluid Mech., **94**(3), pp. 519–540.
[9] Tsutahara, M., and Kimura, T., 1987, "An Application of the Weis-Fogh Mechanism to Ship Propulsion," ASME J. Fluids Eng., **109**, pp. 107–113.
[10] Tsutahara, M., and Kimura, T., 1988, "A Pilot Pump Using the Weis-Fogh Mechanism and Its Characteristics," Trans. Jpn. Soc. Mech. Eng., Ser. B, **54**(498), pp. 393–397.
[11] Tsutahara, M., and Kimura, T., 1994, "Study of a Fan Using the Weis-Fogh Mechanism (An Experimental Fan and Its Characteristics)," Trans. Jpn. Soc. Mech. Eng., Ser. B, **60**(571), pp. 910–915.
[12] Zhang, S. S., Wu, X. H., and Wang, X. F., 1996, "Hydrodynamic Model of Weis-Fogh Mechanism Hydrofoil," J. Hydrodynam., **4**, pp. 35–39.
[13] Ro, K. D., Kim, K. S., and Kim, J. H., 2008, "The Flow Characteristics Around Airfoil Moving Reciprocally in a Channel," Transactions of the Korean Society of Mechanical Engineers. B, **32**(7), pp. 536–541.
[14] Ro, K. D., Zhu, B. S., and Kang, H. K., 2006, "Numerical Analysis of Unsteady Viscous Flow Through a Weis-Fogh Type Ship Propulsion Mechanism Using the Advanced Vortex Method," ASME J. Fluids Eng., **128**, pp. 481–487.
[15] Tsutahara, M., Kimura, T., Ro, K., and Takahashi, K., 1990, "The Propulsion Mechanism of a Ship Using the Weis-Fogh Mechanism (4th Report, Effects of Channel Side Walls and of a Spring Controlling the Opening Angle of the Wing)," Trans. Jpn. Soc. Mech. Eng., Ser. B, **56**(525), pp. 1299–1305.

Experimental Analysis of Microchannel Entrance Length Characteristics Using Microparticle Image Velocimetry

Tariq Ahmad

Ibrahim Hassan[1]
e-mail: ibrahimh@alcor.concordia.ca

Department of Mechanical and Industrial Engineering,
Concordia University,
Montreal,
QC, H3G 1M8, Canada

The study of the entrance region of microchannels and microdevices is limited, yet important, since the effect on the flow field and heat transfer mechanisms is significant. An experimental study has been carried out to explore the laminar hydrodynamic development length in the entrance region of adiabatic square microchannels. Flow field measurements are acquired through the use of microparticle image velocimetry (micro-PIV), a nonintrusive particle tracking and flow observation technique. With the application of micro-PIV, entrance length flow field data are obtained for three different microchannel hydraulic diameters of 500 μm, 200 μm, and 100 μm, all of which have cross-sectional aspect ratios of 1. The working fluid is distilled water, and velocity profile data are acquired over a laminar Reynolds number range from 0.5 to 200. The test-sections were designed as to provide a sharp-edged microchannel inlet from a very large reservoir at least 100 times wider and higher than the microchannel hydraulic diameter. Also, all microchannels have a length-to-diameter ratio of at least 100 to assure fully developed flow at the channel exit. The micro-PIV procedure is validated in the fully developed region with comparison to Navier–Stokes momentum equations. Good agreement was found with comparison to conventional entrance length correlations for ducts or parallel plates, depending on the Reynolds range, and minimal influence of dimensional scaling between the investigated microchannels was observed. New entrance length correlations are proposed, which account for both creeping and high laminar Reynolds number flows. These correlations are unique in predicting the entrance length in microchannels and will aid in the design of future microfluidic devices. [DOI: 10.1115/1.4001292]

1 Introduction

The understanding of fluid flow behavior in microchannels and microdevices has been a strong focus of the research community over the past decade. Microchannels are prevalent in microdevices such as microheat-exchangers [1–3] and micromixers [4–6]. In turn, these microfluidic components are be implemented in complete microsystems such as micropower-plants [7,8] and lab-on-a-chip platforms [9–11]. However, prior to the advanced development of such microsystems, it becomes necessary to further understand the flow characteristics in microchannels and microdevices incorporated in these systems. Although many research groups are in the area of two-phase flow such as flow boiling, single phase flow remains important in terms of applications, and fundamental understanding.

The entrance region, where the flow is hydrodynamically developing, can be very important because the transport properties such as pressure gradient, wall shear stress, and heat transfer coefficient depend strongly on the flow region. Also, it should be stressed that general correlations for friction factor, heat transfer coefficient, and laminar to turbulent transition are only valid if the flow is fully developed. Generally, the hydrodynamic entrance length can be defined as the length from the inlet of a channel to a location over which the maximum local velocity has attained 99% of its fully developed value [12]. For a rectangular channel, the maximum local velocity is at the center of the channel. However, a uniform inlet velocity profile is seldom achieved in practice and is somewhat difficult to simulate in experimental investigations, particularly at the microscale.

Conventionally, numerous hydrodynamic entrance length studies were carried out both experimentally and numerically. Regarding numerical studies for rectangular ducts or parallel plate channels, results found by groups such as Han [13], Fleming and Sparrow [14], Atkinson et al. [15], Wiginton and Dalton [16], and Chen [17] are considered to be standard and accurate regarding the entrance length. Experimental entrance length studies for conventional ducts have been explored by numerous groups such as Sparrow et al. [18], Goldstein and Kreid [19], Beavers et al. [20], and Muchnik et al. [21].

In practical applications of microchannel flow, the majority of microsystem flows are laminar due to the high pressure drop in microchannels caused by relatively small channel dimensions. To apply many conventional laminar correlations it is necessary that the flow be fully developed or errors will result. Conventionally in the laminar regime, the lower the Reynolds number, the shorter the entrance region to achieve fully developed flow. But, it should be emphasized that in microfluidic devices and systems, microchannel lengths can be extremely short in which case within a certain range of Reynolds numbers (Re), hydrodynamic developing flow may dominate the flow field over the entire microchannel length.

With regards to experimental fluid flow analysis in microgeometries, the relatively new method of microparticle image velocimetry (micro-PIV) is an attractive technique. Micro-PIV allows one to obtain comprehensive flow field data by acquiring the local velocity flow fields of fluid flowing through a microchannel or microdevice. The velocity fields are acquired by tracking the trajectories of fluorescent seeding particles. Previous micro-PIV

[1]Corresponding author.

Contributed by the Fluids Engineering Division of ASME for publication in the JOURNAL OF FLUIDS ENGINEERING. Manuscript received September 28, 2008; final manuscript received February 2, 2010; published online April 15, 2010. Assoc. Editor: Juergen Kompenhans.

studies in microchannels focus on the velocity flow field [22–25], laminar to turbulent transition [26–29], and hydrodynamic entrance length.

Very few laminar hydrodynamic entrance length studies have been carried out in microchannels, and of these, all have been analyzed using micro-PIV. Their geometries varied from one another and their studies of developing flows in the entrance region are limited with varying agreement with conventional entrance length correlations.

The micro-PIV experiments of Lee et al. [29] were carried out using deionized water with 1 μm particles flowing through a conventionally machined acrylic rectangular microchannel with a length of 120 mm, a height of 690 μm, and a width of 260 μm, over a range of Reynolds numbers from 250–2100. Images were taken at incremental distances from the microchannel entrance, where averaged correlation velocity profiles were recorded. Through observation, the entrance lengths were found to be shorter than correlations given by Shah and London [12]. The authors concluded that the entrance length is reduced by about 45% due to the predeveloped flow prior to entering the microchannel.

Lee and Kim [30] investigated different inlet shapes of silicon etched microchannels using micro-PIV with deionized water flowing at about Re=1. The microchannels were 30 mm in length, had a depth of 58 μm and a width of 100 μm. Overall, the researchers concluded that the entrance length for microchannels is much smaller than for macroscale channels.

Oak et al. [31] analyzed flow development characteristics of two coflowing laminar streams in a high aspect ratio rectangular microchannel using micro-PIV. The two coflowing streams are separated by 90 deg and are 9.1 mm long, and the Reynolds numbers are of 1 and 10. The development length of the merging flows was shown not to vary with the Reynolds number between 1 and 10, and the authors concluded that high aspect ratio channels result in shorter development lengths.

Hao et al. [27] showed the developing velocity profiles along various axial positions for water flow in a trapezoidal silicon microchannel with a hydraulic diameter of 237 μm. Using micro-PIV, centerline velocity distributions along the axial direction of the channel, over a range of Reynolds numbers between 50 and 1200, were investigated. The authors found the entrance length in their experiments to be about $L_e/D_h=(0.08-0.09)\mathrm{Re}$.

Lee et al. [32] experimentally investigated the entrance length in two rectangular microchannels of different aspect ratios (H/W), one with a hydraulic diameter (D_h) of 370 μm and an aspect ratio of 2.75 made of acrylic, and another with a hydraulic diameter of 56.4 μm and an aspect ratio of 0.40, made of silicon (deep reactive ion etching (DRIE)). The authors used micro-PIV to measure the velocity profiles in the low Reynolds number range, from 1 to 100. For their experimental Re range, the authors concluded that their experimental correlations showed a weaker dependence on Re than existing entrance length correlations, which have a linear dependency Re. Their data showed shorter developing lengths compared to conventional correlations. Overall, they state their discordance is due to the different aspect ratios, the off-center maximum velocity of the inlet profiles, and predevelopment in the vertical plane due to the planar plenum. The discrepancy due to the different microchannel aspect ratios can be resolved if entrance studies be carried out without the influence of aspect ratio.

There is limited fluid flow data available for the laminar entrance region of microchannels, particularly resulting from fundamental inlet geometry, where the flow is not predeveloped. A general entrance length study from a very large reservoir, relative to the microchannel hydraulic diameter, would be a novel and significant contribution in the area of microchannel fluid flow. The objective of the present study is to experimentally investigate the laminar hydrodynamic development length in the entrance region of adiabatic square microchannels. Flow field measurements are acquired through the use of micro-PIV, a nonintrusive particle tracking and flow observation technique. With the application of micro-PIV, test-sections of three different square microchannel hydraulic diameters of 500 μm, 200 μm, and 100 μm are employed. The working fluid is distilled water and the velocity profile data are acquired over a laminar Reynolds number range from 0.5 to 200. The test-sections were designed with a sharp-edged inlet from a large planar reservoir, at least 100 times wider, higher, and longer than the microchannel hydraulic diameter and all microchannels have a length-to-diameter ratio (L/D_h) of at least 100 to assure fully developed flow at the channel exit. In addition, to analyze the effect of dimensional scaling, the experimental data are compared with conventional entrance length correlations.

Length	500 μm Test Section (mm)	200 μm Test Section (mm)	100 μm Test Section (mm)
A	68	35	25
B	50	25	25
C	54	30	30
D	126	76	76
E	60	26	26
F	50.8	20	20
t	0.1	0.076	0.03

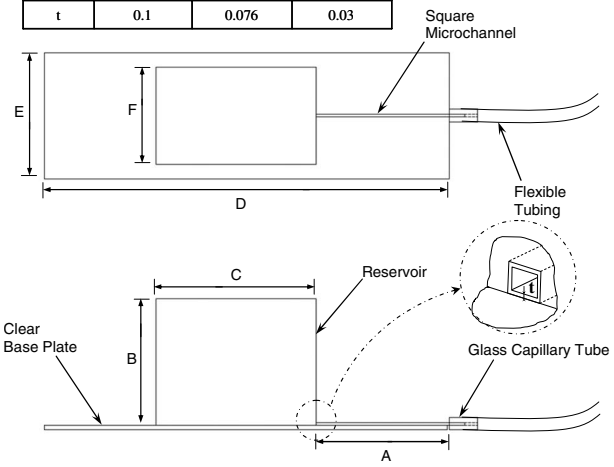

Fig. 1 Top and side views of test-section configuration used in present study

2 Experimental Analysis

2.1 Test-Section. In order to fundamentally study microchannel entrance region characteristics from a very large reservoir, conventional fabrication methods were applied to satisfy this geometrical constraint. Three test-sections, as shown in Fig. 1, were designed to provide a sharp-edged microchannel inlet from a very large reservoir relative to the hydraulic diameter of the channel. For each of the 500 μm, 200 μm, and 100 μm microchannels, an appropriate test-section was fabricated, dimensions of which are also given in Fig. 1. The borosilicate thin-walled glass microchannels used in fabricating the present test-sections are commercially available, manufactured and cut to length by Friedrich & Dimmock, Inc., Millville, NJ. All microchannels possess a square cross-section ($H/W=1$) in order to remove any influence of aspect ratio and to distinctly study the geometric influence of scaling in the microchannel entrance region.

The micro-PIV technique implements a similar method as conventional PIV, in that velocity flow fields are acquired by tracking the trajectories of seeding particles immersed in the flow. However, where conventional PIV typically illuminates a single measurement plane 1–3 mm thick, micro-PIV illuminates the entire volume of the test-section. Illuminating the entire volume is necessary due to the relative dimensions at the microscale, where the formation and aligning of a very thin light sheet would be extremely difficult [25]. Therefore with the entire volume of the flow

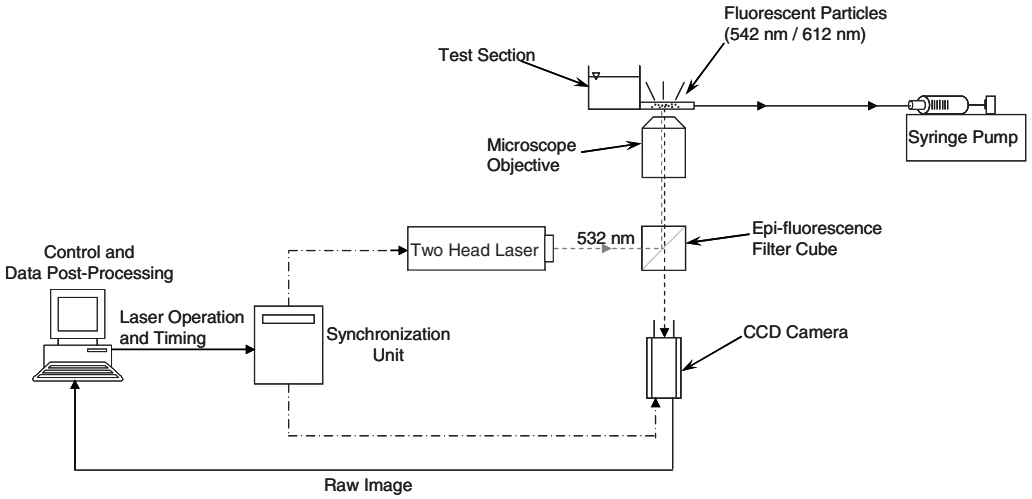

Fig. 2 Experimental setup of micro-PIV system with flow loop

field illuminated, fluorescently dyed particles are necessary to track the flow. Opposed to conventional PIV, where the depth of the measurement volume is defined by the thickness of the laser sheet, in micro-PIV the depth of measurement volume is defined by the numerical aperture and magnification of the microscope objective, the seed particle diameter, the particle emission wavelength, Brownian motion, and out-of-plane motion [33,34]. Therefore, to implement the micro-PIV technique, the test-section must be optically accessible from at least one direction, as is the case with etched silicon microchannels. However, in the present study the entire test-sections are optically clear, having advantages of increased illumination, test-section alignment with the microscope objectives, and a readily observable test setup. In addition, the thin-walled glass microchannels provided good optical qualities ideal for micro-PIV laser emission.

All test-sections were fabricated using a similar method. Depending on microchannel dimension and objective working distance, either a 3 mm thick clear polycarbonate sheet (500 μm channel) or 1 mm thick clear glass slide (200 μm and 100 μm channels) was used as a base plate for the test-section (Fig. 1). The base plate provided rigidity for the test setup, as well as provided an optically clear flat surface for laser emission, necessary for micro-PIV. Four vertical polycarbonate walls were then bonded onto one end of the base plate using general purpose clear epoxy (Permatex), and sealed with silicone. These four walls, along with the base plate, served as the open air inlet reservoir to the microchannel, as shown in Fig. 1. The walls were bonded together and sealed only on the exterior, as not to interfere with the flow inside the reservoir. Using a sawing technique, a small groove (on the order of the external dimensions of the microchannel) was machined at the bottom center of the reservoir wall bordering the microchannel inlet to provide a slot to seat the microchannel. Once the reservoir had been sealed and cured, the respective microchannel was carefully slid into the machined groove until the channel inlet was flush with the interior wall of the reservoir. Also, similar to an etched microchannel in a silicon substrate, from Fig. 1 it can be seen that the base of the inlet reservoir was almost on the same plane as the microchannel base, taking into account the wall thickness of the channel. The microchannel was then bonded to the base plate and reservoir wall using the clear epoxy. A capillary tube was slid onto the microchannel exit and bonded to the base plate. Flexible tubing (Tygon) was then fixed firmly to the capillary tube to provide an adaptable path to the syringe pump.

2.2 Micro-PIV System and Flow Loop. The experimental flow loop, along with a schematic of the micro-PIV system used in the present investigation, is shown in Fig. 2. The flow loop consists of the test-section and a syringe pump. The syringe pump (New Era Pump Systems, Wantagh, NY, model NE-1000) can be operated in either infusion or withdrawal modes and is programmed for desired flowrate and syringe diameter. Within the test-section reservoir is distilled water immersed with fluorescent polymer microspheres dyed seeding particles (Duke Scientific, Palo Alto, CA) with an excitation/emission wavelength of 542 nm/612 nm and a density of 1.05 gm/cm^3. Mean particle diameters were 3 μm, (about 5 pixels in case of the 500 μm channel), 2 μm (about 6 pixels in case of the 200 μm channel), and 1 μm (about 3 pixels in case of the 100 μm channel). With the syringe pump operating in withdrawal mode, the fluid is steadily withdrawn from the inlet reservoir through the microchannel and into a syringe incorporated with the syringe pump, as illustrated in Fig. 2.

Figure 2 includes a schematic of the micro-PIV system, which was acquired as a commercial package from Dantec Dynamics, Ramsey, NJ. The primary components associated with the micro-PIV system are a pulsed laser light, an inverted epifluorescent microscope, a CCD camera, a synchronization unit, and specialized computer software (FLOWMANAGER v4.50).

A dual-pulsed Nd:YAG laser light at 532 nm (New Wave Research, Freemont, CA) is passed through a beam expander assembly, and directed into the inverted microscope (Nikon Eclipse TE2000-S), incorporating both coarse and fine focus knobs. The laser pulses are controlled through the FLOWMANAGER computer software. The test-section is securely positioned on the stage of the inverted microscope below which the objectives are located. The stage is a horizontal table, capable of fine movements in both the streamwise and spanwise directions. The objectives (of magnification 2X, 4X, 10X, 20X, 40X, and 60X) are all mounted on a turret below the stage, for simplicity in changing from one magnification to another. The microscope also incorporates an epifluorescent filter cube (Chroma Technology, Bellows Falls, VT), necessary for tracking the fluorescent particles due to volume illumination. The filter cube is configured for excitation with green laser light (band pass at 535 nm, band width of 50 nm) and fluorescence emission in the orange part of the spectrum (band pass at 610 nm, band width of 75 nm). The filter cube also contains a dichoric mirror, which ensures efficient transfer of laser light to the test-section while providing transmission of the fluorescence signal to detect, as well as reducing background reflections. On one side of the microscope is a camera port to mount the HiSense MkII CCD camera (Hamamatsu Photonics, Hamamatsu-City, Japan). The microscope image is delivered to the camera

through a camera adapter (1X magnification). The camera operation is also controlled through the computer software, and synchronized with the laser through the synchronization unit (Fig. 2).

The particles are excited by the dual-pulsed laser light at a wavelength of 532 nm, and emit fluorescent light at a wavelength of about 612 nm. Imaging of the particles is done using the inverted microscope fitted with the designated objective (i.e., 10X (NA=0.25, DOF=8.5 μm) for 500 μm channel, 20X (NA =0.40, DOF=5.8 μm) for the 200 μm and 100 μm channels), and the epifluorescent filter cube. Within a predetermined time sequence depending on the flowrate, the CCD camera acquires two sequential images in unison with the two pulses from the laser, and transmits it to the computer equipped with the FLOWMANAGER software for post-processing.

2.3 Experimental Parameters and Procedure. Micro-PIV data sets were recorded for the three microchannels at the center plane at incremental axial distances from the microchannel inlet. The overlapping incremental axial distances were at 0.5 mm for the 500 μm channel and 0.25 mm for the 200 μm and 100 μm channels. There was considerable overlap in the axial images, as to reduce the error associated with the process. The particle concentration in the distilled water for the 500 μm channel (3 μm particles) was ~0.0141% by volume, for the 200 μm channel (2 μm particles) was ~0.0168% by volume, and for the 100 μm channel (1 μm particles) was ~0.0223% by volume. These concentrations were used based on an experimental trial process and are very low; hence the mixture can be considered as a single phase liquid. The desired flowrates were programmed into the syringe pump operating in withdrawal mode. With a known volume flowrate Q the Reynolds (Re) number was calculated as

$$\mathrm{Re} = \frac{QD_h}{\upsilon A} \tag{1}$$

where D_h is the hydraulic diameter, υ is the kinematic viscosity, and A is the cross-sectional area of the channel. The kinematic viscosity was assumed constant at room temperature.

Spatial calibration was carried out with the use of the FLOWMANAGER software for each axial position recorded. The maximum energy the laser can supply is 120 mJ/pulse, where 9.6 mJ was employed for the 100 μm channel, 10.8 mJ was employed for the 200 μm channel, and 12 mJ was employed for the 500 μm channel. Based on an initial trial process, 30 sequential image pairs were used for each data set and were recorded three times to assure repeatability in the data. Interrogation areas of 32×64 pixels were used for all channels, and the time between the image pairs (Δt) was chosen as to have mean particle displacement of 25% within the interrogation area. The 30 image pairs were correlated using the adaptive correlation technique (Dantec Dynamics), then filtered (3×3 window) and temporally averaged to produce a vector plot of the flow field. Prior to the entrance length measurements, vector plots for each Re number were recorded in the fully developed region to assure validation with the 2D Navier–Stokes momentum equations for a rectangular duct at the center plane.

2.4 Experimental Uncertainty. The uncertainty in the process, tabulated in Table 1, resulted from the syringe pump (i.e., flowrate), the width of the channels, the channel center plane, transversing along the channel length, as well as the micro-PIV system. The syringe pump employs a stepper motor and worm gear, as well as a plunger-type syringe. The uncertainty was higher at low flowrates due to the friction of the plunger and the operation of the stepper motor. Regardless, the highest uncertainty in the flowrate was observed to be 2–4% using the nominal channel widths. The uncertainty in the channel widths, provided by the manufacturer was ±10% for all channels, giving an uncertainty in Re of ~10.8%. The micro-PIV data were validated at the center plane in the fully developed region using the Navier–Stokes equations with an uncertainty of less than 4%. However the uncertainty in Re, as well as the uncertainty in validation with the Navier–Stokes equations, is largely due to the high uncertainty in the widths of the channels.

Table 1 Uncertainties in experimental parameters of present investigation

Parameter	Maximum uncertainty		
	100 μm test-section	200 μm test-section	500 μm test-section
Channel width (%)	±10	±10	±10
Flowrate (%)	2–4	2–4	2–4
Reynolds number (%)	10.8	10.8	10.8
Navier–Stokes validation (%)	3.8	3	3
Brownian motion (%)	1.51	1.28	1.24
Particle image displacement (nm)	200.9	265.2	444.9

The random errors due to micro-PIV are random error due to Brownian motion and random error due to interrogation and resolution. These are also tabulated in Table 1. When sufficiently small seeding particles are immersed in a fluid, random particle movements become apparent due to fluid-particle interactions on the molecular level, known as Brownian motion. Since the particle is sufficiently small, there is an unbalance in the surrounding fluid molecules colliding with the particle, causing it to randomly move. However, Brownian motion becomes of lesser importance as the seeding particle size increases or as the fluid velocity increases, particularly above 10 μm/s [22]. Regarding the error in Brownian motion, a method in estimating the uncertainty was similar to that given by Santiago et al. [22]. A large error was not expected since the flow velocities are large for microchannels, even at small Re numbers. The largest error due to Brownian motion was 1.51%, which was for the 100 μm channel at Re =0.476.

The random error due to interrogation and resolution is due to the uncertainty in the seeding particle image displacement. Larger particles generally increase these random errors since they have a larger particle image size and occupy more pixels. Also, since a CCD camera is used, the pixel size is fixed; therefore to reduce random errors due to interrogation, the particle image size must be reduced [35]. For micro-PIV, as stated by Santiago et al. [22] since the shape of the particles is known, the relative position of the particles can be determined with a resolution ten times greater than that of the microscope. Using a method similar to that outlined by Santiago et al. [22], the largest uncertainty in particle image displacement was estimated to be approximately 445 nm. As shown in Table 1, this uncertainty was for experiments using the 500 μm channel, where the largest particles (3 μm) were used.

3 Results and Discussion

Experimental velocity flow field data have been acquired in the entrance region of microchannels using micro-PIV. Three square cross-sectional microchannels were investigated in order to remove any effect of cross-sectional aspect ratio. The microchannels have hydraulic diameters (D_h) of 100 μm, 200 μm, and 500 μm, over a laminar Reynolds number range of 0.5–200. The microchannel inlets were sharp-edged from a very large reservoir relative to the microchannel hydraulic diameter, and the reservoir and microchannel share a common wall. The fluid at the reservoir interface is stagnant, as to impose minimal predevelopment upstream of the microchannel entrance, and to obtain a relatively flat inlet velocity profile. Fig. 3 shows the coordinate system used in the present analysis. Since micro-PIV images are acquired through the use of the microscope objectives beneath the test-section, flow field data are attained at the center plane, at half the microchannel height. The height is denoted by the y coordinate, the spanwise

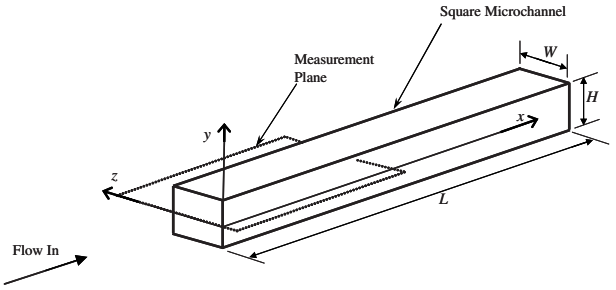

Fig. 3 Experimental coordinate system used in present investigation

direction is denoted by the z coordinate, and the axial direction is denoted by the x coordinate, where the origin is at the microchannel inlet. It should be noted that since the cross-sectional aspect ratio is one, the microchannel width W is identical to the microchannel height H.

3.1 Inlet Flow Mechanism. Figures 4(a) and 4(b) depict the flow separation effects produced by the corners of a sharp-edged inlet. Figure 4(a) shows a schematic of the theoretical flow pattern that is found in the entrance region when the flow enters a channel that is flush with the inlet reservoir, thereby producing sharp-edged corners and acting as an orifice. The corners have a physical effect on the flow field thereby producing a vena contracta, which is characterized by the point of minimum area and maximum flow contraction. As the flow contracts just downstream of the channel inlet, flow separation regions form, as shown in Fig. 4(a). Figure 4(b) shows the experimental vector flow field in the measurement plane, produced using micro-PIV for the 200 μm microchannel at Re=50. It is possible to see the very low velocity flow in the inlet reservoir accelerating as it approaches the sharp-edged inlet of the microchannel. The inlet corners produce a disturbance on the flow field and force the fluid to contract, producing the vena contracta effect, demonstrating the inability of the flow to turn the 90 sharp corner. The flow then diverges to occupy the entire channel area. This figure is useful in demonstrating both the capability of micro-PIV in terms of visualizing the flow field, as well as a qualitative comparison with the conventional physical mechanism associated with the corner effects on the entrance region.

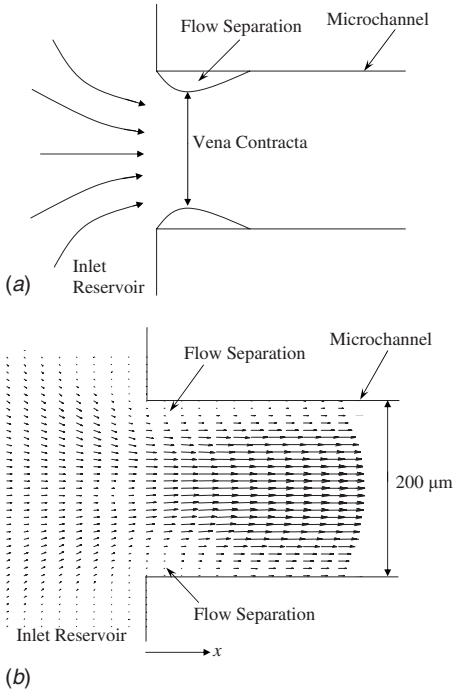

Fig. 4 Flow separation effects produced by sharp edge corners at the entrance region of the microchannel: (*a*) theoretical flow pattern and (*b*) experimental vector flow field for the 200 μm channel at Re=50

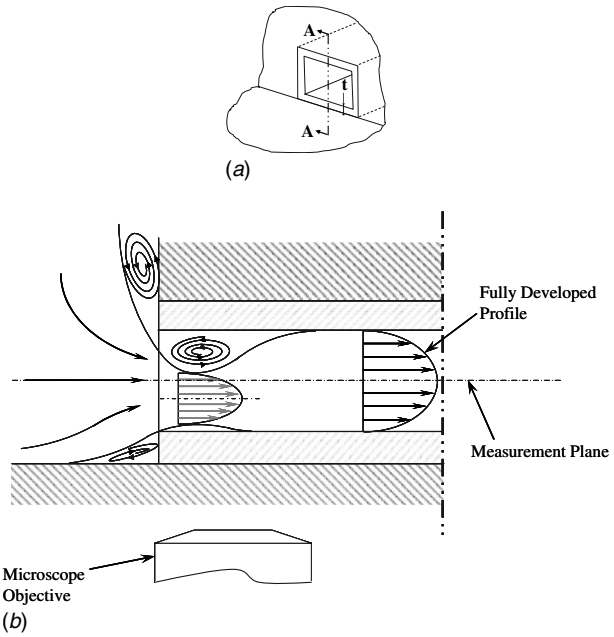

Fig. 5 Test-section microchannel inlet configuration: (*a*) isometric view of the microchannel entrance with the reservoir walls and (*b*) separation zone at section A-A for the microchannel entrance due to the nonsymmetric vena contracta effect

Figure 5(a) shows that the bottom surface of the microchannel is higher than the bottom surface of the reservoir by the microchannel wall thickness, t. In addition, the proximity of the channel bottom wall to the bottom of the reservoir is significantly less relative to the top surface of the microchannel to the top of the reservoir. This configuration is similar to typical microfluidic devices, where the plenum and the microchannel share a wall in the same plane. Consequentially, the separation region size at the bottom of the microchannel entrance is smaller than the separation region size at the top of the microchannel entrance creating a nonsymmetric vena contracta, as shown in Fig. 5(b). In the separation zone, zero or negative velocity is expected due to the vorticity created near the wall at the entrance region of the channel.

In the measurement plane, as shown in Fig. 4(b), a symmetric vena contracta is produced since the proximity of the plenum walls to the microchannel walls are the same. However in the vertical plane the nonsymmetric separation zones shift the inlet velocity profile down, as shown in Fig. 5(b). The inlet maximum velocity is not in the measurement plane at the geometric center of the microchannel. Downstream of the inlet, where the separation zone is reduced, the maximum velocity lies in the measurement plane at the center of the channel. The vena contracta size depends on Re, where the higher the Reynolds number the bigger and more extended the vena contracta size. Also, the vena contracta size has a bigger impact on the flow for smaller width channels due to the proximity of the channel walls to each other.

3.2 Developing Velocity Profiles. Figures 6(a)–6(d), 7(a)–7(d), and 8(a)–8(d) show the developing velocity profiles at incremental axial locations along the microchannel length, for the 100 μm, 200 μm, and 500 μm microchannels, respectively. These figures serve to demonstrate the quantitative as well as qualitative data obtained using micro-PIV, by observing the devel-

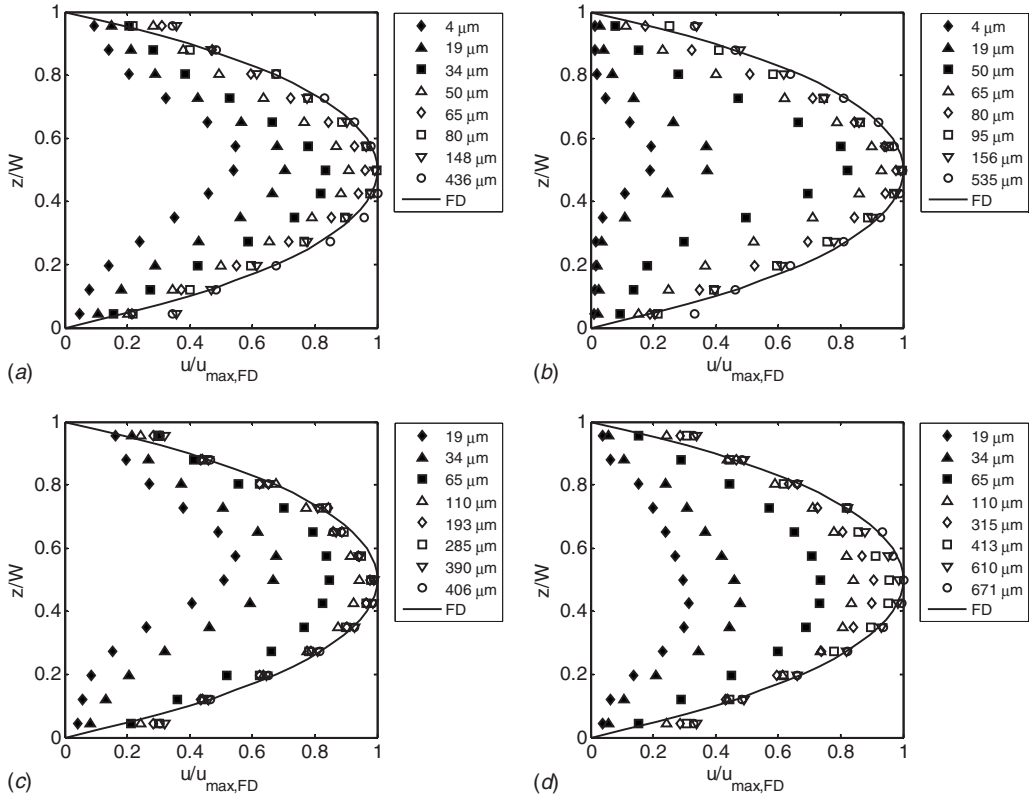

Fig. 6 Developing velocity profiles for the 100 μm channel at Re of (*a*) 0.476, (*b*) 4.76, (*c*) 50, and (*d*) 89

oping velocity profiles. The plots are normalized in the spanwise direction (z) with the microchannel width (W) on the y-axis, and with the theoretical maximum (centerline) fully developed axial velocity on the x-axis ($u/u_{\max,FD}$). In addition, each plot shows the theoretical fully developed velocity profile with a solid line, given by the 2D Navier–Stokes equations. The plots show the physical mechanism of developing flow. When flow enters the channel from a large reservoir, the velocity of the fluid coming in contact with the inner channel wall is immediately reduced to zero. This drag disturbance creates shear waves that propagate from all walls toward the center of the channel. The presence of these shear waves causes the adjacent fluid layers to adjust while the fluid at the center of the channel that is not yet affected by the disturbance, begins to accelerate in order to satisfy continuity. This process continues along the length of the channel, altering the velocity profile within the channel. Once the entire flow field adjusts to the no-slip boundary condition at the channel walls, the flow is said to be fully developed and there is minimal change in the velocity profile downstream. As the experimental data show for the three investigated microchannels, it is evident that there is faster development at lower Re numbers and far downstream from the inlet, there is very little, if any, change in the experimental profile, indicating fully developed flow and good agreement with the theoretical profile.

The inlet flow path is also influenced by the corner effects at the microchannel inlet, causing a vena contracta, as explained in Figs. 4 and 5. However, at higher Re numbers the nonsymmetrical separation zones becomes evident for all channels, in particular for the 100 μm channel due to its relative size. For example, comparing Figs. 6(*a*) and 6(*b*), the maximum velocity at 4 μm from the channel inlet is higher for Re=0.476 ($u/u_{\max,FD}\sim 0.5$) than for Re=4.76 ($u/u_{\max,FD}\sim 0.2$). This is due to the larger nonsymmetrical separation zone in the vertical plane of the channel, causing a greater shift in the inlet velocity profile, as shown in Fig. 5(*b*). Similar comparisons can be seen in Figs. 6(*c*) and 6(*d*) at 19 μm from the channel inlet, and for Figs. 7 and 8.

Also, from Figure 6, it can be seen that for the 100 μm channel the profile just downstream from the inlet (at 4 μm (Re=0.476 and 4.76) or at 19 μm (Re=50 and 89)) is already in its developing shape since the center velocity is beginning to accelerate. Failure to observe a more flat profile just downstream of the inlet is probably due to the interrogation area size in the axial direction, where a smaller size may be necessary. In addition, these initial profiles are slightly skewed and then sequentially level out towards a more uniform shape as the flow develops downstream. This initial skewed inlet flow was also experimentally observed by Lee et al. [32]. The authors explained that it was due to the asymmetric flow path from the reservoir to the channel entrance, which is more evident at smaller channel dimensions. A similar observation can be seen in Fig. 7 for the 200 μm channel, however the skewness of the inlet profiles is less evident than for the 100 μm channel. In most test cases for this channel size, a certain degree flatness of the early developing profiles can be seen, however there is an indent at the center, possibly caused by the flow contraction effects at the inlet. For the 500 μm channel, from Fig. 8, a more classical development can be observed, particularly at higher Re numbers of 50 and 200. At these higher Re numbers, a flat profile just downstream from the inlet is evident, where the drag disturbance from the presence of the channel walls has not yet entirely altered the velocity profile. The profiles then sequentially develop downstream. For low Re numbers (0.5 and 5), similar observations can be seen for the early profiles as stated for the 200 μm channel with slight skewness and flow contraction effects. Qualitatively then, for all three investigated channels, there is good agreement with the physical mechanisms for hydrodynamically developing flow.

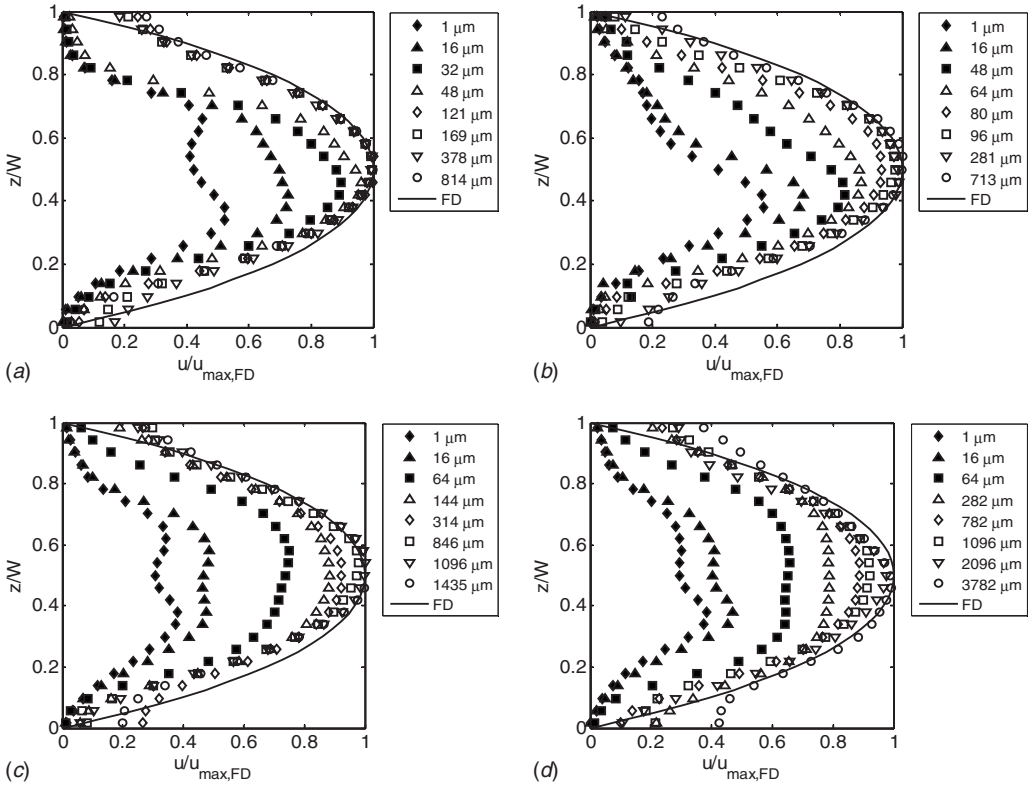

Fig. 7 Developing velocity profiles for the 200 μm channel at Re of (*a*) 0.5, (*b*) 5, (*c*) 50, and (*d*) 200

3.3 Centerline Velocity Development. Figures 9(*a*)–9(*d*), 10(*a*)–10(*d*), and 11(*a*)–11(*d*), show the centerline velocity development along the microchannel axial distance for the 100 μm, 200 μm, and 500 μm channels, respectively. The y-axis shows the local centerline velocity (u_{cl}) normalized with the theoretical fully developed centerline velocity ($u_{cl,FD}$), whereas the x-axis shows the nondimensional axial distance, normalized with the channel hydraulic diameter, as well as the Re number ($x/\mathrm{Re}\,D_h$) to incorporate its effect. The plots show the general hydrodynamic entrance length criterion, which is the location, where the local centerline velocity has attained 99% of its fully developed value. It should be emphasized that theoretically speaking, the velocity continually increases and the distance required to attain the fully developed profile is infinitely large [13]. However, for engineering applications, the 99% criterion is suitable in defining the entrance length in a channel. From all plots, a common trend can be seen; it is evident that there is a definite increase in the centerline velocity, which levels out toward a somewhat constant value at $u_{cl}/u_{cl,FD} \sim 0.99$. For the 100 μm channel, from Figs. 9(*c*) and 9(*d*), it can be seen that at higher Re numbers of 50 and 89, both trends reach $u_{cl}/u_{cl,FD} \sim 0.99$ at relatively the same nondimensional axial distance, between 0.065 and 0.085. A similar observation can be seen from Figs. 10(*c*) and 10(*d*) for the 200 μm channel and from Figs. 11(*c*) and 11(*d*) for the 500 μm channel, at Re numbers of 50 and 200, respectively. Regarding the plots at lower Re numbers of 0.476 and 4.76 for the 100 μm channel (Figs. 9(*a*) and 9(*b*)), the axial distance at which the data reach $u_{cl}/u_{cl,FD} \sim 0.99$ is observed to be rather high, at about 0.17 for Re=4.76 and increases to about 1.7 for Re=0.476. Similarly for the 200 μm channel (Figs. 10(*a*) and 10(*b*)), at Re=0.5 and Re =5, the axial distances at which fully developed flow (0.99) is reached are high at 0.19 and 1.2, respectively. A similar observation can be made for the 500 μm channel at Re=0.5 and Re=5 (Figs. 11(*a*) and 11(*b*)), where the axial distance is roughly 0.7. With these results, it can be seen that there is little influence of dimensional scaling for the three channels investigated but a higher dependence of the entrance length on the Reynolds number.

One can conclude that, similar to the statement of Lee et al. [32] since the channel bottom wall and reservoir bottom wall lie on the same plane, the inlet velocity profile is not completely uniform, and because of this, as stated by Shah and London [12] and Atkinson et al. [15], the entrance length at higher Re numbers are less affected by the inlet velocity profile. However, for lower Re numbers, as stated by Vrentas et al. [36], there is a high dependence of the entrance length on the inlet velocity profile due to the axial diffusion of vorticity. Vrentas et al. [36] numerically showed the effect of vorticity for a pipe with an upstream inlet reservoir. The fluid in the inlet reservoir, initially free of vorticity, develops a vorticity field as it enters the pipe. This vorticity is generated at the walls of the pipe, and then transmitted from the wall to the fluid by convection and diffusion. The authors found that the vorticity transfer from the walls to the fluid is influenced by the Re number, in that at low Re numbers, vorticity appears in the reservoir, causing some flow development upstream from the tube entrance, and hence not a uniform velocity profile at the inlet. The degree of centerline velocity profile development upstream from the channel inlet increases as Re is decreased, particularly below 50 ($\mathrm{Re} < 50$), which will have an effect on the entrance length. This can be the case for the lower Re numbers of 0.5 and 5 for the three investigated channels.

3.4 Hydrodynamic Entrance Length. Figure 12 depicts the entrance length (L_e/D_h) for the 100 μm, 200 μm, and 500 μm channels, versus the Re number, in logarithmic scale in order to amplify the effects at low Re numbers. There are four data points for the 100 μm channel (Re=0.476, 4.76, 50, and 89), four data points for the 200 μm channel (Re=0.5, 5, 50, and 200), and four

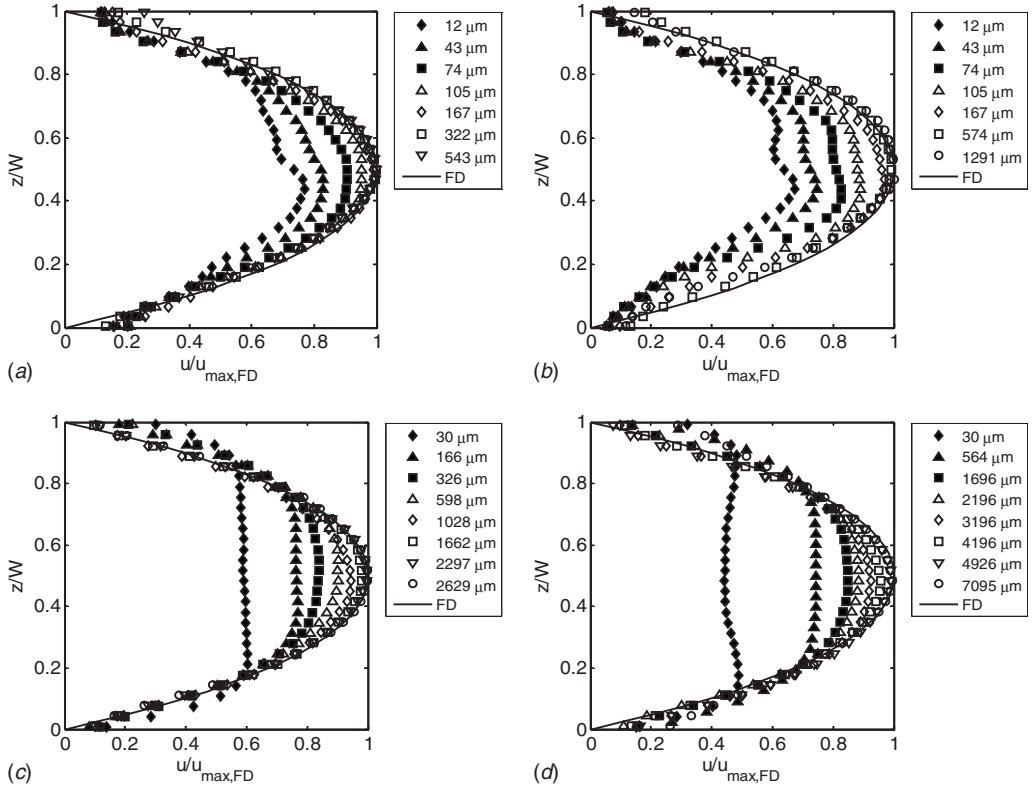

Fig. 8 Developing velocity profiles for the 500 μm channel at Re of (*a*) 0.5, (*b*) 5, (*c*) 50, and (*d*) 200

data points for the 500 μm channel (Re=0.5, 5, 50, and 200). The entrance length was taken from the data collected in Figs. 9–11, for the 100 μm, 200 μm, and 500 μm channels, respectively, and it is the length (L_e) at which $u_{cl}/u_{cl,FD} \sim 0.99$. Regarding this criterion experimentally, the entrance length was taken as the length at which $u_{cl}/u_{cl,FD}$ remained relatively steady at 0.99 or crossed 0.99, depending on the trend of data. To analyze any effect of scaling, the overlapping range of data points for the investigated channels were also compared. From the figure, it can be seen that for high Re numbers (Re$>$10) there is no influence of dimensional scaling. However, it can be seen that at lower Re numbers (Re$<$10), there is a minor discrepancy between the entrance lengths of the 100 μm and 200 μm channels compared with that of the 500 μm channel. This can lead to a slight dimensional scaling effect at low Re numbers for the 500 μm channel. In addition, the experimental data are compared with conventional entrance length correlations. The numerical correlations given by Han [13] and Wiginton and Dalton [16] are linear correlations, where the entrance length is proportional to the Reynolds number by some constant, depending on the cross-sectional aspect ratio. For an aspect ratio of 1, the correlation of Han [13] is given by

$$\frac{L_e}{D_h} = 0.0752\ \mathrm{Re} \tag{2}$$

whereas the correlation of Wiginton and Dalton [16], for an aspect ratio of 1, is given by

$$\frac{L_e}{D_h} = 0.09\ \mathrm{Re} \tag{3}$$

According to Shah and London [12], the equation given by the model of Wiginton and Dalton [16] is more accurate, whereas that of Han [13] is low since he calculated rapid flow development. From Fig. 12, it can be seen that at high Re numbers (Re$>$10), there is good agreement between the experimental data and the correlations given by Han [13] and Wiginton and Dalton [16]. However, at low Re numbers, below 10, there is not good agreement. This is due to the fact that since these correlations are linear, and at very low Re numbers, L_e/D_h goes towards zero. This may have little effect in conventional ducts where modest Reynolds numbers are applied. However, at the microscale, very low Reynolds numbers can be practically applied, where there indeed exists a finite value for the entrance length. This is apparent from the data, where at low Re numbers (i.e., Re=0.5 or 5), there is a definite entrance length value. For low Re numbers one can consider entrance length correlations given by Atkinson et al. [15] and Chen [17], both for parallel plates. The parallel plate correlation of Atkinson et al. [15] is given by

$$\frac{L_e}{D_h} = 0.625 + 0.044\ \mathrm{Re} \tag{4}$$

whereas the given correlation of Chen [17] for parallel plates is given by

$$\frac{L_e}{D_h} = \frac{0.63}{0.035\ \mathrm{Re} + 1} + 0.044\ \mathrm{Re} \tag{5}$$

It should be noted in Eqs. (4) and (5) the hydraulic diameter of a square channel ($D_h=W=H$) is used in the definitions of Re and D_h. Looking at these two above correlations, when Re is high, a linear curve is depicted. However, when Re is low, both correlations level out to a constant value and are independent of Re. This is shown in Fig. 12. Comparison of the present experimental data with these two parallel plate correlations reveals very good agreement for the 100 μm and 200 μm channels, particularly at low Re numbers (0.5 and 5). Regarding the 500 μm channel, adequate agreement is found at lower Reynolds numbers; however the error is greater than for the 100 μm and 200 μm channels (a possible scaling effect). At the higher Re range ($>$10) there is adequate agreement for all investigated channels, however better

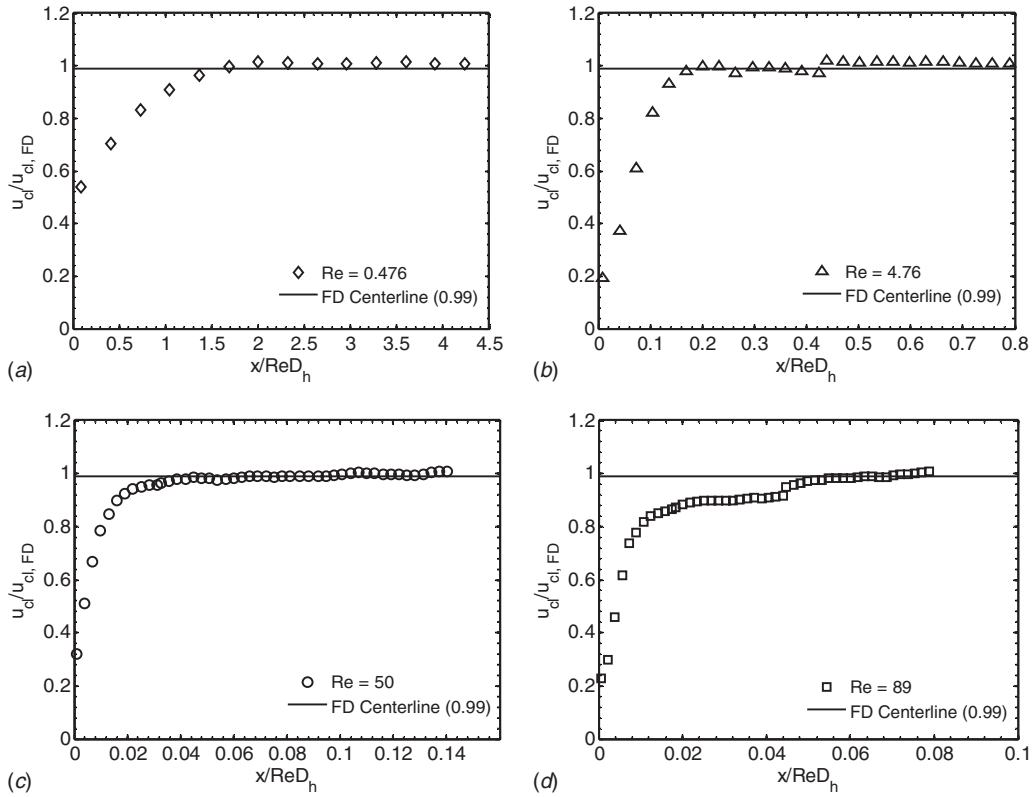

Fig. 9 Centerline velocity development for the 100 μm channel at Re of (*a*) 0.476, (*b*) 4.76, (*c*) 50, and (*d*) 89

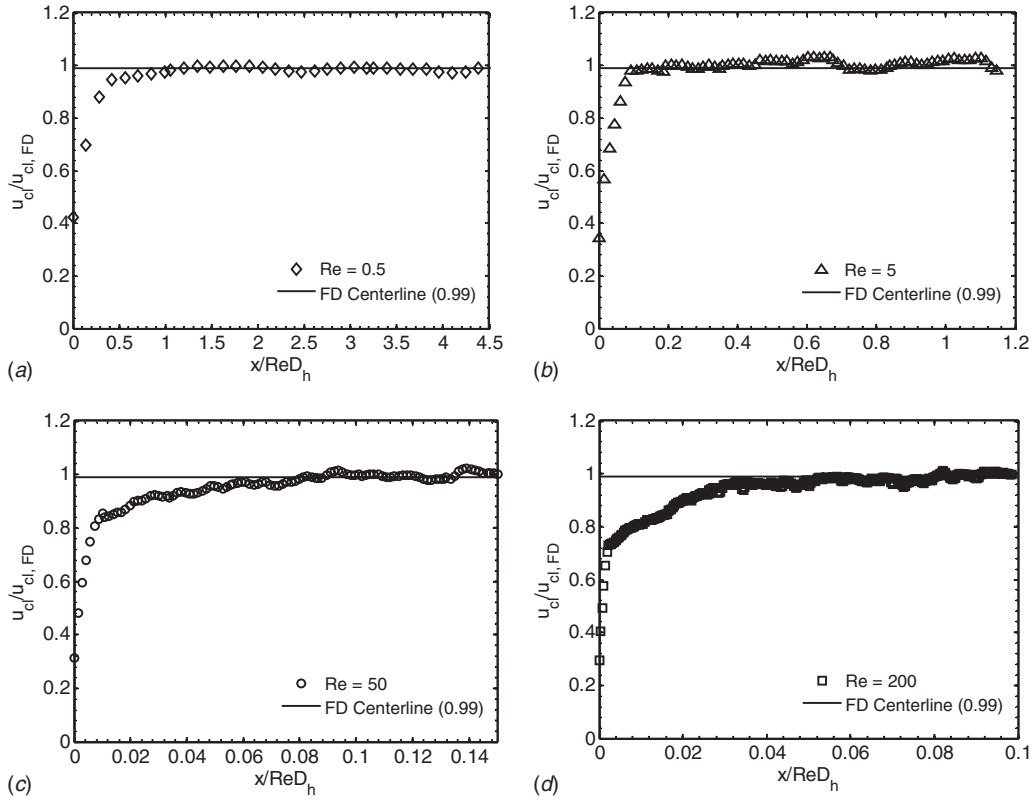

Fig. 10 Centerline velocity development for the 200 μm channel at Re of (*a*) 0.5, (*b*) 5, (*c*) 50, and (*d*) 200

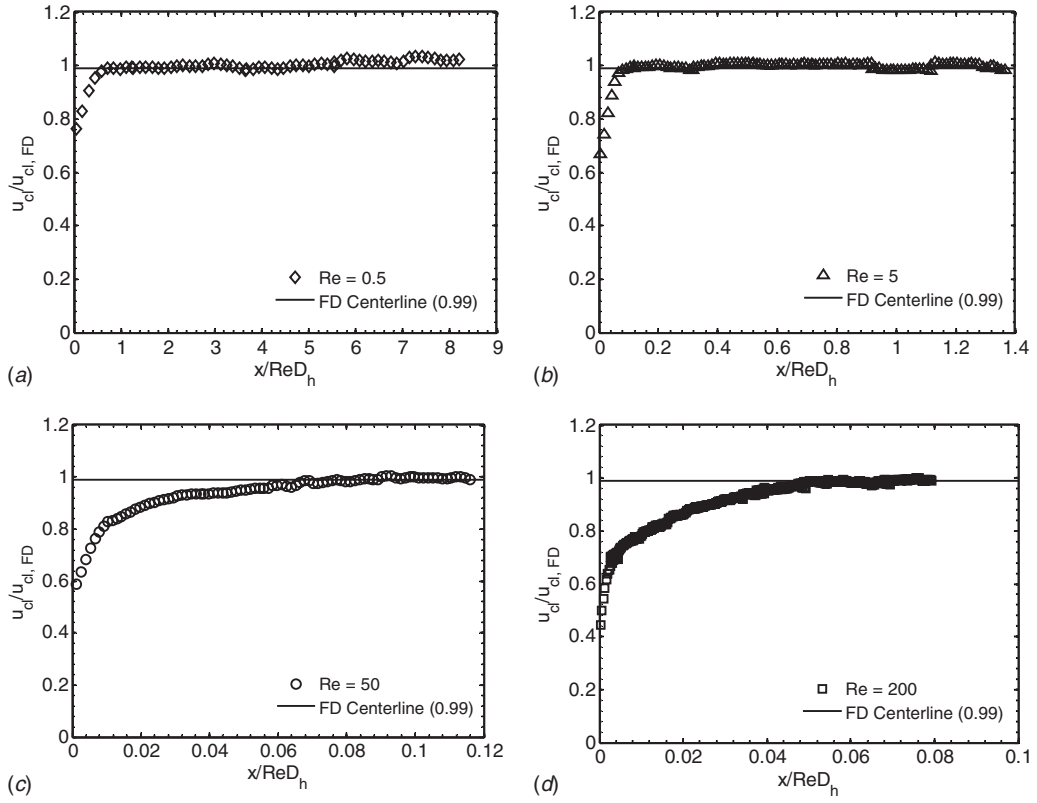

Fig. 11 Centerline velocity development for the 500 μm channel at Re of (*a*) 0.5, (*b*) 5, (*c*) 50, and (*d*) 200

agreement was found with comparison to the conventional correlations for ducts, notably that of Han [13]. From the present experimental data, these parallel plate correlations are better suited for the prediction of the entrance length in microchannels at very low Reynolds numbers (<10).

3.5 Entrance Length Correlations. In light of the previous discussion with comparison of the present entrance length experimental data with conventional correlations, new entrance length correlations are proposed. These new correlations are applicable in predicting the entrance length in microchannels and will aid in the design of future microfluidic devices. As was seen in Fig. 12, there was very good agreement at high Reynolds ($\mathrm{Re}>10$) numbers with conventional correlations for ducts, notably that of Han [13] from Eq. (2). For lower Re numbers ($\mathrm{Re}<10$), there was very good agreement with parallel plate correlations, given by Atkinson et al. [15] and Chen [17] from Eqs. (4) and (5). These two entrance length parallel plate correlations were established by numerically solving for the creeping flow solution at low Re numbers, and adding the result to a high Re number asymptote provided by Bodoia and Osterle [37], which is 0.044 Re. However, from Fig. 12, it can be seen that at higher Re numbers there is poor agreement with these parallel plate correlations but better agreement with conventional duct correlations, particularly that of Han [13]. Applying a similar method and form of equation as Chen [17] but replace the high Reynolds number asymptote with the correlation of Han [13], the following empirical correlation is obtained:

$$\frac{L_e}{D_h} = \frac{0.63}{0.035\ \mathrm{Re} + 1} + 0.0752\ \mathrm{Re} \tag{6}$$

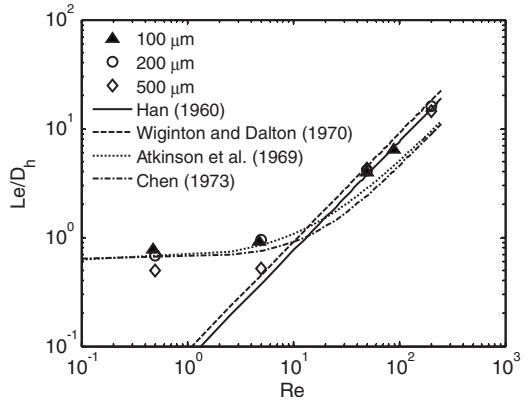

Fig. 12 Entrance length comparison between present data and conventional correlations

Figure 13(*a*) shows Eq. (6) plotted along with the present experimental entrance length data for the 100 μm and 200 μm channels. From the figure, excellent agreement can be seen over the whole range on Re numbers, and quantitatively, from Fig. 13(*b*), the correlation fits all the data to within 15%. This correlation however, does not fit well with the experimental data obtained for the 500 μm channel. Therefore, it can be said that Eq. (6) is well suited in predicting the entrance length in square microchannels ($H/W=1$) for hydraulic diameters below 500 μm, over a wide range of laminar Reynolds numbers from 0.5 to 1000.

In finding an empirical correlation that fits all the present experimental data for the 100 μm, 200 μm, and 500 μm channels, another correlation is developed. Once again, an equation in the form of the correlation of Chen [17] is applied. From Fig. 12, it can be seen that at high Re numbers ($\mathrm{Re}>10$), all present experimental data fit the correlation of Han [13] very well, therefore once again it will be used for the high Reynolds number asymp-

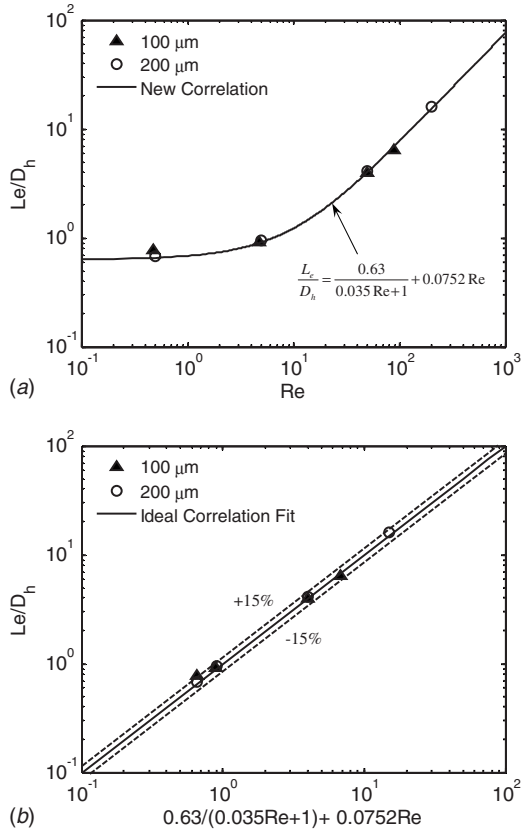

Fig. 13 Proposed entrance length correlation for square microchannels below 500 μm with present experimental data of the 100 μm and 200 μm channels and the error in the fit

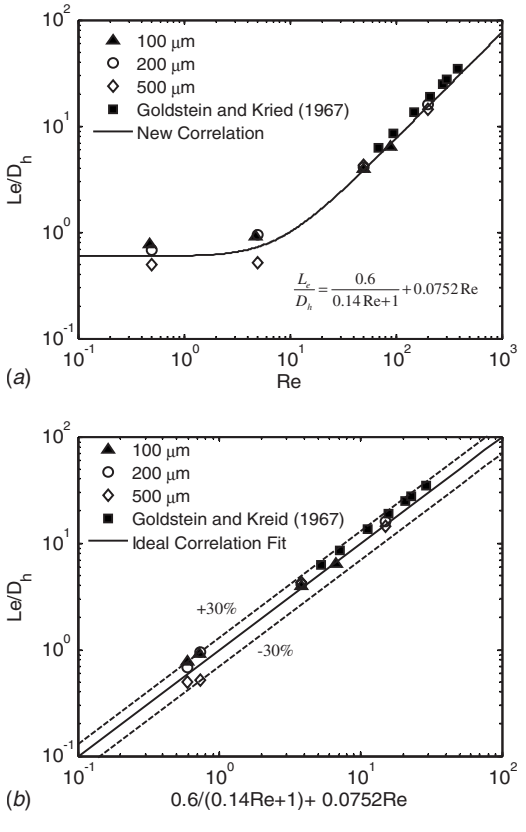

Fig. 14 Proposed entrance length correlation for square channels at the microscales and macroscales and the error in the fit

tote. Applying a curve fit in the form of the correlation of Chen [17] at the low Re numbers, the following correlation is found:

$$\frac{L_e}{D_h} = \frac{0.6}{0.14\,\mathrm{Re}+1} + 0.0752\,\mathrm{Re} \tag{7}$$

Figure 14(*a*) shows Eq. (7) plotted with the present experimental data (100 μm, 200 μm, and 500 μm channels) along conventional experimental data produced from Goldstein and Kreid [19] for a square duct within a Re range of 69–387. These authors investigated flow development using a laser-Doppler flowmeter in a square duct with a hydraulic diameter of 1 cm, as shown in Table 2. From Fig. 14(*b*), it can be seen that the experimental data fit the empirical correlation to within 30%. Equation (7) shows to fit well with all the data over the whole range of Re numbers, and can be used as a general entrance length correlation for channels of square cross-section ($H/W=1$) at both the microscales and macroscales. It should be noted that the correlations developed in Figs. 13 and 14, would be most accurate if applied to a configuration, where the plenum and microchannel share a wall in the same plane, which is typical to microfluidic devices.

Theoretically, the hydrodynamic entrance length of a channel is dependent on its cross-sectional aspect ratio (H/W). This is shown in analytical studies by Han [13], Fleming and Sparrow [14], and Wiginton and Dalton [16]. This is due to the proximity of the walls relative to the internal flow field, the drag disturbance they impose, and the shear waves they cause to propagate toward the center of the channel. Therefore the height and width of the solid walls of a channel, and their relative size to each other, have a great influence on the flow development. However, since there is not many experimental works associated with the hydrodynamic entrance region in microgeometries, a correlation applicable to microchannels regardless of aspect ratio would be useful, where practical applications are concerned, even though the error is expected to be great due to the physics of the boundary layer. In light of this, previous experimental works for the hydrodynamic entrance length in microchannels [27,29,32], in addition to the present experimental data, are used in developing an empirical correlation. Also, conventional experimental data for the entrance length in ducts given by Goldstein and Kreid [19] and Muchnik et al. [21] were included to broaden the analysis. Table 2 shows the geometric parameters associated with the previous experimental data. Also, it should be noted that where conventional sized ducts are concerned, all available experimental data are above a Reynolds number of 10 due to reasons of practicality at the macroscale. However, where microchannels are concerned, there are available experimental data well below Re=10 since these low Reynolds numbers are applicable at the microscale, primarily due to the pressure drop imposed at higher Reynolds numbers. In order to determine an empirical correlation to fit the data, an equation in the form of Chen [17] was once again applied; however both the high Reynolds number asymptote, as well as the low Reynolds number solution are found using a curve fit. The following correlation is obtained:

Table 2 Experimental entrance length geometries used in previous studies

Authors	D_h	H/W
Goldstein and Kreid [29]	1 cm	1
Muchnik et al. [21]	1.33 cm	2
Lee et al. [29]	380 μm	2.65
Hao et al. [27]	237 μm	Trapezoidal
Lee et al. [32]	370 μm	2.75
Lee et al. [32]	56.4 μm	0.40

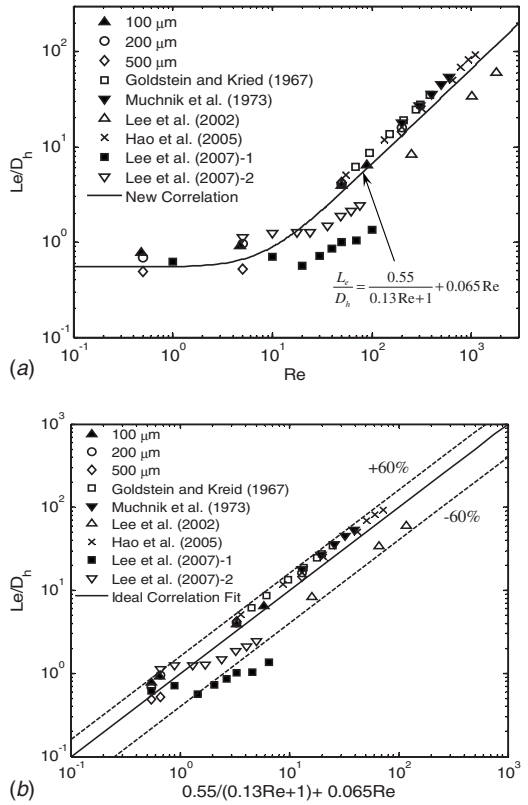

Fig. 15 Proposed general entrance length correlation for microchannels, independent of cross-sectional aspect ratio, and the error in the fit

$$\frac{L_e}{D_h} = \frac{0.55}{0.13\ \mathrm{Re} + 1} + 0.065\ \mathrm{Re} \tag{8}$$

Figure 15(*a*) depicts Eq. (8) plotted with the aforementioned entrance length experimental data for ducts and microchannels. The figure also shows that the conventional experimental data given by Muchnik et al. [21], at higher Re numbers ($\mathrm{Re} > 10$), have good agreement between the present experimental data, where their aspect ratio (H/W) was 2. In addition, the experimental data given by Hao et al. [27] also have very good agreement with the present data at high Re values, where interestingly their microchannels had a trapezoidal cross-section. As shown in Fig. 15(*b*), the error between the proposed correlation and the experimental data are high as expected, where the correlation fits majority of the data to within 60%. However, the high error results from the experimental data for the entrance length in microchannels from Lee et al. [29] and Lee et al. [32], which both have a similar planar microchannel/reservoir wall configuration as the present test-sections. Similar to their findings, this leads to off-center maximum velocity of the inlet profiles, and some predevelopment in the vertical plane due the planar plenum. However the expected high error is due to the cross-sectional aspect ratio of the microchannels, which is much greater than the present investigation. From the data in Fig. 15, it can be seen that the aspect ratio becomes more important at lower Re numbers. Nonetheless, this proposed correlation can be used as a general correlation for the entrance length in microchannels for aspect ratios below 3 ($H/W < 3$) and possibly trapezoidal microchannels, as shown by the data of Hao et al. [27].

4 Conclusion

An experimental investigation regarding the hydrodynamic entrance length in square microchannels was carried out over a laminar Reynolds number range of 0.5–200. Three microchannels with hydraulic diameters of 100 μm, 200 μm, and 500 μm were used to investigate scaling effects. The micro-PIV experimental technique was utilized to obtain flow field data at different axial locations from the microchannel inlet. To remove any effect of cross-sectional aspect ratio, square microchannels were used, whose inlet reservoir was very large, compared to the hydraulic diameter of the channels. The test-sections' configuration is similar to typical microfluidic devices, where the plenum and the microchannel share a wall in the same plane.

Good agreement was found regarding the physical mechanism describing developing flow, in terms of the observed developing velocity profiles downstream from the microchannel inlet. A slight influence of dimensional scaling was observed in comparing the entrance length of the 500 μm channel with the 100 μm and 200 μm channels at low Reynolds numbers. However, at higher Reynolds numbers, above 10, there was no effect of scaling. Also, very good agreement was found in comparing the entrance length data with conventional correlations developed for ducts at high Reynolds numbers (above 10) for all microchannels studied, and for parallel plates at lower Reynolds numbers (below 10), particularly for the 100 μm and 200 μm channels. At very low Reynolds numbers, below 10, the parallel plate correlations are well suited for the prediction of the entrance length in microchannels with planar plenum configurations. This is important since for practical applications of microscale flow in microchannels and microdevices, the flow is highly laminar due to the high pressure drop. Therefore, conventional entry pressure loss correlations developed for ducts may not be applicable for microchannels at very low Reynolds numbers. In addition, three new empirical entrance length correlations were proposed using the present data, whereby both creeping and high laminar Reynolds number correlations are combined. The first correlation applies the experimental data for the 100 μm and 200 μm channels, and is applicable to square microchannels with hydraulic diameters below 500 μm with an error of less than 15%. The second correlation includes all present experimental data, along with conventional experimental data for square ducts, and can be applied as a general entrance length correlation for channels of square cross-section at both the microscales and macroscales. This correlation fit the experimental data to within 30%. The first and second correlations are most accurate for microchannel aspect ratios of 1 and planar reservoir configurations, where the microchannel and reservoir share a common wall. The third correlation proposed includes all previous microchannel experimental entrance length data and some conventional experimental data, regardless of cross-sectional aspect ratio. Despite the large error in fitting the data to this new correlation, it can be used as a general entrance length correlation for microchannels of aspect ratios below three.

Acknowledgment

The authors would like to thank Dr. Roland Muwanga, a former member of the Microscale Heat Transfer Research Group at Concordia University, for his guidance and efforts in the present study, particularly in the early stages of establishing the experimental methods. This research group has been funded by the Natural Sciences and Engineering Research Council of Canada (NSERC).

References

[1] Tuckerman, D. B., and Pease, R. F. W., 1981, "High-Performance Heat Sinking for VLSI," IEEE Electron Device Lett., **EDL-2**(5), pp. 126–129.
[2] Mishan, Y., Mosyak, A., Pogrebnyak, E., and Hestroni, G., 2007, "Effect of Developing Flow and Thermal Regime on Momentum and Heat Transfer in Micro-Scale Heat Sink," Int. J. Heat Mass Transfer, **50**, pp. 3100–3114.
[3] Muwanga, R., Hassan, I., and MacDonald, R., 2007, "Characteristics of Flow Boiling Oscillations in Silicon Microchannel Heat Sinks," ASME J. Heat Transfer, **129**, pp. 1341–1351.
[4] Nguyen, N.-T., and Wu, Z., 2005, "Micromixers—A Review," J. Micromech. Microeng., **15**, pp. R1–R16.
[5] deMello, A. J., 2006, "Control and Detection of Chemical Reactions in Microfluidic Systems," Nature (London), **442**, pp. 394–402.

[6] Chang, C.-C., and Yang, R.-J., 2007, "Electrokinetic Mixing in Microfluidic Systems," Microfluid. Nanofluid., **3**, pp. 501–525.
[7] Epstein, A. H., 2004, "Millimeter-Scale, Micro-Electro-Mechanical Systems Gas Turbine Engines," ASME J. Eng. Gas Turbines Power, **126**, pp. 205–226.
[8] Suzuki, Y., Okada, Y., Ogawa, J., Sugiyama, S., and Toriyama, T., 2008, "Experimental Study on Mechanical Power Generation From MEMS Internal Combustion Engine," Sens. Actuators, A, **141**, pp. 654–661.
[9] Whitesides, G. M., 2006, "The Origins and the Future of Microfluidics," Nature (London), **442**, pp. 368–373.
[10] Yager, P., Edwards, T., Fu, E., Helton, K., Nelson, K., Tam, M. R., and Weigl, B. H., 2006, "Microfluidic Diagnostic Technologies for Global Public Health," Nature (London), **442**, pp. 412–418.
[11] Chaw, K. C., Manimaran, M., Tay, E. H., and Swaminathan, S., 2007, "Multi-Step Microfluidic Device for Studying Cancer Metastasis," Lab Chip, **7**, pp. 1041–1047.
[12] Shah, R. K., and London, A. L., 1978, *Laminar Flow Forced Convection in Ducts, Advances in Heat Transfer—Supplement 1*, Academic, New York.
[13] Han, L. S., 1960, "Hydrodynamic Entrance Lengths for Incompressible Laminar Flow in Rectangular Ducts," ASME J. Appl. Mech., **27**, pp. 403–409.
[14] Fleming, D. P., and Sparrow, E. M., 1969, "Flow in the Hydrodynamic Entrance Region of Ducts of Arbitrary Cross Section," ASME J. Heat Transfer, **91**, pp. 345–354.
[15] Atkinson, B., Brocklebank, M. P., Card, C. C., and Smith, J. M., 1969, "Low Reynolds Number Developing Flows," AIChE J., **15**(4), pp. 548–553.
[16] Wiginton, C. L., and Dalton, C., 1970, "Incompressible Laminar Flow in the Entrance Region of a Rectangular Duct," ASME J. Appl. Mech., **37**, pp. 854–856.
[17] Chen, R.-Y., 1973, "Flow in the Entrance Region at Low Reynolds Numbers," ASME J. Fluids Eng., **95**, pp. 153–158.
[18] Sparrow, E. M., Hixon, C. W., and Shavit, G., 1967, "Experiments on Laminar Flow Development in Rectangular Ducts," J. Basic Eng., **89**, pp. 116–124.
[19] Goldstein, R. J., and Kreid, D. K., 1967, "Measurement of Laminar Flow Development in a Square Duct Using a Laser-Doppler Flowmeter," ASME J. Appl. Mech., **34**, pp. 813–818.
[20] Beavers, G. S., Sparrow, E. M., and Magnuson, R. A., 1970, "Experiments on Hydrodynamically Developing Flow in Rectangular Ducts of Arbitrary Aspect Ratio," Int. J. Heat Mass Transfer, **13**, pp. 689–701.
[21] Muchnik, G. F., Solomonov, S. D., and Gordon, A. R., 1973, "Hydrodynamic Development of a Laminar Velocity Field in Rectangular Channels," J. Eng. Phys., **25**(4), pp. 1268–1271.
[22] Santiago, J. G., Wereley, S. T., Meinhart, C. D., Beebe, D. J., and Adrian, R. J., 1998, "A Particle Image Velocimetry System for Microfluidics," Exp. Fluids, **25**, pp. 316–319.
[23] Meinhart, C. D., Wereley, S. T., and Santiago, J. G., 1999, "PIV Measurements of a Microchannel Flow," Exp. Fluids, **27**, pp. 414–419.
[24] Koutsiaris, A. G., Mathioulakis, D. S., and Tsangaris, S., 1999, "Microscope PIV for Velocity-Field Measurement of Particle Suspensions Flowing Inside Glass Capillaries," Meas. Sci. Technol., **10**, pp. 1037–1046.
[25] Meinhart, C. D., Wereley, S. T., and Gray, M. H. B., 2000, "Volume Illumination for Two-Dimensional Particle Image Velocimetry," Meas. Sci. Technol., **11**, pp. 809–814.
[26] Sharp, K. V., and Adrian, R. J., 2004, "Transition From Laminar to Turbulent Flow in Liquid Filled Microtubes," Exp. Fluids, **36**, pp. 741–747.
[27] Hao, P.-F., He, F., and Zhu, K.-Q., 2005, "Flow Characteristics in a Trapezoidal Silicon Microchannel," J. Micromech. Microeng., **15**, pp. 1362–1368.
[28] Zeighami, R., Laser, D., Zhou, P., Asheghi, M., Devasenathipathy, S., Kenny, T., Santiago, J., and Goodson, K., 2000, "Experimental Investigation of Flow Transition in Microchannels Using Micro-Resolution Particle Image Velocimetry," *Proceedings of the IEEE Seventh Intersociety Conference on Thermomechanical Phenomena in Electronic Systems*, IEEE, Las Vegas, NV, May 23–26, Vol. 2, pp. 148–153.
[29] Lee, S.-Y., Wereley, S. T., Gui, L., Qu, W., and Mudawar, I., 2002, "Microchannel Flow Measurement Using Micro Particle Image Velocimetry," *Proceedings of the ASME International Mechanical Engineering Congress and Exposition (IMECE2002)*, ASME, New Orleans, LA, Nov. 17–22, Vol. 258, pp. 493–500.
[30] Lee, S.-J., and Kim, G.-B., 2003, "Analysis of Flow Resistance Inside Microchannels With Different Inlet Configurations Using Micro-PIV System," ASME Paper No. ICMM2003-1108.
[31] Oak, J., Pence, D. V., and Liburdy, J. A., 2004, "Flow Development of Co-Flowing Streams in Rectangular Micro-Channels," Microscale Thermophys. Eng., **8**, pp. 111–128.
[32] Lee, S.-Y., Jang, J., and Wereley, S. T., 2008, "Effects of Planar Inlet Plenums on the Hydrodynamically Developing Flows in Rectangular Microchannels of Complementary Aspect Ratios," Microfluid. Nanofluid., **5**, pp. 1–12.
[33] Olsen, M. G., and Adrian, R. J., 2000, "Brownian Motion and Correlation in Particle Image Velocimetry," Opt. Laser Technol., **32**, pp. 621–627.
[34] Olsen, M. G., and Bourdon, C. J., 2003, "Out-of-Plane Motion Effects in Microscopic Particle Image Velocimetry," ASME J. Fluids Eng., **125**, pp. 895–901.
[35] Prasad, A. K., Adrian, R. J., Landreth, C. C., and Offutt, P. W., 1992, "Effect of Resolution on the Speed and Accuracy of Particle Image Velocimetry Interrogation," Exp. Fluids, **13**, pp. 105–116.
[36] Vrentas, J. S., Duda, J. L., and Bargeron, K. G., 1966, "Effect of Axial Diffusion of Vorticity on Flow Development in Circular Conduits: Part I. Numerical Solutions," AIChE J., **12**(5), pp. 837–844.
[37] Bodoia, J. R., and Osterle, J. F., 1961, "Finite Difference Analysis of Plane Poiseuille and Couette Flow Development," Appl. Sci. Res., Sect. A, **10**, pp. 265–276.

Combined Effect of Surface Roughness and Heterogeneity of Wall Potential on Electroosmosis in Microfluidic/Nanofuidic Channels

S. Bhattacharyya[1]
Department of Mathematics,
Indian Institute of Technology,
Kharagpur 721302, India
e-mail: somnath@maths.iitkgp.ernet.in

A. K. Nayak
Department of Chemical Engineering,
Norwegian University of Science and Technology,
NO-7491 Trondheim, Norway

The motivation of the present study is to generate vortical flow by introducing channel wall roughness in the form of a wall mounted block that has a step-jump in ζ-potential on the upper face. The characteristics for the electrokinetic flow are obtained by numerically solving the Poisson equation, the Nernst–Planck equation, and the Navier–Stokes equations, simultaneously. A numerical method based on the pressure correction iterative algorithm (SIMPLE) is adopted to compute the flow field and mole fraction of the ions. The potential patch induces a strong recirculation vortex, which in turn generates a strong pressure gradient. The strength of the vortex, which appears adjacent to the potential patch, increases almost linearly with the increase in ζ-potential. The streamlines follow a tortuous path near the wall roughness. The average axial flow rate over the block is enhanced significantly. We found that the ionic distribution follow the equilibrium Boltzmann distribution away from the wall roughness. The solutions based on the Poisson–Boltzmann distribution and the Nernst–Planck model are different when the inertial effect is significant. The combined effects due to geometrical modulation of the channel wall and heterogeneity in ζ-potential is found to produce a stronger vortex, and hence a stronger mixing, compared with either of these. Increase in ζ-potential increases both the transport rate and mixing efficiency. A novelty of the present configuration is that the vortex forms above the obstacle even when the patch potential is negative.
[DOI: 10.1115/1.4001308]

Keywords: micromixer, overpotential, numerical solution, vortex strength

1 Introduction

Electroosmotic flow is the bulk liquid motion that results when an externally applied electric field interacts with the net surplus of charged ions in the diffuse part of an electric double layer (EDL). Because of several important characteristics, EOF has become one of the most useful mechanisms for pumping, separating, and mixing in microfluidics and nanofluidics based on lab-on-a-chip [1–6]. Several studies have been performed on EOF in a smooth long channel of heights on a micrometer to nanometer scale with homogeneous potential. A great amount of work on this has been reviewed recently in articles by Conlisk [7] and Ghosal [8]. The steady EOF is primarily unidirectional, i.e., along the direction of the applied electric field and laminar with low Reynolds number.

The electroosmotic flows are strongly related to the surface properties of the capillaries used. The electroosmotic flow depends on the ζ-potential, which varies with solution pH, ionic strength, dielectric constant, and solute molecules adsorbed onto the walls. For a system with a simple electrolyte solution and a homogeneous channel wall, the ζ-potential is considered uniform along the channel. However, in many cases, the ζ-potential on the channel wall is not uniform due to manufacturing defects or special designs. If the surface has a patch of positive potential, a surplus of negative ions are attracted by the patch while a surplus of positive ions are attracted by the negatively charged wall. Due to the external electric field parallel to the wall, the flow near the patch will be in the opposite direction to the bulk flow, which may lead to a recirculation region. Small region of nonuniform wall potential creates pressure gradient every where in the flow and the inertial effect in the electroosmotic flow may become significant. Thus, the convection effect in electroosmotic flow becomes important in the context of surface roughness and heterogeneous surface potential. Bio-MEMS devices are frequently required to have an effective mixing capability. Several studies have been made in the recent past on enhanced microfluidic mixing devices based on surface roughness and surface potential heterogeneity. In a recent article, Chang and Yang [9] provided a detailed account on the development of research related to electrokinetic mixing in microfluidic systems.

The surface of microfluidic and nanofluidic channels may have a roughness of a few angstroms to a few micrometers [10]. Hu et al. [11] studied the effect of surface roughness on the electroosmotic flow in microchannels at the thin EDL limit. Their study indicates that the electroosmotic flow in microchannels can be significantly affected by surface roughness and pressure can be induced in it. Subsequently, Hu et al. [12] analyzed the three-dimensional EOF through rough microchannels. The geometric modulation of channel wall to increase the interfacial area between the liquids to be mixed was studied by Ramirez and Conlisk [13]. Datta and Ghosal [14] made an asymptotic analysis on the transport of a solute in a straight microchannel of axially variable cross-sectional shape in the presence of an inhomogeneous flow field and an adsorption-desorption process on the wall. Re-

[1]Corresponding author.

Contributed by the Fluids Engineering Division of ASME for publication in the JOURNAL OF FLUIDS ENGINEERING. Manuscript received March 23, 2009; final manuscript received January 30, 2010; published online April 15, 2010. Assoc. Editor: Neelesh A. Patankar.

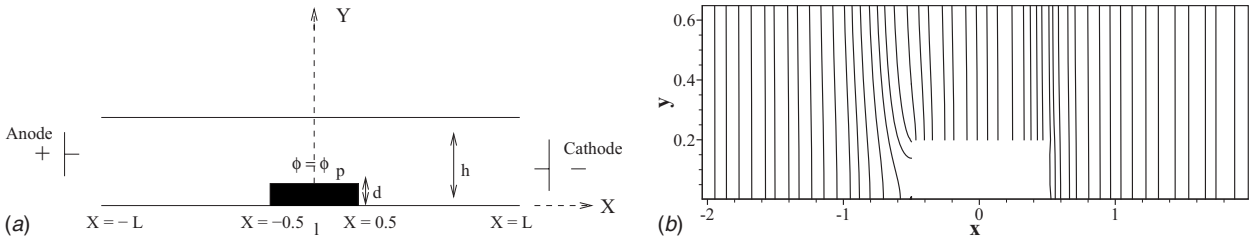

Fig. 1 (*a*) Schematic diagram of the computational domain and (*b*) electric potential distribution of the external electric field when E_0 corresponds to 10^6 V/m

cently, Wang and Chen [15] made a study on roughness and cavitations effects on EOFs in microchannels through a lattice Boltzmann simulation of the governing equations based on the Boltzmann distribution of ions (P-B model).

The EOF in microchannel with nonuniform ζ-potential along the conduit wall may promote mixing [16]. Adjari [17] showed that spatial modulation of the surface charge density can generate vortex. Erickson and Li [18] found that the recirculation is strongest when the ζ-potential of the heterogeneous surface is of equal and opposite sign to that of the homogeneous surface. Ghosal [19] employed lubrication theory to study the EOF in microchannel with nonhomogeneous ζ-potential. Fu et al. [20] observed that a step change in ζ-potential causes a significant variation in the velocity profile and pressure distribution. However, their result could not predict any flow recirculation. Tian et al. [21] concluded in their study on EOF in a heterogeneous microchannel that an excellent mixing could lead to a poor liquid transport. Luo [22] made an extensive study on transient EOF in a microchannel with nonhomogeneous surface charge distribution. Chen and Conlisk [23] studied the effect of nonuniform surface potential by solving the Poisson–Nernst–Planck equations. It may be noted in all the forgoing studies, a quantitative measure of the vortex strength and the dependence of induced vortical flow on several flow parameters is lacking.

Most of the previous studies on EOF in heterogeneous channel are based on the Boltzmann distribution of ions, which leads to the Poisson–Boltzmann equation for electric potential (P-B model). Although the computational cost for the numerical computation of full governing equations is high compare with that for the simple P-B model, the advantage of the exact N-P model can overshadow this weakness. When the channel height is comparable to the EDL thickness, the core of the channel is no longer electrically neutral and hence the validity of the Poisson–Boltzmann equation is questionable. Additionally, the Boltzmann distribution neglects the convection effect and the external electric field. The EOF near a step-jump in surface potential or close to surface roughness, the convection effect may not be negligible. Comparison of the two models to describe the EOF in microchannel with a step change in surface ζ-potential has been made by Park et al. [24]. They observed a discrepancy between the results predicted by the two models near the region of inhomogeneous ζ-potential, when the electric double layer is thicker and/or the applied electric field is stronger. Recently, Wang et al. [25] examined the validity of the P-B model in microscale and nanoscale EOF. One of the objectives of the present study is to investigate the validity of the Poisson–Boltzmann model in the present configuration where both surface roughness and heterogeneity in wall potential occurs. The EOF conditions, such as, external electric field, EDL thickness, and overpotential of the patch, which influences the difference between the P-B model from the exact N-P model, are also addressed in the present analysis.

The mixing in heterogeneous channel depends on the strength of the vortices induced by the potential patches. The EOF is proportional to the wall ζ-potential as well as the applied external electric field. The enhancement in electroosmotic flow in nanochannel also occurs with the increase in channel height. In the present study we have measured the vortex strength as a function of channel height, wall ζ-potential and overpotential of the patch.

The EOF around a wall mounted rectangular block, whose height is a fraction of the channel height and length is on the order of the channel height has been investigated here. In addition, we assume that the upper face of the block has a step-jump in ζ-potential. The height of the channel is assumed to vary between 20 nm and 60 nm. Far away from the block, it is a fully developed electroosmotic flow, thus the flow is along the direction of the applied electric field. The characteristics for the electrokinetic flow are obtained by numerically solving the Poisson equation, the Nernst–Planck equation, and the Navier–Stokes equations, simultaneously. The formation of vortex and strong transverse velocity near the block is observed. The form of the recirculation vortex and its dependence on several flow parameters such as channel height, EDL thickness, overpotential of the patch, and wall ζ-potential is discussed. We have compared our model with the solution where the charge potential is governed by the Poisson–Boltzmann equation.

2 Mathematical Model

Consider that a long rectangular channel whose height h is comparable with the EDL thickness is filled with an incompressible Newtonian electrolyte of uniform permittivity ϵ_e and viscosity μ, and subjected to a uniform external electric field directed along the length of the channel, say x-axis. An obstacle of the form of a rectangular block of length l ($\sim O(h)$) and height d is considered to be mounted along the lower wall of the channel (see Fig. 1(a)). We assume that the electrodes are placed at the inlet and outlets of the channel and a constant voltage is applied along x-direction.

The dimensional electric field $\boldsymbol{E}^*=(E_x,E_y,E_z)$ satisfying the Maxwell equations $\boldsymbol{E}^*=-\boldsymbol{\nabla}\Phi^*$ is governed by the following equation:

$$\nabla\cdot(\epsilon_e\boldsymbol{E}^*)=\rho_e=F\sum_i z_i c_i=Fc\sum_i z_i X_i \tag{1}$$

ρ_e is the charge density per unit volume, Φ^* is the electric potential, and c_i is the molarity of ionic species i and c is the total molar concentration, which is assumed to be constant. z_i is the valence and $X_i=c_i/c$ is the mole fraction of species i.

The electric potential Φ^* can be written as $\Phi^*(x,y,z)=\phi^*_{\text{ext}}+\phi^*(x,y,z)$. Here, ϕ^*_{ext} and ϕ^* are the external electric potential and the induced electric potential, respectively. Using Eq. (1), the nondimensional form of the equation for the induced potential can be written as

$$\frac{\partial^2\phi}{\partial y^2}+\epsilon_1^2\frac{\partial^2\phi}{\partial x^2}+\epsilon_2^2\frac{\partial^2\phi}{\partial z^2}=-\frac{\beta}{\epsilon^2}\sum_i z_i X_i \tag{2}$$

The potential is scaled by $\phi_0=RT/F$. For nondimensionalization we have used (l,h,W) for coordinates (x,y,z) for example, $x=x^*/l$. We define $\epsilon_1=h/l$, $\epsilon_2=h/W$, $\epsilon=\lambda/h$, and $\beta=c/I$. Here, λ,

the EDL thickness, is estimated as $\sqrt{\epsilon_e RT}/FI^{1/2}$ and the ionic strength $I=\Sigma_i z_i^2 c_i$. We assume that the fluid and transport properties are constants. If we consider the electrolyte consists of symmetric ions, then $\Sigma_i z_i X_i = g - f$. Here, g and f are the mole fraction of cation and anions, respectively.

The external electric field is created by applying a voltage difference across the channel so that a constant electric field of strength E_0 generates in a channel of uniform cross section. The number $\Lambda = hE_0/\phi_0$ measures the strength of the external electric field in nondimensional form. Owing to the presence of the surface mounted block, the external electric field is neither necessarily along the x-direction nor constant. The external electric potential is obtained by solving the Laplace equation, $\nabla^2 \phi_{\text{ext}} = 0$. The walls and all the sides of the block are electrically insulated, i.e., the normal gradient of ϕ_{ext} is zero. We considered that ϕ_{ext} is a linear function of x, i.e., $\phi_{\text{ext}} = -\Lambda x$, far upstream and downstream of the block. The Laplace equation along with the prescribed boundary conditions is solved in the computational domain to obtain the external electric field for a given value of Λ. A line-by-line iterative method along with the successive-over-relaxation technique (SOR) is used to compute the discretized equation. The grids are considered to be the same as that of the grids used for computing the flow field. Detailed discussions on grids are made in Sec. 4. Figure 1(b) shows that except in the region close to the block, ϕ_{ext} varies linearly with the axial position. The electric field is predominantly along x-axis except in the region near the block, where the y-component of electric field exists and has maximum magnitude about 8% of Λ. The strength of the electric field is enhanced in the downstream side and above the block. The electric field is about 1.12 times of Λ in this region.

The molar flux of species i oriented perpendicular to the flow of the species can be obtained as [26]

$$\boldsymbol{n}_i = -D_i \nabla c_i + c_i \omega_i z_i F \boldsymbol{E} + c_i \boldsymbol{q}^* \tag{3}$$

Here, $\boldsymbol{q}^*$ is the velocity field of the fluid. The mobility ω_i is $\omega_i = D_i/RT$.

The transport equation for species i in steady EOF is governed by

$$\nabla \cdot \boldsymbol{n}_i = 0 \tag{4}$$

Using Eqs. (3) and (4) the concentration equation for molar flux in nondimensional form can be expressed as

$$\frac{\partial^2 X_i}{\partial y^2} + \epsilon_1^2 \frac{\partial^2 X_i}{\partial x^2} + \epsilon_2^2 \frac{\partial^2 X_i}{\partial z^2} = \text{Pe}\left(\epsilon_1 u \frac{\partial X_i}{\partial x} + v \frac{\partial X_i}{\partial y} + \epsilon_2 w \frac{\partial X_i}{\partial z} \right) + \left(\epsilon_1 z_i \frac{\partial X_i E_x}{\partial x} + z_i \frac{\partial X_i E_y}{\partial y} + \epsilon_2 z_i \frac{\partial X_i E_z}{\partial z} \right) \tag{5}$$

Thus, the nondimensional electric field $\boldsymbol{E}$ in (x,y,z) directions is of the form:

$$E_x = -\left(\epsilon_1 \frac{\partial \phi_{\text{ext}}}{\partial x} + \epsilon_1 \frac{\partial \phi}{\partial x} \right)$$

$$E_y = -\left(\frac{\partial \phi_{\text{ext}}}{\partial y} + \frac{\partial \phi}{\partial y} \right)$$

$$E_z = -\left(\epsilon_2 \frac{\partial \phi_{\text{ext}}}{\partial z} + \epsilon_2 \frac{\partial \phi}{\partial z} \right)$$

We assume that the electrolyte solution composed of two species, cations, and anions, and have the symmetric physical properties.

The corresponding momentum equation in dimensional form is

$$\rho\left(\frac{\partial \boldsymbol{q}}{\partial t} + (\boldsymbol{q} \cdot \nabla)\boldsymbol{q} \right) = -\nabla p + \mu \nabla^2 \boldsymbol{q} + \rho_e \boldsymbol{E} \tag{6}$$

where $\boldsymbol{q} = (u^*, v^*, w^*)$. The continuity equation is

$$\epsilon_1 \frac{\partial u}{\partial x} + \frac{\partial v}{\partial y} + \epsilon_2 \frac{\partial w}{\partial z} = 0 \tag{7}$$

The velocity components are scaled by the electroosmotic velocity U_0, where $U_0 = \epsilon_e E_0 \phi_0/\mu$. The Reynolds number Re is $U_0 h/\nu$, Schmidt number $\text{Sc} = \nu/D_i$, and $\text{Pe} = \text{Re} \cdot \text{Sc}$ is the Peclet number. The Peclet number is related to the height of the channel and the magnitude of the imposed electric field.

The nondimensional pressure is defined by $p = p^*/\mu U_0/h$ and

$$\nabla^2 = \frac{\partial^2}{\partial y^2} + \epsilon_1^2 \frac{\partial^2}{\partial x^2} + \epsilon_2^2 \frac{\partial^2}{\partial z^2}$$

We consider the width of the channel to be of the order of the length of the channel, so $\epsilon_2 = h/W \ll 1$. Thus, all gradients with respect to z can be neglected and the flow can be treated as two-dimensional.

The velocity field is coupled with the mass transfer equation (5) and the equation for the potential (2). The mass transfer equation is subject to boundary conditions at a solid surface. We can either specify the ion concentration or the flux at the surface. Since only the gradients of ϕ appears in the governing equations, we can subtract the wall ζ-potential from ϕ and set $\phi = 0$ along the walls ($y=0$ and $y=1$). Thus, the boundary condition along the channel walls ($y=0$ and $y=1$) and along the side faces of the block can be expressed as

$$u = v = 0, \quad \phi = 0, \quad f = f^0, \quad g = g^0 \tag{8}$$

Many investigators [27] have experimentally determined the ζ-potential or surface charge density for various oxide-solution systems as a function of solution pH and concentration.

We consider a potential patch of overpotential ϕ_p to be embedded along the upper face of the block. The boundary condition along the upper face of the block ($-0.5 \le x \le 0.5$, $y = d/h$) is

$$u = v = 0, \quad \phi = \phi_p, \quad f = f^p, \quad g = g^p \tag{9}$$

The wall mole fractions on the upper face of the obstacle are $f^p = f^0 e^{\phi_p}$ and $g^p = g^0 e^{-\phi_p}$, which satisfies the equilibrium condition of the electrochemical potential at $y=0$ and $y=1$.

The channel is assumed to be sufficiently long upstream and downstream of the wall mounted block and the flow is assumed to be fully developed EOF at the far upstream and downstream of the block. Far upstream of the block ($x=-L$)

$$u = u^{\text{in}}, \quad v = 0, \quad \phi = \phi^{\text{in}}$$

$$g = g^{\text{in}}, \quad f = f^{\text{in}}, \quad \frac{\partial p}{\partial x} = 0 \tag{10}$$

Far downstream of the block ($x=L$), we consider a symmetry condition

$$\frac{\partial u}{\partial x} = 0, \quad \frac{\partial v}{\partial x} = 0, \quad \frac{\partial \phi}{\partial x} = 0$$

$$\frac{\partial g}{\partial x} = 0, \quad \frac{\partial f}{\partial x} = 0, \quad \frac{\partial p}{\partial x} = 0 \tag{11}$$

The values for u^{in}, ϕ^{in}, g^{in}, and f^{in} are due to the fully developed EOF. The governing equations and boundary conditions for the fully developed EOF is discussed in Ref. [28].

The presence of the wall mounted rectangular block and the potential patch creates a pressure gradient, which makes the inertial effect non-negligible. This makes the governing equations nonlinear and coupled. Hence, an analytic solution for velocity and mole fractions are difficult. For computation purposes we have scaled the mole fractions with the wall value of g^0, i.e., $\bar{g} = g/g^0$, $\bar{f} = f/g^0$. The governing equations are invariant to this rescaling of the mole fractions with the parameter $\delta^2 = \epsilon^2/\beta g^0$.

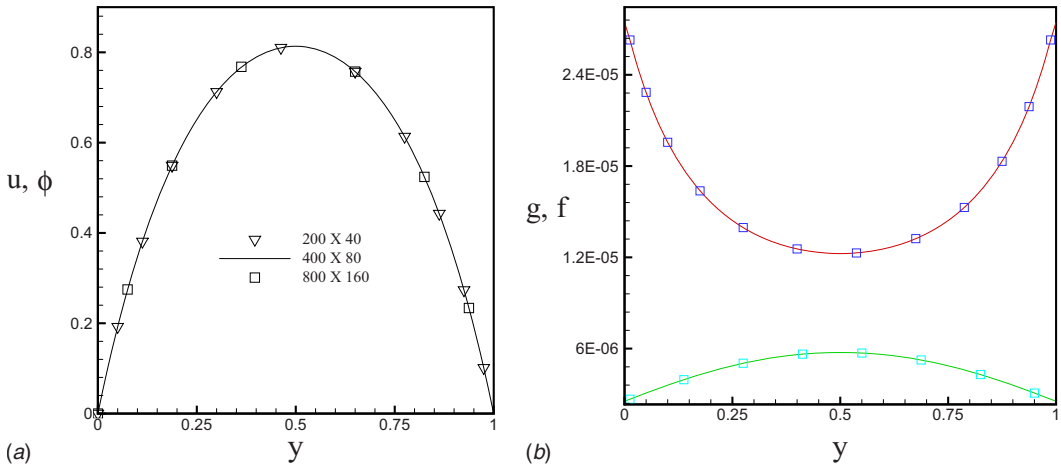

Fig. 2 Comparison of the present solutions in the fully developed region ($x=-1.7$) with that of Ramirez and Conlisk [13] when $h=50$ nm, $g^0=2.77\times10^{-5}$, $f^0=2.54\times10^{-6}$, and $E_0=1.7143$ V/μm. (*a*) Axial velocity profile and (*b*) mole fractions. (□) denote the results due to Ramirez and Conlisk [13]. Grid size effect on the solution is shown in (*a*).

3 Numerical Scheme and Accuracy

We compute the governing nonlinear, coupled set of PDEs (i.e., Eqs. (5) and (6)) through a numerical scheme based on the semi-implicit method for pressure-linked equations (SIMPLE) algorithm. The Poisson equation for induced potential, Eq. (2), is solved through a SOR technique.

We consider a nonuniform grid distribution with dense grids close to the channel walls, where the gradients are large. The total number of grids is taken to be 400×80. Further reduction in the grid size does not produce any change. The minimum grid size for 400×80 grids is 0.01×0.01. The grid independency test is shown in Fig. 2(*a*). The algorithm has been tested for accuracy by comparing with the previously published results. We have compared our computed solution for the fully developed EOF with the results due to Ramirez and Conlisk [13] and found them in good agreement. Figures 2(*a*) and 2(*b*) present the comparisons for u, ϕ, g, and f when $h=50$ nm and the wall mole fractions $Na^+=0.00154M$ and $Cl^-=0.000141M$, under the external electric field 3.5×10^6 V/m. The EDLs are thick and the velocity profile shows a parabolic form.

A comparison of our computed solution for the streamwise velocity component with the lattice Boltzmann solution of the Poisson–Boltzmann model (LPBM) for a channel of height 0.8 μm as obtained by Wang et al. [25] is shown in Fig. 3 at different values of the external electric field and ζ-potential. Figure 3 shows that the agreement is excellent with our computed solution based on the present model (N-P model). Axial flow rate increases with the rise of ζ-potential as well as external electric field. We found our results for plane EOF in a channel of height 5 nm (Fig. 4) are comparable with the experimental results presented in Ref. [29].

We have compared our results for ionic concentration with Fu et al. [20] when a step change in ζ-potential is considered (Fig. 5). The results are presented for $h=50$ μm and the patch ζ-potential is −75 mV. The ζ-potential outside the patch is zero. Our result based on the present model is in good agreement with the result obtained by Fu et al. [20] through the Nernst–Planck model. For comparison, we have included in Fig. 5 the result based on the Boltzmann distribution of ions. We find a difference in ionic distribution obtained by those two different models, though both the models yields similar pattern.

In Fig. 6, a comparison of our result for axial velocity obtained by the N-P model with the result based on the Poisson–Boltzmann equation (P-B model) due to Luo [22] is made for channel height 30 μm. The channel is considered to have potential patches placed symmetrically along both the upper and lower walls. The ζ-potential along the channel wall is 75 mV, whereas, the ζ-potential along the patches is −75 mV. We find that our results compare well when the flow away from the patches is considered. Near the patch ($x=0$) there is a discrepancy between our result obtained by the N-P model with the results of Luo [22] based on the P-B model. Here, the velocity scale is 0.0018 m/s, which is the same as that considered in Ref. [22]. A detailed discussion on the difference between the N-P model and the P-B model is made in Sec. 4.

4 Results and Discussion

The EOF here is investigated for a weak electrolyte, for which the EDL thickness is large, as well as a strong electrolyte, for which the EDL thickness is low. The block height could be any fraction of the channel height. In the present analysis, we consider the rectangular block height as 0.2 times the height of the channel and length is same as the channel height. The values of the other EOF parameters are provided in Table 1.

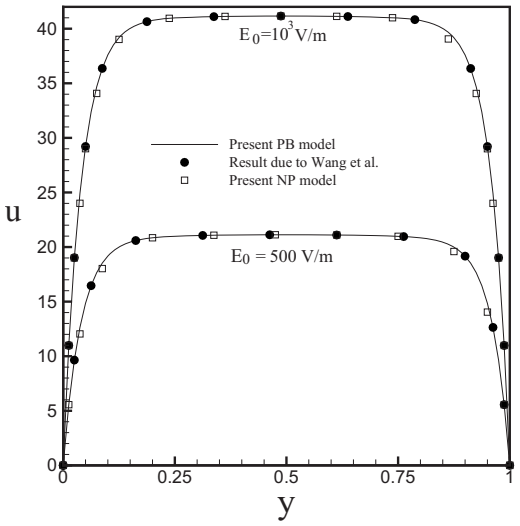

Fig. 3 Comparison of axial velocity with different models and the results due to Wang et al. [25] for various external electric fields in plane channels of height 0.8 μm with zeta potential as −50 mV and the ionic concentration is $10^{-4}M$

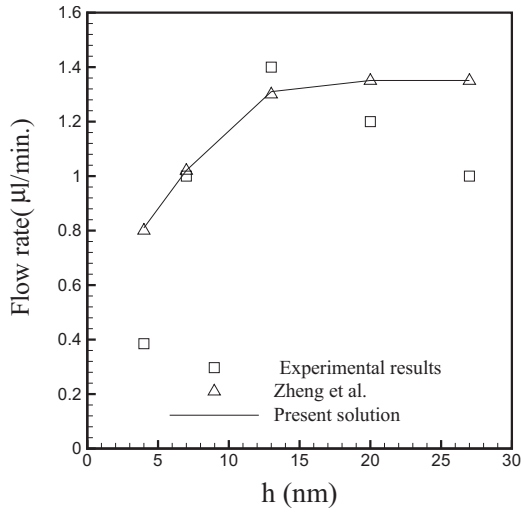

Fig. 4 Comparison of our result for flow rates at different channel heights in a plane nanochannel with Ref. [29]. The molarity of ions at the walls are $Na^+=9.6871M$ and $Cl^-=0.0009M$. The external electric field E_0 corresponds to 0.05 V over a channel of length 3.5 μm. Experimental results are as provided in Ref. [29].

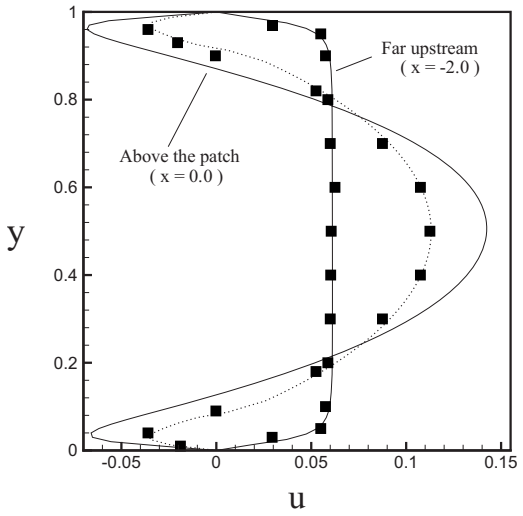

Fig. 6 Comparison of the axial velocity (N-P model and P-B model) at different sections of the channel with Ref. [22] (P-B model) in a channel with heterogeneous ζ-potential. Here, $E_0=10^4$ V/m, $h=30$ μm, $g^0=2.7\times10^{-6}$, $f^0=2.5\times10^{-6}$, and ϕ_p is −2.853. Solid line, result due to the N-P model; dotted line, result due to the P-B model; ■ [22].

4.1 Electroosmotic Flow and Ion Distribution. The distribution of velocity components, mole fractions, electric potential, and pressure along the channel for a strong solution case is presented in Figs. 7(*a*)–7(*f*). We consider a strong electrolyte for which the concentration at the wall corresponds to $Na^+=0.154M$, $Cl^-=0.141M$ and water is $55.6M$. This leads to an EDL thickness of 0.8 nm. We choose the overpotential of the patch ϕ_p as 0.2, which corresponds to the EDL thickness along the patch as 0.78 nm. Away from the obstacle, the flow is predominantly along the direction of the applied electric field and is similar to the EOF within a plane nanochannel. In this region, the bulk fluid is electrically neutral and the flow is governed by the viscous effect, which leads to a constant bulk flow. Along the potential patch, a different EDL forms compared with the EDL, which develops along the channel walls. Due to this difference in strength of the ζ-potential, different fluid flow rates occur in different sections of the channel. This nonuniform flow rate leads to the development of a pressure gradient. The fluid velocity adjacent to the patch is in the opposite direction of the bulk flow. As a result, a vortical motion develops above the obstacle. Reversal of the fluid flow close to the potential patch situated on the upper face of the obstacle is evident from the results. Besides, fluid encounters an adverse pressure gradient as it approaches the block. Thus, the fluid velocity is much reduced near the upstream side of the block. Above the vortex adjacent to the patch, fluid accelerates in order to satisfy the continuity requirement. In a fully developed EOF, the asymptotic value of u corresponds to 0.044 [28]. The maximum value of the streamwise velocity (u) in the region above the obstacle is 54% higher than the corresponding u due to a fully developed EOF. The Reynolds number based on the EOF velocity for $h=60$ nm is 0.1. It is also evident from Figs. 7(*a*) and 7(*b*) that the EOF is symmetric about the vertical axis $x=0$.

The distribution of pressure in Fig. 7(*e*) clearly shows that the pressure is high near the upstream side of the obstacle, whereas a strong favorable pressure gradient develops above the obstacle. The vertical velocity is quite strong and the form of the velocity distribution suggests that the vortex is symmetric about the verti-

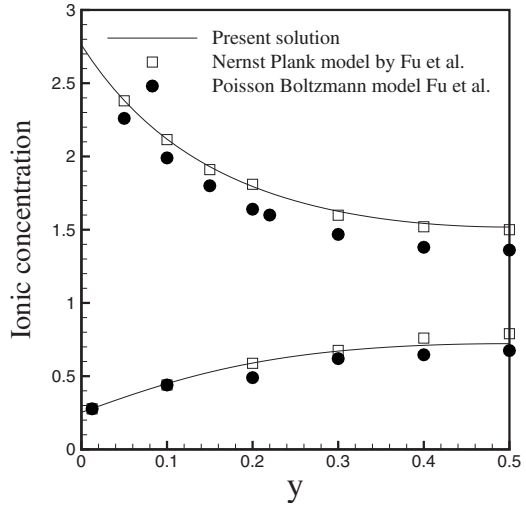

Fig. 5 Comparison of the ionic concentrations of cations and anions of the solution near a step-jump in ζ-potential ($x=1.55$) with the results due to Fu et al. [20]. The ionic strength of the solution (I) is $10^{-5}M$ with $h=50$ μm, $g^0=2.7\times10^{-5}$, $f^0=2.5\times10^{-5}$, ϕ_p is −2.853, and $E_0=10^5$ V/m.

Table 1 Values of the parameters used for computation

Parameter	Value
z_i	±1
F	96,500 °C mol^{-1}
K_B	1.38066×10^{-23} J/K
T	300 K
e	1.60219×10^{-19} °C
N_A	6.023×10^{23} mol^{-1}
ρ	1000 kg/m^3
μ	10^{-3} kg/ms
Sc	7692.23 NaCl, 500 KCl
U_0	0.02274 m/s
ϕ_0	0.02586 V
R	8.315 J mol^{-1} K^{-1}
D_i	1.3×10^{-10} m^2/s (NaCl)
D_i	2.5×10^{-9} m^2/s (KCl)
E_0	10^6 V/m or 10^8 V/m

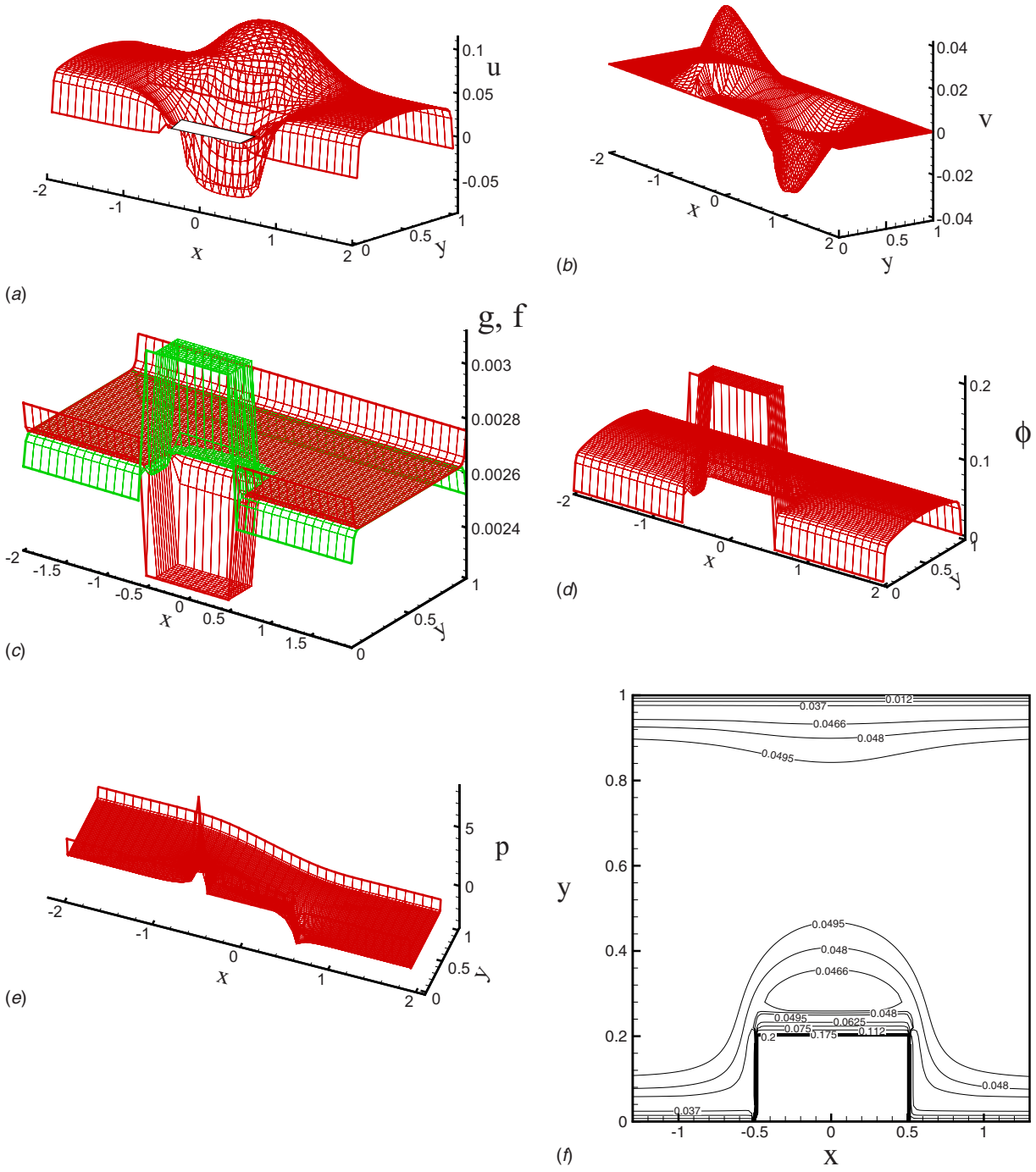

Fig. 7 Distribution of axial velocity, transverse velocity, mole fractions, potential, pressure, and lines of constant potential for nanochannel of height 60 nm with ionic species concentration at the wall is Na^+=0.154*M* and Cl^-=0.141*M* (strong electrolyte) and imposed electric field is 10^6 V/m and ϕ_p=0.2

cal axis (x=0). We have shown later in this section that the present configuration produces a vortical flow even if the patch have negative ζ-potential. It may be noted that in a smooth heterogeneous channel, vortex occurs only when the potential patch has ζ-potential of opposite sign to that of the homogeneous part.

The mole fraction distributions (Fig. 7(*c*)) show that for the strong solution the bulk fluid is electrically neutral except near the obstacle. The surplus of positive ions (g) in the region above the potential patch is evident from the results. The force due to electric field in EOF is proportional to (g-f), which is highest within the EDL. We find from the distribution of g and f that the convection has almost no effect on the molar concentration of ions in the core region at this small Peclet number.

The lines of constant potential for a strong solution with ϕ_p =0.2 is presented in Fig. 7(*f*). The potential lines are no longer parallel above the obstacle. Therefore, the electric field is not uniform in this region. We observed previously that the fluid flow is not uniform in the bulk. The pressure gradient, which develops due to the nonuniformity of the form of EDLs and surface roughness, generates a nonuniform flow field in the bulk region above the obstacle.

The distribution of velocity components, mole fractions, and electric potential along the channel for the weak solution case is presented in Figs. 8(*a*)–8(*d*). For a weak electrolyte solution, we

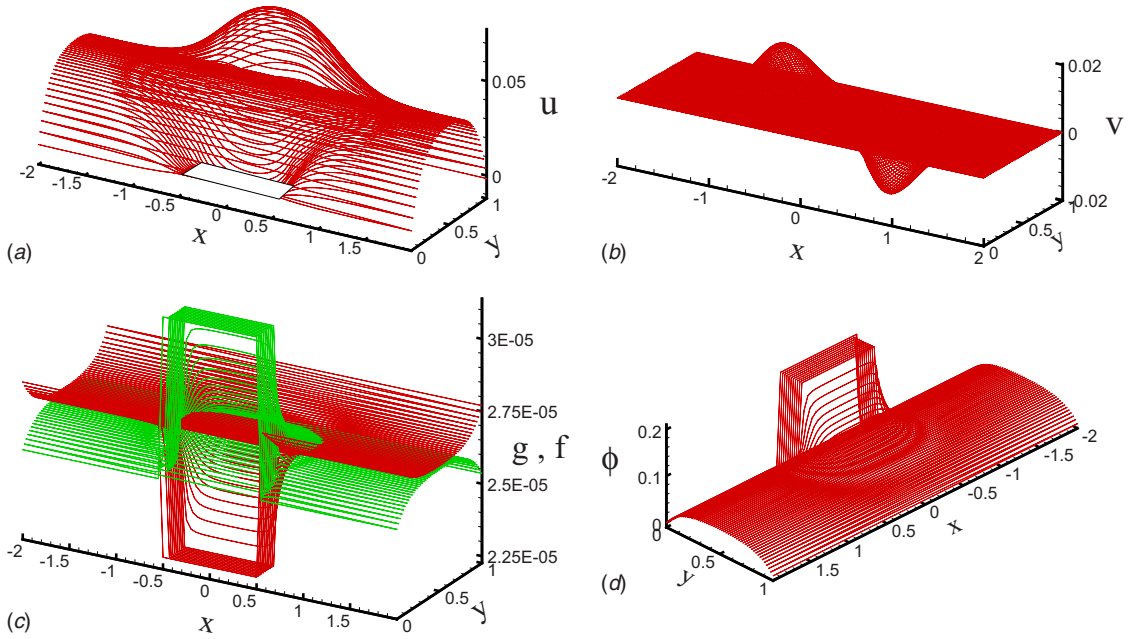

Fig. 8 Distribution of axial velocity, transverse velocity, mole fractions, potential for channel height h =60 nm with ionic species concentration at the wall is Na^+=0.00154M, Cl^-=0.00141M (weak electrolyte), and ϕ_p=0.2

consider that the concentration at the wall as Na^+=0.00154M, Cl^-=0.00141M, and water is 55.6M. The EDL thickness is estimated to be 8 nm. Away from the obstacle, the flow is primarily along the axial direction. The axial velocity profiles assume a parabolic shape as the bulk fluid is not electrically neutral. Flow recirculation occurs in the region above the obstacle. The axial flow rate and the strength of the recirculation are reduced compare with the case of strong solution (Figs. 7(a) and 7(b)). The mole fraction distribution for the case of weak solution is presented in Fig. 8(c). The electroneutrality in the core is not established in this case.

We present the streamlines close to the obstacle (Figs. 9(a) and 9(b)) both for strong and weak solution cases. Far upstream of the obstacle, the streamlines are almost straight lines and the flow is along the primary direction, the x-direction. As the fluid approaches the obstacle, an induced pressure field develops and the flow close to the obstacle no longer remains one-dimensional. We find that the flow separation from the channel wall does not occur when the EDL is thin (strong solution), whereas, small zones of recirculating eddy occur near the upstream and downstream corners of the obstacle when a weak solution (thick EDL) is considered. It may be noted that for a pressure driven flow, flow separates from the channel wall at any value of Reynolds number. The adverse pressure gradient close to the obstacle induces a flow separation. The mechanism of the EOF is different from that of a pressure driven flow. The electrical body force in the x-momentum equation, i.e., the source term

$$\left(1 - \frac{\epsilon_1}{\Lambda}\frac{\partial \phi}{\partial x}\right)\frac{\beta}{\epsilon^2}(g - f)$$

supplies extra momentum to overcome the induced adverse pressure gradient and hence no flow separation is found. When we consider the flow due to a weak solution (Fig. 9(b)), the electrical body force is not strong enough to overcome the momentum loss near the obstacle; thus, the adverse pressure gradient induces a small zone of recirculating fluid both upstream and downstream of the obstacle. It is clear from the streamline patterns that a strong

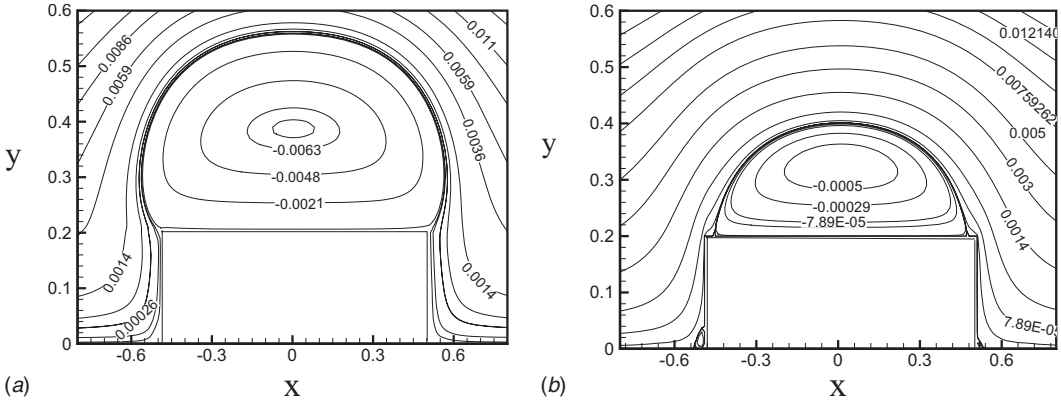

Fig. 9 Streamlines close to the block when the channel height is h=60 nm with block having overpotential ϕ_p=0.2 on the upper face. (a) Strong electrolyte g^0=0.00276(Na^+=0.154M), f^0=0.00252(Cl^-=0.141M). (b) Weak electrolyte g^0=0.0000276(Na^+=0.00154M), f^0=0.0000252(Cl^-=0.00141M).

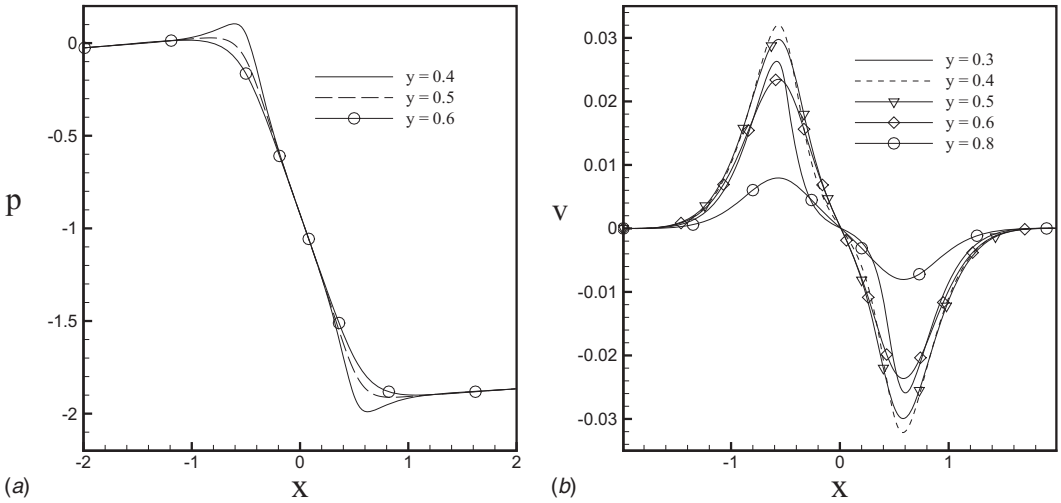

Fig. 10 Distribution of pressure and transverse velocity along the *x*-axis, at different *y*, when $h=60$ nm, $g^0=0.00276(Na^+=0.154M)$, $f^0=0.00252(Cl^-=0.141M)$, and $\phi_p=0.2$. (*a*) Pressure and (*b*) transverse velocity.

vortex sets in above the obstacle. The streamlines follow a linear path as we move away from the obstacle and follow a tortuous path above the block. Fluid flow is enhanced above the vortex.

The pressure distribution along the central line is presented in Fig. 10(*a*), for the case of a strong solution. This clearly shows that a large pressure drop occurs in the region above the patch. The favorable pressure gradient (Fig. 10(*a*)) which develops outside the vortex formed adjacent to the patch, induces an acceleration in fluid velocity. The pressure remains constant thereafter.

The vertical velocity distribution above the upper face of the obstacle is presented in Fig. 10(*b*), at different heights from the obstacle. The vertical velocity diminishes with the increase in distance from the obstacle. The distribution of v within the vortex suggests that the vortex above the patch resembles a Lamb vortex.

For strong electrolytes, the EDLs are thin and the variation in potential in the core is almost zero in the flow direction. The dimensionless bulk velocity is constant in the region far upstream and downstream of the obstacle and is 0.045 when the channel height is 20 nm with $\Lambda=0.762$. Hence, the streamwise velocity of the cations in the bulk is constant and its nondimensional value $u_{\text{cation}}=2.09$. Thus, the fluid velocity in the core is small compared with the movements of species (cation). The dimensionless streamwise velocity of anions in the bulk is $u_{\text{anion}}=-2.09$, so the anions move in opposite direction to the cations and the bulk flow. At a channel height of 60 nm, the dimensionless bulk velocity is 0.05, which yields $u_{\text{cation}}=2.16$ and $u_{\text{anion}}=-2.16$. It may be noted that for the case of weak electrolytes, the bulk flow is not constant.

4.2 Vortex Strength. The circulation of vortex is obtained by integrating the vorticity in the vortical region, i.e., $\Gamma=\int\int_D \omega dx dy$. The vorticity ω is scaled by $\epsilon_e \phi_0 E_0/\mu h$ and is obtained as

$$\omega = \epsilon_1 \frac{\partial v}{\partial x} - \frac{\partial u}{\partial y}$$

Figure 11(*a*) presents the variation in circulation with channel height at an overpotential 0.2 of the patch. The magnitude of circulation increases with the increase in channel height in the range of h considered here. The increment in magnitude of circulation is 21% when the channel height varies from 20 nm to 60 nm. Increase in h leads to an increment in bulk velocity, which in turn results into an increment in circulation. The effect of ζ-potential on the circulation is presented in Fig. 11(*b*). Here, we keep the wall value of the ionic species Cl^- fixed at $0.141M$ and Na^+ increases from $0.154M$ to $1.232M$, so that the dimensionless ζ-potential varies from -0.0441 to -1.0840. The overpotential of the patch is kept constant, i.e., $\phi_p=0.2$. In several situations, the wall acquires more negative charge and thus attract more positive ions. We find that the increase in ζ-potential produces a monotonic

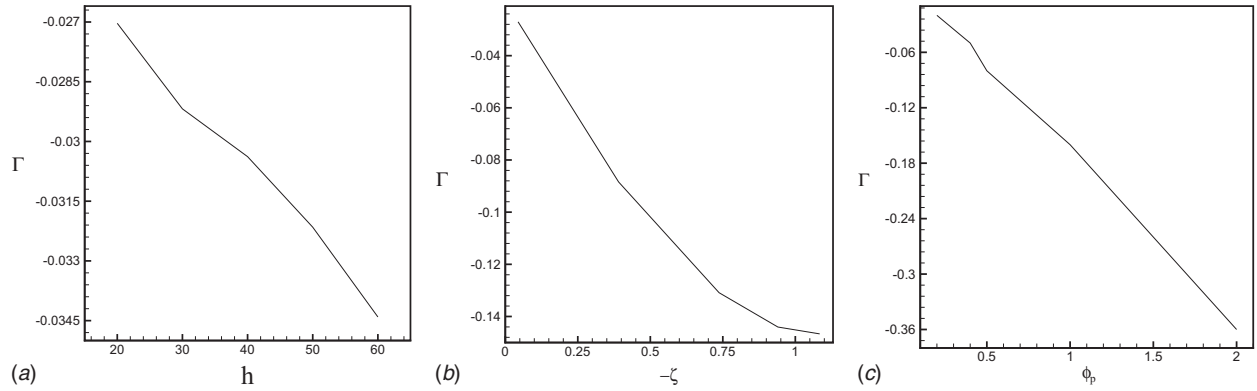

Fig. 11 Effect of channel height, ζ-potential, and overpotential of the patch on the circulation strength of the vortex. (*a*) $Na^+=0.154M$, $Cl^-=0.141M$ (strong electrolyte), $\phi_p=0.2$, and 20 nm $\le h \le$ 60 nm; (*b*) $Cl^-=0.141M$ and $0.154M \le Na^+ \le 1.232M$, $\phi_p=0.2$, and $h=20$ nm; and (*c*) $Na^+=0.154M$, $Cl^-=0.141M$, and $h=60$ nm.

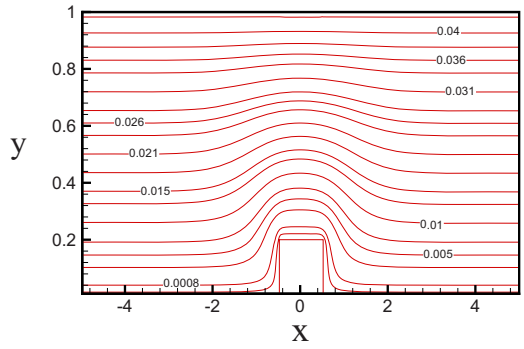

Fig. 12 Results for streamlines for a strong electrolyte case at the channel height 20 nm. The electrical field corresponds to 10^6 V/m. The overpotential $\phi_p=0.0$.

increment in Γ, though the step-jump in ζ-potential is kept constant ($\phi_p=0.2$). Fluid velocity increases with the increase in ζ-potential and also induces stronger vortex adjacent to the patch. Thus, both the mixing and transport of fluids can be enhanced through the increment in ζ-potential, keeping the step-jump in ζ-potential constant at a fixed value of channel height.

We find from Fig. 11(b) that a recirculation vortex appears above the obstacle even when the ζ-potential along the patch is negative, i.e., $\zeta_p<0$, but $-\zeta_p<-\zeta$. It may be noted that in a smooth channel, the patch potential should be of opposite sign in order to induce a local vortex. In presence of an obstacle, an adverse pressure gradient develops as fluids encounter the front face of the obstacle. The momentum loss due to this adverse pressure gradient along with the reduced electric body force in the EDL over the upper face of the block leads to the formation of a recirculation vortex. The separation and reattachment points are fixed at the upstream and downstream corners of the block. The local Reynolds number, based on the Helmholtz–Smoluchowski velocity, increases with the rise of ζ, and hence the vortex strength increases. We expect that the strength of the vortex must depend on the block height as well as the patch overpotential. Figure 11(c) shows that the increase in patch overpotential produces a monotonic increment in the vortex strength. Increase in ϕ_p induces a higher pressure gradient and hence a stronger vortex.

4.3 Individual Effects of Wall Modulation. We now compare the results due to the present configuration with the cases where (a) a smooth channel with step-jump in ζ-potential is considered, and (b) channel of homogeneous ζ-potential with a single roughness element. The presence of a single block with homogeneous wall potential ($\phi_p=0$) on EOF for $h=20$ nm is shown in Fig. 12. We find that the flow is two-dimensional but no vortex appears above the obstacle. The maximum magnitude of v is found to be 0.012, which is 57% less than the present case. Thus, the mixing effect is not pronounced when the overpotential is set to zero. A significant reduction in the average axial flow rate is found in absence of the overpotential ($\phi_p=0$). The reduction in u at $h=20$ nm is estimated to be 40%. It may be noted that the streamline patterns for the case-b, as shown in Fig. 12, are qualitatively similar to the streamlines presented in Chang and Yang [30] for flow past a single block in a microchannel.

Vortex can be induced through the heterogeneity in wall ζ-potential in a smooth channel. In this case, for a channel of height $h=20$ nm with patch overpotential $\phi_p=0.2$, the vortex strength $\Gamma=0.025$, which is 8% less compare with the present configuration.

We find from the above discussions that the present configuration produces a stronger vortex, thus the mixing efficiency is enhanced. Furthermore, as observed in Fig. 11(b), vortex could be generated even if the upper face of the block has negative ζ-potential. The vortex, which develops adjacent to the potential patch, is well organized and its strength can be regularized through the adjustment of the patch overpotential at a fixed value of the channel height.

4.4 Comparisons of N-P and P-B models. Near the surface modulation, the EDL changes its form and thickness abruptly and consequently the form of EOF is different. Due to this an induced pressure gradient develops, which makes the convective transport of ions non-negligible even for a microchannel. The Boltzmann distribution of ions neglect the dynamic behavior, consequently near a surface modulation the validity of the model based on the Poisson–Boltzmann equation along with the Stokes equation for fluid transport is questionable. We have compared the results based on the present model (N-P model) with the model based on the Boltzmann distribution of ions (P-B model). In the later case, the induced electric potential is governed by the Poisson–Boltzmann equation. In the P-B model, we have not neglected the externally imposed electric field in evaluating the electric body force. Thus, the difference in velocity profile determined by the two models is possible only when there is a difference in normal component of electric body force.

In Fig. 3, we compare the result for axial velocity due to N-P and P-B models in homogeneous channel of height 0.8 μm with EDL thickness estimated to be 30 nm. The axial velocity profile assumes a plug-like form for those parameter values. We find that both the N-P model and P-B model yield an identical result.

In Fig. 5, we find that the ionic distribution obtained by the N-P model deviates from the Boltzmann distribution near a step-jump in ζ-potential for microchannel with thick EDLs (weak electrolyte). The velocity profile (see Ref. [20]) shows a parabolic shape in this region. The comparison of solution for u, as presented in Fig. 6, established the fact that the P-B model differs from the N-P model in a heterogeneous microchannel. The maximum u above the patch is 0.0033 m/s with $\lambda=320$ nm, $\phi_p=-2.853$, and E_0 is 10^4 V/m. Away from the potential patch both the models are in good agreement. It may be noted that the N-P and P-B models differ in a heterogeneous microchannel for thick EDLs, but both the models yield similar results when a strong electrolyte (thin EDL) is considered. The EDL thickness above the patch for these parameter values is estimated to be 25 nm for thin EDL and 250 nm for thick EDL and the flow field is considered at electric field 40 V/m with $\phi_p=1.0$.

From the above results for microchannel, we find that the ions obey the equilibrium Boltzmann distribution away from the surface potential heterogeneity. The u-profile assumes a plug-like shape away from the surface potential heterogeneity. We observe a discrepancy in the P-B model from the N-P model in a heterogeneous microchannel with thick EDL. This difference of the P-B model from the exact N-P model grows with the increase in EDL thickness and the overpotential of the patch as well as strong external electric field and ζ-potential.

We now compare the validity of Poisson–Boltzmann model in nanosized channel with thin EDL. The comparisons of result for axial velocity profile at various sections of the channel is presented in Fig. 13. The wall values of the ionic species correspond to the strong solution, i.e., $Na^+=0.154M$ and $Cl^-=0.141M$, leading to the EDL thickness estimated to be 0.8 nm along the homogeneous part of the channel. The nondimensional overpotential on the upper face of the obstacle is considered to be $\phi_p=0.2$, so the EDL thickness along the patch is estimated to be $\lambda=0.78$ nm. The applied electric field is taken to be 10^6 V/m and the channel height is 20 nm. The maximum axial flow rate above the block is 0.002 m/s. Here, the EDLs are not overlapping and the flow outside the EDLs in the region far upstream and downstream of the patch is constant. We find a significant difference in solutions between the two models in the region above the block with maximum percentage difference in u is 39.13%. It may be noted that the trend of the solutions obtained by both the models are similar. We expect that the solutions of N-P and P-B models will differ

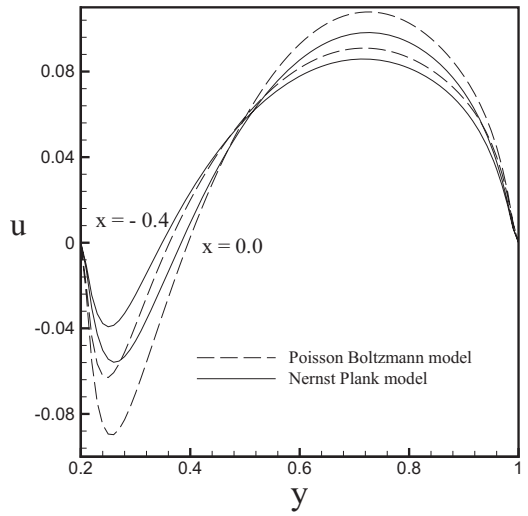

Fig. 13 Comparison of the results for axial velocity at different sections of the channel above the obstacle obtained by the present model (N-P) and Poisson–Boltzmann model (P-B) at h =20 nm with ϕ_p=0.2. The species concentration at the wall are Na^+=0.154M and Cl^-=0.141M (strong electrolyte) with imposed electric field 10^6 V/m.

when a overlap of EDL occurs and convection effect is stronger. Higher external electric field leads to stronger EOF. In the N-P model, direct impact of external electric field on the ionic distribution is considered and thus the dependence of EDL on external electric field is reflected.

5 Summary

We consider a new form of surface modulation involving geometric and surface potential heterogeneity, which causes a stronger convection effect. Here the EDLs are considered to be close. The imbalance in charge distribution along the EDLs leads to a formation of vortex adjacent to the potential patch. Presence of the surface mounted block induces a pressure gradient. A linear pressure drop along the centerline above the obstacle is observed, which induces acceleration in fluid flow. Flow merges to the fully developed EOF as we move upstream or downstream of the obstacle.

The circulation strength of the vortex formed above the patch increases linearly with the increase in ζ-potential. At a given value of the overpotential of the potential patch, increase in ζ-potential enhances both the fluid transport rate as well as the circulation strength. The circulation strength also increases linearly with the increase in channel height and overpotential of the patch.

Our result shows that the geometric modulation of the channel wall alone has much less impact on mixing efficiency compare with the effect due to modulation of the wall potential. However, the present configuration produces enhanced recirculation. Besides, vortex occurs even for the case where the patch potential is negative.

We have compared our results based on the N-P model with the results obtained by considering the Poisson–Boltzmann model for various values of the channel height, ζ-potential and external electric field. The ionic distribution in EDL on the surface modulation is greatly effected by convection, which leads to a difference in the P-B model from the exact N-P model near a surface modulation. This difference grows with the increase in EOF velocity. Thus the difference between the two models grow with the stronger external electric field and increase in ϕ_p.

The present study shows that through surface modulation, the flow separation and vortex formation can be initiated within a nanochannel even at Reynolds number of the order of 0.02. The formation of vortical flow is an important aspect in developing electrokinetically driven micromixers. The configuration considered here may also provide a simple model of some type of fabrication flaw.

Acknowledgment

One of the authors (S.B.) acknowledge the financial support received from the Department of Science and Technology, Government of India through a project grant.

References

[1] Guenat, O. T., Ghiglione, D., Morf, W. E., and de Rooij, N. F., 2001, "Partial Electroosmotic Pumping in Complex Capillary Systems: Part 2: Fabrication and Application of a Micro Total Analysis System (μTAS) Suited for Continuous Volumetric Nanotitrations," Sens. Actuators B, **72**, pp. 273–282.
[2] Lagally, E. T., Medintz, I., and Mathies, R. A., 2001, "Single Molecule DNA Amplification and Analysis in an Integrated Microdevice," Anal. Chem., **73**, pp. 565–570.
[3] Srinirasan, V., Pamula, V. K., and Fair, R. B., 2004, "An Integrated Digital Microfluidic Lab-on-a-Chip for Clinical Diagnostics on Human Physiological Fluids," Lab Chip, **4**, pp. 310–315.
[4] Stone, H. A., Stroock, A. D., and Ajdari, A., 2004, "Engineering Flows in Small Devices: Microfluidics Towards a Lab-on-a-Chip," Annu. Rev. Fluid Mech., **36**, p. 381411.
[5] Pugia, M. J., Blankenstien, G., Peters, R. P., Profit, J. A., Kadel, K., Willuis, T., Sommer, R., Kuo, H. H., and Schulman, L. S., 2005, "Microfluidic Tool Box as Technology Platform for Hand-Held Diagnostics," Clin. Chem., **51**, pp. 1923–1932.
[6] Squires, T., and Quake, S., 2005, "Microfluidics: Fluid Physics at the Nanoliter Scale," Rev. Mod. Phys., **77**, pp. 977–1026.
[7] Conlisk, A. T., 2005, "The Debye-Hückel Approximation: Its Use in Describing Electroosmotic Flow in Micro and Nano-Channels," Electrophoresis, **26**, pp. 1896–1912.
[8] Ghosal, S., 2006, "Electrokinetic Flow and Dispersion in Capillary Electrophoresis," Annu. Rev. Fluid Mech., **38**, pp. 309–338.
[9] Chang, C. C., and Yang, R. J., 2007, "Electrokinetic Mixing in Microfluidic Systems," Microfluid. Nanofluid., **3**, pp. 501–525.
[10] Watzig, H., Kaupp, S., and Graf, M., 2003, "Inner Surface Properties of Capillaries for Electrophoresis," Trends Analyt. Chem., **22**, pp. 588–604.
[11] Hu, Y., Werner, C., and Li, D., 2003, "Electrokinetic Transport Through Rough Microchannels," Anal. Chem., **75**, pp. 5747–5758.
[12] Hu, Y., Werner, C., and Li, D., 2004, "Influence of the Three-Dimensional Heterogeneous Roughness on Electrokinetic Transport in Microchannels," J. Colloid Sci., **280**, pp. 527–536.
[13] Ramirez, S., and Conlisk, A. T., 2006, "Formation of Vortices Near Abrupt Nano-Channel Height Changes in Electro-Osmotic Flow of Aqueous Solutions," Biomed. Microdevices, **8**, pp. 325–330.
[14] Datta, S., and Ghosal, S., 2008, "Dispersion Due to Wall Interactions in Microfluidic Separation Systems," Phys. Fluids, **20**, p. 012103.
[15] Wang, M., and Chen, S., 2008, "On Applicability of Poisson-Boltzmann Equation in Micro- and Nanoscale Electroosmotic Flows," Commun. Comput. Phys., **3**, pp. 1087–1099.
[16] Towns, J., and Regnier, F., 1992, "Impact of Polycation Adsorption on Efficiency and Electroosmotically Driven Transport in Capillary Electrophoresis," Anal. Chem., **64**, pp. 2473–2478.
[17] Ajdari, A., 1995, "Electro-Osmosis on Inhomogeneously Charged Surfaces," Phys. Rev. Lett., **75**, pp. 755–758.
[18] Erickson, D., and Li, D., 2002, "Influence of Surface Heterogeneity on Electrokinetically Driven Microfluidic Mixing," Langmuir, **18**, pp. 1883–1892.
[19] Ghosal, S., 2002, "Lubrication Theory for Electroosmotic Flow in a Microfluidic Channel of Slowly Varying Cross-Section and Wall Charge," J. Fluid Mech., **459**, pp. 103–128.
[20] Fu, L. M., Lin, J. Y., and Yang, R. J., 2003, "Analysis of Electroosmtoic Flow With Step Change in Zeta Potential," J. Colloid Interface Sci., **258**, pp. 266–275.
[21] Tian, F., Li, B., and Kwok, D. Y., 2005, "Tradeoff Between Mixing and Transport for Electroosmotic Flow in Heterogeneous Microchannels With Nonuniform Surface Potentials," Langmuir, **21**, pp. 1126–1131.
[22] Luo, W. J., 2006, "Transient Electro-Osmotic Flow Induced by AC Electric Field in Micro-Channel With Patchwise Surface Heterogeneities," J. Colloid Interface Sci., **295**, pp. 551–561.
[23] Chen, L., and Conlisk, A. T., 2009, "Effect of Nonuniform Surface Potential on Electroosmotic Flow at Large Applied Electric Field," Biomed. Microdevices, **11**, pp. 251–258.
[24] Park, H. M., Lee, J. S., and Kim, T. W., 2007, "Comparision of the Nernst–Plank Model and the Poissson–Boltzmann Model for Electroosmotic Flows in Microchannels," J. Colloid Interface Sci., **315**, pp. 731–739.
[25] Wang, J., Wang, M., and Li, Z., 2006, "Lattice Poisson-Boltzmann Simulations of Electro-Osmotic Flows in Microchannels," J. Colloid Interface Sci., **296**, pp. 729–736.
[26] Probstien, R. F., 1999, *Physiochemical Hydrodynamics*, Butterworth, Boston.
[27] Sverjensky, D. A., 2005, "Prediction of Surface Charge on Oxides in Salt Solutions: Revisions for 1:1 (M^+L^-) Electrolytes," Geochim. Cosmochim.

Acta, **69**, pp. 225–257.
[28] Conlisk, A., McFerran, J., Zheng, Z., and Hansford, D., 2002, "Mass Transfer and Flow in Electrically Charged Micro- and Nanochannels," Anal. Chem., **74**, pp. 2139–2150.
[29] Zheng, Z., Hansford, D., and Conlisk, A. T., 2003, "Effect of Multivalent Ions on Electroosmotic Flow in Micro- and Nanochannels," Electrophoresis, **24**, pp. 3006–3017.
[30] Chang, C. C., and Yang, R. J., 2004, "Computational Analysis of Electrokinetically Driven Flow Mixing in Microchannels With Patterned Blocks," J. Micromech. Microeng., **14**, pp. 550–558.

Babak Emami[1]
e-mail: bemami@mie.utoronto.ca

Markus Bussmann
Professor
e-mail: bussmann@mie.utoronto.ca

Department of Mechanical and Industrial Engineering,
University of Toronto,
Toronto, ON, M5S 3G8, Canada

Honghi Tran
Professor
Department of Chemical Engineering and Applied Chemistry,
University of Toronto,
Toronto, ON, M5S 3E5, Canada
e-mail: honghi.tran@utoronto.ca

Application of Realizability and Shock Unsteadiness to $k-\varepsilon$ Simulations of Under-Expanded Axisymmetric Supersonic Free Jets

An explicit cell-centered finite volume solver coupled to a $k-\varepsilon$ turbulence model corrected for structural compressibility fails to satisfactorily predict the behavior of under-expanded supersonic jets exhausting into still air, because the model does not properly account for the turbulence/shock wave interaction. Two approaches are examined: imposing a realizability constraint and taking into account shock unsteadiness effects. Although both corrections yield better agreement with experimental data of under-expanded jets, the realizability constraint yields better results than the shock unsteadiness correction. [DOI: 10.1115/1.4001341]

1 Introduction

The fouling of heat transfer surfaces in kraft recovery boilers is a significant concern for the pulp and paper industry. The usual approach to controlling fouling is the use of so-called "sootblowers" that utilize boiler steam to generate supersonic steam jets that are literally used to knock deposits off of boiler tubes. The high energy cost of operating sootblowers requires that they be run as efficiently as possible. Optimizing the performance of these jets is essential, and numerical simulation is an appropriate tool for this purpose.

Sootblower nozzles are nominally designed to expand steam to ambient pressure at the nozzle exit, but in practice, sootblower jets never perform at exactly the design condition, and so the jet pressure at the nozzle exit P_e is never exactly the ambient pressure P_∞ inside the boiler. When the exit pressure ratio $P_e/P_\infty > 1$, a multicell shock structure forms, which consists of shock and expansion waves through which the jet pressure drops to the ambient value. Under-expanded free jets involve simple flow geometries yet very complicated phenomena because of these shock waves and because the shock cells decay with distance from the nozzle exit due to an interaction with turbulence (see Fig. 1). The flow structure of an under-expanded jet can be considered to consist of near and far field areas. The near field includes the first few shock cells from the nozzle exit; this is an almost inviscid shock structure, where turbulent effects are insignificant. In the far field, further downstream, turbulent mixing reaches the jet centerline and so engulfs the whole flow field. At low exit pressure ratios ($1 < P_e/P_\infty < 2$), the multicell shock structure consists of several oblique shock waves; when $P_e/P_\infty \gg 2$, the first few shock cells contain normal shock waves, known as Mach disks [1].

Under-expanded jets have been the subject of many numerical studies. Because of the complex nature of the flow structure, it is a challenge to numerically simulate such jets, and so nearly all of the numerical literature is of 2D axisymmetric simulations. 3D simulations of under-expanded jets are extremely expensive, because of the fine computational mesh required to capture the shock wave phenomena. Some researchers have simplified the simulations by assuming the supersonic region inviscid [1–4], and obtained satisfactory predictions of available experimental measurements. Others have used various modified $k-\varepsilon$ turbulence models to simulate both mildly and highly under-expanded jets [5–7]; in all of these cases, the best agreement with experiment was obtained by considering dilatational compressibility effects (related to the extra dilatational terms that appear in the compressible turbulence kinetic energy k equation), as proposed by Sarkar et al. [8]. Yet, as pointed out by Wilcox [9], the model of Sarkar is based on early direct numerical simulation (DNS) results and is not universally accepted. In fact, the effects of the dilatational compressibility are thought to be negligible compared with the structural compressibility (related to the change in the structure of the k distribution) [9,10]; the model of Sarkar et al. overestimates these effects. This was further confirmed by applying Sarkar's model to simulate the fully expanded supersonic jet of Tandra [11]: the model underpredicted the eddy viscosity and yielded rather poor agreement with the measurements.

The present work focuses on the simulation of an under-expanded supersonic air jet exhausting into still air, and compares the results to some available experimental data. All the results are computed using CFDLIB 3.02, a computational fluid dynamics code developed at the Los Alamos National Laboratory. As will be shown, a $k-\varepsilon$ turbulence model that has been corrected for structural compressibility fails to satisfactorily predict the behavior of under-expanded jets. This failure comes as no surprise, as it is known that two-equation turbulence models predict a spuriously large growth of the turbulent kinetic energy, and thus eddy viscosity, near stagnation points [12], shock waves [13], massive separations, and generally anywhere in a flow field that experiences large strain rates [14]. Under-expanded jets are largely characterized by the shock/turbulence interaction, and so further corrections are required to take this phenomenon into account. In the present work, the problem is addressed by applying two different corrections in conjunction with the structural compressibility correction: imposing a realizability constraint and accounting for shock unsteadiness. It is demonstrated that both of these changes yield much improved predictions of the available experimental data. Both of these corrections have been successfully used for rather simple flows that involve shock waves (e.g., Refs. [15,16]); the present work seems to be the first attempt to apply these to

[1]Corresponding author.

Contributed by the Fluids Engineering Division of ASME for publication in the JOURNAL OF FLUIDS ENGINEERING. Manuscript received June 26, 2009; final manuscript received February 12, 2010; published online April 15, 2010. Assoc. Editor: Paul Durbin.

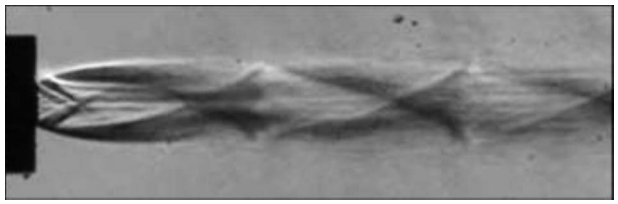

Fig. 1 The decaying shock-cell structure: flow visualization of an under-expanded jet with an exit Mach number of 2.53 and $P_e/P_\infty=3.12$

under-expanded jets, where the shock wave phenomena are complex.

The structure of this paper is as follows. The numerical method and turbulence model are presented in Sec. 2, with an emphasis on the aspects of interest. The results are presented and discussed in Sec. 3. Conclusions are presented in Sec. 4.

2 Methodology

2.1 Governing Equations. To calculate the motion of a compressible flow, the Favre averaged equations of conservation of mass (Eq. (1)), momentum (Eq. (2)), and energy (Eq. (3)) must be solved, along with an equation of state $\bar{p}=\bar{\rho}R\tilde{T}$

$$\bar{\rho}\dot{\bar{v}}=\frac{\partial\tilde{u}_i}{\partial x_i} \tag{1}$$

$$\bar{\rho}\dot{\tilde{u}}_i=-\frac{\partial\bar{p}}{\partial x_i}+\frac{\partial\bar{t}_{ij}}{\partial x_j}+\frac{\partial\tau_{ij}}{\partial x_j} \tag{2}$$

$$\bar{\rho}\dot{\tilde{E}}=-\frac{\partial\bar{p}\tilde{u}_j}{\partial x_j}+\frac{\partial\tilde{u}_i\bar{t}_{ij}}{\partial x_j}+\tilde{u}_i\frac{\partial\tau_{ij}}{\partial x_j}-\frac{\partial(q_{Lj}+q_{Tj})}{\partial x_j}+\bar{\rho}\varepsilon \tag{3}$$

where ρ is the density; v is the specific volume; u_i is the velocity vector; x_i is the coordinate vector; p is the pressure; t_{ij} is the molecular stress tensor; τ_{ij} is the Reynolds stress tensor; E is the specific total energy (which contains k); q_{Lj} and q_{Tj} are the laminar and turbulent heat flux vectors, respectively; ε is the turbulence dissipation rate; T is the temperature; and "$\bar{}$," "$\tilde{}$," and "$\dot{}$" represent the Reynolds average, Favre average, and Lagrangian derivative, respectively.

These equations were solved using a finite volume, explicit, cell-centered, total variation diminishing (TVD) method that utilizes an arbitrary Lagrangian–Eulerian (ALE) time split operator for advancing the averaged flow variables. The reader may refer to Ref. [17] for details.

2.2 Turbulence Model. The turbulence model is the standard $k-\varepsilon$ model, with modifications applied to account for the effects of structural compressibility, realizability, and shock unsteadiness. The equation for the turbulence kinetic energy k for a compressible flow is [9]

$$\bar{\rho}\dot{k}=\tau_{ij}\frac{\partial\tilde{u}_i}{\partial x_j}-\bar{\rho}\varepsilon+\frac{\partial}{\partial x_j}\left[\bar{\rho}\left(\nu+\frac{\nu_T}{\sigma_k}\right)\frac{\partial k}{\partial x_j}\right] \tag{4}$$

and the equation for ε is postulated as

$$\bar{\rho}\dot{\varepsilon}=C_{\varepsilon1}\frac{\varepsilon}{k}\tau_{ij}\frac{\partial\tilde{u}_i}{\partial x_j}-C_{\varepsilon2}\bar{\rho}\frac{\varepsilon^2}{k}+\frac{\partial}{\partial x_j}\left[\bar{\rho}\left(\nu+\frac{\nu_T}{\sigma_\varepsilon}\right)\frac{\partial\varepsilon}{\partial x_j}\right] \tag{5}$$

where $C_{\varepsilon1}=1.44$, $C_{\varepsilon2}=1.92$, $\sigma_k=1.0$, and $\sigma_\varepsilon=1.3$ are constant closure coefficients, and as the kinematic eddy viscosity $\nu_T=C_\mu(k^2/\varepsilon)$, C_μ is an additional closure coefficient. The value of C_μ is calculated locally to account for the effects of structural compressibility, as will be discussed in Sec. 2.2.1.

2.2.1 Compressibility Effects. Compressibility effects may be categorized into two groups: those related to the change in the structure of the turbulence kinetic energy distribution and those related to the extra dilatational terms that appear in the compressible turbulence kinetic energy equation. DNS research has shown that the effects of the dilatational compressibility are usually negligible compared with the structural effects [9,10].

DNS results [18] show that in a compressible turbulent shear layer the spatial distribution of k varies tremendously: the streamwise component of k increases with the compressibility level [10], which Sarkar [18] suggested can be characterized by the gradient Mach number M_g. Based on DNS results of an initially homogeneous compressible shear flow, Sarkar suggested

$$M_g=\frac{S_g l_g}{a} \tag{6}$$

where $S_g=\partial U_1/\partial x_2$ is the mean shear rate; U_1 and x_2 are the streamwise mean velocity and shear direction coordinate, respectively; l_g is the correlation length of the streamwise fluctuating velocities in the shear direction; and a is the local sound speed. The greater the gradient Mach number, the stronger the compressibility. DNS results of Sarkar also suggest that the normal and shear Reynolds stresses vary exponentially with the gradient Mach number, implying that the streamwise normal Reynolds stress increases with the gradient Mach number, while the normal Reynolds stresses in other directions and the shear Reynolds stresses decrease. As a result, the eddy viscosity decreases as the gradient Mach number increases. Using these relations, Heinz [10] suggested that

$$C_\mu=0.07\exp(-0.4M_g) \tag{7}$$

Tandra et al. [19] further generalized this model by suggesting that the mean shear rate be calculated as

$$S_g=\sqrt{2\left[\tilde{S}_{ij}\tilde{S}_{ji}-\tfrac{1}{3}\tilde{S}_{kk}\tilde{S}_{ll}\right]} \tag{8}$$

in which $\tilde{S}_{ij}$ is the local mean shear rate, and that l_g be calculated in a way similar to the characteristic length scale used in Prandtl's one-equation turbulence model [9]

$$l_g=C_D\frac{k^{3/2}}{\varepsilon} \tag{9}$$

where C_D is a closure coefficient usually considered to be 0.09.

The $k-\varepsilon$ model in CFDLIB, corrected for structural compressibility as per Tandra et al. [19], has been validated against a wide range of available data corresponding to properly expanded (and therefore, shock wave free) high speed jet flows [11,20–25]; the simulations successfully predicted all of the examined cases.

2.2.2 Realizability Constraint. The compressibility-corrected turbulence model was improved by imposing a realizability constraint. This section presents the constraints proposed by Durbin [12] and Thivet et al. [26].

Durbin [12] suggested suppressing the eddy viscosity as follows. Since $k=\frac{1}{2}\overline{u_k''u_k''}$, one should have (for each $i=1,2,3$)

$$0\le\overline{u_i''^2}\le 2k \tag{10}$$

$\overline{u_i''^2}\ge 0$ (energy positivity) is more restrictive than $\overline{u_i''^2}\le 2k$, in that the second follows if the first is met (for a proof, see Ref. [12]). Durbin showed that energy positivity is satisfied if

$$\nu_T\le\frac{1}{\sqrt{6}}\frac{k}{S_D} \tag{11}$$

where $S_D=\sqrt{\bar{S}_{ij}\bar{S}_{ji}}$ is a measure of the shear rate for an incompressible flow. When used for compressible flow, S_D must be redefined as

$$S_D = \sqrt{\tilde{S}_{ij}\tilde{S}_{ji} - \tfrac{1}{3}\tilde{S}_{kk}\tilde{S}_{ll}} \tag{12}$$

To satisfy realizability, the eddy viscosity should then be calculated as

$$\nu_T = \min\left(C_\mu \frac{k^2}{\varepsilon}, \frac{\eta}{\sqrt{6}}\frac{k}{S_D}\right) \tag{13}$$

where η is an empirical constant less than one, which is used to obtain agreement with experimental data [12]. In this work, Eq. (13) is referred to as Durbin's realizability constraint.

Thivet et al. [26] proposed an alternative constraint on eddy viscosity. They argued, based on experimental data, that the Boussinesq approximation $\tau_{ij} = 2\bar{\rho}\nu_T\left(\tilde{S}_{ij} - \frac{1}{3}\tilde{S}_{kk}\delta_{ij}\right) - \frac{2}{3}\bar{\rho}k\delta_{ij}$ is highly unrealistic in the presence of an adverse pressure gradient (e.g., across a shock wave). Under such conditions, the Reynolds stress is not proportional to the strain rate, but to the turbulence kinetic energy, such that

$$\tau_{ij} = C_\mu^{01/2}\bar{\rho}k \tag{14}$$

where $C_\mu^0 = 0.09$ is the value of C_μ in the standard $k-\varepsilon$ model. Thivet et al. suggested that the simplest way to reconcile the Boussinesq approximation with Eq. (14) in a reference frame-independent expression was to constraint the coefficient C_μ to $\min(C_\mu^0, C_\mu^{01/2}k/S_D\varepsilon)$. For a $k-\varepsilon$ turbulence model, this leads to

$$\nu_T = \min\left(C_\mu^0 \frac{k^2}{\varepsilon}, \frac{C_\mu^{01/2}}{\sqrt{2}}\frac{k}{S_D}\right) \tag{15}$$

In the present work, because this constraint is used in conjunction with the compressibility correction, C_μ^0 is replaced by C_μ (calculated by Eq. (7)), and so

$$\nu_T = \min\left(C_\mu \frac{k^2}{\varepsilon}, \frac{C_\mu^{1/2}}{\sqrt{2}}\frac{k}{S_D}\right) \tag{16}$$

In this paper, Eq. (16) is referred to as Thivet's realizability constraint.

As Thivet [27] pointed out more recently, although the Durbin and Thivet constraints are based on different approaches, they have similar forms, as can be seen from Eqs. (13) and (16). The two constraints become identical when $\eta = (3C_\mu)^{1/2}$. To fairly compare the results using the Durbin and Thivet realizability constraints, we set the value of the constant η to $(3\bar{C}_\mu)^{1/2}$, where $\bar{C}_\mu$ is an average value of C_μ, calculated as

$$\bar{C}_\mu = \frac{1}{M_{g,\max} - M_{g,\min}} \int_{M_{g,\min}}^{M_{g,\max}} C_\mu(M_g)\, dM_g \tag{17}$$

$M_{g,\min}$ and $M_{g,\max}$ are the minimum and maximum values, respectively, of M_g calculated by Thivet's realizability constraint.

Finally, note that both constraints yield discontinuous values of eddy viscosity and therefore of Reynolds stress in the flow. These discontinuities occur across a shock wave (i.e., different values of eddy viscosity upstream and downstream of a shock) and are physically realistic, as the theoretical work of Zank et al. [28] confirms a jump in turbulence across a normal shock wave. As well, by comparing DNS results of isotropic turbulence across a normal shock wave with the results obtained from a $k-\varepsilon$ model, Sinha et al. [13] concluded that the Durbin and Thivet constraints improve the prediction of the turbulence kinetic energy, and correctly reduce eddy viscosity.

2.2.3 Effect of Shock Unsteadiness. Shock unsteadiness plays an important role in the interaction of turbulence with shock waves [13], by increasing the mean shock thickness. The unsteady motion can be correlated with turbulence fluctuations [29], which disturb and distort the shock wave front [28,30]. Specifically in under-expanded jets, shock unsteadiness has been observed experimentally (e.g., Refs. [31,32]).

Sinha et al. [13] suggested that overprediction of the turbulence production in the presence of shock waves is due to the fact that the effect of shock unsteadiness is not taken into account in turbulence models. They proposed a modification to the $k-\varepsilon$ model to account for unsteadiness of a normal shock wave in an isotropic homogeneous uniform turbulent flow. More recently, Sinha et al. [16] extended this model and proposed a more general correction for flows with additional mean gradients. The turbulence production term $P_k = \tau_{ij}(\partial\tilde{u}_i/\partial x_j)$ can be written as

$$P_k = \bar{\rho}\nu_T\left(2\tilde{S}_{ij}\tilde{S}_{ji} - \tfrac{2}{3}\tilde{S}_{kk}\tilde{S}_{ll}\right) - \tfrac{2}{3}\bar{\rho}k\tilde{S}_{kk} \tag{18}$$

They suggested replacing ν_T in Eq. (18) with $c'_\mu\nu_T$, where

$$c'_\mu = 1 - f_s\left[1 + \frac{1}{\sqrt{6}}\frac{b'_1\varepsilon}{C_\mu k S_D}\right] \tag{19}$$

where

$$f_s = \frac{1}{2} - \frac{1}{2}\tanh\left(5\frac{\tilde{S}_{kk}}{\sqrt{2}S_D} + 3\right) \tag{20}$$

with S_D defined by Eq. (12), and b'_1 is a function of the local Mach number M

$$b'_1 = \max(0, 0.4(1 - e^{1-M})) \tag{21}$$

Equation (20) defines f_s as close to one in high compressibility regions and close to zero elsewhere. Here, this correction is referred to as the Sinha-2005 correction. The performance of this model is also evaluated in this paper.

3 Results and Discussion

This section is divided into three parts. The failure of the compressibility-corrected $k-\varepsilon$ turbulence model to simulate under-expanded jets is demonstrated in the first part. The effects of the turbulence model corrections are then evaluated in the second part, by comparing results to the measurements of the under-expanded air jet of Seiner and co-worker [33–35]. Finally, the corrected turbulence models are used to predict some other available data.

The simulations were run on a Pentium 4 workstation with a 3.0 GHz dual core CPU. Various simulations were performed on computational domains of different sizes, and using different meshes, to determine the domain and mesh sizes required to yield nearly independent results. All simulations were run in a 2D axisymmetric coordinate system. As mentioned in Sec. 1, 3D simulations of under-expanded jets are extremely expensive, because of the fine computational mesh required to capture the shock and expansion waves, and so cannot be carried out without access to very large computing resources. But given the nature of RANS simulations, a 3D calculation is unlikely to provide any mean flow information beyond that of a 2D axisymmetric simulation. This was confirmed by 2D and 3D simulations of the fully expanded supersonic jet of Tandra [11], for which the type of boundary conditions and the domain size were similar to those of the simulations presented here. As that flow did not contain shock waves, 2D and 3D simulations could be run on much coarser meshes. The 2D axisymmetric and 3D results were nearly indistinguishable.

3.1 Failure of the Compressibility-Corrected Turbulence Model. The compressibility-corrected model was applied to predict the measurements of Seiner and co-worker [33–35] of an under-expanded air jet ($P_e/P_\infty = 1.45$ and an exit Mach number of 2.0); these data sets are frequently used to assess numerical models. The ambient pressure was specified as the boundary condition far from the jet centerline. The inlet boundary conditions (velocity, density, and temperature) at the nozzle exit were calculated

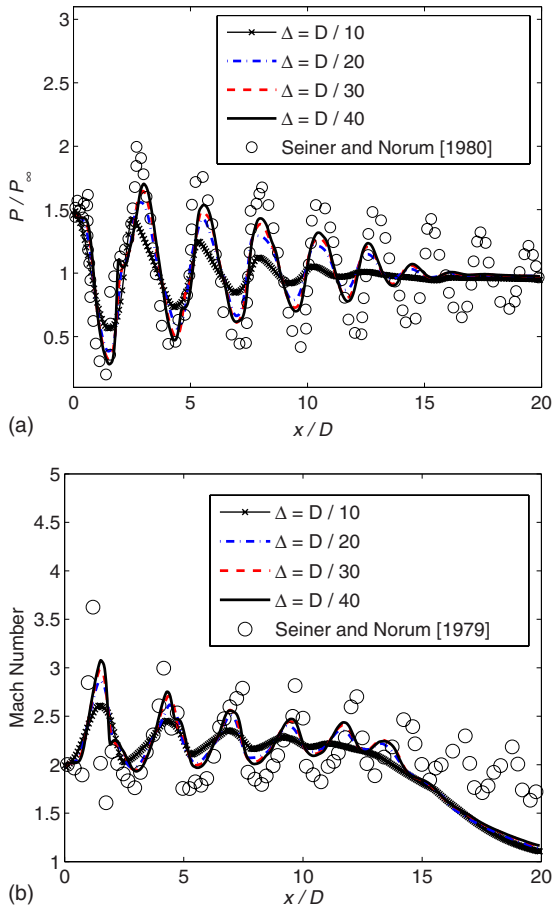

Fig. 2 Normalized pressure (top) and Mach number (bottom) along the centerline of an under-expanded jet, as a function of mesh size, calculated by the compressibility-corrected model

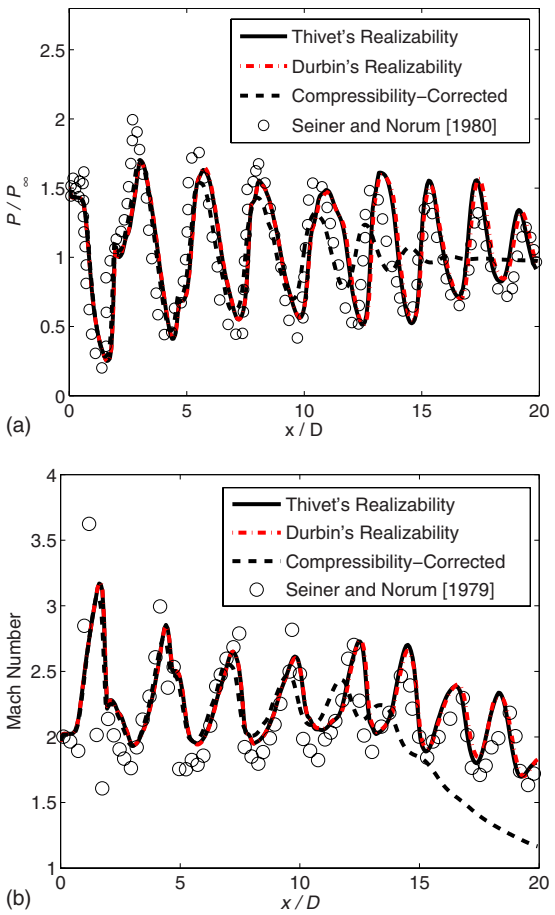

Fig. 3 Calculations of normalized pressure (top) and Mach number (bottom) with Thivet and Durbin realizability constraints

based on the value of P_e/P_∞. Top-hat (uniform) profiles were specified at the inlet, as other profiles (with the same momentum) are unlikely to yield a significantly different jet mean flow [36].

Figure 2 presents normalized centerline pressure (top) and centerline Mach number (bottom) versus axial distance from the nozzle exit, calculated on various computational meshes, compared with the experimental data. All the meshes were uniform and the mesh size ranged from $\Delta=D/10$ to $\Delta=D/40$, where D is the nozzle exit diameter. At mesh sizes of $D/30$-$D/40$ the solution is nearly independent of the computational mesh. This is in accord with Fairweather and Ranson [7], who obtained a mesh independent solution of an under-expanded jet at $\Delta=D/32$. The slight difference between the wave amplitudes calculated at $\Delta=D/30$ and $D/40$ is due to numerical diffusion that could be further reduced by calculating even finer results, but as the D/40 simulation ran about 240 h, such simulations were not run. Returning to Fig. 2, however, and especially the Mach number results, it should be clear that the predicted decay of the jet downstream of the first few shock cells must be due to something other than numerical diffusion, as will be demonstrated in Sec. 3.2 by considering corrections to the turbulence model.

All subsequent results presented in this paper were calculated at $D/40$. The simulations were run on a computational domain of $20D$ by $5D$ in the axial and radial directions, respectively; extending the domain size to $30D$ by $15D$ did not change the results.

3.2 Effects of the Turbulence Model Corrections. To examine the role of the turbulence model, two realizability constraints and a shock unsteadiness model were each incorporated into the structural compressibility-corrected $k-\varepsilon$ model.

Figure 3 shows pressure (top) and Mach number (bottom) when the Thivet and Durbin realizability constraints were imposed. The amplitudes of the first few shock cells calculated by either of the two realizability constraints vary little from the compressibility-corrected model, but the results in the far field are clearly better, as the overprediction of the eddy viscosity has been eliminated. Note, too, that the two realizability constraints yield almost identical results. This is no surprise, because the value of the coefficient η in Durbin's constraint was set to $(3\bar{C}_\mu)^{1/2}=0.4368$, where $\bar{C}_\mu$ is the average C_μ calculated from the results using Thivet's constraint, calculated via Eq. (17). Using a value of $\eta=0.5$, as proposed by Thivet et al. [15] for boundary layer/shock wave interactions, yielded results which were not as accurate in the far field; setting η to 1 yielded very similar results to the compressibility-corrected model alone. Finally, the fact that the two realizability constraints yield nearly identical results indicates that the C_μ variations in Thivet's constraint (Eq. (16)) do not significantly affect the computations. For the remainder of this paper we present results using Thivet's constraint, although these results are nearly identical to those obtained by Durbin's constraint.

Returning to Fig. 3, the wave amplitudes are expected to decrease monotonically with distance from the nozzle exit, as can be observed from the experimental data, because of the dissipation that results from the turbulent mixing of the flow field. This is not properly captured by the model with either of the realizability constraints, perhaps because these constraints lead to underprediction of the eddy viscosity in the vicinity of shock waves. However, the overall agreement with the measurements is fairly rea-

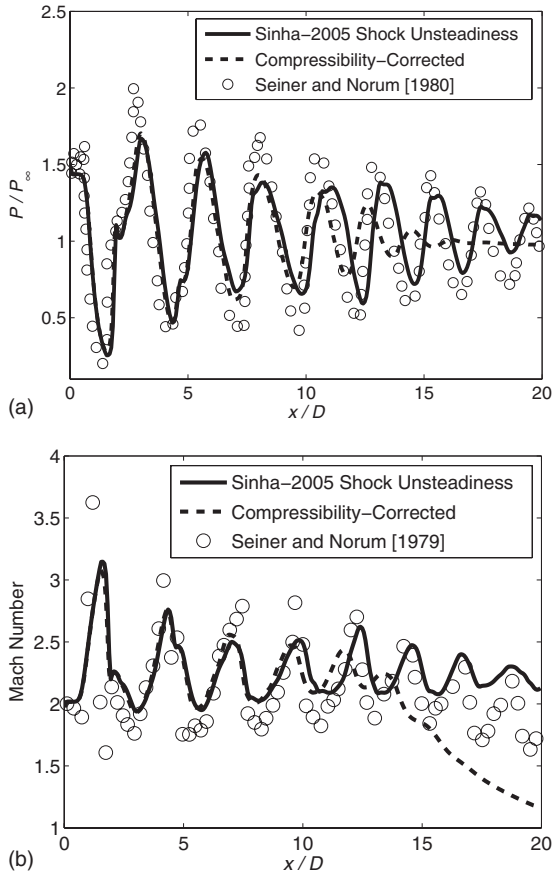

Fig. 4 Calculations of normalized pressure (top) and Mach number (bottom) with the Sinha-2005 shock unsteadiness correction

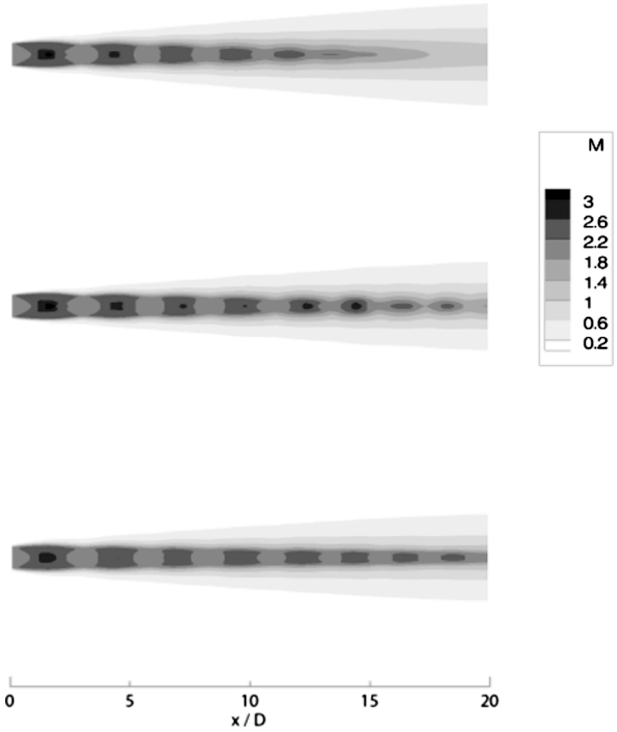

Fig. 5 Mach number contours corresponding (from top to bottom) to calculations with the compressibility-corrected model, Thivet's realizability constraint, and the Sinha-2005 correction

sonable, and much improved over the results without a constraint.

Turning to shock unsteadiness, Fig. 4 illustrates that the Sinha-2005 correction also improves the model predictions significantly, by eliminating the overdamping in the far field. Overall, however, the improvement is not as good as that offered by the realizability constraints, especially when considering the Mach number.

The Mach number contours calculated by the compressibility-corrected model, by Thivet's constraint, and by the Sinha-2005 correction, are presented in Fig. 5. As can also be seen from the corresponding plots of the centerline pressure (Figs. 2–4), the compressibility-corrected solution is too diffusive, and so the far field shock cells are damped, while both Thivet's realizability constraint and the Sinha-2005 correction result in less diffusive solutions that preserve the shock-cell structure further downstream. Note, too, that Fig. 5 reinforces that both corrections, but especially Thivet's constraint, yield nonmonotonic results, especially around the fifth shock cell ($x/D \approx 12$), which is more intense than the one immediately upstream.

These results can be better understood by examining the eddy viscosity calculated by each model. Figure 6 (top) shows the distribution of the eddy viscosity along the jet centerline, calculated using the compressibility-corrected model, Thivet's realizability constraint, and the Sinha-2005 correction. The eddy viscosity calculated by the three models is rather small in the near field, up to $x/D \approx 14$. Figure 6 (bottom) presents a close-up of the eddy viscosity in the near field, at a very different scale. Comparing Fig. 6 (bottom) with Fig. 3 (top) and Fig. 4 (top) shows that the eddy viscosity along the jet centerline increases when the pressure increases (i.e., across a shock wave) and decreases as the pressure drops across the expansion waves. This agrees with the analytical work of Zank et al. [28], which indicates that turbulence is enhanced across a shock wave, and then decays downstream of the shock. Note, too, that the oscillations of the eddy viscosity calculated by Thivet's realizability constraint are not damped monotonically, especially between $x/D \approx 10$ and 14, which explains the nonmonotonic behavior observed in Fig. 3. Turning back to Fig. 6 (top), the compressibility-corrected model predicts a dramatic increase in the eddy viscosity at $x/D \approx 14$, which results in the overdamping of the solution, and so eliminates the shock cells beyond $x/D \approx 14$ (see Fig. 2). The Sinha-2005 correction reduces the far field eddy viscosity, but fails to capture the oscillations. Only the realizability constraint reduces the eddy viscosity and captures the oscillating behavior in the far field, which may explain why the realizability constraint yields the most accurate results.

3.3 Comparisons With Other Experimental Data. The corrected turbulence models (with Thivet's realizability constraint and the Sinha-2005 shock unsteadiness correction) were used to predict some other available measurements. Figure 7 shows a comparison of the results calculated by Thivet's constraint and the Sinha-2005 correction with the data of Norum and Seiner [35] for an under-expanded jet similar to that of Seiner and Norum [34]; the plot illustrates the axial pressure distribution at $r/D=0.25$, where r is the radial coordinate. Similar to Figs. 3 and 4, both modified turbulence models improve the prediction noticeably compared with the compressibility-corrected model. But again, Thivet's constraint yields better agreement with the data than the Sinha-2005 correction.

A simulation was also run to demonstrate that the corrections do not affect the results much when the uncorrected model predicts the measurements reasonably well. The model with Thivet's constraint was used to simulate the measurements of Panda and Seasholtz [32] for the normalized density distribution along the centerline of a strongly under-expanded jet, as shown in Fig. 8. In this case, $P_e/P_\infty=3.0$ and $M_e=1.0$. The agreement with the experimental data is reasonably good, especially near the exit, and the corrections to the turbulence model do not significantly affect

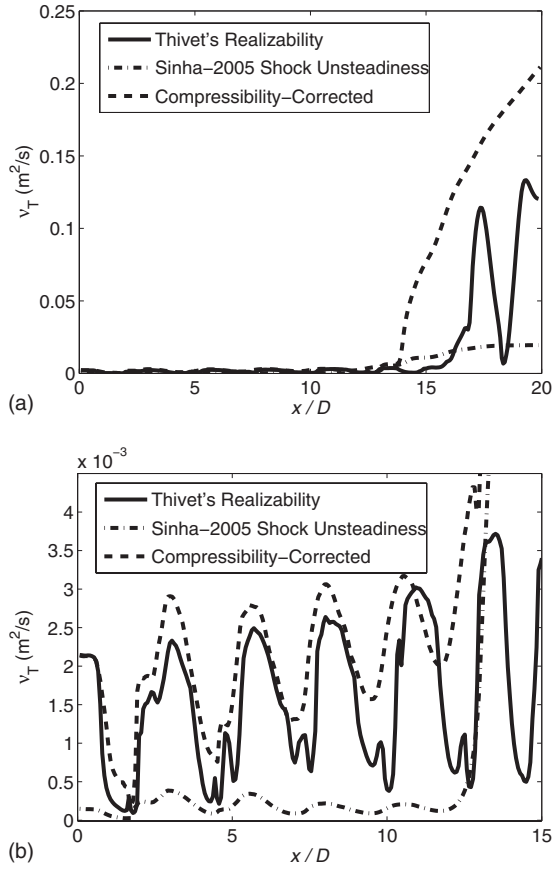

Fig. 6 Distribution of the eddy viscosity along the jet centerline, calculated with the compressibility-corrected model, Thivet's realizability constraint, and the Sinha-2005 correction

the results, because this set of data is limited to the near field region, while the turbulence model corrections affect primarily the far field region of the jet. The Sinha-2005 correction yielded a similar result, and so the corresponding figure is not presented here.

4 Conclusion

The simulation of under-expanded jets was examined accounting for the turbulence/shock wave interaction, by adding realizability constraints and a shock unsteadiness correction to a compressibility-corrected $k-\varepsilon$ turbulence model. Both approaches yielded much more accurate far field predictions, but the results indicate that a realizability constraint is required for simulation of an under-expanded jet, as the results are better than those obtained using the shock unsteadiness correction. The two realizability constraints, which were used, the Durbin and the Thivet constraints, yielded nearly identical results when the constant η in Durbin's model was set to a value calculated using the average C_μ from Thivet's results. This indicates that the C_μ variations in Thivet's constraint do not significantly affect the calculations. Investigation of the calculated eddy viscosities indicates that both the realizability constraint and shock unsteadiness correction suppress the overprediction of eddy viscosity in the far field, but only the realizability constraints predict an oscillating eddy viscosity in the far field, which may explain the better performance.

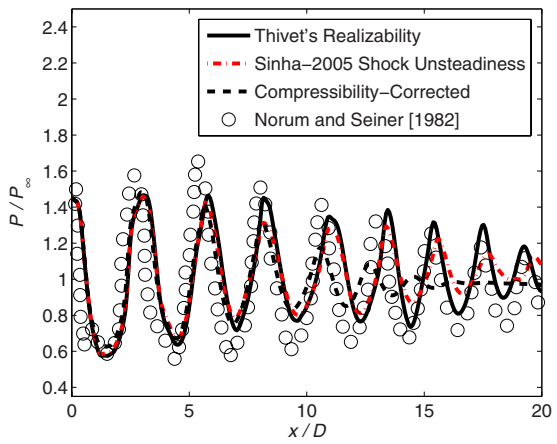

Fig. 7 Calculation of the under-expanded jet of Norum and Seiner [35] with Thivet's realizability constraint, and the Sinha-2005 correction, *r*/*D*=0.25

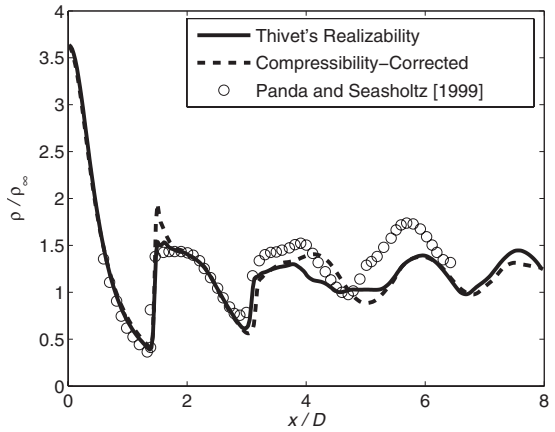

Fig. 8 Calculations of the under-expanded jet of Panda and Seasholtz [32] with Thivet's realizability constraint

Acknowledgment

The authors thank Ameya Pophali of the University of Toronto for the schlieren image of an under-expanded jet (Fig. 1).

References

[1] Chuech, S. G., Lai, M. C., and Faeth, G. M., 1989, "Structure of Turbulent Sonic Underexpanded Free Jets," AIAA J., **27**(5), pp. 549–559.
[2] Dash, S. M., Wolf, D. E., and Seiner, J. M., 1985, "Analysis of Turbulent Underexpanded Jets, Part I: Parabolized Navier-Stokes Model, SCIPVIS," AIAA J., **23**(4), pp. 505–514.
[3] Dash, S. M., and Wolf, D. E., 1984, "Interactive Phenomena in Supersonic Jet Mixing Problems, Part II: Numerical Studies," AIAA J., **22**(10), pp. 1395–1404.
[4] Dash, S. M., and Wolf, D. E., 1984, "Interactive Phenomena in Supersonic Jet Mixing Problems, Part I: Phenomenology and Numerical Modeling Techniques," AIAA J., **22**(7), pp. 905–913.
[5] Cumber, P. S., Fairweather, M., Falle, S. A. E. G., and Giddings, J. R., 1994, "Predictions of the Structure of Turbulent, Moderately Underexpanded Jets," ASME J. Fluids Eng., **116**(4), pp. 707–713.
[6] Cumber, P. S., Fairweather, M., Falle, S., and Giddings, J. R., 1995, "Predictions of the Structure of Turbulent, Highly Underexpanded Jets," ASME J. Fluids Eng., **117**(4), pp. 599–604.
[7] Fairweather, M., and Ranson, K. R., 2006, "Prediction of Underexpanded Jets Using Compressibility-Corrected, Two-Equation Turbulence Models," Prog. Comput. Fluid Dyn., **6**(1/2/3), pp. 122–128.
[8] Sarkar, S., Erlebacher, G., Hussaini, M. Y., and Kreiss, H. O., 1991, "Analysis and Modelling of Dilatational Terms in Compressible Turbulence," J. Fluid Mech., **227**, pp. 473–493.
[9] Wilcox, D. C., 2004, *Turbulence Modeling for CFD*, DCW Industries, La Canada, CA.
[10] Heinz, S., 2003, "A Model for the Reduction of the Turbulent Energy Redistribution by Compressibility," Phys. Fluids, **15**(11), pp. 3580–3583.
[11] Tandra, D., 2005, "Development and Application of a Turbulence Model for a Sootblower Jet Propagating Between Recovery Boiler Superheater Platens," Ph.D. thesis, Department of Chemical Engineering and Applied Chemistry, University of Toronto, Toronto, Canada.
[12] Durbin, P. A., 1996, "On the *k*-3 Stagnation Point Anomaly," Int. J. Heat Fluid

Flow, **17**(1), pp. 89–90.
[13] Sinha, K., Mahesh, K., and Candler, G. V., 2003, "Modeling Shock Unsteadiness in Shock/Turbulence Interaction," Phys. Fluids, **15**(8), pp. 2290–2297.
[14] Shih, T., Liou, W. W., Shabbir, A., Yang, Z., and Zhu, J., 1995, "New $k-\varepsilon$ Viscosity Model for High Reynolds Number Turbulent Flows," Comput. Fluids, **24**(3), pp. 227–238.
[15] Thivet, F., Knight, D. D., Zheltovodov, A. A., and Maksimov, A. I., 2001, "Insights in Turbulence Modeling for Crossing-Shock-Wave/Boundary-Layer Interactions," AIAA J., **39**(6), pp. 985–995.
[16] Sinha, K., Mahesh, K., and Candler, G. V., 2005, "Modeling the Effect of Shock Unsteadiness in Shock/Turbulent Boundary-Layer Interactions," AIAA J., **43**(3), pp. 586–594.
[17] Emami, B., 2009, "Numerical Simulation of Kraft Recovery Boiler Sootblower Jets," Ph.D. thesis, Department of Mechanical and Industrial Engineering, University of Toronto, Toronto, Canada.
[18] Sarkar, S., 1995, "The Stabilizing Effect of Compressibility in Turbulent Shear Flow," J. Fluid Mech., **282**, pp. 163–186.
[19] Tandra, D. S., Kaliazine, A., Cormack, D. E., and Tran, H. N., 2006, "Numerical Simulation of Supersonic Jet Flow Using a Modified Model," Int. J. Comput. Fluid Dyn., **20**(1), pp. 19–27.
[20] Alvi, F. S., Ladd, J. A., and Bower, W. W., 2002, "Experimental and Computational Investigation of Supersonic Impinging Jets," AIAA J., **40**(4), pp. 599–609.
[21] Debonis, J. R., and Scott, J. N., 2002, "Large-Eddy Simulation of a Turbulent Compressible Round Jet," AIAA J., **40**(7), pp. 1346–1354.
[22] Du P. Donaldson, C., and Gray, K. E., 1966, "Theoretical and Experimental Investigation of the Compressible Free Mixing of Two Dissimilar Gases," AIAA J., **4**(11), pp. 2017–2025.
[23] Du P. Donaldson, C., and Snedeker, R. S., 1971, "A Study of Free Jet Impingement, Part 1, Mean Properties of Free and Impinging Jets," AIAA J., **45**(2), pp. 281–319.
[24] Panda, J., and Seasholtz, R. G., 1999, "Velocity and Temperature Measurement in Supersonic Free Jets Using Spectrally Resolved Rayleigh Scattering," AIAA Paper No. 99-0296.
[25] Wang, Z., and Andreopoulos, Y., 2003, "Compressibility Effects in Turbulent Subsonic Jets," Fourth ASME/JSME Joint Fluids Engineering Conference.
[26] Thivet, F., Knight, D. D., Zheltovodov, A. A., and Maksimov, A. I., 2001, "Importance of Limiting the Turbulent Stresses to Predict 3D Shock Wave/Boundary Layer Interactions," 23rd Symposium on Shock Waves, Paper No. 2761.
[27] Thivet, F., 2002, "Lessons Learned From RANS Simulations of Shock-Wave/Boundary Layer Interactions," AIAA Paper No. 2002-0583.
[28] Zank, G. P., Zhou, Y., Matthaeus, W. H., and Rice, W. K. M., 2002, "The Interaction of Turbulence With Shock Waves: A Basic Model," Phys. Fluids, **14**(11), pp. 3766–3774.
[29] Mahesh, K., Lele, S. K., and Moin, P., 1997, "The Influence of Entropy Fluctuations on the Interaction of Turbulence With a Shock Wave," J. Fluid Mech., **334**, pp. 353–379.
[30] Moore, F. K., 1954, "Unsteady Oblique Interaction of a Shock Wave With a Plane Disturbance," Technical Report No. NACA TN 2879.
[31] Panda, J., 1998, "Shock Oscillation in Underexpanded Screeching Jets," J. Fluid Mech., **363**, pp. 173–198.
[32] Panda, J., and Seasholtz, R. G., 1999, "Measurement of Shock Structure and Shock Vortex Interaction in Underexpanded Jets Using Rayleigh Scattering," Phys. Fluids, **11**(12), pp. 3761–3777.
[33] Seiner, J. M., and Norum, T. D., 1979, "Experiments on Shock Associated Noise of Supersonic Jets," AIAA Paper No. 79-1526.
[34] Seiner, J. M., and Norum, T. D., 1980, "Aerodynamic Aspects of Shock Containing Jet Plumes," AIAA Paper No. 80-0965.
[35] Norum, T. D., and Seiner, J. M., 1982, "Measurements of Mean Static Pressure and Far-Field Acoustics of Shock-Containing Supersonic Jets," NASA Technical Memorandum 84521.
[36] Boersma, B. J., Brethouwer, G., and Nieuwstadt, F. T. M., 1998, "A Numerical Investigation on the Effect of the Inflow Conditions on the Self-Similar Region of a Round Jet," Phys. Fluids, **10**(4), pp. 899–908.

Analysis of Unsteady Confined Viscous Flows With Variable Inflow Velocity and Oscillating Walls

Dan Mateescu
Professor

Manuel Muñoz

Olivier Scholz

Department of Mechanical Engineering,
McGill University,
Montreal, QC, H3A 2K6, Canada

The inflow velocities in various components of many engineering systems often display variations in time (fluctuations) during the operation cycle, which may substantially affect the flow-induced vibrations and instabilities of these systems. For this reason, the aeroelasticity study of these systems should include the effect of the inflow velocity variations, which until now has not been taken into account. This paper presents a fluid-dynamic analysis of the unsteady confined viscous flows generated by the variations in time of the inflow velocities and by oscillating walls, which is required for the study of flow-induced vibration and instability of various engineering systems. The time-accurate solutions of the Navier–Stokes equations for these unsteady flows are obtained with a finite-difference method using artificial compressibility on a stretched staggered grid, which is a second-order method in space and time. A special decoupling procedure, based on the utilization of the continuity equation, is used in conjunction with a factored alternate direction scheme to substantially enhance the computational efficiency of the method by reducing the problem to the solution of scalar tridiagonal systems of equations. This method is applied to obtain solutions for the benchmark unsteady confined flow past a downstream-facing step, generated by harmonic variations in time of the inflow velocity and by an oscillating wall, which display multiple flow separation regions on the upper and lower walls. The influence of the Reynolds number and of the oscillation frequency and the amplitudes of the inflow velocity and oscillating wall on the formation of the flow separation regions are thoroughly analyzed in this paper. It was found that for certain values of the Reynolds number and oscillation frequency and amplitudes, the flow separation at the upper wall is present only during a portion of the oscillatory cycle and disappears for the rest of the cycle, and that for other values of these parameters secondary flow separations may also be formed. [DOI: 10.1115/1.4001184]

1 Introduction

The steady and unsteady fluid-structure interaction problems are present in numerous engineering fields such as in thermofluid systems, pumps, nuclear reactors, gas and hydraulic turbines, aeronautics, and other areas. This explains why the study of fluid-structure interaction problems and flow-induced vibrations received a topical interest worldwide. Thus, fluid-structure interaction problems in axial and annular configurations and the corresponding unsteady flows have been studied theoretically (using simplified models for idealized geometries) and experimentally by, among others, Inada and Hayama [1,2], Mateescu and Paidoussis [3], and Mateescu et al. [4,5].

The accurate analysis of fluid-structure interaction problems requires the simultaneous solution of the equations of the unsteady (or steady) flows and those of the deformation motion (often oscillatory) of the structure. As a result, the numerical methods of solution for the unsteady flows have to be characterized by an excellent computational efficiency, in addition to a very good accuracy. This requirement is made even more difficult by the complexity of the fluid flow problems, involving usually oscillating boundaries and flow separation regions, which require solutions of the Navier–Stokes equations capable to accurately capture these separation regions. Several studies have been based on numerical methods using finite-difference formulations, such as those developed by Mateescu et al. [6–9], Belanger et al. [10], Mateescu and Venditti [11], and others, which were validated by experiments (see Ref. [12]), or using spectral and hybrid-spectral formulations, such as those developed by Mateescu et al. [13–16].

All the above mentioned studies considered the case when the inflow velocities were constant in time. However, the inflow velocities in various components of the engineering systems often display variations in time (fluctuations), which may substantially affect the flow-induced vibrations and instabilities of these systems. For this reason, there is a need to take also into account in these studies the variation in time (fluctuations) of the inflow velocity.

A first attempt to study the effect of the inflow velocity fluctuations (but without considering the wall oscillations) was presented at an ASME Symposium on Flow-Induced Vibration by Mateescu et al. [17].

Recently, with the development of the microelectromechanical systems (MEMSs), a research interest has been developed for steady and unsteady confined fluid flows at low Reynolds numbers. With a research interest in the confined fluid flow with heat transfer in MEMS at low Reynolds numbers for cooling purpose, Velasquez et al. [18] studied the effect of the forced flow pulsations on the laminar heat transfer enhancement behind a 2D backward-facing step in a channel with fixed walls at Reynolds numbers between 20 and 200. In this study, the numerical method used a finite point formulation, in which the spatial derivatives are computed by using a least-squares approximation in a cloud of

Contributed by the Fluids Engineering Division of ASME for publication in the JOURNAL OF FLUIDS ENGINEERING. Manuscript received September 3, 2009; final manuscript received January 31, 2010; published online April 16, 2010. Assoc. Editor: Meng Wang.

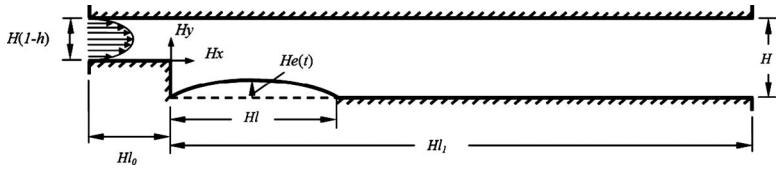

Fig. 1 Geometry of the flow past a downstream-facing step with an oscillating wall

points, with second-order Taylor polynomials as approximating functions, and a Crank–Nicholson scheme for the integration in pseudotime.

Gerber et al. [19] studied the unsteady response of a curved backward-facing compliant step in a flow model related to the aluminum continuous casting operation to a near-net shape. The Reynolds numbers considered in this flow model were 536 and 1055, and the numerical method used a finite element/finite volume discretization with an arbitrary-Lagrangian–Eulerian (ALE) approach.

A special research interest has also been devoted recently to the aerodynamics of airfoils at low Reynolds numbers, with applications to the unmanned and micro-air vehicles (MAVs). Several authors, such as Kunz and Kroo [20], found that many successful aerodynamic codes developed for the normal range of the Reynolds number are not well suited for low Reynolds numbers. Kunz and Kroo [20] used in their computational study on airfoil flows at low Reynolds numbers (between 1000 and 6000) the INS2D code developed at NASA Ames based on an upwind finite differencing scheme developed by Rogers and Kwak [21].

The aerodynamics of airfoils at low Reynolds numbers, between 400 and 6000, have also been studied by Mateescu and Abdo [22] and Abdo and Mateescu [23] with a numerical method based on a finite-difference formulation with artificial compressibility, and using a domain decomposition with different coordinate transformations for various domains.

The aim of this paper is to present time-accurate solutions of the Navier–Stokes equations for the analysis of the unsteady viscous flows in confined configurations generated by variations in time of the inflow velocities and by oscillating walls. A special interest is to study the effect of the inflow velocity variations in the flow separations appearing in confined flows with oscillating walls. No previous solutions were found by the authors for this type of unsteady confined flows generated by variable inflow velocities and oscillating walls. As an example, the numerical method presented is applied to obtain solutions for the unsteady flows with separation regions past the benchmark configuration with a downstream-facing step, which is generated by harmonic variations in time of the inflow velocity and by oscillating walls.

2 Problem Formulation

As an example of unsteady confined flows, consider the benchmark 2D flow past a downstream-facing step shown in Fig. 1, which is defined by the downstream channel height H, the step height Hh, and by the upstream and downstream channel lengths Hl_0 and Hl_1, respectively. This flow is referred to the Cartesian coordinates Hx and Hy centered at the step corner, where x and y are the nondimensional coordinates (with respect to H).

At the channel inlet ($Hx=-Hl_0$), there is a fully developed laminar flow defined by the axial velocity $U(y,t)$, which is variable in time according to the equation

$$U(y,t) = U_0(1 - a \sin \omega t)6y(1 - h - y)/(1 - h)^2, \qquad (1)$$

where $t=U_0t^*/H$ and $\omega=\omega^*HU_0$ represent the nondimensional time and the reduced frequency of oscillations ($\omega^*=2\pi f$ is the radian frequency of the oscillations), a is the nondimensional amplitude of the inflow velocity oscillations, and $U_0(1-a \sin \omega t)$ is the mean inflow velocity at time t.

A portion of the lower wall of length Hl, situated just behind the downstream-facing step, is assumed to execute transverse oscillations defined by the following lower wall equation

$$Hy = \begin{cases} H[g(x,t) - h] & \text{for} \quad x \in [0,l] \\ -Hh & \text{for} \quad x > l \end{cases} \qquad (2)$$

where $g(x,t)$ is the oscillation mode defined as

$$g(x,t) = e(t)\sin(\pi x/l) \quad \text{where} \quad e(t) = A \cos(\omega t) \qquad (3)$$

in which A is the nondimensional amplitude of oscillations (nondimensionalized with respect to H).

The time-dependent Navier–Stokes and continuity equations for unsteady incompressible flows can be expressed in nondimensional conservation law form as

$$\frac{\partial \mathbf{V}}{\partial t} + \mathbf{Q}(\mathbf{V},p) = \mathbf{0}, \quad \nabla \cdot \mathbf{V} = 0 \qquad (4)$$

where $\mathbf{V}$, which represents the dimensionless fluid velocity vector, is nondimensionalized with respect to the time-average mean flow velocity U_0 (that is, $\mathbf{V}=\mathbf{V}^*/U_0$), and $\mathbf{Q}(\mathbf{V},p)$, which includes the convective derivative, pressure and viscous terms, are expressed in two-dimensional Cartesian coordinates in the forms

$$\mathbf{V} = \{u,v\}^T, \quad \mathbf{Q}(\mathbf{V},p) = \{Q_u(u,v,p), Q_v(u,v,p)\}^T \qquad (5)$$

$$Q_u(u,v,p) = \frac{\partial(uu)}{\partial x} + \frac{\partial(vu)}{\partial y} + \frac{\partial p}{\partial x} - \frac{1}{\mathrm{Re}}\left(\frac{\partial^2 u}{\partial x^2} + \frac{\partial^2 u}{\partial y^2}\right) \qquad (6)$$

$$Q_v(u,v,p) = \frac{\partial(uv)}{\partial x} + \frac{\partial(vv)}{\partial y} + \frac{\partial p}{\partial y} - \frac{1}{\mathrm{Re}}\left(\frac{\partial^2 v}{\partial x^2} + \frac{\partial^2 v}{\partial y^2}\right) \qquad (7)$$

$$\nabla \cdot \mathbf{V} = \frac{\partial u}{\partial x} + \frac{\partial v}{\partial y} \qquad (8)$$

in which $\mathrm{Re}=HU_0/\nu$ represents the time-average mean Reynolds number based on the downstream channel height, and u, v, and p represent the dimensionless velocity components and pressure, nondimensionalized with respect to U_0 and ρU_0^2, respectively (where ρ and ν are the fluid density and the kinematic viscosity).

No-slip boundary conditions are considered at the solid walls. The inflow and outflow boundaries of the computational domain are situated at distances Hl_0 and Hl_1 upstream and downstream from the step, respectively, with $l_0=2$ and $l_1=30$ in the present computations. The inflow boundary condition is defined by Eq. (1), and the outflow boundary conditions for the velocity components are based on an extrapolation to second-order accuracy from inside the computational domain. The outlet pressure is obtained by integrating the normal momentum equation from the bottom wall [11], and in the final solution the pressure is adjusted to zero at the concave step corner.

3 Method of Solution

For a rigorous implementation of the boundary conditions on the oscillating walls, the real fluid flow domain with moving boundaries is transformed into a fixed computational domain by the time-dependent coordinate transformation

$$X = x, \quad Y = f(x,y,t), \quad t = t \tag{9}$$

where $f(x,y,t)$ is defined in terms of the oscillation mode, $g(x,t)$, in the form

$$f(x,y,t) = \begin{cases} y/(1-h) & \text{for} \quad x < 0 \\ 1 - \dfrac{1-h-y}{1-g(x,t)} & \text{for} \quad 0 < x < l \\ 1-(1-h-y) & \text{for} \quad x > l \end{cases} \tag{10}$$

Thus, in the fixed computational domain (X,Y), the lower and upper boundaries of the duct after the step (and also before the step) are defined by the equations $Y=0$ and $Y=1$, respectively.

In this fixed computational domain, the Navier–Stokes and continuity equations can be expressed as

$$\frac{\partial \mathbf{V}}{\partial t} + \mathbf{G}(\mathbf{V},p) = \mathbf{0}, \quad D\mathbf{V} = 0 \tag{11}$$

where

$$\mathbf{V} = \{u,v\}^T, \quad \mathbf{G}(\mathbf{V},p) = \{G_u(u,v,p), G_v(u,v,p)\}^T \tag{12}$$

$$G_u(u,v,p) = \frac{\partial(uu)}{\partial X} + C_1\frac{\partial^2 u}{\partial X^2} + C_2\frac{\partial(uu)}{\partial Y} + C_3\frac{\partial(vu)}{\partial Y} + C_4\frac{\partial u}{\partial Y} + \frac{\partial p}{\partial X} + C_2\frac{\partial p}{\partial Y} + C_5\frac{\partial^2 u}{\partial Y^2} + C_6\frac{\partial^2 u}{\partial Y\,\partial X} \tag{13}$$

$$G_v(u,v,p) = \frac{\partial(uv)}{\partial X} + C_1\frac{\partial^2 v}{\partial X^2} + C_2\frac{\partial(uv)}{\partial Y} + C_3\frac{\partial(vv)}{\partial Y} + C_4\frac{\partial v}{\partial Y} + C_3\frac{\partial p}{\partial Y} + C_5\frac{\partial^2 v}{\partial Y^2} + C_6\frac{\partial^2 v}{\partial Y\,\partial X} \tag{14}$$

$$D\mathbf{V} = \frac{\partial u}{\partial X} + C_2\frac{\partial u}{\partial Y} + C_3\frac{\partial v}{\partial Y} \tag{15}$$

in which

$$C_1 = -\frac{1}{\mathrm{Re}}, \quad C_2 = \frac{\partial f}{\partial x}, \quad C_3 = \frac{\partial f}{\partial y} \tag{16}$$

$$C_4 = \frac{\partial f}{\partial t} - \frac{1}{\mathrm{Re}}\left(\frac{\partial^2 f}{\partial x^2} + \frac{\partial^2 f}{\partial y^2}\right), \quad C_5 = -\frac{1}{\mathrm{Re}}\left[\left(\frac{\partial f}{\partial x}\right)^2 + \left(\frac{\partial f}{\partial y}\right)^2\right], \quad C_6 = -\frac{2}{\mathrm{Re}}\frac{\partial f}{\partial x} \tag{17}$$

In the present approach, the momentum equation is discretized in real time based on a second-order three-point-backward implicit scheme:

$$(\partial \mathbf{V}/\partial t)^{n+1} = (3\mathbf{V}^{n+1} - 4\mathbf{V}^n + \mathbf{V}^{n-1})/(2\Delta t) \tag{18}$$

where the superscripts $n-1$, n, and $n+1$ indicate three consecutive time levels, and $\Delta t = t^{n+1} - t^n = t^n - t^{n-1}$ represents the time step. Thus, Eq. (11) can be expressed at the time level t^{n+1} in the form

$$\mathbf{V}^{n+1} + \alpha\mathbf{G}^{n+1} = \mathbf{F}^n, \quad D\mathbf{V}^{n+1} = 0 \tag{19}$$

where $\alpha = 2\Delta t/3$, $\mathbf{G}^{n+1} = \mathbf{G}(\mathbf{V}^{n+1}, p^{n+1})$, and $\mathbf{F}^n = (4\mathbf{V}^n - \mathbf{V}^{n-1})/3$.

An iterative pseudotime relaxation procedure with artificial compressibility is then used in order to advance the solution of the semidiscretized equations from the real time level t^n to t^{n+1} in the form

$$\partial\breve{\mathbf{V}}/\partial\tau + \breve{\mathbf{V}} + \alpha\breve{\mathbf{G}} = \mathbf{F}^n, \quad \delta(\partial\breve{p}/\partial\tau) + D\breve{\mathbf{V}} = 0 \tag{20}$$

where $\breve{\mathbf{V}}(\tau)$ and $\breve{p}(\tau)$ denote the pseudofunctions corresponding to the variable velocity and pressure at pseudotime τ, between the real time levels t^n and t^{n+1}, and δ represents an artificially added compressibility.

An implicit Euler scheme is then used to discretize equations (20) between the pseudotime levels τ^ν and $\tau^{\nu+1} = \tau^\nu + \Delta\tau$, and the resulting equations are expressed in terms of the pseudotime variations $\Delta u = \breve{u}^{\nu+1} - \breve{u}^\nu$, $\Delta v = \breve{v}^{\nu+1} - \breve{v}^\nu$, and $\Delta p = \breve{p}^{\nu+1} - \breve{p}^\nu$, in the matrix form

$$[\mathbf{I} + \alpha\Delta\tau(\mathbf{D}_X + \mathbf{D}_Y)]\Delta\mathbf{f} = \Delta\tau\mathbf{S} \tag{21}$$

where $\Delta\mathbf{f} = [\Delta u, \Delta v, \Delta p]^T$, $\alpha = 2\Delta t/3$, $\mathbf{I}$ is the identity matrix, and where

$$\mathbf{D}_X = \begin{bmatrix} M + \dfrac{1}{\alpha} & 0 & \dfrac{\partial}{\partial X} \\ 0 & M & 0 \\ \dfrac{1}{\alpha\delta}\dfrac{\partial}{\partial X} & 0 & 0 \end{bmatrix}, \quad \mathbf{D}_Y = \begin{bmatrix} N & 0 & C_2\dfrac{\partial}{\partial Y} \\ 0 & N + \dfrac{1}{\alpha} & C_3\dfrac{\partial}{\partial Y} \\ \dfrac{C_2}{\alpha\delta}\dfrac{\partial}{\partial Y} & \dfrac{C_3}{\alpha\delta}\dfrac{\partial}{\partial Y} & 0 \end{bmatrix} \tag{22}$$

$$\mathbf{S} = \begin{bmatrix} F_u^n - \breve{u}^\nu - \alpha G_u^\nu \\ F_v^n - \breve{v}^\nu - \alpha G_v^\nu \\ -(1/\delta)D\breve{\mathbf{V}}^\nu \end{bmatrix} \tag{23}$$

in which the differential operators M and N are defined as

$$M\phi = \frac{\partial(\breve{u}^\nu\phi)}{\partial X} + C_1\frac{\partial^2\phi}{\partial X^2} \tag{24}$$

$$N\phi = C_2\frac{\partial(\breve{u}^\nu\phi)}{\partial Y} + C_3\frac{\partial(\breve{v}^\nu\phi)}{\partial Y} + C_4\frac{\partial\phi}{\partial Y} + C_5\frac{\partial^2\phi}{\partial Y^2} + C_6\frac{\partial^2\phi}{\partial Y\,\partial X} \tag{25}$$

The optimal value of the artificial compressibility, δ, and the size of the pseudotime step, $\Delta\tau$, are determined, in a similar manner to that used in Ref. [11], based on the characteristic propagation velocity in the axial direction, $\lambda_+ = \alpha q + \sqrt{(\alpha q)^2 + \alpha/\delta}$, in the form

$$\delta = \frac{1}{2q^2\Delta\tau}, \quad \Delta\tau = \frac{C\Delta x}{\lambda_+} \tag{26}$$

where q is a representative velocity of the unsteady flow, Δx is an average value of the mesh size, and C is the Courant–Friedrichs–Levy number, for which a value between 30 and 40 is considered in the present computations. The resulting values for δ and $\Delta\tau$ are eventually optimized by numerical experimentation.

A factored alternate direction implicit (ADI) scheme is used to separate Eq. (21) into two successive sweeps in the X and Y directions, defined by the equations

$$[\mathbf{I} + \alpha\Delta\tau\mathbf{D}_Y]\Delta\mathbf{f}^* = \Delta\tau\mathbf{S}, \quad [\mathbf{I} + \alpha\Delta\tau\mathbf{D}_X]\Delta\mathbf{f} = \Delta\mathbf{f}^* \tag{27}$$

where $\Delta\mathbf{f}^* = [\Delta u^*, \Delta v^*, \Delta p^*]^T$ is a convenient intermediate variable vector.

These equations are further spatially discretized by central differencing on a stretched staggered grid, in which the flow variables u, v, and p are defined at different positions, as shown in Fig. 2. By using a staggered grid, this method avoids the odd-and-even point decoupling while preserving the second-order accuracy in space of the method. The grid stretching is defined by hyperbolic sine and tangent functions in the X and Y directions, in the form

$$X_i = X_o + (X_I - X_o)\frac{\sinh(\gamma i/I)}{\sinh(\gamma)},$$

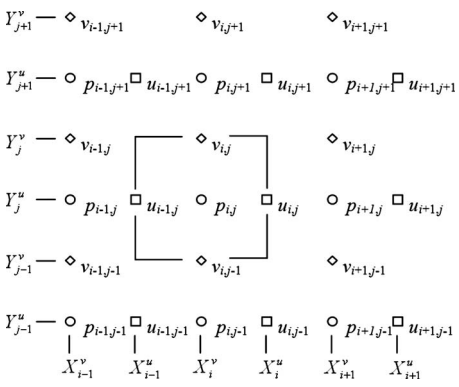

Fig. 2 Staggered grid geometry

$$Y_j = Y_o + (Y_J - Y_o)\left[\frac{1}{2} + \frac{\tanh(\gamma(2j-J)/2J)}{2\tanh(\gamma/2)}\right] \tag{28}$$

where γ is a convenient stretching parameter and where I and J represent the number of grid points in the X and Y directions.

A special decoupling procedure [11], based on the utilization of the continuity equation, is used for each sweep to eliminate the pressure from the other equations. The following relations, which are derived using Eqs. (27), (22), and (23) from the continuity equation expressed for each sweep,

$$\Delta p^* = -\frac{\Delta\tau}{\delta}\left[D\check{\mathbf{V}}^{\nu} + C_2\frac{\partial(\Delta u^*)}{\partial Y} + C_3\frac{\partial(\Delta v^*)}{\partial Y}\right],$$

$$\Delta p = \Delta p^* - \frac{\Delta\tau}{\delta}\frac{\partial(\Delta u)}{\partial X} \tag{29}$$

are used to eliminate the pseudotime variations of the pressure from the systems of equations for the pseudotime variations of the velocity components in each sweep.

In this manner, the problem is reduced to the solution of two sets of decoupled scalar tridiagonal systems of equations, for each sweep. As a result, this method is characterized by excellent computational efficiency and accuracy, displayed in all cases studied; for example, an average computational time of 32 min is needed to run the computer program (on a dual core of 3 GHz computer with 4 Gbytes of RAM) for one unsteady confined flow case with unsteady inflow variation and wall oscillations.

The method has been successfully validated by comparison with previous computational and experimental results available for steady flows past a downstream-facing step (not shown here due to space limitation).

4 Numerical Solutions for the Unsteady Confined Flows With Variable Inflow Velocity Past a Downstream-Facing Step With Oscillating Walls

This method is applied to obtain solutions for the unsteady confined flows past downstream-facing steps generated by harmonic variations in time of the inflow velocities defined by Eq. (1) and by the lower wall oscillations defined by Eqs. (2) and (3).

Computations have been performed for the step height $Hh = H/2$, the length of the oscillating wall $Hl = 10H$, and for various values of the Reynolds number, $\mathrm{Re} = HU_0/\nu$, the amplitudes of the inflow velocity a, and wall oscillations A and of the reduced frequency of oscillations ω. The numerical results were obtained using a stretched staggered grid with 360×71 grid points for each variable (that is, to 719×141 grid points in total). The mesh spacing in the x-direction was minimum at the step, $\Delta x_{\min} = 0.03121$, and maximum at the outlet boundary, $\Delta x_{\max} = 0.1583$, while in the y-direction the minimum mesh spacing was at the walls and the step corner, $\Delta y_{\min} = 0.00923$, and the maximum mesh spacing was $\Delta y_{\max} = 0.0224$ in the middle of the upstream channel. The size of the nondimensional real time step was $\Delta t = 2\pi/(\omega N)$ with the number of real time steps during an oscillation period taken between $N = 80$ and $N = 160$ depending on the unsteady flow case. The pseudotime computations have been performed using $\delta = 0.25$ and $\Delta\tau = 0.05$, and convergence was assumed to be reached when the rms residuals were less than 10^{-5} (which required in average between 60 and 100 pseudotime iterations until convergence for each real time step). The real time integration was started from the steady flow solution for fixed walls and no inflow velocity variation, and was performed until all variables in the computational domain were executing repeatable harmonic oscillations from one period to the next (usually after 3 oscillation cycles or less).

Table 1 Grid sensitivity of the numerical solution for $Hh = H/2$, $\mathrm{Re} = 800$, and $l_0 = 0$ based on the computed nondimensional lengths of separation and reattachment

Grid points used for each variable	Lower wall	Upper wall		
	L_l	$L_u = x_r - x_s$	x_s	x_r
201×41	5.92	5.66	4.67	10.33
251×51	5.99	5.65	4.74	10.39
301×61	6.02	5.65	4.77	10.44
351×71	6.04	5.64	4.80	10.42
401×81	6.05	5.64	4.81	10.45
501×101	6.07	5.63	4.83	10.46
601×121	6.08	5.63	4.83	10.47
801×161	6.09	5.63	4.84	10.47
1001×201	6.09	5.63	4.85	10.47
1201×241	6.09	5.63	4.85	10.48
1401×281	6.09	5.63	4.85	10.48

The sensitivity of the numerical solution with the mesh refinement has been investigated for the case of steady flow at Reynolds number $\mathrm{Re} = 800$ and $l_0 = 0$, using as criteria of comparison the lower wall separation length, Hl_l, and the upper wall separation and reattachment locations, Hx_s and Hx_r (with the upper separation length $Hl_u = Hx_r - Hx_s$), which represent characteristic features of this flow. The results of the grid-sensitivity test are indicated in Table 1. One can notice that the solution obtained by using 401×81 grid points for each variable (or 801×161 grid points in total for the staggered grid) is very close to the fully converged solution, which is practically obtained with 1001×201 grid points, and beyond this the numerical solution is not influenced by grid refinement.

After the grid-sensitivity test, the method is applied to obtain solutions for the unsteady confined flows past downstream-facing steps generated by harmonic variations in time of the inflow velocities defined by Eq. (1) and by the lower wall oscillations defined by Eqs. (2) and (3).

Typical patterns of the computed streamlines for this unsteady flow at several moments in time during the oscillatory cycle, $t/T = 3$, 3.25, 3.5, and 3.75 (where t is the nondimensional time and T is the dimensionless period of the oscillations), are shown in Fig. 3 for Reynolds number $\mathrm{Re} = 400$, reduced frequency of oscillations $\omega = 0.05$, and for the nondimensional amplitudes of the inflow velocity variation, $a = 0$, 0.05, and 0.1, and of the wall oscillations, $A = 0$ and 0.05.

One can notice from the computed streamlines shown in Fig. 3 that the upper separation region practically disappears for a portion of the oscillatory cycle for certain flow conditions, such as in the case $a = 0.05$ and $A = 0.05$. This newly discovered unsteady flow feature of disappearing and reappearing upper separation region during the oscillation cycle can be better observed in Figs. 4–8.

The variations in the lower wall separation length, l_l, and of the upper wall separation and reattachment locations, x_s and x_r (with

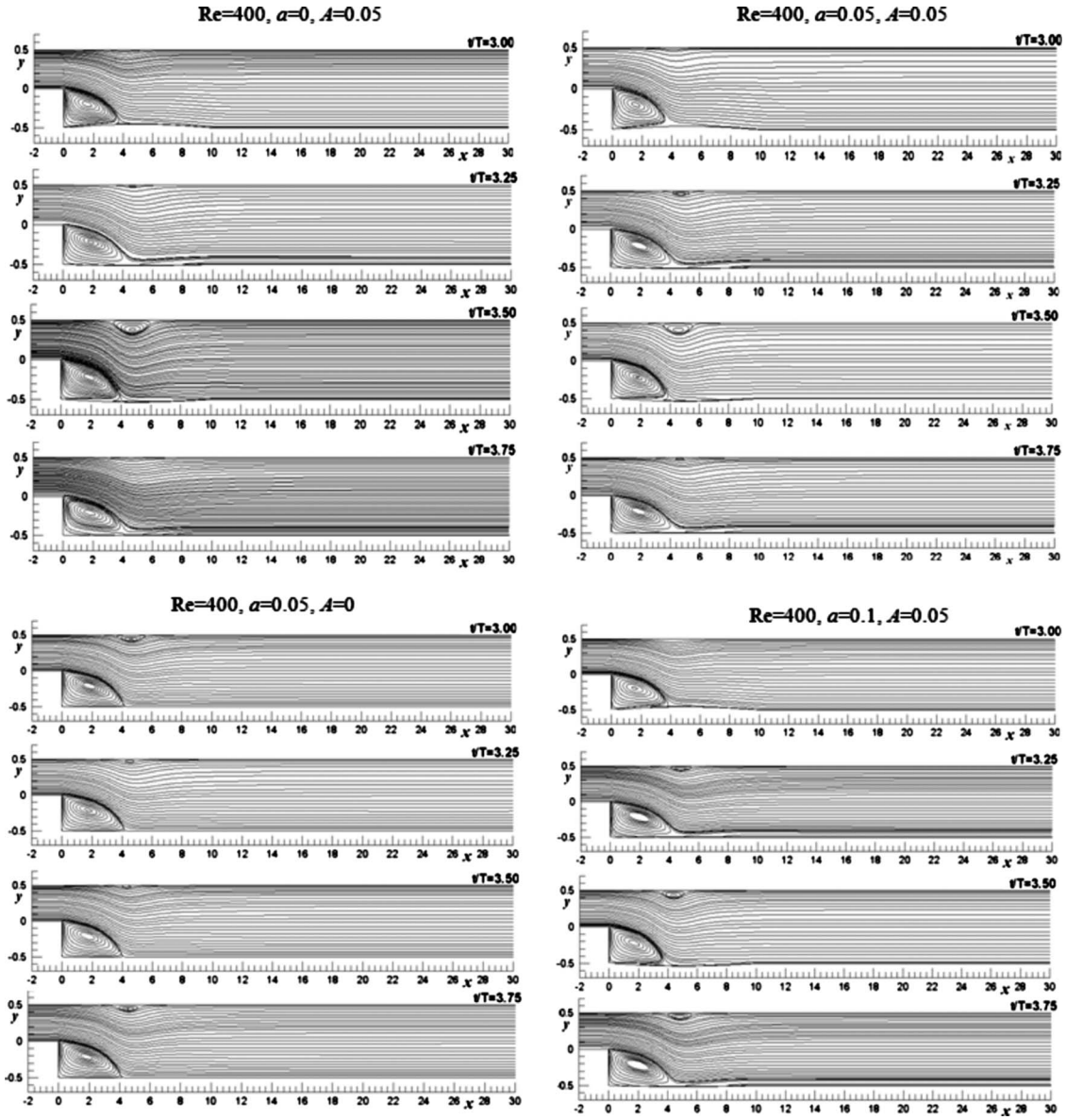

Fig. 3 Streamline patterns of the unsteady confined flow at various moments during the oscillatory cycle, *t*/*T*, for Re=400, ω=0.05 and for two values the amplitude of the oscillating wall, *A*=0 and 0.05 and three values of the amplitude of the inflow velocity variation, *a*=0, 0.05, and 0.1.

the upper separation length $l_u=x_r-x_s$), represent characteristic features of these unsteady flows and will be used further to illustrate the influence of the main flow parameters, the Reynolds number, and the oscillation amplitudes and frequency.

4.1 Influence of the Amplitude of the Inflow Velocity Fluctuations on the Unsteady Flow Separations. The typical influence of the inflow velocity oscillation amplitude, a, on the lower wall separation length (l_l) and on the upper wall separation and reattachment locations (x_s and x_r) is illustrated for several values of the wall oscillation amplitudes A in Fig. 4, for Re=400, ω=0.05, and in Fig. 5 for Re=600, ω=0.05. It is interesting to note that the upper wall flow separation is present only for a portion of the oscillatory cycle (being absent for the rest of the cycle) when the inflow velocity amplitude is larger, such as $a>0.05$ for Re=400, $A=0$ and $a\geq 0.2$ for Re=600, $A=0$. At Re=600, one can notice the formation of a secondary flow separation on the lower wall for $a=0.4$ in the absence of the wall oscillations ($A=0$); this secondary separation appears only during a small portion (about one quarter) of the oscillatory cycle.

4.2 Influence of the Wall Oscillation Amplitude on the Unsteady Flow Separations. The typical influence of the wall oscillation amplitude, A, on the lower wall separation length (l_l) and on the upper wall separation and reattachment locations (x_s and x_r) is shown for several values of the inflow velocity oscillation amplitudes a in Fig. 6 for Re=400, ω=0.05, and in Fig. 7 for Re=600, ω=0.05. One can see that the length of the upper flow separation region increases with A and the duration of its presence during the oscillation cycle decreases with the increase in A.

At Re=600 the upper separation region also disappears for a certain portion of the oscillatory cycle when $A\geq 0.1$ for both cases $a=0$ and $a=0.05$.

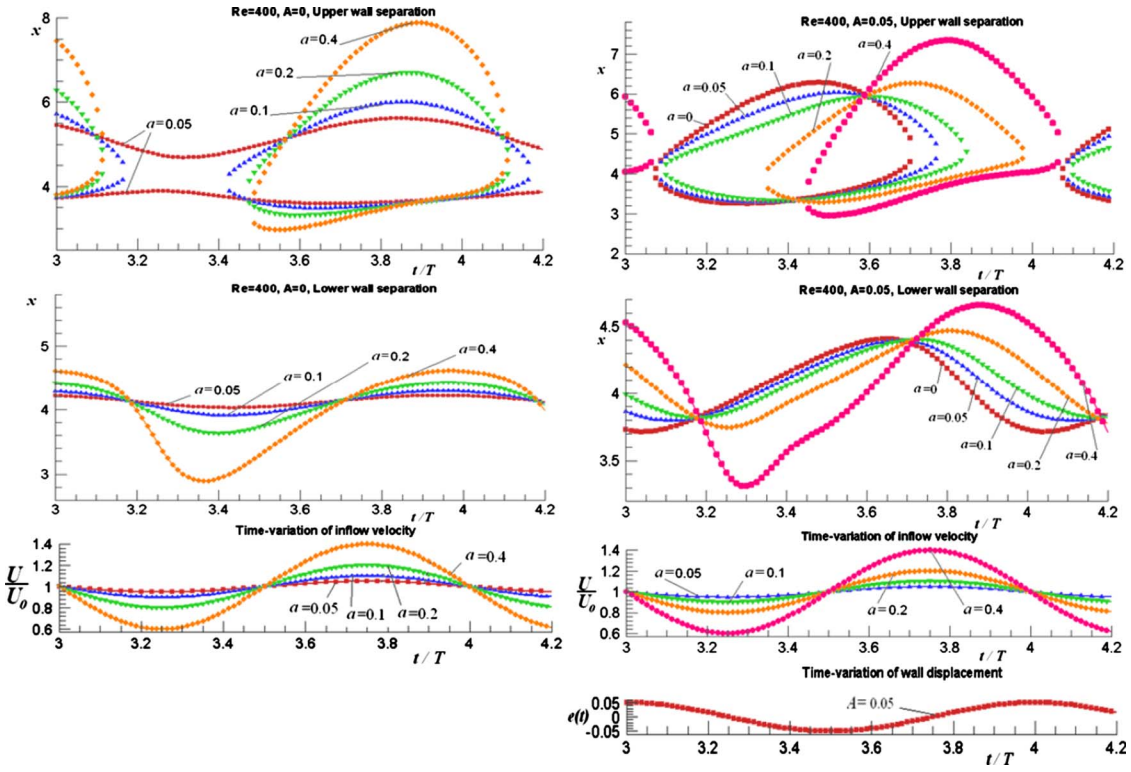

Fig. 4 ***Influence of the inflow velocity amplitude, a*: Variation during the oscillatory cycle, *t/T*, of the upper wall separation and reattachment locations and of the lower wall reattachment location for Re=400, ω=0.05 and for two values of the amplitude of the wall oscillations, *A*=0 and 0.05.**

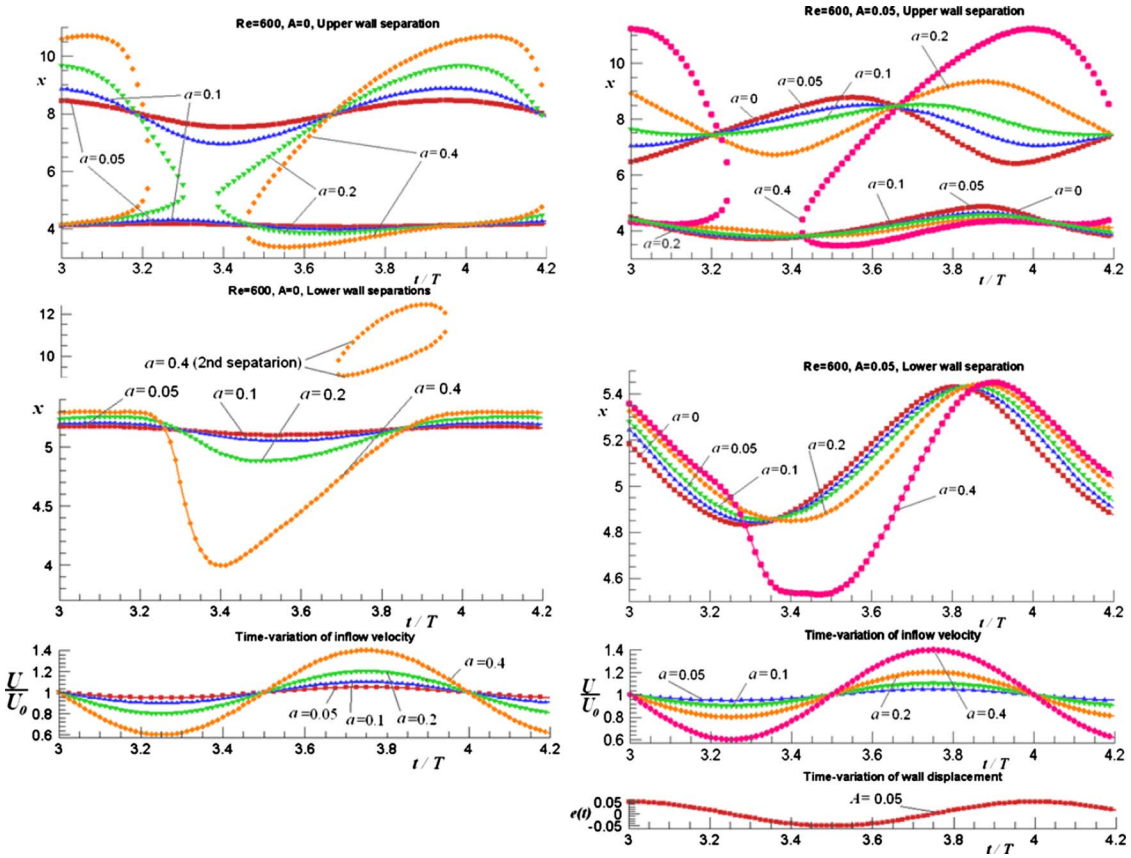

Fig. 5 ***Influence of the inflow velocity amplitude, a*: Variation during the oscillatory cycle, *t/T*, of the upper wall separation and reattachment locations and of the lower wall reattachment location for Re=600, ω=0.05 and for two values of the amplitude of the wall oscillations, *A*=0 and 0.05.**

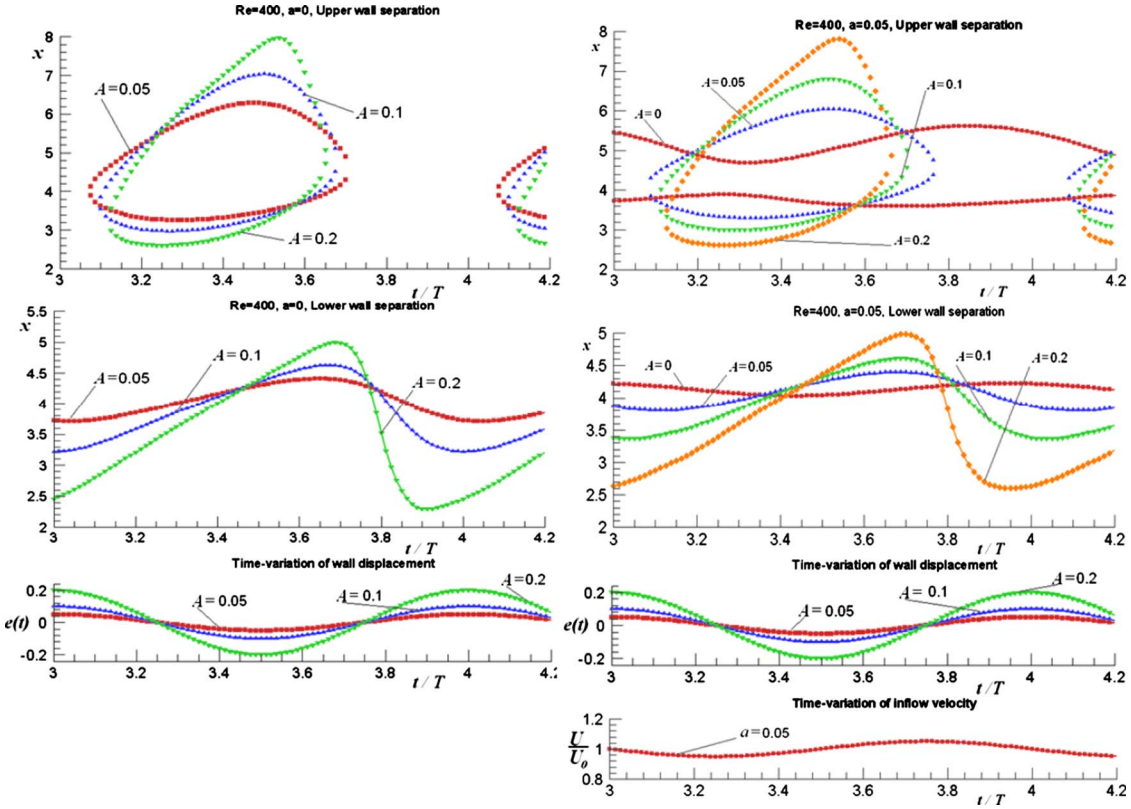

Fig. 6 ***Influence of the wall oscillation amplitude, A*: Variation during the oscillatory cycle, *t*/*T*, of the upper wall separation and reattachment locations and of the lower wall reattachment location for Re=400, ω=0.05 and for two values of the amplitude of the wall oscillations, *a*=0 and 0.05.**

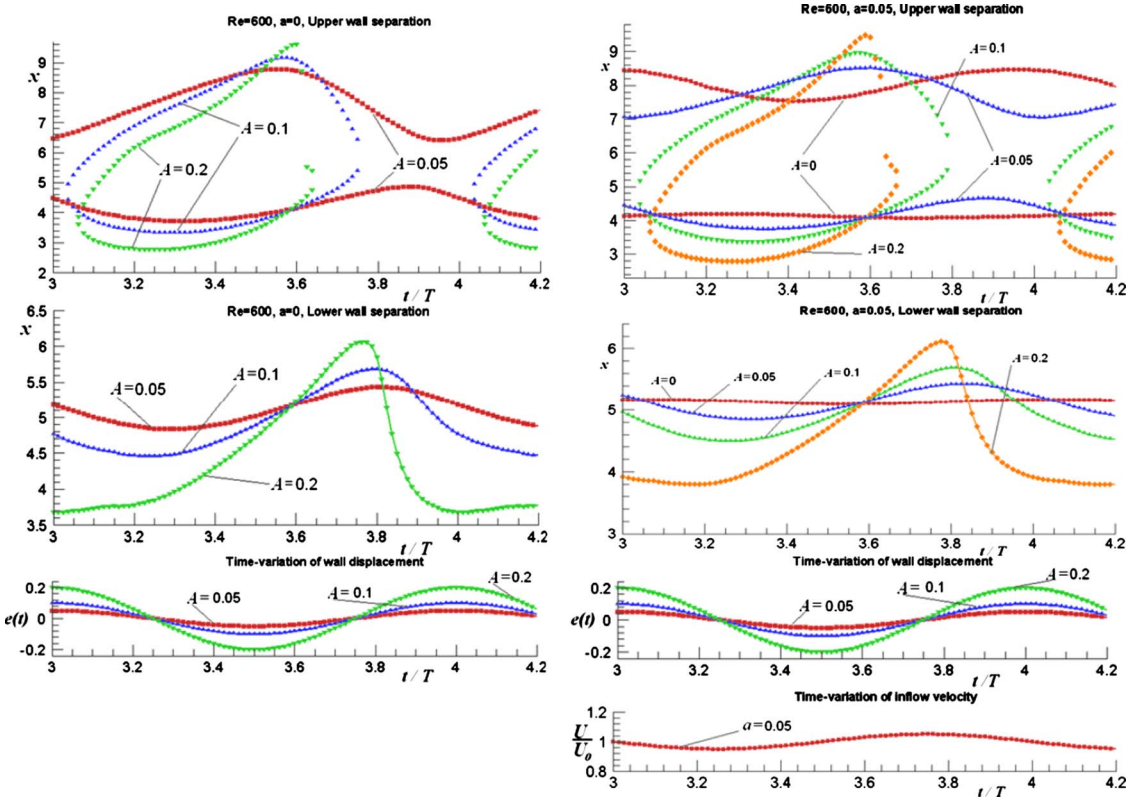

Fig. 7 ***Influence of the wall oscillation amplitude, A*: Variation during the oscillatory cycle, *t*/*T*, of the upper wall separation and reattachment locations and of the lower wall reattachment location for Re=600, ω=0.05 and for two values of the amplitude of the wall oscillations, *a*=0 and 0.05.**

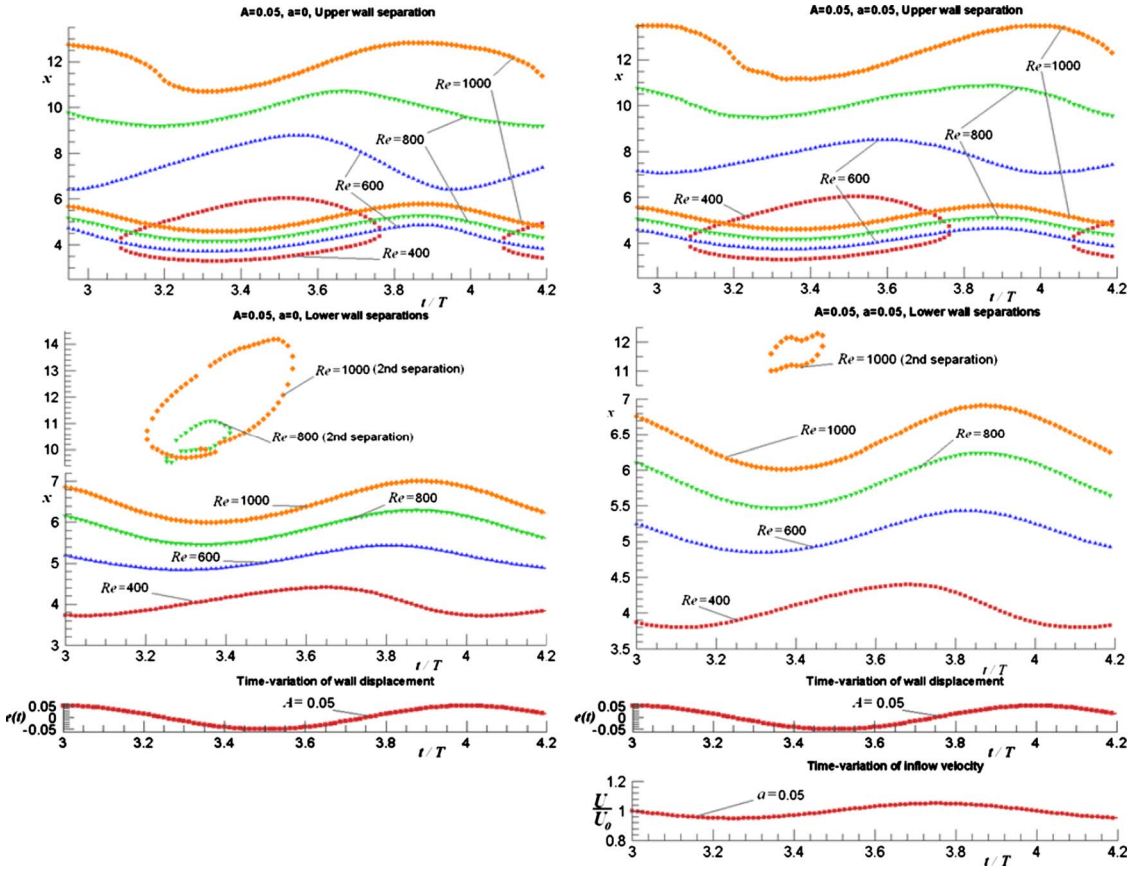

Fig. 8 ***Influence of the Reynolds number*, Re: Variation during the oscillatory cycle, *t*/*T*, of the upper wall separation and reattachment locations and of the lower wall reattachment location for ω=0.05 and for *A* =0.05, *a*=0, and *A*=0.05, *a*=0.05.**

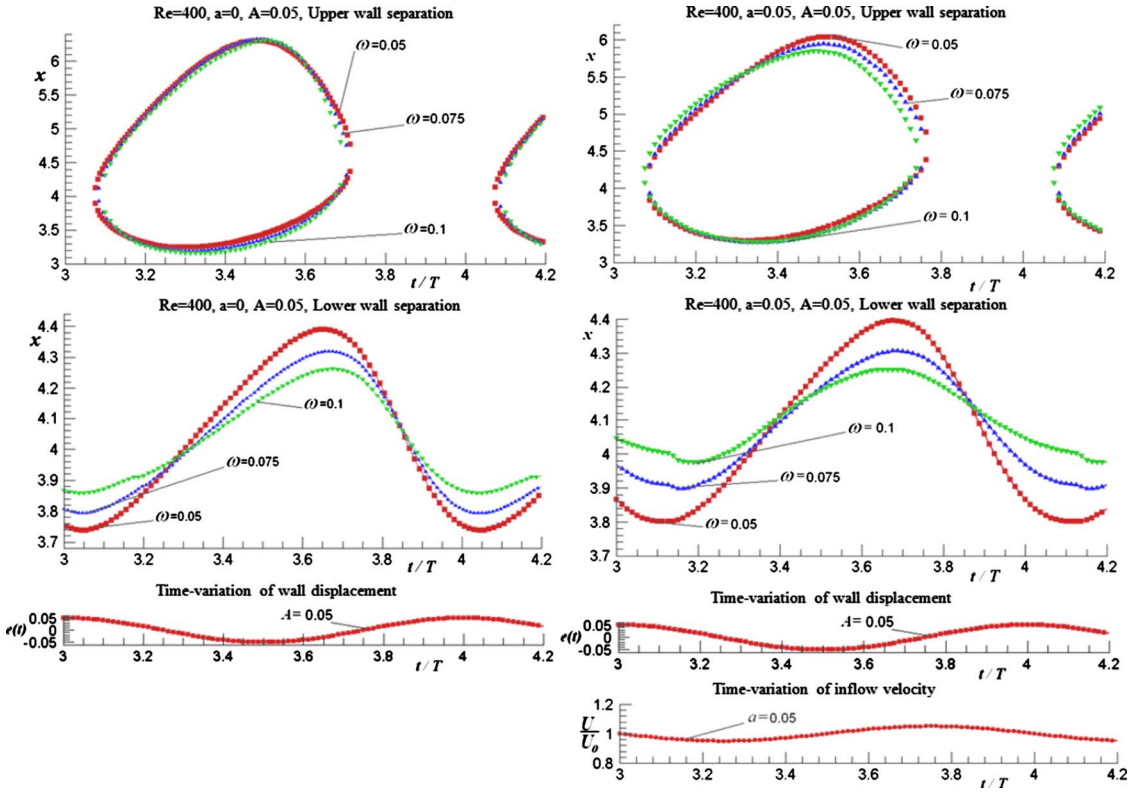

Fig. 9 ***Influence of the nondimensional frequency of oscillation*, ω: Typical variations during the oscillatory cycle, *t*/*T*, of the upper wall separation and reattachment locations and of the lower wall reattachment location for Re=400, *A*=0.05 and *a*=0.05.**

4.3 Influence of the Reynolds Number on the Unsteady Flow Separations. The influence of the time-average Reynolds number is illustrated in Fig. 8 for several values of the amplitudes of the inflow velocity fluctuations, a, and of the wall oscillation, A. One can notice that the length of the separation regions formed on the lower and the upper walls increases substantially with the Reynolds number. Secondary separation regions also appear on the lower wall at larger Reynolds numbers (starting from Re $=800$ for $a=0$ and from Re$=1000$ for $a=0.05$). At the larger Reynolds numbers, the upper flow separation region is continuously present during the oscillatory cycle, while at Re$=400$, it is present only during a portion (about half) of the oscillation cycle and disappears during the rest of the cycle.

4.4 Influence of the Oscillation Frequency on the Unsteady Flow Separations. The influence of the nondimensional frequency of oscillation, ω, is shown in Fig. 9 for Re$=400$, $a=0.05$, and $A=0.05$. One can notice that the oscillatory amplitude of the lower flow separation length increases with the frequency of the oscillation, ω, while the upper flow separation is very little changed.

5 Conclusions

This paper presents the analysis of the unsteady confined viscous flows generated by the variations in time of the inflow velocities and by the wall oscillations, which is required for the study of flow-induced vibration and instability of various engineering systems (until now, the inflow velocity fluctuations, which occur in many engineering systems during the operation cycle, have not been taken into account in the aeroelastic studies of these systems).

The time-accurate solutions of the Navier–Stokes equations for these unsteady flows are obtained with a finite-difference method using artificial compressibility on a stretched staggered grid, which is a second-order accurate method in space and time. A special decoupling procedure, based on the utilization of the continuity equation, is used in conjunction with a factored ADI scheme to substantially enhance the computational efficiency of the method by reducing the problem to the solution of scalar tridiagonal systems of equations.

This method is applied to obtain solutions for the benchmark unsteady confined flow past a downstream-facing step, generated by harmonic variations in time of the inflow velocity and by the lower wall oscillations, which display multiple flow separation regions on the upper and lower walls. The flow pattern of these unsteady flows is illustrated by the computed streamlines at various moments during the oscillatory cycle, which clearly indicate the flow separation regions appearing at the upper and lower walls. The influence of the Reynolds number and the influence of the oscillation frequency and of the amplitudes of the inflow velocity and the oscillating wall on the formation of the flow separation regions are thoroughly analyzed in the paper. It was found that for certain values of the Reynolds number and oscillation frequency and amplitudes, the flow separation at the upper wall is present only during a portion of the oscillatory cycle and disappears for the rest of the cycle, and that for other values of these parameters secondary flow separations may also be formed on the lower wall.

Acknowledgment

The support of the Natural Sciences and Engineering Research Council of Canada (NSERC) and of the Consejo Nacional de Ciencia y Tecnologia of Mexico (CONACYT) is gratefully acknowledged.

References

[1] Inada, F., and Hayama, S., 1990, "A Study on Leakage-Flow-Induced Vibrations. Part 1: Fluid-Dynamic Forces and Moments Acting on the Walls of a Narrow Tapered Passage," J. Fluids Struct., **4**, pp. 395–412.
[2] Inada, F., and Hayama, S., 1990, "A Study on Leakage-Flow-Induced Vibrations. Part 2: Stability Analysis and Experiments for Two-Degree-of-Freedom Systems Combining Translational and Rotational Motions," J. Fluids Struct., **4**, pp. 413–428.
[3] Mateescu, D., and Païdoussis, M. P., 1987, "Unsteady Viscous Effects on the Annular-Flow-Induced Instabilities of a Rigid Cylindrical Body in a Narrow Duct," J. Fluids Struct., **1**, pp. 197–215.
[4] Mateescu, D., Païdoussis, M. P., and Bélanger, F., 1989, "A Theoretical Model Compared With Experiments for the Unsteady Pressure on a Cylinder Oscillating in a Turbulent Annular Flow," J. Sound Vib., **135**(3), pp. 487–498.
[5] Mateescu, D., Païdoussis, M. P., and Bélanger, F., 1988, "Unsteady Pressure Measurements on an Oscillating Cylinder in Narrow Annular Flow," J. Fluids Struct., **2**, pp. 615–628.
[6] Mateescu, D., Païdoussis, M. P., and Bélanger, F., 1994, "Unsteady Annular Viscous Flows Between Oscillating Cylinders. Part I: Computational Solutions Based on a Time-Integration Method," J. Fluids Struct., **8**, pp. 489–507.
[7] Mateescu, D., Païdoussis, M. P., and Bélanger, F., 1994, "Unsteady Annular Viscous Flows Between Oscillating Cylinders. Part II: A Hybrid Time-Integration Solution Based on Azimuthal Fourier Expansions for Configurations With Annular Backsteps," J. Fluids Struct., **8**, pp. 509–527.
[8] Mateescu, D., Païdoussis, M. P., and Bélanger, F., 1994, "A Time-Integration Method Using Artificial Compressibility for Unsteady Viscous Flows," J. Sound Vib., **177**(2), pp. 197–205.
[9] Mateescu, D., Mekanik, A., and Païdoussis, M. P., 1996, "Analysis of 2-D and 3-D Unsteady Annular Flows With Oscillating Boundaries Based on a Time-Dependent Coordinate Transformation," J. Fluids Struct., **10**(1), pp. 57–77.
[10] Bélanger, F., de Langre, E., Axisa, F., Païdoussis, M. P., and Mateescu, D., 1994, "A Computational Method for the Simultaneous Integration of the Navier-Stokes and Structural Equations Applied to Laminar Annular Flows," J. Fluids Struct., **8**(7), pp. 747–770.
[11] Mateescu, D., and Venditti, D., 2001, "Unsteady Confined Viscous Flows With Oscillating Walls and Multiple Separation Regions Over a Downstream-Facing Step," J. Fluids Struct., **15**, pp. 1187–1205.
[12] Lee, T., and Mateescu, D., 1998, "Experimental and Numerical Investigation of 2-D Backward-Facing Step Flow," J. Fluids Struct., **12**, pp. 703–716.
[13] Mateescu, D., Pottier, T., Perotin, L., and Granger, S., 1995, "Three-Dimensional Unsteady Flows Between Oscillating Eccentric Cylinders by an Enhanced Hybrid Spectral Method," J. Fluids Struct., **9**(6), pp. 671–695.
[14] Mateescu, D., Païdoussis, M. P., and Sim, W.-G., 1995, "3-D Unsteady Viscous Flows Between Concentric Cylinders Executing Axially-Variable Oscillations: A Hybrid Spectral/Finite-Difference Solution," ASME J. Appl. Mech., **62**, pp. 667–673.
[15] Mateescu, D., Païdoussis, M. P., and Sim, W.-G., 1994, "Spectral Solutions for Unsteady Annular Flows Between Eccentric Cylinders Induced by Transverse Oscillations," J. Sound Vib., **177**(5), pp. 635–649.
[16] Mateescu, D., Païdoussis, M. P., and Sim, W.-G., 1994, "A Spectral Collocation Method for Confined Unsteady Flows With Oscillating Boundaries," J. Fluids Struct., **8**(2), pp. 157–181.
[17] Mateescu, D., Mei, C.-B., and Zuppel, E., 2005, "Computational Solutions for Unsteady Confined Viscous Flows With Variable Inflow Velocities for Unsteady Fluid-Structure Interaction Problems," ASME Paper No. PVP-2005-71777.
[18] Velazquez, A., Arias, J. R., and Mendez, B., 2008, "Laminar Heat Transfer Enhancement Downstream of a Backward Facing Step by Using a Pulsating Flow," Int. J. Heat Mass Transfer, **51**(7–8), pp. 2075–2089.
[19] Gerber, A. G., Holloway, A. G., and Ng, C., 2007, "A Model of the Unsteady Response of a Backward-Facing Compliant Step," Int. J. Numer. Methods Fluids, **55** (1), pp. 57–80.
[20] Kunz, P., and Kroo, L., 2000, "Analysis and Design of Airfoils for Use at Ultra-Low Reynolds Numbers," Proceedings of the AIAA Fixed, Flapping and Rotating Wing Aerodynamics at Very Low Reynolds Numbers Conference, Notre Dame, Jun. 5–7, pp. 35–60.
[21] Rogers, S., and Kwak, D., 1990, "An Upwind Differencing Scheme for the Time-Accurate Incompressible Navier-Stokes Equations," AIAA J., **28**, pp. 253–262.
[22] Mateescu, D., and Abdo, M., 2004, "Aerodynamic Analysis of Airfoils at Very Low Reynolds Numbers," Applied Aerodynamics Conference, 42nd AIAA Aerospace Sciences Meeting, Reno, NV, AIAA Paper 2004-1053, pp. 1–11.
[23] Abdo, M., and Mateescu, D., 2005, "Low-Reynolds Number Aerodynamics of Airfoils at Incidence," Applied Aerodynamics Conference, 43rd AIAA Aerospace Sciences Meeting, Reno, NV, AIAA Paper No. 2005-1038, pp. 1–26.

L. Momayez
Thermofluids Complex Flows and Energy Research Group-LTN-CNRS-UMR 6607, Ecole Polytechnique, Université de Nantes, BP 50609, 44306 Nantes, France; LRPMN, IUT d'Alençon, Université de Caen, 61250 Damigny, France

G. Delacourt
Thermofluids Complex Flows and Energy Research Group-LTN-CNRS-UMR 6607, Ecole Polytechnique, Université de Nantes, BP 50609, 44306 Nantes, France

P. Dupont
LGCGM, EA3913, INSA de Rennes, Campus Beaulieu, 35043 Rennes, France

H. Peerhossaini[1]
Thermofluids Complex Flows and Energy Research Group-LTN-CNRS-UMR 6607, Ecole Polytechnique, Université de Nantes, BP 50609, 44306 Nantes, France
e-mail: hassan.peerhossaini@univ-nantes.fr

Eddy Heat Transfer by Secondary Görtler Instability

Experimental measurements of flow and heat transfer in a concave surface boundary layer in the presence of streamwise counter-rotating Görtler vortices show conclusively that local surface heat-transfer rates can exceed that of the turbulent flat-plate boundary layer even in the absence of turbulence. We have observed unexpected heat-transfer behavior in a laminar boundary layer on a concave wall even at low nominal velocity, a configuration not studied in the literature: The heat-transfer enhancement is extremely high, well above that corresponding to a turbulent boundary layer on a flat plate. To quantify the effect of freestream velocity on heat-transfer intensification, two criteria are defined for the growth of the Görtler instability: P_z for primary instability and P_{rms} for the secondary instability. The evolution of these criteria along the concave surface boundary layer clearly shows that the secondary instability grows faster than the primary instability. Measurements show that beyond a certain distance the heat-transfer enhancement is basically correlated with P_{rms}, so that the high heat-transfer intensification at low freestream velocities is due to the high growth rate of the secondary instability. The relative heat-transfer enhancement seems to be independent of the nominal velocity (global Reynolds number) and allows predicting the influence of the Görtler instabilities in a large variety of situations. [DOI: 10.1115/1.4001307]

1 Flow Stability and Related Heat-Transfer Mechanisms

The stability of a boundary layer over a concave wall was studied for the first time by Görtler [1]. In analogy with Couette–Taylor instability (well known at that time), he argued that the unstable flow should consist of a laminar boundary layer over which an array of counter-rotating vortices (similar to the Taylor vortices) is superposed. He then proposed a linear stability analysis of the problem and obtained a critical value for the control parameter, later known as the Görtler number.

Streamwise Görtler vortices develop in a concave surface boundary layer due to centrifugal instability [2]. The related control parameter (the Görtler number) is the ratio between the time scale of the destabilizing mechanism and the viscous time scale. It is theoretically shown that the growth and breakdown of the Görtler instability in the *low-wavelength* domain are initial conditions dependent (see Ref. [3]). On the other hand, Boiko et al. [4] recently showed that the linear theory is valid for the wave number range of unity or greater if the measurements are carried out far enough from the disturbance source, i.e., where the most unstable modes are sufficiently amplified to dominate (see also Ref. [5] and references therein). As a result, emphasis in recent studies has been placed on the receptivity problem (see Ref. [2] for a comprehensive review), where the aim is to understand the source of the initial disturbances rather than the details of later local developments.

Görtler instability has been shown to be initial-condition dependent [6]. Sabry and Liu [7] and Lee and Liu [8] studied numerically the development of downstream nonlinear momentum, and Liu and Sabry [9] and Liu and Lee [10] showed that the heat and mass transfer are closely related to the initial conditions imposed on the flow. The wavelength and strength of the initial perturbations are among the most pertinent parameters in the nonlinear development of Görtler vortices and hence in heat-transfer enhancement, so that these parameters are particularly important in controlling heat (and mass and momentum) transfer in many applications of technological interest.

The evolution of Görtler vortices was studied by Hall [6]. He showed that initially the perturbations have exponential amplification, as envisaged in the linear theory, but that later an asymptotic development saturation appears because of unsaturated nonlinear effects. The nonlinear studies allow consideration of the perturbation and the transfer of energy between the basic flow and the various harmonics of the perturbation flow. More details are given in Refs. [11,12].

Liu [13] formulated the heat-transfer problem assuming an incompressible flow for which thermal buoyancy is negligible compared with inertial effects. Lee and Liu [8] discussed the insensitivity of the location where the weak initial disturbance (Görtler vortex) is injected into the mean flow, provided that this initial condition is consistent with the prevailing local flow. To study the development of heat transfer under nonlinear instabilities, Liu and Sabry [9] and Liu and Lee [10] began the analysis with the Reynolds splitting of velocity and temperature fields.

[1]Corresponding author.

Contributed by the Fluids Engineering Division of ASME for publication in the JOURNAL OF FLUIDS ENGINEERING. Manuscript received October 14, 2008; final manuscript received February 19, 2010; published online April 15, 2010. Assoc. Editor: Juergen Kompenhans.

Liu [13] and Girgis and Liu [14] examined the downstream development of iso-θ contour lines in the cross-sectional yz-plane (Fig. 1a of Ref. [14]), in the parameter range of the experiments of Ref. [15]. These contours are the inferred mean temperature structure from Ref. [15] with the effects of the secondary instabilities present; i.e., the contour lines are subjected to the effect of wavy (sinuous) instability. From these results, it is observed that the iso-θ contour lines are compressed near the wall due to mainly downward transport of cold fluid by the downward velocity of the steady Görtler vortices, and also the downward eddy transport brought about by the fluctuations correlations, $\overline{v'\theta'} = -\overline{v'u'} > 0$, inferred from the Reynolds shear stress [13] by assuming that the Reynolds analogy is valid in this case. The authors compared these iso-θ contours with those obtained in the steady-flow structure without fluctuation effects (Fig. 1b of Ref. [13]). Although the strength of the mushroom structure is equal or higher, downward squeezing of the iso-θ lines is weaker in the latter case, especially near the wall. It is apparent from Figs. 1a and 1b of Ref. [13] that the averaged effect of the unsteady wavy fluctuation heat flux in the mushroom structure is to compress the entire θ distribution toward the wall region. This gives rise to a further enhancement of surface heat transfer.

Finally, using the Reynolds analogy for Pr=1, the inferred Stanton number (from $C_f/2$) development of Liu [13] is plotted in Fig. 1(a) as a function of the Görtler number and compared with the laminar and turbulent flat-plate boundary layer expressions as follows:

$$\mathrm{St} = \frac{C_f}{2} = \frac{\nu}{U_0^2}\left(\frac{dU}{dy}\right) \quad \text{with} \quad \frac{dU}{dy} = 0.364\sqrt{\frac{U_0^3}{x\nu}} \quad \text{laminar flat-plate boundary layer} \tag{1}$$

$$\mathrm{St} = \frac{C_f}{2} = \frac{\nu}{U_0^2}\left(\frac{dU}{dy}\right) \quad \text{with} \quad \frac{dU}{dy} = 0.014\left(\frac{U_0^{13}}{x\nu^6}\right)^{1/7} \quad \text{turbulent flat-plate boundary layer} \tag{2}$$

Figure 1(b) compares our experimental Stanton number results for U_0=3 m s^{-1} and R=0.65 m [16] to the expressions for a flat-plate boundary layer. For these comparisons, we have recast the classical correlations for Stanton number over a flat plate [17]:

$$\mathrm{St}_{fp} = 0.453\ \mathrm{Pr}^{-2/3}\ \mathrm{Re}_x^{-1/2} \quad \text{(laminar flow)} \tag{3}$$

$$\mathrm{St} = 0.03\ \mathrm{Pr}^{-0.4}\ \mathrm{Re}_x^{-0.2} \quad \text{(turbulent flow)} \tag{4}$$

in St$-G_\theta$ coordinates, assuming that the momentum thickness is not modified by the curvature effects.

For laminar flow, Eq. (3)becomes

$$\mathrm{St} = 0.453\ \mathrm{Pr}^{-2/3}\left(\frac{x}{R}\frac{1}{G_\theta^2}\right) \tag{5}$$

obtained by replacing Re_x by $(R^2/x^2)G_\theta^4$ in Eq. (3). For the turbulent regime, Eq. (4)becomes

$$\mathrm{St} = 0.03\ \mathrm{Pr}^{-0.4}\left(\frac{x^{2/5}}{R^{2/5}}\frac{1}{G_\theta^{4/5}}\right) \tag{6}$$

These correlations are good approximations for two-dimensional boundary layer flows over concave wall with neither primary nor secondary Görtler instability. The same conversions have been carried out for the expressions in Fig. 1(a).

Figure 1(b) shows the conjugate effects of the steady and wavy instability mode on the Stanton number. The steady-flow contribution from the most amplified mode has already been shown to be able to reach the local flat-plate turbulent boundary layer value downstream. Additional excitation of the most amplified wavy instability mode (the sinuous mode [12,14]) provides additional surface heat-transfer enhancement beyond the local turbulent value through the averaged effect of the fluctuating heat flux. Based on Figs. 1(a) and 1(b), we infer that the effect of the secondary instability on heat-transfer enhancement observed numerically by Liu [13] is also apparent in our experimental results for the Stanton number [16].

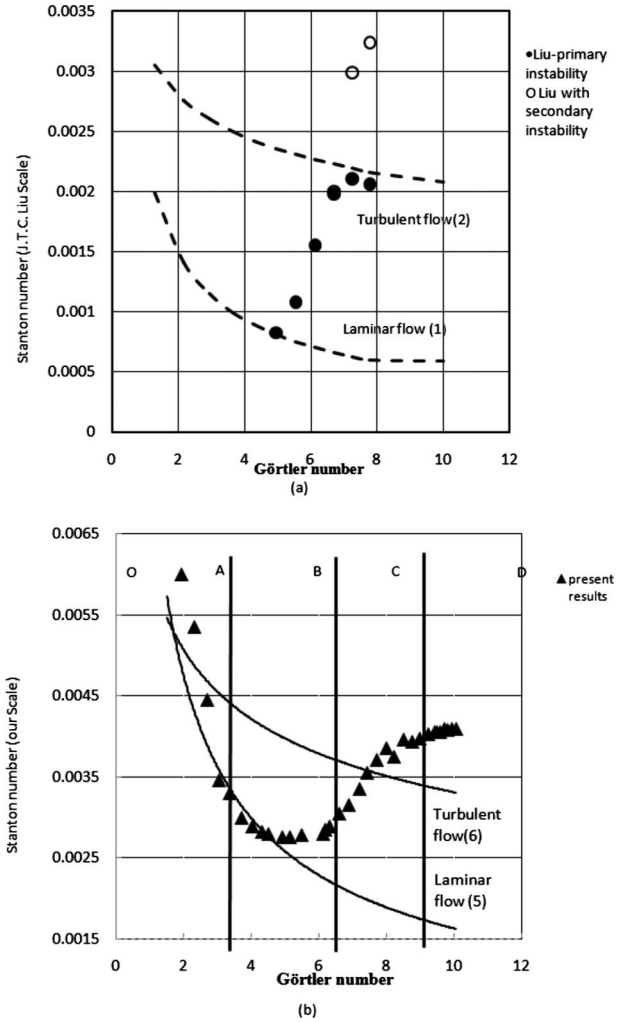

Fig. 1 Evolution of Stanton number as a function of Görtler number: (*a*) numerical results of Liu [13] without secondary instability (●) and with secondary instability (○); (*b*) present experimental results (▲) for U_0=3 m/s and R=0.65 m. The curves correspond to the equations of the flat-plate laminar and turbulent boundary layers.

Experimental confirmation and an endeavor to explain this overshoot in heat-transfer enhancement are the main aims of this paper.

2 Experimental Apparatus and Techniques

Experiments were carried out in a boundary layer over a concave-convex model mounted in a laminar open-loop wind tunnel, as described in Ref. [16]. The nominal freestream velocity is in the range 0.5–9 m/s with a freestream turbulence intensity of 0.7%.

The concave-convex model (Fig. 2) is 45 cm wide and has four main parts:

- the leading edge, shaped like a thick laminar airfoil (NACA-0025)

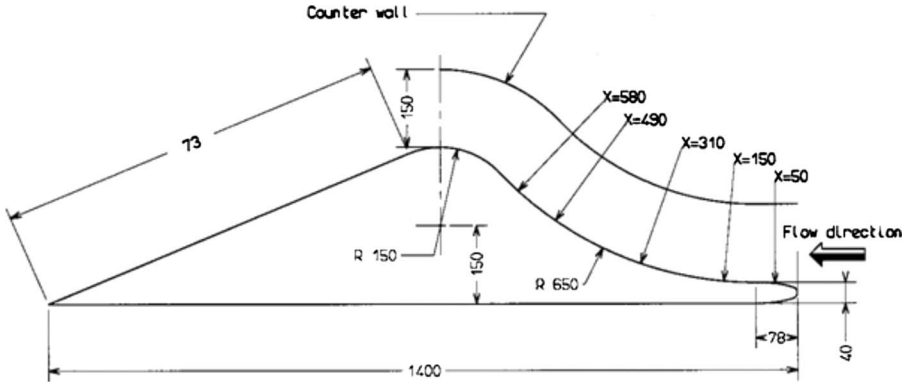

Fig. 2 Schematic diagram of the concave-convex model (values in mm)

- the concave part (radius of curvature 65 cm) in which measurements were made
- the convex part (radius of curvature 15 cm)
- the trailing edge: a flat plate that can rotate around the center of curvature of the convex section

The origin of the curvilinear axial coordinate x is fixed at the leading edge and the concave wall starts at $x=9$ cm.

In order to measure the heat transfer on the concave surface, a quasiconstant heat flux of 200 W/m^2 was imposed on the wall by a thin (130 μm) resistance film made of a 70 μm Constantan layer glued to a 60 μm Kapton film. Then the wall temperatures were measured with 196 chromel-alumel thermocouples of 80 μm beads on the Kapton side of the heating film, embedded between the back of the heating film and the double-faced adhesive film as shown in Fig. 3.

Mean and fluctuating velocity fields were measured by a hot-wire anemometry system (streamline-Dantec). The signal was digitized at 200 Hz through a 16 bit resolution DAQ card. The sampling time was at least 10 s. The diameter of the sensitive part of the hot wire was 5 mm and its length was 3 mm. The prongs of the probe had a 50 μm diameter, so that the probing range was limited to 50 μm from the wall. A traversing mechanism in the wind tunnel provided probe movements in the x, y, and z directions with 7 μm precision. The nominal flow velocity was measured by a Pitot tube and the three-dimensional positioning of the probe and all data acquisition were carried out by microcomputer through an IEEE interface. For further details on the experimental setup, see Ref. [16].

2.1 Heating Effects. Longitudinal vortices in a heated concave surface boundary layer can be generated by both centrifugal force (centrifugal instability) and buoyancy force (thermoconvective instability). Since the aim of the present work is to assess the effects of centrifugal instability on heat-transfer enhancement, we work in the "low heating hypothesis" domain by choosing $T_w - T_{air} \leq 30°C$, thus avoiding the occurrence of thermoconvective instability. To examine the validity of this condition in the experiments, we define the thermal Richardson number Ri_T as

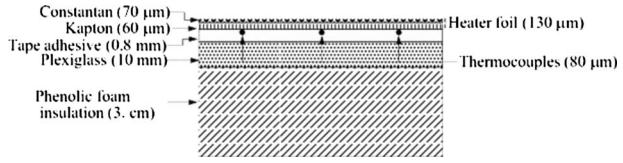

Fig. 3 Thermal instrmentation of the wall

$$Ri_T = \frac{\Delta\rho g}{\rho \frac{U_0^2}{L}} = \frac{\frac{\Delta\rho}{\rho} gR}{U_0^2}$$

where L, the characteristic length scale, is replaced by the wall radius of curvature R. By using numerical values representative of our experimental conditions, $T=300$ K, $\Delta T=30$ K, $R=0.65$ cm, and $U_0 \geq 0.5$ m/s, we obtain

$$\frac{\Delta\rho}{\rho} = \frac{30}{300} \leq 0.1$$

Thus,

$$Ri_T = \frac{(0.1)(9.8)(0.65)}{(0.5)^2} = 2.548$$

This gives the upper limit of the thermal Richardson number because $U_0=0.5$ m s^{-1} was the lowest value of the nominal velocity in all experiments, below which the effect of buoyancy force could no longer be neglected. However, for $U_0=2$ m s^{-1} (the lowest nominal velocity in this paper), the effect of buoyancy force is insignificant.

$$Ri_T = \frac{\Delta\rho g}{\rho \frac{U_0^2}{L}} = \frac{\frac{\Delta\rho}{\rho} gR}{U_0^2} \leq \frac{(0.1)(9.8)(0.65)}{(2)^2} = 0.147$$

Therefore, the effect of thermoconvective instability in the experiments is negligible for nominal velocities $U_0=2$ m s^{-1}. This result is in agreement with Fig. 8 in Ref. [16].

In order to consider the effect of centrifugal force on density variation, we defined a centrifugal Richardson number as:

$$Ri_C = \frac{F_{centrifugal}}{F_{inertial}} = \frac{\Delta\rho \frac{U_0^2}{R}}{\rho \frac{U_0^2}{L}} = \frac{\Delta\rho}{\rho}\frac{L}{R} = 0.1\frac{L}{R} \cong 0.1$$

where L is a length scale of the order of magnitude of the wall curvature radius R: $R \approx L$. Therefore, $Ri_c \approx 0.1$ for all nominal velocities; this density variation mechanism is as negligible as that of the thermoconductive mechanism.

A criterion suggested by Kamotani et al. [18] shows that thermal destabilization occurs if the ratio of Grashof number to the square of Görtler number becomes larger than 1. According to this criterion, the minimum nominal velocity for which thermal destabilization can be neglected is around 0.5 m s^{-1}. Since the smallest

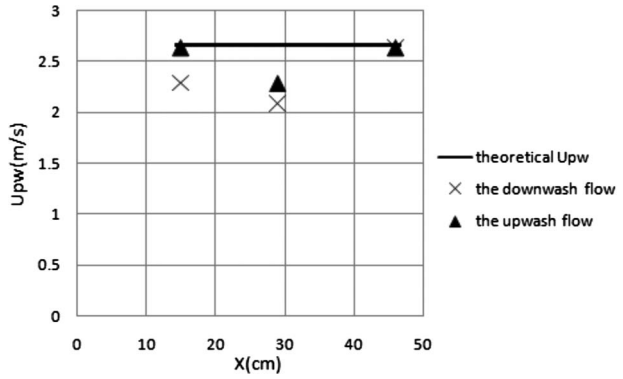

Fig. 4 Evolution of U_{pw} as a function of x in the region of up-wash flow (▲) and down-wash flow (x) for U_0=3 m/s

nominal velocity in this work is 0.5 m s^{-1}, thermal destabilization by this criterion could be negligible except perhaps for this lowest velocity.

2.2 Measurement Uncertainties. Uncertainties in the estimated Görtler and Stanton numbers come from basic uncertainties in the velocity, heat flux, wall temperature, and deduced kinematic viscosity. The velocity is measured with a relative precision of around 1%. The precision in the wall heat flux depends on the value of the heat loss by conduction from the back of the model that is a function of the longitudinal position x. The result shows that the average relative uncertainty in the wall heat flux $(\Delta\varphi/\varphi)$ is about 4%.

The thickness of the resistance film (e=60 μm), the high thermal conductivity of Kapton (0.2 W/m K), and the heat loss (below 9 W/m^2) caused temperature differences between the *measured* and the *real* wall temperature less than 0.0024°C, i.e., less than the uncertainty in the thermocouple measurements, which is of the order of 0.05°C.

Estimated values of experimental U_{pw} in the various positions (x) are shown in Fig. 4 and these values are compared with the theoretical value. $U_{pw} \approx 0.88.U_0$. Then, the relative uncertainty on U_{pw} is about 10%.

To estimate the uncertainty in the Stanton number measurements, we define the local Stanton number by

$$\mathrm{St}(x,z) = \left| \frac{\varphi_p(x,z)}{(\rho C_p)_{T_f}(T_w(x,z) - T_0)U_{pw}(x,z)} \right|_Z$$

The uncertainty in temperature measurement is 0.05°C and the maximum temperature difference between the wall and the air temperature is 30°C. Toé [19] showed that the difference between the *experimental* values of U_{pw} at different positions and the *theoretical* U_{pw} [20] are of the order of 10%. The Stanton relative uncertainty becomes

$$\frac{\Delta \mathrm{St}}{\mathrm{St}} = \frac{\Delta\varphi}{\varphi} + \frac{\Delta(\Delta T)}{\Delta T} + \frac{\Delta U_{pw}}{U_{pw}} = 0.143$$

Uncertainty in the Görtler number is due to the basic uncertainties in the velocity and the kinematic viscosity because of temperature dependence. From the definition $G_\theta = \mathrm{Re}_\theta\sqrt{\theta/R}$, the dependence of the Görtler number on the kinematic viscosity ν is

$$G_\theta = U_0^{1/4}\nu^{-1/4}(0.664^{3/2}R^{-1/2}x^{3/4})$$

Then the relative uncertainty is

$$\frac{\Delta G_\theta}{G_\theta} = \frac{1}{4}\left[\frac{\Delta U_0}{U_0} + \frac{\Delta\nu(T)}{\nu}\right] \leq 3\%$$

With $\Delta\nu = 9.48\times10^{-6}$ m^2 s^{-1}, ΔT=100°C, and $\Delta U_0/U_0$=1% [21].

3 Results and Discussion

3.1 Heat-Transfer Intensification by Görtler Vortices. A large number of experiments have been carried out to investigate the effects of Görtler vortices on wall heat transfer, especially with variation in the freestream velocity [20,21]. The analysis of the variation in the Stanton number with the Reynolds number at different nominal velocities shows that the Reynolds number similarity is not valid in the presence of the Görtler centrifugal instability [20] and that the Görtler number based on the Blasius momentum thickness clarifies the different stages of development of the Görtler instability.

It is of interest to emphasize that the heat transfer in some stages of Görtler flow development is more intense at low freestream velocities, even exceeding the turbulent heat transfer. The interest of this domain, which has been largely ignored in the literature, has been emphasized in Ref. [20]. Figure 1(b) shows an example of the evolution of spanwise-averaged Stanton number

$$\mathrm{St}(x) = \frac{1}{l}\int_0^l \mathrm{St}(x,z)dz$$

along the concave wall.

For U_0=3 m/s, the different flow regions are as follows.

- *Zone OA*: This zone corresponds to the leading edge and its junction with the concave part of the model. The flow is a laminar boundary layer type (two-dimensional steady laminar flow) with acceleration on the leading edge.
- *Zone AB*: Heat transfer on the concave wall deviates gradually from the flat plate due to the growth of the Görtler vortices under the influence of centrifugal instability (three-dimensional steady laminar flow).
- *Zone BC*: The heat-transfer coefficient gradually reaches values close to or above turbulent boundary layer values on a flat plate due to the secondary instability of the Görtler vortices [20] (three-dimensional unsteady flow).
- *Zone CD*: Heat transfer ceases to increase and follows the flat-plate turbulent boundary layer curve. The turbulent flow over a concave wall has a higher Stanton number, as previously noted [10]

Although the temporal fluctuations usually signify transition to turbulence, here they are clearly related to the secondary instabilities in the zone BC and thus turbulence is strictly not present in this zone. It is hypothesized here that the extra heat-transfer enhancement beyond the turbulent limit is due to the secondary instability of the Görtler vortices rather than to the boundary layer transition to turbulence. Henceforth, we concentrate on the appearance and amplification of the secondary instability inferred from flow visualization and velocity field measurements in order to support the above hypothesis and quantify the role of the secondary instability in the heat-transfer increase Table 1.

3.2 Secondary Instability of Görtler Vortices. Figures 5 and 6 plot isocontour lines of U_0/U_p and $u_{\mathrm{rms}}/U_0(\%)$ in the cross-sectional flow plane. Figure 5(a) (corresponding to point A in Figs. 1(a) and 1(b)), Fig. 5(b) (corresponding to point B in Fig. 1(b)), and Fig. 5(c) (corresponding to point C in Fig. 1(b)) depict the experimental development of the Görtler longitudinal vortices. Figure 6(a) (corresponding to point A in Fig. 1(b)), Fig. 6(b) (corresponding to point B in Fig. 1(b)), and Fig. 6(c) (corresponding to C in Fig. 1(b)) show the strong relation between the velocity fluctuations due to the secondary instability and the spatial gradient of the mean velocity due to the primary Görtler instability. It is seen that u_{rms} maxima (around 5% of U_0) in Fig. 6(c) occur at the positions nearest the wall (y=1–2 mm) corresponding to a transitional flow; in Fig. 6(b), on the other hand, the u_{rms} maxima are in the up-wash region (between 3 mm and 6 mm), far from the

Table 1 P_z and P_{rms} values for different nominal velocities at $x=29$ cm ($x/R=0.45$) and $x=45$ cm ($x/R=0.71$)

		$x/R=0.45$		
U_0	0.5 m s^{-1}	1 m s^{-1}	2 m s^{-1}	3 m s^{-1}
St	8.89×10^{-3}	6×10^{-3}	3.55×10^{-3}	2.78×10^{-3}
G_θ	3.98	4.3	4.95	5.49
P_z	1.649	3.609	9.424	18.200
P_{rms}	1.49×10^{-3}	3.59×10^{-3}	2.81×10^{-3}	11.7×10^{-3}
		$x/R=0.71$		
U_0	0.5 m s^{-1}	1 m s^{-1}	2 m s^{-1}	3 m s^{-1}
St	8.85×10^{-3}	6.8×10^{-3}	4.41×10^{-3}	3.79×10^{-3}
G_θ	5.5	6.2	7.05	7.85
P_z	1.354	7.803	12.140	4.901
P_{rms}	0.70×10^{-3}	12.2×10^{-3}	26.1×10^{-3}	13.2×10^{-3}

wall. Thus in this case, heat-transfer intensification can only be due to secondary instability of the Görtler vortices.

Several numerical analyses of the Görtler secondary instability have suggested that the Görtler vortices are susceptible to two modes of secondary instability: a sinuous mode (waves in xz plane) and a varicose mode (waves in xy plane). Figure 7 shows a flow visualization image of the varicose mode of the secondary instability in the concave surface boundary layer for freestream velocity 3 m s^{-1}. The measured axial wavelength is around $\lambda_x=2.5$ cm, in agreement with a temporal fluctuation around 40 Hz. To determine the secondary instability mode of the Görtler vortices, we also used a two-hot-wire probe anemometer. Each hot wire is positioned on one side of the "up-wash" region of a Görtler vortex in the flow and the temporal output signals E of both hot wires were recorded simultaneously (Fig. 8). The sampling frequency was 500 Hz during 16 s (8000 measures). For the sinuous (odd) mode the hot-wire output signals are in phase opposition, while for the varicose (even) mode the signals are in phase.

Figure 8 shows that the signals are mostly in phase, suggesting that the varicose mode predominates in the flow in this zone. However, closer to the wall, periods (not shown here) appear in which the signals are in phase opposition (similar to the flow visualizations of Peerhossaini and Wesfreid 22, suggesting the simultaneous presence of both sinuous and varicose modes. Both modes exhibit the same characteristic frequency.

To investigate the spatial amplification of the secondary instability and compare it with the amplification rate of the Görtler vortices (primary instability), we have calculated, from the power spectral density (PSD) of the hot-wire velocity signal, the axial evolution of the energy content in the flow at a given frequency band. In fact, the axial velocity starts to fluctuate with time once the secondary instability sets in. To estimate the secondary instability amplitude at a given streamwise position, we located the position in the direction normal to the wall at which the fluctuations are at their maxima. At each of these positions, the energy of the signal, e, is measured and plotted in Fig. 9. Despite the few axial positions, Fig. 9 indicates that the turbulent regime saturates the growth of the secondary instability for $x>35$ cm; however, it should be noted that in this very unsteady flow uncertainty in the probe position can cause important uncertainties in the results. For $U_0=3$ m/s, it is found that 90% of the energy is contained in a rather narrow frequency band (38–45 Hz) staggered around 41 Hz. For each axial position, the power spectral density e was then integrated in this frequency band and is plotted as a function of axial position x in Fig. 9. By assuming an exponential law for the spatial amplification of the secondary instability with x ($e^{\beta x}$), we obtain an amplification rate of $\beta=0.4$ comparable to the amplification of $P_{rms}=\int_0^\infty\int_0^{\lambda_z}(u_{rms}(y,z))^2dydz\approx\int_0^{3\delta}\int_0^{\lambda_z}(u_{rms}(y,z))^2dydz$. This amplification rate is to be compared with the amplification

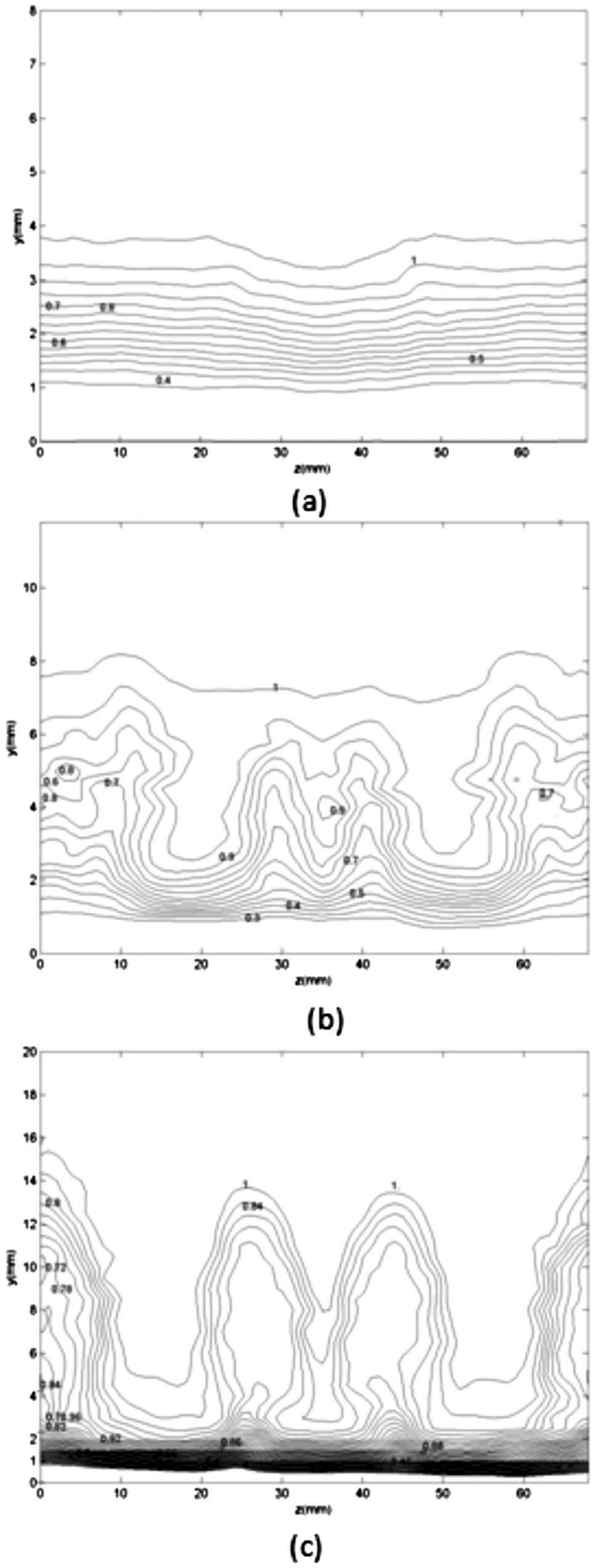

Fig. 5 Isocontour lines of U/U_p: (*a*) at $x=15$ cm, (*b*) $x=29$ cm, and (*c*) $x=49$ cm; plotted as a function of spanwise coordinate z; $U_0=3$ m s^{-1} in the absence of vortex-triggering grid

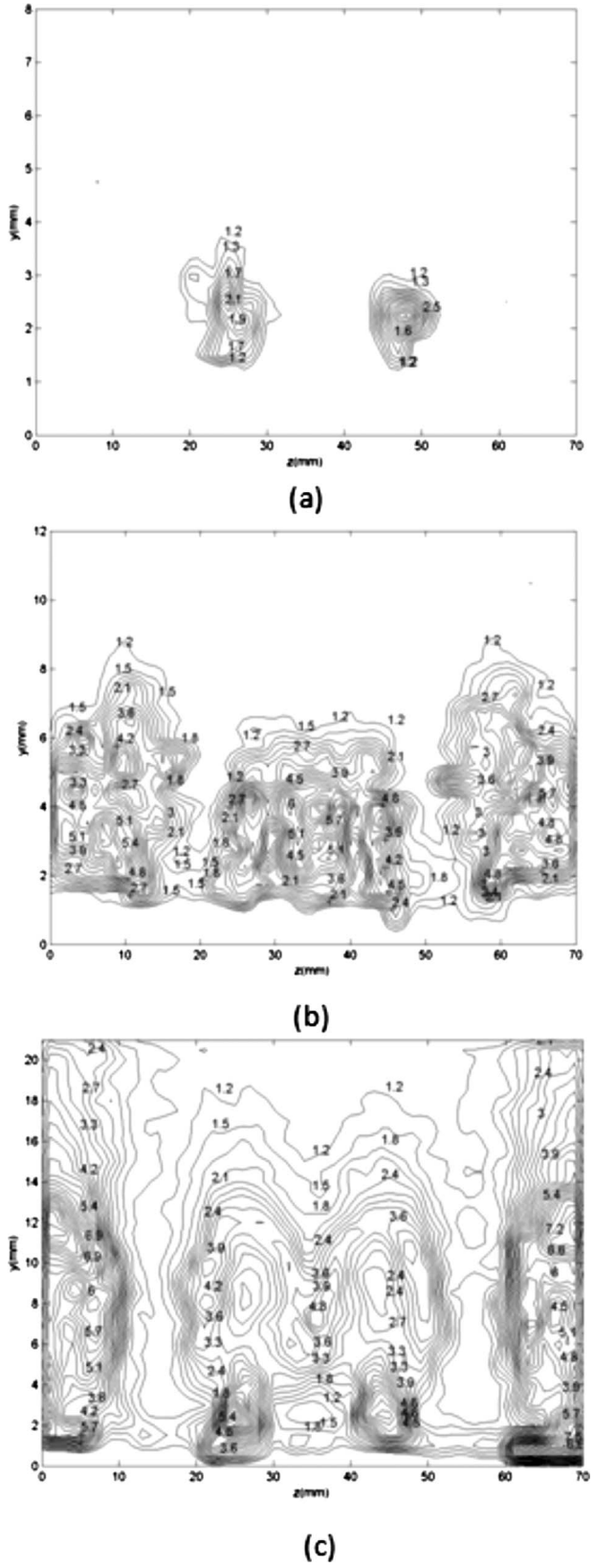

Fig. 6 Isocontour lines of $u_{rms}/U_0(\%)$: (*a*) at $x=15$ cm, (*b*) $x=29$ cm, and (*c*) $x=49$ cm; plotted as a function of spanwise coordinate z; $U_0=3$ m s^{-1}, in the absence of vortex-triggering grid

rate of the primary Görtler instability obtained for the mean flow from the expression $P_z=\int_0^\infty\int_0^{\lambda_v}|\partial U/\partial z|dydz\approx\int_0^{3\delta}\int_0^{\lambda_v}|\partial U/\partial z|dydz$ and shown in Figs. 10(*a*) and 10(*b*). This latter figure reveals that the amplification rate of the parameter P_z is $\beta=0.15$, that is, 2.5 times smaller than that of the secondary instability amplification. Note that the infinite upper limits of integration in P_z and P_{rms} are approximated, in our finite domain of measurement, by 3δ, where δ is the Blasius boundary layer thickness.

Figure 10(*a*) also shows that the primary instability appears at $x=12$ cm from the model leading edge and increases exponentially up to $x=30$ cm. From Figs. 9 and 10(*b*), it appears that the birth of secondary instability is detected at $x=24$ cm and the turbulent regime is detected at $x=35$ cm with the decrease in P_z in Fig. 10(*a*) and increase in P_{rms} in Fig. 10(*b*). The parameter β^{-1} is usually interpreted as the characteristic length scale of spatial amplification. For $\beta=0.4$, we have

$$\beta^{-1}=2.5\ \text{cm}\simeq\lambda_x$$

(λ_x = axial wavelength of the horseshoe vortices (varicose mode))

This result demonstrates that the oscillation (varicose secondary mode) growth rate is very large. At the extreme limit, if β^{-1} is much less than λ, then no oscillation could grow. The signal energy e in the characteristic frequency band centered around 41 Hz characterizes the destabilization of the longitudinal vortices in the flow rather than the energy of a single frequency.

The high growth rate of the secondary instability before the appearance of turbulence at $x=35$ cm explains the overshoot of Stanton number beyond the local turbulent value observed in zone BC of Fig. 1(*b*). This increase above the turbulent value arises from an "eddy heat flux" type. Girgis and Liu [14] argue that, in the presence of the secondary instability, regions of $-v'u'>0$ in the flow cross section dominate, especially after spanwise averaging. The zones located on both sides of the mushroom vortex structure reveal a higher eddy heat flux due to the downward flow in this region. In their argument, using a general Reynolds analogy, Girgis and Liu [14] identified the θ_{rms} concentration in the thermal field with u_{rms} concentration in the fluctuation velocity field. To confirm their conclusions, we examine below the correlation between the axial evolution of the Stanton number and the P_z and P_{rms} amplification.

In order to exhibit the expected correlation between the heat-transfer enhancement and the Görtler instabilities, we normalized the heat-transfer enhancement, the Görtler vortex growth, and the secondary instability growth in order to set 0 for the flat-plate boundary layer values and 1 for the maximum increase over the flat-plate values. Figure 11 plots the evolution of these parameters with x for a fixed nominal velocity. It shows that at the early stages ($x=15-29$ cm) the Stanton number increases due both to the primary instability (P_z) and the secondary instability (P_{rms}), but in the last stage ($x=49$ cm), its increase can only be explained by the secondary instability amplification (P_{rms}). To go further, this correlation is examined on Fig. 12 at a fixed position ($x=49$ cm or $x/R=0.45$) as a function of nominal velocity. Surprisingly, the relative heat-transfer enhancement $((St-St_{fp})/(St-St_{fp})_{max})$ is a decreasing function of the velocity. In conclusion, the Görtler number and the subsequent Görtler strength parameters are not sufficient to explain the heat-transfer intensification. This is in agreement with Momayez et al. [23,24], who showed the impossibility of correlating the Stanton number with only one flow parameter (for example, the Görtler number).

The characteristic properties of the boundary layer in which the secondary instability takes place are also important and in the present work they can be represented by the Reynolds number. One can then split the Stanton number dependence in two parts. The first part represents the heat transfer at the beginning of the heat-transfer enhancement process (before the appearance of the

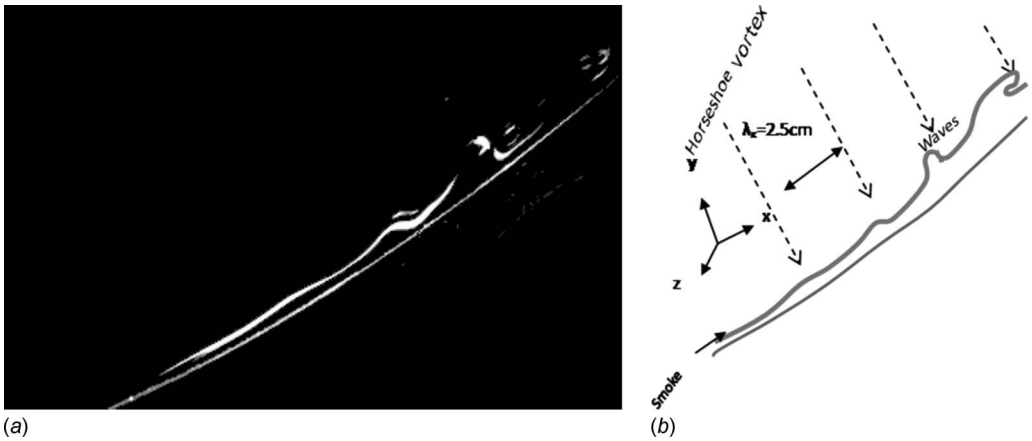

(*a*) (*b*)

Fig. 7 The photographs of flow visualizations of horseshoe vortices due to varicose mode of secondary instability in (*x*-*y*) plane for nominal velocity U_0=3 m/s [19]

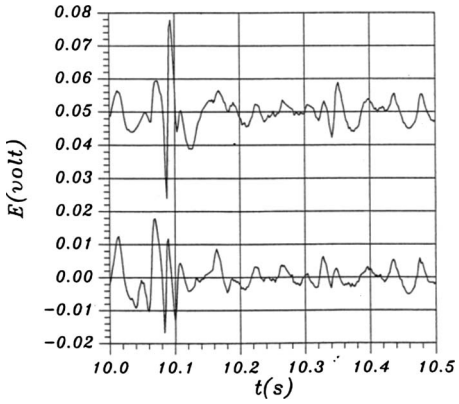

Fig. 8 Hot wire signals on both sides of up-wash zone at position *x*=32 cm, Y/δ=0.5 for a nominal velocity U_0=3 m/s

secondary instability), which is controlled by the Görtler vortices (Go=3.5); we call this Stanton number St_0. The second part is the heat-transfer enhancement due to the Görtler *secondary instability*, which is a function of the Görtler number $A(G_\theta)$. Then the Stanton number can be written as

$$St(x) = St_0^* A(G_\theta(x)) \quad \text{with} \quad St_0 = St_{fp} \text{ at } G_\theta = 3.5$$

Figure 13 plots the evolution of St/St_0 for four different nominal velocities. For $G_\theta > 3.5$, all the curves collapse satisfactorily. This result supports the present description of this dual heat-transfer dependence.

4 Concluding Remarks

Heat-transfer intensification by both primary and secondary Görtler instabilities is addressed. In moderate Görtler and Reynolds number regimes, it has been observed experimentally that

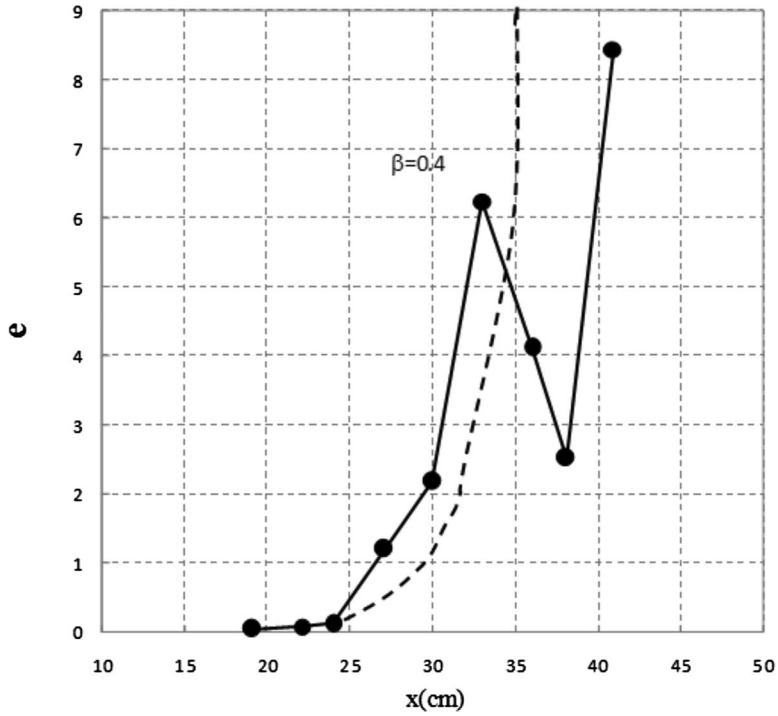

Fig. 9 Axial evolution of the energy signal of the most amplified mode of secondary instability

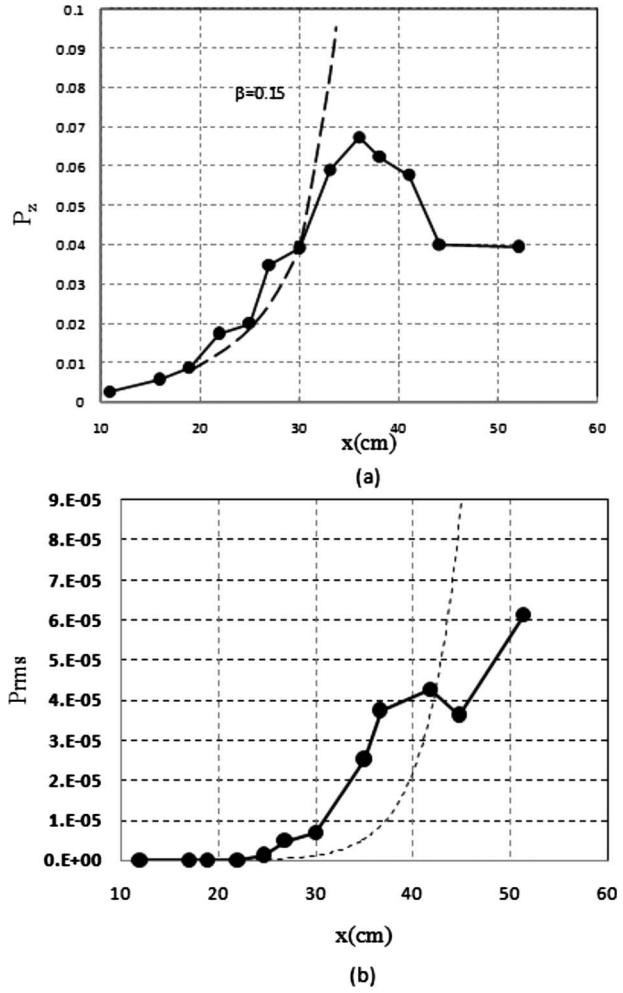

Fig. 10 Axial evolution of parameter P_z (*a*) representing the strength of primary Görtler instability and P_{rms} (b), representing the strength of secondary Görtler instability

the Stanton number can exceed the local turbulent values while the flow is not yet turbulent (as judged by the intermittency factor). It is argued here that in these transitional cases the heat-transfer intensification is mainly due to a secondary instability in the Görtler vortices in which heat is transported by an "eddy heat-transfer" mechanism caused by $\overline{v'\theta'}$ in the presence of the secondary instability (quantified by u_{rms}). Once the secondary instability is saturated, the vortex structure breaks down, a fine-grained turbulent flow sets in, and the Stanton number decreases and converges to the local turbulent value, slightly above that for a turbulent flat-plate boundary layer.

To test these observations, mean and fluctuating velocity fields were measured and their isocontour lines were plotted. These velocity fields show a concentration of u_{rms} on both sides of the mushroomlike structure (in the cross-sectional plane), a good deal farther from the wall than in the turbulent case. The efficiency of the secondary instability on the wall heat transfer is explained by the larger u_{rms} amplitude and the better correlation between u' and v' or θ' and v' in the secondary instability flow than in the boundary layer flow. Liu [13] explained that the eddy transfer in the mushroom structure can increase the temperature gradient near the wall in the same manner as turbulence but more efficiently.

To quantify the effect of freestream velocity on heat-transfer intensification, two criteria are defined for the growth rate of the Görtler instability: P_z for the primary instability and P_{rms} for the secondary instability. The evolution of these criteria along the concave surface boundary layer clearly shows the high growth rate of the secondary instability compared with the primary instability. We looked for a correlation between the axial evolution of the Stanton number and the P_z and P_{rms} amplification. Measurements show that beyond $x=45$ cm the heat-transfer enhancement is basically correlated with P_{rms}, so that the high heat-transfer intensification at low freestream velocities is due to the high growth rate of the secondary instability. Even at very low freestream velocities (1 m/s and below), the boundary layer remains transitional (in the secondary instability state) up to the trailing edge of the concave wall. In this case, the heat-transfer enhancement by the secondary instability of Görtler vortices is much greater than local turbulent values.

Acknowledgment

The authors would like to thank Professor J.T.C. Liu for many stimulating discussions and his collaboration on this work during his sabbatical visit to the Laboratoire de Thermocinétique of the University of Nantes, France.

Nomenclature

C_p = heat capacity
e = signal energy in the characteristic frequency band (arbitrary units)

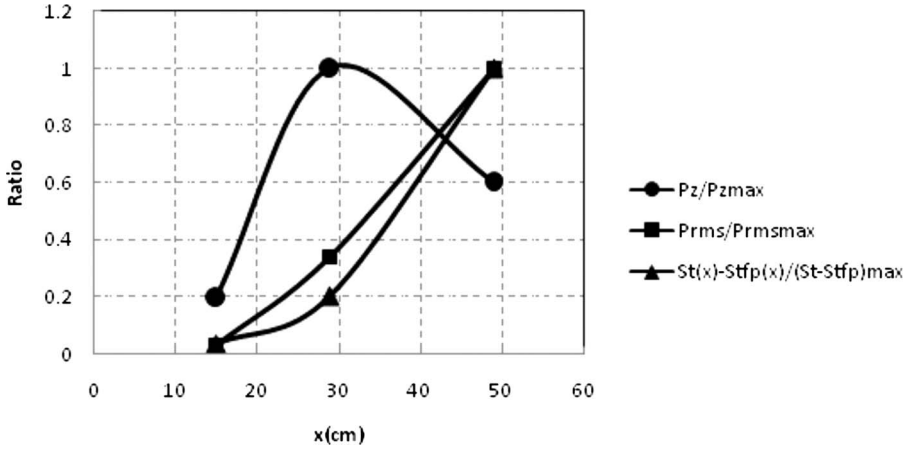

Fig. 11 Comparison of the relative increases of heat transfer $(St(x)-St_{fp}(x)/(St-St_{fp})_{max})$, primary instability $(P_z/P_{z\,max})$ growth and secondary instability $(P_{rms}/P_{rms\,max})$ growth along the concave wall for $U_0=3$ m/s

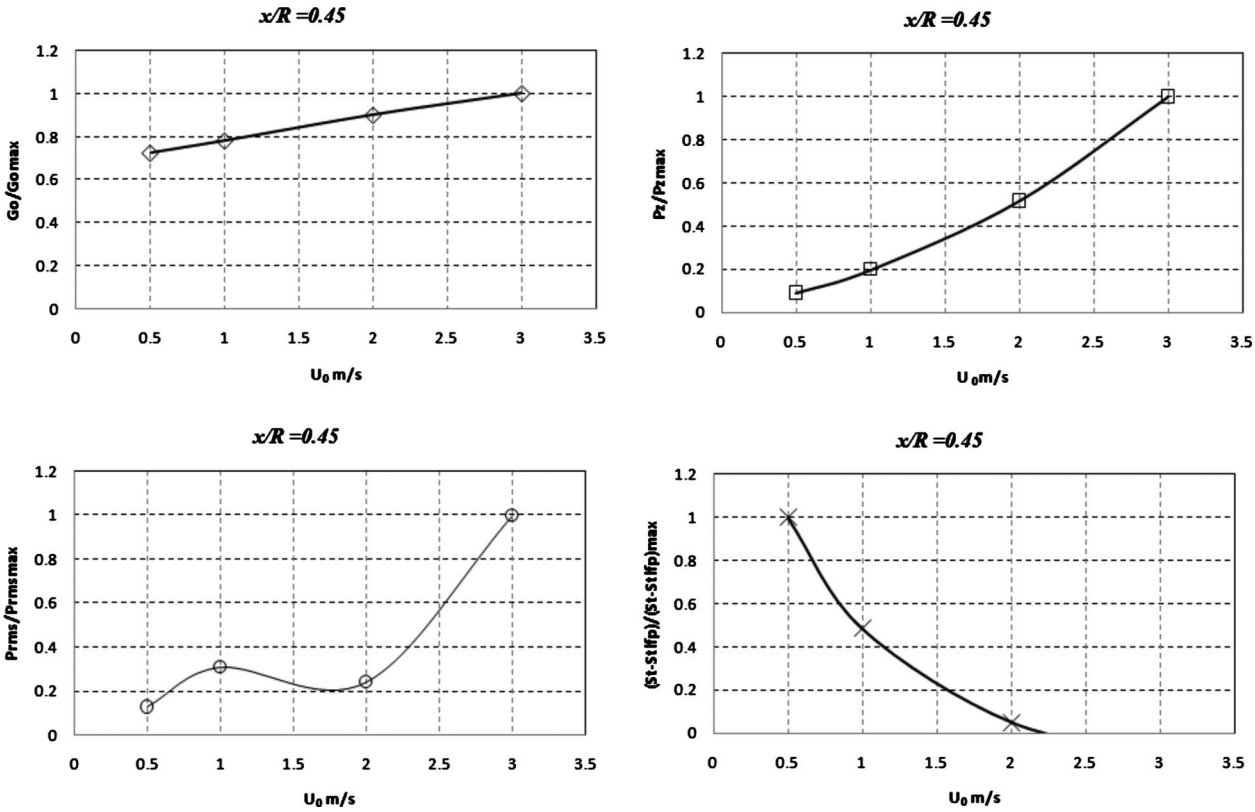

Fig. 12 Influence of U_0 on ($G_\theta/G_{\theta\,\max}$), relative primary instability ($P_z/P_{z\,\max}$) growth, relative secondary instability ($P_{\rm rms}/P_{\rm rms\,max}$) growth and relative increases of heat-transfer enhancement ($\mathrm{St}-\mathrm{St}_{\rm flatplate}/(\mathrm{St}-\mathrm{St}_{\rm flatplate})_{\max}$), at $x/R=0.45$ ($x=29$ cm and $R=65$ cm)

E = signal output (V)
g = gravitational acceleration ($\mathrm{m/s^2}$)
G_θ = Görtler number $(U_0\theta/\upsilon)\sqrt{\theta/R}$ (dimensionless number)
$G_{\theta c}$ = critical value of G_θ (dimensionless number)
H = height of the counter wall, $H=0.15$ m
Pr = Prandtl number, $\mathrm{Pr}=\upsilon/k$ (dimensionless number)
R = wall radius of curvature, $R=0.65$ m
Re_x = Reynolds number based on length scale x, $\mathrm{Re}_x=U_0x/\upsilon$ (dimensionless number)
Re_c = critical value of Re_x (dimensionless number)
Ri_C = centrifugal Richardson number (dimensionless number)
Ri_T = thermal Richardson number(dimensionless number)

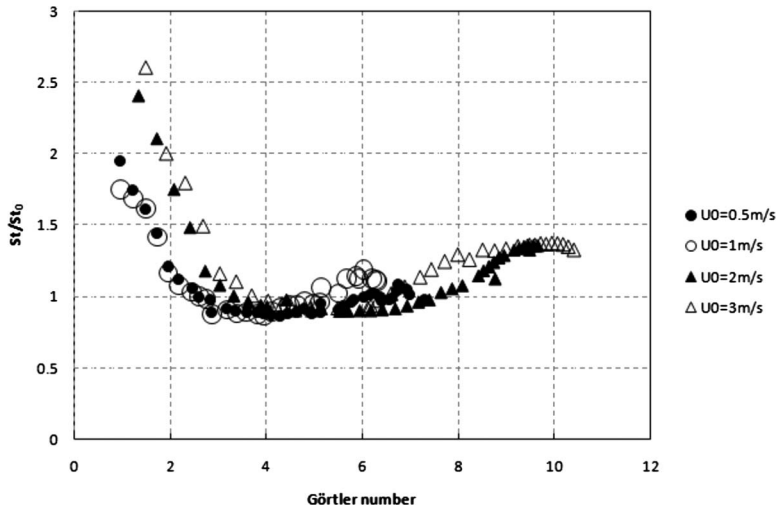

Fig. 13 Relative heat-transfer transfer enhancement ($\mathrm{St}/\mathrm{St}_0$) as a function of Görtler number for different nominal velocities (St_0=critical Stanton number)

St = local Stanton number $St=\varphi_w/\rho C_p U_{pw}(T_{wall}-T_0)$ (dimensionless number)
T_0 = freestream temperature (K)
T_w = wall temperature (K)
ΔT = $\Delta T=(T-T_w)/(T_0-T_w)$, dimensionless mean temperature
u', v', w' = fluctuating velocity components (m s^{-1})
U_0 = freestream velocity (m s^{-1})
U, V, W = components of the local mean velocity (m s^{-1})
U_P = potential velocity $U_p=U_{pw}/1-y/R$ (m s^{-1})
U_{pw} = wall potential velocity, $U_{pw}\approx 0,88\ U_0$ (m/s), $U_{pw}=U_p$ in $y=0$
u_{rms} = velocity root mean square (m s^{-1})
x = streamwise direction (m)
y = normal-to-wall direction (m)
z = spanwise direction (m)

Brief Letter

max = maximum value

Greek Letters

α = thermal expansion coefficient (K^{-1}), $\alpha=1/T$
δ = Blasius boundary layer thickness $\delta=4.910(x/\sqrt{Re_x})$ (m)
ν = kinematic viscosity (m^2 s^{-1})
λ = wavelength of initial perturbations
ρ = fluid density (kg/m^3)
ρ_0 = standard fluid density (kg/m^3)
θ' = $\theta'=T'/(T_0-T_W)$, dimensionless fluctuating temperature
θ = boundary layer momentum thickness $\theta=0.664x(Re_x)^{-1/2}$ (m)
φ_w = wall heat flux (W m^{-2})

References

[1] Görtler, H., 1954, "Three-Dimensional Instability of Laminar Boundary Layers on Concave Walls," Nacher. Ges. Wiss. Göttingen, **2**, pp. 1–26.
[2] Saric, W. S., 1994, "Görtler Vortices," Rev. Fluid Mech., **26**, pp. 379–409.
[3] Hall, P., 1990, "Görtler Vortices in Growing Boundary Layers: The Leading Edge Receptivity Problem, Linear Growth and the Nonlinear Breakdown Stage," Mathematical, **37**, pp. 151–189.
[4] Boiko, A. V., Ivanov, A. V., Kachanov, Y. S., and Mischenko, D. A., 2007, "Quasi-Steady and Unsteady Görtler Vortices on Concave Wall: Experiment and Theory," *Advances in Turbulence XI*, Proceedings of the 11th EUROMECH European Turbulence Conference, Jun. 25–28, 2007, Porto, Portugal, J. M. L. M. Palma and A. Silva Lopes, eds., Springer, Heidelberg, p. 174.
[5] Mitsudharmadi, H., S.H. Winoto, and D.A. Shah, 2006, "Development of Most Amplified Wavelength Görtler Vortices," Phys. Fluids, **18**(1), p. 014101.
[6] Hall, P., 1983, "The Linear Development of Görtler Vortices in Growing Boundary Layer," J. Fluid Mech., **130**, pp. 41–58.
[7] Sabry, A. S., and Liu, J. T. C., 1991, "Longitudinal Vorticity Elements in Boundary Layers: Nonlinear Development From Initial Görtler Vortices as a Prototype Problem," J. Fluid Mech., **231**, pp. 615–663.
[8] Lee, K., and Liu, J. T. C., 1992, "On the Growth of Mushroom-Like Structures in Nonlinear Görtler Vortex Flow," Phys. Fluids A, **4**, pp. 95–103.
[9] Liu, J. T. C., and Sabry, A. S., 1991, "Concentration and Heat Transfer in Nonlinear Görtler Vortex Flow and the Analogy With Longitudinal Momentum Transfer," Proc. R. Soc. Lond., **432**, pp. 1–12.
[10] Liu, J. T. C., and Lee, K., 1995, "Heat Transfer in a Strongly Non-Linear Spatially Developing Longitudinal Vortices System," Phys. Fluids, **7**(3), pp. 559–599.
[11] Hall, P., and Lakin, W. D., 1988, "The Fully Nonlinear Development of Görtler Vortices in Growing Boundary Layers," Proc. R. Soc. London, Ser. A, **415**, pp. 421–444.
[12] Yu, X., and Liu, J. T. C., 1994, "On the Mechanism of Sinuous and Varicose Modes in Three-Dimensional Viscous Secondary Instability of Nonlinear Görtler Rolls," Phys. Fluids, **6**, pp. 736–750.
[13] Liu, J. T. C., 2008, "Nonlinear Instability of Developing Streamwise Vortices With Applications to Boundary Layer Heat Transfer Intensification Through an Extended Reynolds Analogy," Philos. Trans. R. Soc. London, Ser. A, **366**, pp. 2699–2716.
[14] Girgis, I. G., and Liu, J. T. C., 2002, "Mixing Enhancement via the Release of Strongly Nonlinear Longitudinal Görtler Vortices and Their Secondary Instabilities Into the Mixing Region," J. Fluid Mech., **468**, pp. 2975.
[15] Swearingen, J. D., and Blackwelder, R. F., 1987, "The Growth and Breakdown of Streamwise Vortices in the Presence of a Wall," J. Fluid Mech., **182**, pp. 255–290.
[16] Momayez, L., Dupont, P., and Peerhossaini, H., 2004, "Some Unexpected Effects of Wavelength and Perturbation Strength on Heat Transfer Enhancement by Görtler Instability," Int. J. Heat Mass Transfer, **47**, pp. 3783–3795.
[17] Kays, W. M., and Crawford, M. E., 1993, *Convection Heat and Mass Transfer*, McGraw-Hill, New York.
[18] Kamotani, Y., Lin, J. K., and Ostrach, S., 1985, "Effect of Destabilizing Heating on Görtler Vortices," ASME J. Heat Transfer, **107**, pp. 877–882.
[19] Toé, R., 1999, "Etude Expérimentale De L'instabilité De Görtler: Instabilité Secondaire Et Effets Des Tourbillons De Görtler Sur Les Phénomènes De Transfert Thermique," Ph.D. thesis, Université de Nantes, France.
[20] Momayez, L., 2004, "Intensification Des Transferts Pariétaux Par L'instabilité De Görtler: Influence De La Longueur D'onde Et De L'amplitude Des Perturbations Amont," Ph.D. thesis, Université de Nantes, France.
[21] Momayez, L., Dupont, P., and Peerhossaini, H., 2004, "Effects of Vortex Organization on Heat Transfer Enhancement by Görtler Instability," Int. J. Heat Fluid Flow, **43**, pp. 753–760.
[22] Peerhossaini, H., and Wesfreid, J. E., 1988, "On the Inner Structure of Streamwise Görtler Rolls," Int. J. Heat Fluid Flow, **9**, pp. 12–18.
[23] Momayez, L., P. Dupont, B. Popescu, O. Lottin, H. Peerhossaini, 2009, "Genetic Algorithm Based Correlation for Heat Transfer Calculation on Concave Surfaces, Appl. Therm. Eng., **29**, pp. 3476–3481.
[24] Momayez, L., Dupont, P., and Peerhossaini, H., 2006, "Higher Heat-Transfer Efficiency in Laminar Structured Boundary Layers Than in Turbulent Boundary Layers," International Heat Transfer Conference IHTC-13, Sydney, Australia, Aug. 13–18.

On Self-Similarity in the Inner Wall Layer of a Turbulent Channel Flow

Bérengère Podvin

Yann Fraigneau

LIMSI-CNRS,
BP133,
Orsay 91403, France

Julien Jouanguy

J.-P. Laval

LML, Lille,
Bd. Paul Langevin,
Villeneveuve d'Asq Cedex 59655, France

We use proper orthogonal decomposition (POD) to estimate the flow in the near-wall region based on information from the outer buffer layer. Our goal is to assess how the flow structures in the inner wall region are connected to those further away from the wall, and to investigate the nature of the coupling between the inner and the outer region in the POD framework. Reconstructions are carried out for numerical simulations of a plane channel flow at two different Reynolds numbers. We show that elongated structures with a spanwise wavelength smaller than a critical value tend to be concentrated in the inner layer. The critical wavelength is shown to scale with the inner layer height, and interactions between the inner and the outer layer appear to take place predominantly over a self-similar, height-dependent, range of wavenumbers, in agreement with Townsend's attached eddy hypothesis. The reconstructed field appears to capture an adequate energy content and to remain correlated with the real field even close to the wall, which reflects the persistence of energetic structures over the extent of the buffer layer.
[DOI: 10.1115/1.4001385]

1 Introduction

Most of the phenomenological description of the turbulent boundary layer revolves around the concept of "hairpin" vortices, first introduced by Theodorsen [1], and for which early experimental evidence was obtained by Head and Bandyopadhay [2]. Perry and Chong [3] established a link between the model of a hairpin vortex and standard turbulence statistics. These authors noted the connection between hairpin vortices and Bakewell and Lumley's [4] "counter-rotating vortex pairs of elongated streamwise extent," which were educed with the proper orthogonal decomposition (POD) technique. Perry and Chong's model, based on hierarchies of independent hairpin vortices, progressively gave way to new models centered on packets of hairpin vortices. Zhou et al. [5] examined how sufficiently strong hairpin vortices were able to generate new upstream hairpin vortices in a numerical simulation. Adrian et al. [6] carried out a particle image velocimetry (PIV) visualization of the turbulent boundary layer for Reynolds numbers in the range $930 < R_\theta < 6845$, where R_θ is the Reynolds number based on the momentum thickness deficit and incoming flow speed, and produced evidence of packets of vortices, which would account for the disparity in scale between the streamwise and the wall-normal components of the velocity.

The identification of coherent structures is linked to the search for evidence of self-similarity in the flow. Morrison and Kronauer [7] found experimental evidence of self-similar waves in the log layer, as well as in the wall sublayer. Liu et al. [8] showed that POD eigenfunctions in the outer layer were independent of the Reynolds number when scaled with the wall friction velocity and boundary layer height. More recently, del Álamo et al. [9] identified the self-similar characteristics of vortex clusters extending from the logarithmic layer down to the wall. In this paper, we investigate self-similarity in the wall layer, by determining to which extent the flow close to the wall, i.e., below a given height y_1 depends on the flow in the upper region $y > y_1$. To do this we use proper orthogonal decomposition to estimate the flow, and compare the reconstructed field in the inner layer with the true one. As we will show below, this leads us to identify the characteristics of POD spatial eigenfunctions, which we find related to those of hairpin vortices.

The basic question underlying this paper may seem artificial, yet appears legitimate in the context of wall layer models. It is well-known [10] that the near-wall region constitutes a severe limitation for the computation of turbulent flows at high Reynolds numbers and over complex geometries. Over the years, wall layer modeling for large-eddy simulations included the use of approximate boundary conditions based on the logarithmic velocity profile [11,12], zonal approaches [13], optimal formulations [14,15], and more recently, Reynolds averaged Navier Stokes equations (RANS equations) formulations [10]. It should be made very clear at this point that producing a successful wall model for large Eddy simulation (LES) is not the goal of the present paper. First of all, in all that follows, we assume that the flow is known with a high spatial resolution, which could not be available in large-eddy simulations. Moreover, there is evidence [16] that in some cases, using exact (resolved) versions of the wall stresses at the wall may not be sufficient to constitute a robust wall model. Finally, the domain we consider is currently limited to the buffer layer $yu_\tau/\nu = y+ < 200$ of a plane channel, where + denotes wall units, which are based on the friction velocity u_τ and the fluid viscosity ν. This is different from a truly inertial region, especially as we are considering relatively low Reynolds numbers. The reconstruction technique we will use throughout the paper should primarily be seen as an investigation tool, and evaluating its performance as a way to gain insight into the physics of the flow. There is some ground to expect that the estimate should be relevant, as it is generally considered that the outer region drives the inner wall layer to some extent [17–19]. Moreover, recent studies showed that the influence of very large structures in the outer flow at high Reynolds numbers can be felt in the near-wall statistics such as the maximum of the streamwise fluctuation rms [20]. It can also be detected as a slow modulation of the small-scale fluctuations [21,22].

Our objective is therefore to use the POD framework to determine how much the flow in the inner region can be determined from events in the outer region, and to infer from that how the different structures interact with each other, in particular, across horizontal planes. The POD [23] breaks down the velocity field into a hierarchy of three-dimensional spatial structures. The de-

Contributed by the Fluids Engineering Division of ASME for publication in the JOURNAL OF FLUIDS ENGINEERING. Manuscript received September 15, 2009; final manuscript received February 11, 2010; published online April 16, 2010. Assoc. Editor: Ugo Piomelli.

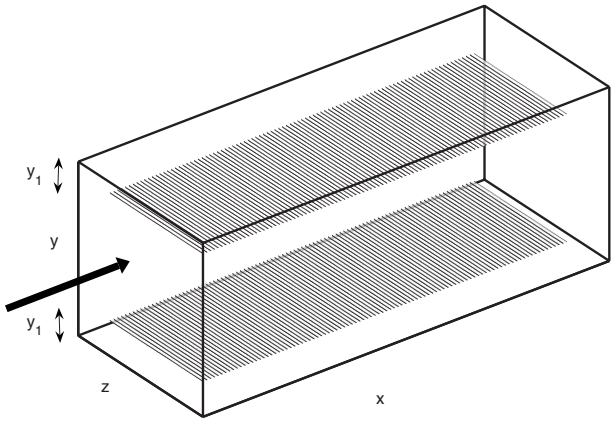

Fig. 1 Numerical domain-the arrow indicates the mean flow direction. The limit between the inner and the outer wall region is materialized by the dark planes.

composition is optimal in the sense that the first N modes capture at least as much energy as any set of N independent functions from another basis. The idea here is to identify the signature of a finite number of POD structures over the top portion of the layer, and to deduce from it information about the coupling of the inner and the outer regions. We note that POD modes are intrinsequely three-dimensional, so that it is not possible to separate streaks from vortices, which may involve different spatial scales [24,25]. Perhaps the most difficult aspect of the reconstruction is to reconcile POD eigenfunctions, which are nonlocal Fourier modes in the horizontal direction (owing to statistical homogeneity), with compact vortices and packets of vortices. This issue was addressed in the early work by Moin and Moser [26], who tested different techniques to reconstruct compact eddies from POD spatial eigenfunctions in the wall region. In the present study, the temporal amplitude of the spatial eigenfunctions is recovered from partial instantaneous measurements. We note that the reverse configuration was studied by Podvin and Lumley [27], where the field in the near-wall region was estimated from wall shear information. The POD-based reconstruction method we use here was also implemented by Podvin et al. [28], where a 3D reconstruction of the flow over a cavity was performed based on statistical information and instantaneous, planar measurements.

The paper is organized as follows. The reconstruction technique is presented in Sec. 2. It is evaluated for different numerical simulations (direct numerical simulation (DNS) and LES) at two different Reynolds numbers. The effect of including symmetries in the POD basis (leading to a Fourier representation in the horizontal direction) is also examined. The numerical test cases are presented in Sec. 3. Flow reconstruction is discussed in Sec. 4. Conclusions are drawn in Sec. 5.

2 The Reconstruction Method

In all that follows, we will consider an incompressible turbulent plane channel flow, whose characteristics are represented in Fig. 1. We will refer to wall units and denote with a+units based on the wall friction velocity u_τ and the fluid kinematic viscosity ν. The streamwise, wall-normal, and spanwise directions of the flow will be denoted by x, y, and z, and the corresponding components of the velocity field u,v,w.

The goal of the reconstruction technique presented in this section is to provide an estimate of the flow in the lower part of the wall region, based on instantaneous information in the outer wall region. We define the following partition of the wall region: $\Omega = \Omega_1 \cup \Omega_2$, where Ω_1 represents the inner wall layer $0 < y+ < y_1$ and Ω_2 the upper wall layer $y_1 < y+ < y_2$. Throughout the paper, we will refer to Ω_2 as the information domain, and to Ω_1 as the reconstruction domain.

The starting point for the reconstruction is the proper orthogonal decomposition of the flow over the full wall region Ω. We refer the reader to the book by Holmes et al. [29] for an introduction to the POD. By application of the proper orthogonal decomposition to the fluctuating velocity field $\underline{u}$, we write

$$\underline{u}(\underline{x},t) = \sum_{n=1}^{\infty} a^n(t)\,\underline{\phi}^n(\underline{x}) \tag{1}$$

where $\underline{\phi}^n$ represents the empirical eigenfunctions and a^n as the associated POD modes. The POD modes a^n have zero mean since they are extracted from the fluctuating field. Their variance (or average energy) is λ^n. By definition, the temporal coefficients or POD modes $a^n(t)$ are determined by projecting the velocity field over the spatial eigenfunctions

$$a^n(t) = \int_\Omega \underline{u}(\underline{x},t) \cdot \underline{\phi}^n(\underline{x})\,d\underline{x} \tag{2}$$

where "." represents an appropriate scalar product.

If the flow is statistically homogeneous in the horizontal directions, as is the case for the turbulent channel flow, POD modes can be shown to coincide with Fourier modes, and the decomposition will be written in Fourier space

$$\underline{u}(x,y,z,t) = \sum_l \sum_k \underline{u}_{lk}(y,t) e^{2i\pi(lx/L_x)} e^{2i\pi(kz/L_z)} \tag{3}$$

where $\underline{x}=(x,y,z)$, L_x and L_z are the periodic dimensions of the flow, $i=\sqrt{-1}$, and

$$\underline{u}_{lk}(y,t) = \sum_{n=1}^{\infty} \sum_l \sum_k a^n_{lk}(t)\,\underline{\phi}^n_{lk}(y) \tag{4}$$

The POD modes are obtained from

$$a^n_{lk}(t) = \int_{y_1}^{y_2} \underline{u}_{lk}(y,t) \cdot \underline{\phi}^{*n}_{lk}(y)\,dy \tag{5}$$

where $*$ represents the complex conjugate.

For a given truncation N, given a velocity field $\underline{u}$ on Ω_2, our goal is to find $\underline{u}^{\text{estimated}}$ on Ω_1, such that

$$\underline{u}^{\text{estimated}}(\underline{x},t) = \sum_{n=1}^{N} a^n(t)\,\underline{\phi}^n(\underline{x}) \tag{6}$$

such that

$$\int_{\Omega_2} |\underline{u}(\underline{x},t) - \underline{u}^{\text{estimated}}(\underline{x},t)|^2 d\underline{x}$$

is minimum. This defines a least mean squares problem, and the solution is such that

$$\int_{\Omega_2} \underline{u}^{\text{estimated}}(\underline{x},t) \cdot \underline{\phi}^n(\underline{x})\,d\underline{x} = \int_{\Omega_2} \underline{u}(\underline{x},t) \cdot \underline{\phi}^n(\underline{x})\,d\underline{x} \tag{7}$$

which is equivalent to finding $\{\tilde{a}^n, n=1,\ldots,N\}$ such that

$$\int_{\Omega_2} \underline{u}(\underline{x},t) \cdot \underline{\phi}^n(\underline{x})\,d\underline{x} = \sum_m \tilde{a}^m(t) \int_{\Omega_2} \underline{\phi}^m(\underline{x}) \cdot \underline{\phi}^n(\underline{x})\,d\underline{x} \tag{8}$$

$B_{mn} = \int_{\Omega_2} \underline{\phi}^m(\underline{x}) \cdot \underline{\phi}^n(\underline{x})\,d\underline{x}$ represents the correlation of the empirical eigenfunctions on the information domain. On the full domain, one has

$$\int_\Omega \underline{\phi}^m(\underline{x}) \cdot \underline{\phi}^n(\underline{x})\,d\underline{x} = \delta_{mn} \tag{9}$$

where δ_{mn} is the Kronecker symbol. We naturally have $-1 < B_{mn} < 1$.

Table 1 The numerical test cases

Case	Code	Re_τ	Domain size (L_x,L_y,L_z)	Domain resolution (N_x,N_y,N_z)	POD in x and z	y_1 (+)	y_2 (+)
1-a	DNS (finite differences)	180	$(4\pi,2,4\pi/3)$	(96,96,96)	Physical	50	70
1-b	DNS (spectral)	180	$(4\pi,2,4\pi/3)$	(96,65,96)	Spectral	50	70
2	LES	550	$(2\pi,2,\pi)$	(128,65,64)	Spectral	50,100,150	200

If we consider exclusively the influence of the information b^n, where

$$b^n = \int_{\Omega_2} \underline{u}(\underline{x},t) \cdot \underline{\phi}^n(\underline{x}) d\underline{x} \tag{10}$$

on the estimation of the mode a^n, one can show by comparing the full and the truncated system that the effect of the truncation at order N is to introduce an error e^n

$$e^n = \sum_{p>N} \frac{B_{pn}}{B_{nn}} a^p \tag{11}$$

Since the modes are uncorrelated, the relative variance of the error is

$$\frac{\mathrm{Var}[e^n]}{\lambda^n} = \sum_{p>N} \frac{|B_{pn}|^2}{|B_{nn}|^2} \frac{\lambda^p}{\lambda^n} \tag{12}$$

Using the Schwarz inequality

$$|B_{pn}|^2 \leq B_{pp} B_{nn} \tag{13}$$

we have

$$\frac{\mathrm{Var}[e^n]}{\lambda^n} \leq \frac{B_{pp}}{B_{nn}} \sum_{p>N} \frac{\lambda^p}{\lambda^n} \leq \frac{1}{B_{nn}} \sum_{p>N} \frac{\lambda^p}{\lambda^n} \tag{14}$$

The error is therefore related to the decrease in the POD spectrum and also to the strength of the partial autocorrelation B_{nn}, which corresponds to the scalar product of the structure with itself on the information domain. In particular, if $B_{nn} \sim 0$, the error may not be small. B_{nn} represents the autocorrelation of the nth structure limited to the information domain Ω_2, in other words, the relative energy or signature of the structure in the outer layer.

In the case of spatial homogeneity, the derivation is similar and the system is now solved for each Fourier mode (l,k)

$$B^{nm}_{lk} a^m_{lk} = b^n_{lk} \tag{15}$$

where $b^n_{lk} = \int_{y_1}^{y_2} \underline{u}_{lk}(y,t) \cdot \underline{\phi}^{*n}_{lk}(y,t) dy$ and $B^{nm}_{lk} = \int_{y_1}^{y_2} \underline{\phi}^{*n}_{lk}(y,t) \cdot \underline{\phi}^m_{lk}(y,t) dy$

It now remains to determine appropriate values for y_1 and y_2. With some arbitrariness, we chose to set the upper boundary of the full domain at $0.4h$, where h is the channel half-height. Given that we are considering numerical simulations at relatively low Reynolds numbers, this means that the entire study is conducted in the buffer layer (y_1 and $y_2 > y_1$ will be in the range of [40,200] wall units). Earlier POD analyses [26,29] pinpointed counter-rotating streamwise vortices, whose center was found to be about at $y+ = 65$. Although typically, only about 10% of the boundary layer height can be considered to scale universally in wall units [30], we will exclusively use wall units throughout the paper.

The reconstruction method is based on the knowledge of spatial second-order statistics (as the POD eigenfunctions are extracted from the decomposition of the spatial autocorrelation tensor). This requirement is a strong limitation for the estimation, since it means that direct numerical simulation or an experiment has to be carried out a priori. Identifying universal characteristics in the wall region could precisely help circumvent this limitation, so that one could for instance imagine that the spatial eigenfunctions could be extrapolated from a simulation carried out at a lower Reynolds number. However, such a derivation is outside the scope of the present paper and will be left for future work.

We now add a few more definitions. In the rest of the paper, we will call the projected field the projection of the fluctuating flow field onto a truncation of the POD basis

$$\underline{u}^p(\underline{x},t) = \sum_{n=1}^{N} a^n(t) \underline{\phi}^n(\underline{x}) \tag{16}$$

where

$$a^n(t) = \int_{\Omega} \underline{u}(\underline{x},t) \cdot \underline{\phi}^n(\underline{x}) d\underline{x} \tag{17}$$

In contrast, we will call the reconstructed field the combination of spatial eigenfunctions modulated by a temporal amplitude (POD) estimated from the information domain

$$\underline{u}^R(\underline{x},t) = \sum_{n=1}^{N} \tilde{a}^n(t) \underline{\phi}^n(\underline{x}) \tag{18}$$

where $\tilde{a}^n(t)$ is an approximate solution of

$$B^{nm} \tilde{a}^m = b^n \tag{19}$$

where B and b have been defined previously. Equivalent definitions hold in spectral space.

3 The Numerical Test Cases

We studied two different Reynolds numbers ($R_\tau = 180$ and $R_\tau = 550$, where $R_\tau = u_\tau h/\nu$ is the Reynolds number based on the channel half-height h and friction velocity u_τ). For the lower Reynolds number, we used two different simulation codes, which allowed us to test the robustness of the reconstruction procedure. We also applied the reconstruction method in the physical (case 1-a) and spectral space (case 1-b). Only the spectral method was used at the higher Reynolds number (case 2). The characteristics of the different test cases are summarized in Table 1.

3.1 Direct Numerical Simulation of a Channel Flow at $R_\tau = 180$

3.1.1 Method of Snapshots. The first case is the direct numerical simulation of a channel flow at $R_\tau = 180$. It was obtained with the code OLORIN, which is based on the numerical method used by Gadoin et al. [31]. Momentum equations are discretized with a finite volume approach on a staggered structured grid with a second-order approximation in time and space. Advection fluxes and viscous terms are calculated with a second-order centered scheme. The time discretization is a backward Euler. The viscous terms are treated implicitly with the Adams–Bashforth scheme. Momentum equations are integrated using an alternating direction implicit (ADI) method [32]. The incompressibility of the velocity field is enforced by using a projection method to compute a correction term to the velocity field. The correction term is obtained from the solution of a Poisson equation.

The dimensions of the box are $(L_x,L_y,L_z) = (4\pi,2,4\pi/3)h$, where h is the channel half-height. The number of grid points was taken to be 96 in each direction, with a regular grid in the

horizontal direction and a hyperbolic mesh in the wall-normal direction.

To compute the empirical eigenfunctions, we used 300 snapshots separated by one integral time scale of U_c/h, where U_c is the velocity at the center of the channel. No additional symmetry was imposed to the flow by deliberate choice (see Sec. 3.1.2).

Due to the relatively small total height of the boundary layer, the total extent of the domain was taken to be $0<y+<70$. The measurements were limited to the region $50<y+<70$, which corresponds to the buffer layer.

3.1.2 Spectral POD. We also used another DNS code, which was validated and used in previous studies [27,33–35]. As will be seen in Sec. 3.2, using a different code allowed us to test the reconstruction procedure for realizations that did not belong to the basis of the snapshots. The Reynolds number and the domain size are kept the same. The code is based on a spectral formulation, with Fourier modes in the streamwise and spanwise directions x and z, and Chebyshev modes in the wall-normal direction y. We used 96 modes in both horizontal directions and 65 modes in the wall-normal direction. Periodic boundary conditions are imposed in the horizontal directions. The linear terms are discretized with a Crank–Nicolson scheme. A low-storage third-order Runge–Kutta scheme is used to advance the nonlinear terms in time.

By deliberate choice, the spatial eigenfunctions obtained with the method of snapshots did not reflect the symmetries of the flow, which include invariance by translation in both horizontal directions and by reflection with respect to a longitudinal plane. We note that it is, in general, possible to include symmetries by adding "symmetrized" snapshots. However, if statistical homogeneity is enforced, POD modes coincide with Fourier modes, and we can directly compute the autocorrelation tensor in Fourier space. The eigenproblem is then solved in the wall-normal direction for each wavenumber pair [29].

We obtained flow realizations from the numerical simulation based on this spectral code. We used over 200 fields sampled at intervals of three integral time scales h/U to compute the autocorrrelation tensor. As in Sec. 3.1.1, the Reynolds number and the box dimensions were kept the same, the POD was applied to the region $0<y+<70$, and the information was also limited to the region $y+\in[50,70]$.

3.2 Large-Eddy Simulation of a Channel Flow at $R_\tau=550$. In order to be able to attribute some generality to the reconstruction results, we consider another test case at a higher Reynolds number with $R_\tau=550$. The velocity fields were extracted from a large-eddy simulation, based on a numerical code developed by the Laboratoire de Mécanique de Lillle. For space discretization, fourth-order central finite differences are used for the second derivatives in the streamwise x-direction. All first derivatives of the flow quantities appear explicitly in the time-advancing scheme, and the first derivatives in x are discretized using eighth-order finite differences. The Chebyshev-collocation is used in the wall-normal y-direction. The transverse direction z is assumed periodic and is discretized using a spectral Fourier expansion with N_z modes, the nonlinear coupling terms being computed using the conventional dealiasing technique with $M>3N_z/2$. For time-integration, implicit second-order backward Euler differencing is used; the Cartesian part of the Laplacian is taken implicitly, whereas an explicit second-order Adams–Bashforth scheme is used for the nonlinear convective terms. The three-dimensional system uncouples into N_z two-dimensional subsystems and the resulting 2D-Poisson equations are solved efficiently using the matrix-diagonalization technique. The dimensions of the numerical domain are $(L_x,L_y,L_z)=(2\pi,2,\pi)h$, where h is the channel half-height. 128 grid points were used in the streamwise direction and 129 in the spanwise direction. 65 Chebyshev modes were used in the wall-normal direction. The flow is symmetric with respect to the longitudinal plane xOy, where O is the center of the channel at each instant in time. The eddy viscosity is based on a dynamic Smagorinsky model [36] with the modification of Lilly [37]. Validation of the code was carried out and is reported in Ref. [38].

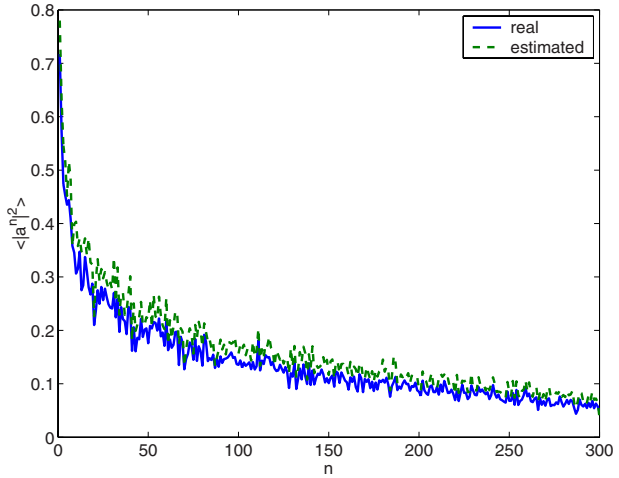

Fig. 2 Energy of the real and reconstructed POD modes

We applied the direct version of the POD to the fluctuating flow field, assuming statistical homogeneity in the streamwise and spanwise direction so that the reconstruction could be carried out directly in Fourier space.

The POD was carried out based on 200 realizations of the velocity field, sampled at about 1 integral time scale. The wall-normal extent of the region Ω was 220 wall units, which corresponds to about 40% of the total channel height, which represents about the same fraction as in the case at $R_\tau=180$. We found that 25 modes captured more than 99.9% of the energy and five modes over 95%. Tests for the reconstruction procedure were carried out with three different layer heights were considered: $y_1=50,100,160$. We typically used 25 modes for the reconstruction, although results were not significantly altered when only five wall-normal modes were included.

4 Results

4.1 Flow Reconstruction in the DNS $R_\tau=180$ Case With the Method of Snapshots. The snapshot-based POD spectrum is shown in Fig. 2, and is compared with that obtained by applying the reconstruction procedure. The decrease in the POD spectrum is relatively slow. The reconstruction method clearly provides an adequate energy content of the POD modes. The correlation coefficient between the real and the reconstructed modes is plotted in Fig. 3 and is on the order of 0.9 for all modes.

To evaluate the relevance of the estimation, we compared planar sections of the real field with its reconstruction. Figure 4 compares the real and the reconstructed fields on the plane $y+=45$, which is just below the domain over which the measurements are obtained. We computed for each ith component of the velocity the relative error

$$e_{u_i}(y,t)=\frac{\int_x\int_z \|u_i(x,z,y,t)-u_i^R(x,z,y,t)\|^2 dxdz}{\int_{xz}\|u_i(x,z,y,t)\|^2} \tag{20}$$

The relative error was found to be on the order of 30% for the streamwise, wall-normal, and spanwise components, and the correlation coefficient between the fields on the order of 0.8. These results constitute a quantitative measure of the information in the near-wall region, which can be obtained from the outer region at

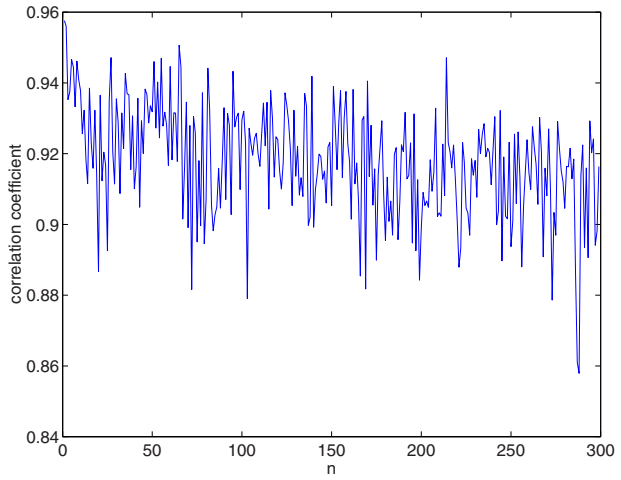

Fig. 3 Correlation coefficient between the real and the reconstructed POD modes

the present Reynolds number. Note that the error is the same for all components, while one would have expected the POD-based reconstruction to be biased toward the most energetic component, i.e., the streamwise component.

The calculation was performed again on the plane $y+=10$, which is the extremity of the so-called viscous sublayer, away from the information domain. The velocity on the plane $y+=10$ was found to be well correlated with the wall shear [27], as can be seen in Fig. 5. The relative error levels and correlation coefficients were found to be the same than on the plane $y+=50$. This result may appear surprising, as there seems to be no loss of information as one moves further away from the information domain. However, this particular test is in some sense biased, since the field that is estimated is also one of the snapshots of the database, so that it can be exactly described by the basis of spatial eigenfunctions. The method of snapshots embeds the POD spatial basis in the linear subspace spanned by a number of independent realizations of the flow, and each spatial eigenfunction is a linear combination of a particular set of flow realizations.

In order to evaluate objectively the reconstruction procedure, we need to apply it to a field, which does not belong to the original subset of snapshots. We note that, since the Reynolds number

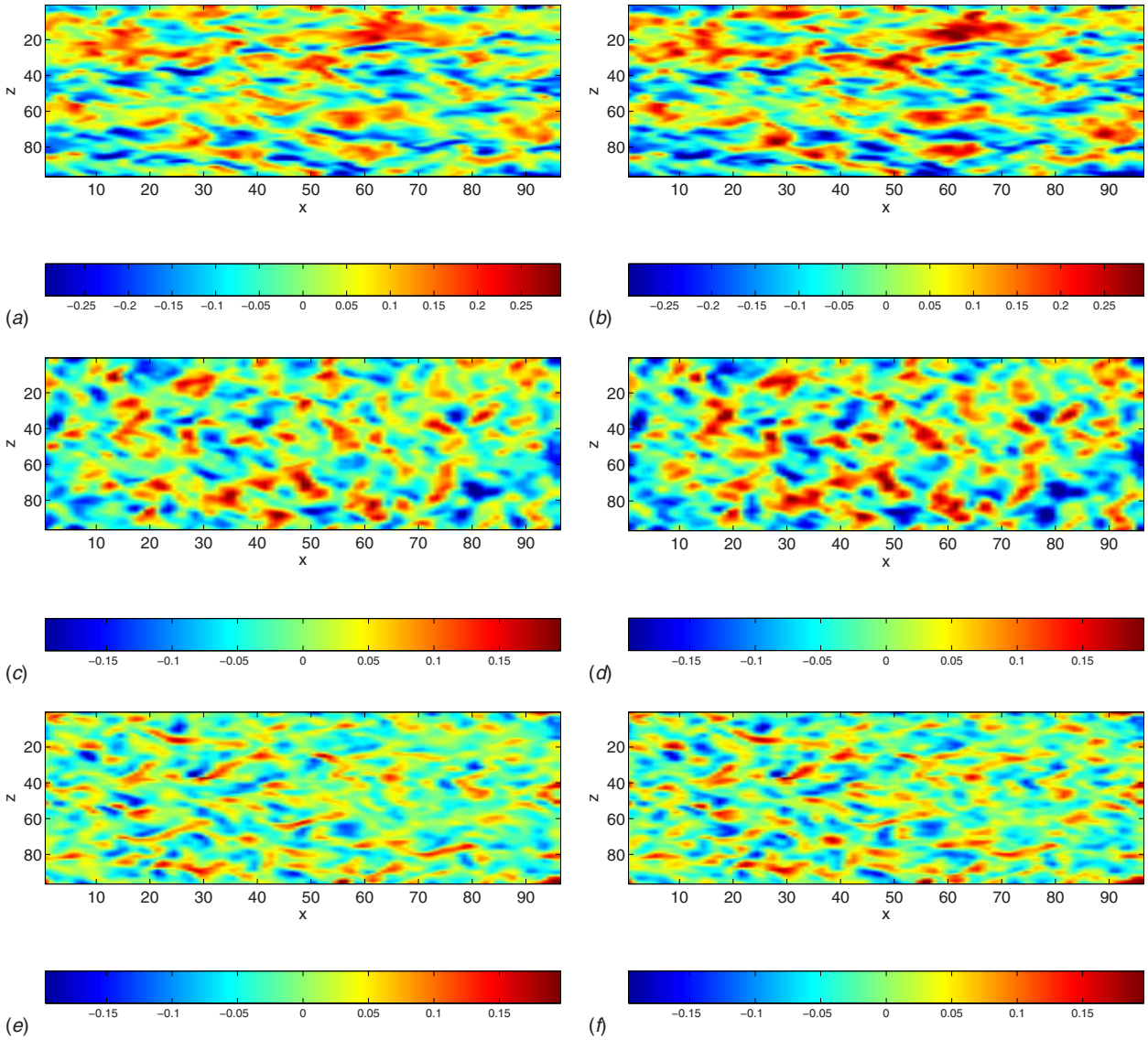

Fig. 4 Plane reconstruction of a flow realization at $y+=45$: (*a*) real *u*, (*b*) reconstructed u^R, (*c*) real *v*, (*d*) reconstructed v^R, (*e*) real *w*, and (*f*) reconstructed w^R

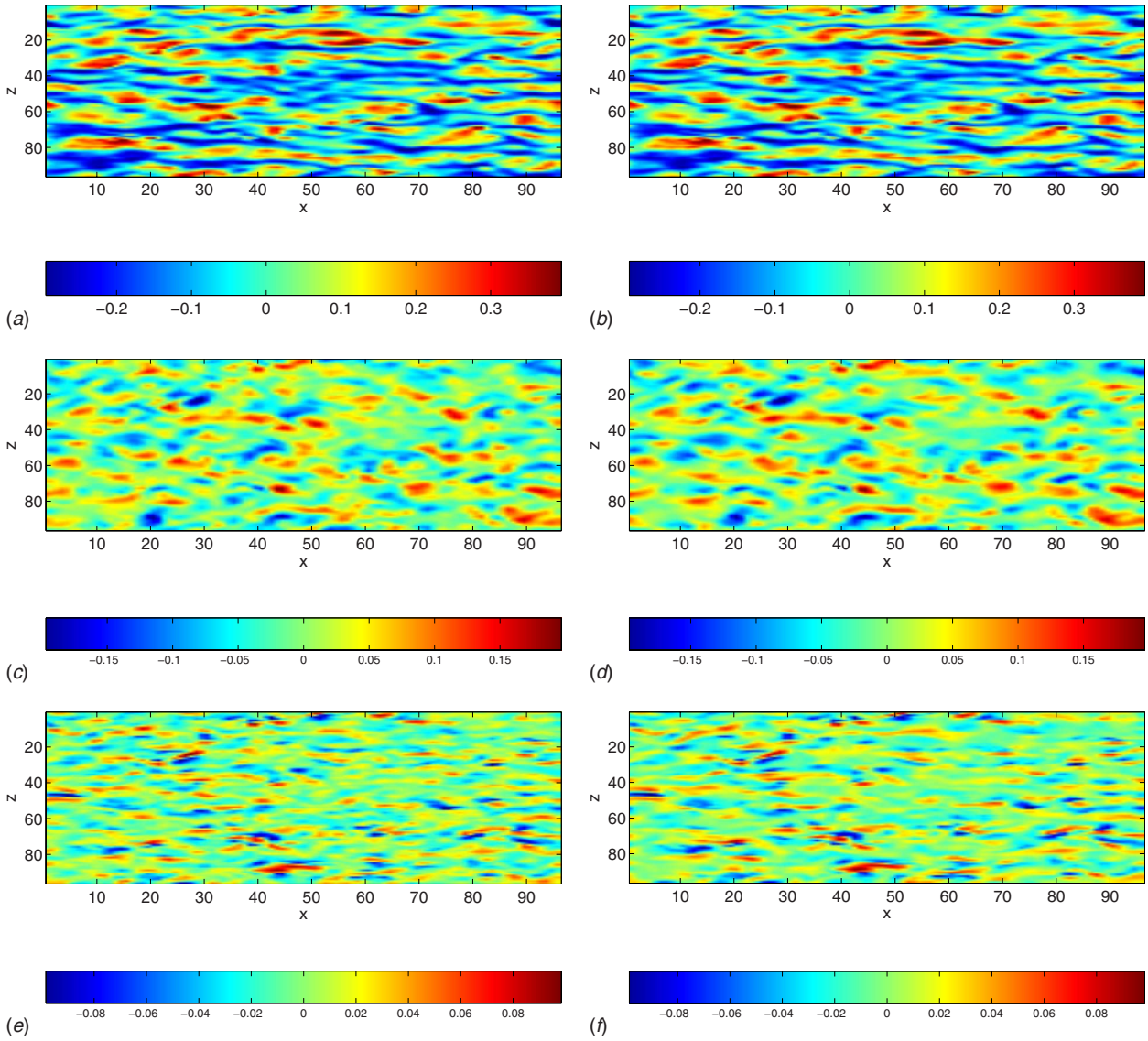

Fig. 5 Plane reconstruction of a flow realization at $y+=10$: (*a*) real u, (*b*) reconstructed u^R, (*c*) real v, (*d*) reconstructed v^R, (*e*) real w, and (*f*) reconstructed w^R

is low ($R_\tau=180$), the box dimensions are small in wall units, and the correlation time scales are very long so that a given realization from the simulation is likely to remain close to the space spanned by the snapshots.

For this reason we used a flow realization obtained from a totally different simulation. The Reynolds number and the numerical box dimensions were kept the same. Since the wall-normal positions are different as we use a Chebyshev grid in the present code, while the OLORIN wall-normal grid is based on a hyperbolic tangent stretching function, the flow field was interpolated on the OLORIN mesh in the wall-normal direction in order to carry out the reconstruction.

The correlation between the reconstruction and the projection was respectively 0.84, 0.65, and 0.6 at $y+=45$ for the streamwise, normal, and spanwise components, and 0.6 at $y+=10$ for all three components, which appears to indicate that the POD modes characterizing the full domain can be relatively well estimated from the information domain alone at the present Reynolds number. However, the correlation between the reconstruction and the real field was close to zero for all three components at $y+=10$. This reflects the fact that the real field does not coincide with its projection. A spectral analysis of the field shown in Fig. 6 confirms that the projection contains less energy than the real flow, while the spectrum of the reconstructed field agrees well with that of the real flow. The only discrepancy for the spectra is observed in the high-wavenumber range of the streamwise velocity component, which we attribute to the limitations of the second-order spatial discretization. The discrepancy between the reconstructed and the projected fields suggests that the projection misses some energy from the reconstruction domain, i.e., the region close to the wall. Further analysis of the error in the spectral space is carried out in Sec. 4.2.

4.2 DNS at $R_\tau=180$—Spectral POD

4.2.1 Structure of the Partial Autocorrelation Matrix B_{lk}^{nm}. The spectral POD modes were estimated by solving the linear system (15). Figure 7 shows the value of the diagonal term of the partial autocorrelation matrix B_{lk}^{nm} for the first wall-normal mode, which contains about 60% of the total fluctuating kinetic energy [39]. The diagonal term represents the relative energy of the first eigenmode on the inner portion of the layer. A striking result here is the self-similar structure of the partial autocorrelation matrix. On one hand, low-order modes corresponding to large spanwise structures

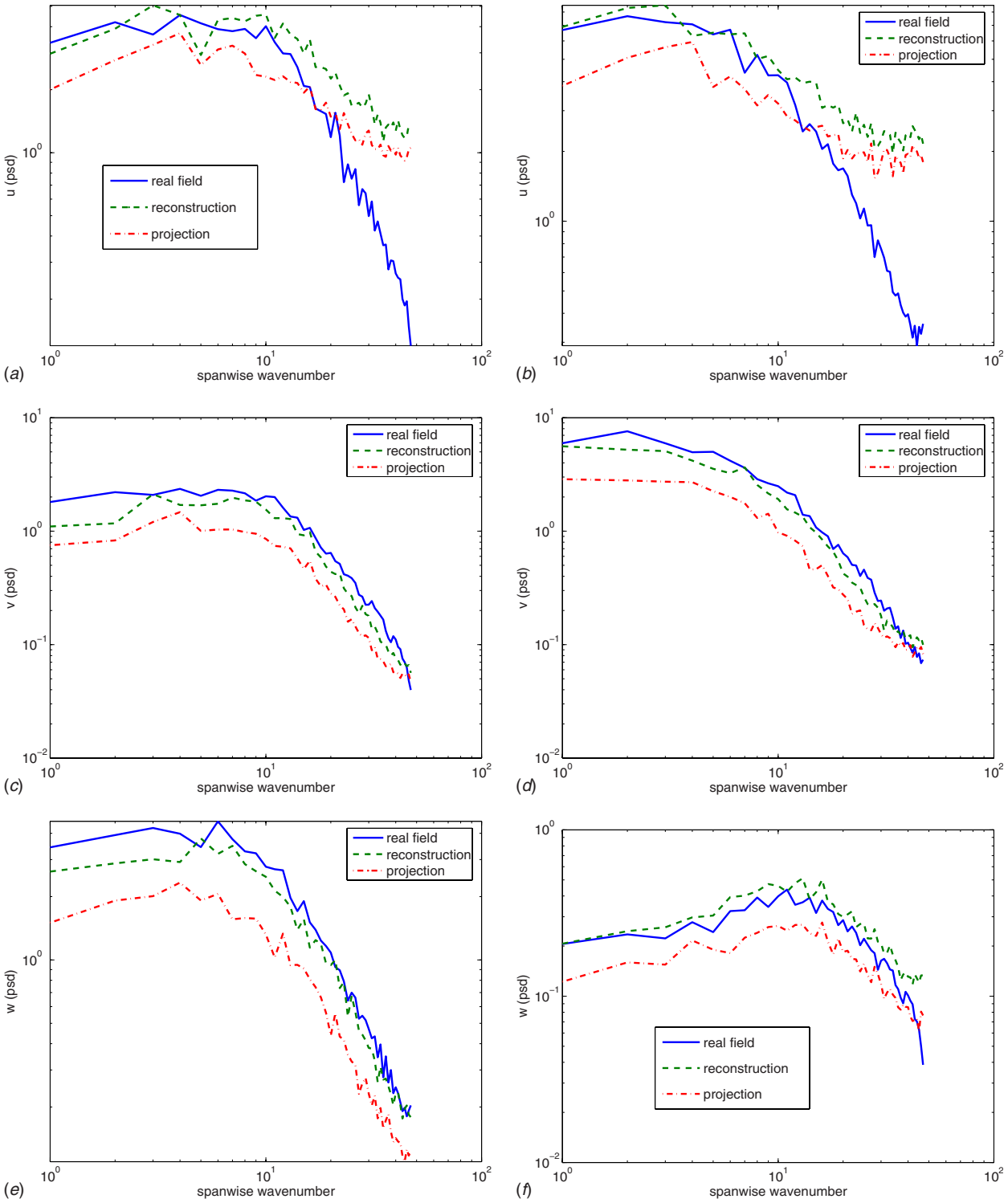

Fig. 6 Spectral comparison of a flow realization with its reconstruction and its projection: (*a*) streamwise component at $y+=45$, (*b*) streamwise component at $y+=10$, (*c*) wall-normal component at $y+=45$, (*d*) wall-normal component at $y+=10$, (*e*) spanwise component at $y+=45$, and (*f*) spanwise component at $y+=10$—the spectra are averaged in the streamwise direction

and smaller, more isotropic structures have a signature close to 1 in the outer layer, while on the other hand, smaller spanwise structures elongated in the streamwise direction have a signature close to zero, which means that they are confined to the inner wall region.

The "frontier" region, which one can define as the region over which the partial autocorrelation falls from 0.9 to 0.1, is relatively confined in wavenumber space and extends over a range of wavenumbers (k_x, k_z), such that

$$k_0 + \alpha k_x < k_z < k_0 + \beta k_x$$

with $\alpha \sim 1.27$ and $\beta \sim 2.08$, and k_0 corresponds to a length scale of 62 wall units, which is comparable to the height of the inner

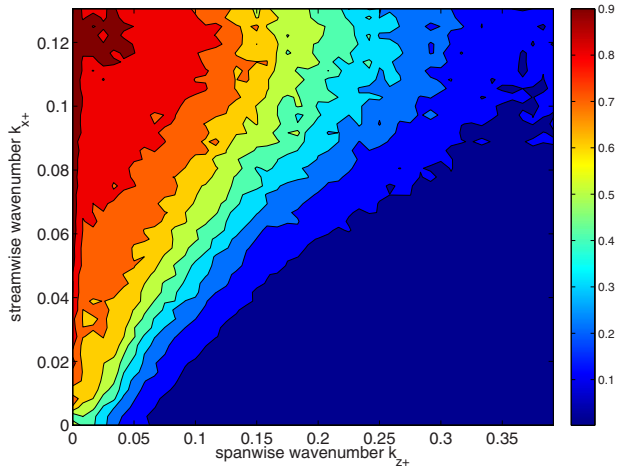

Fig. 7 Diagonal term of the correlation matrix B_{lk}^{11}

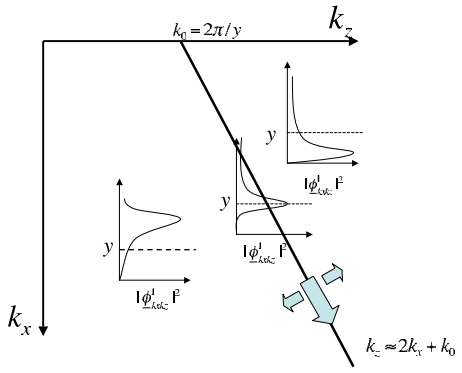

Fig. 8 Spatial distribution of the first-order POD eigenfunctions as a function of the wavenumber—arrows indicate the possible direction of the average energy transfer across the horizontal plane. Energy transfer to higher-order wall-normal modes is not represented.

layer y_1. We point out that all spectral plots shown in the paper are based on wavenumbers expressed in wall units ($k\nu/u_\tau$). As mentioned earlier, the POD eigenfunctions are inherently three-dimensional, so that it is not possible to split the contribution of vortices and streaks. However, we also computed separately the partial autocorrelation for each component of the velocity, and found in all cases the same characteristics as reported above. Although it is difficult, in the absence of phase information, to relate a linear combination of Fourier modes with localized eddies, it appears that the structure of the partial autocorrelation matrix described above agrees with a number of observations. Near the wall, motions corresponding to the "legs" of the hairpin vortices tend to be streamwise invariant, while the "heads" of the vortices further up in the layer correspond to spanwise invariant motions. The fact that energy-containing, streamwise invariant structures are almost entirely confined to the inner region is consistent with Jiménez and Pinelli's [40] evidence of autonomous dynamics in the wall region $y+<70$. Computation of the partial autocorrelation matrix B_{lk}^{11} allows us to quantify in Fourier space the view of these authors, conjectured in Ref. [40] and substantiated by further work [41], according to which "the autonomous wall layer would form by itself long structures, and [...] the effect of the outer flow is to break these long structures into pieces which are shorter than a given length."

The structure of the partial autocorrelation is also consistent with the attached eddy model of Townsend [17], and the proposition that eddies attached to the wall grow in proportion to their distance from the wall in a self-similar fashion. It also supports the observation of Rajaee et al. [42] that the mean streak spacing scales linearly with the wall distance very close to the wall in the region $y+<30$. This is in further agreement with Tomkins and Adrian [24], who also found that structure spacing grows linearly with the distance from the wall, and that energetic modes grow at similar rates in x and z. The value of the scale ratio between the streamwise and the spanwise direction matches the aspect ratio of 1:2 for vortex clusters identified in the logarithmic layer by del Álamo et al. [9]. The characteristics of what they call "tall-attached, clusters" were found to be $\Delta x=6y_c$, $\Delta z=3y_c$, $\Delta y=2y_c$, which match our findings well, even if these are limited to the buffer layer. We also note that the range of wavenumbers $k_x<k_z$ was identified as one where transient linear energy amplification can occur [43].

The partial autocorrelation matrix B_{lk}^{11} also provides a detailed picture of the energy transfer between spatial structures. Podvin [35] recently considered a set of POD modes $\{a_{lk}^1\}$, with $|l|<L$ and $|k|<K$, and computed the contribution of the unresolved modes $\tau_{lk}^>$ to the dynamics of that set. This contribution comes from the nonlinear term in the Navier–Stokes equation and can be represented with a spectral eddy viscosity

$$\tau_{lk}^> = \nu_{lk}^T a_{lk}^1$$

The sign of ν_{lk}^T determines whether the unresolved modes are extracting energy or providing it to the mode a_{lk}^1. Examination of ν_{lk}^T showed that energy was being transferred from elongated, narrow structures (i.e., streamwise invariant, high spanwise modes) toward wavy, wider structures (streamwise modes with a relatively low spanwise variation) for the first wall-normal mode. This energy transfer was computed over the full layer height $0<y+<70$. Examination of B_{lk}^{11} suggests that this global transfer can be broken down into a cascade of interactions across successive horizontal planes between structures characterized by a narrow, height-dependent band of wavenumbers. Figure 8 describes this process (to be compared with Fig. 22 in Perry and Chong's paper [3]). Most of the transfer over a given plane y occurs between for a_{lk}^1, such that $k_z \sim 2k_x+k_0$ with $k_0 \sim 2\pi/y$. A major contribution to the generation of small scales comes from the destabilization of the streamwise invariant structures $(0,k_0)$ by the modes of the form a_{lk}, verifying $k_z \sim 2k_x+k_0$.

4.2.2 Flow Reconstruction. In the context of the method of snapshots, the matrix was found to be diagonally dominant, and each mode a^n was solved for independently from each contribution b^n. In other words, the influence of other wall-normal modes was considered irrelevant, which seems like a valid approximation, to the extent that the POD modes are uncorrelated. In fact, we found that solving the system $B_{lk}^{nm}a_{lk}^m=b_{lk}^n$, assuming that B_{lk} was diagonal-dominant, i.e., setting for each (l,k,m), $a_{lk}^m=b_{lk}^m/B_{lk}^m$, yielded a more accurate estimate than solving for the full system, even when B_{lk} was no longer diagonal-dominant.

The energy of the reconstructed and the true POD modes is plotted in Fig. 9 (the energy maxima are in the upper-left corner of the pictures). We observe an overestimation of the energy in the lower-right region, which corresponds to wavenumbers of the form $k_z>k_0+2k_x$. This error is due to the fact that these modes have almost no energy in the reconstruction domain and are therefore barely detectable there. This issue will be further addressed in Sec. 4.3.

Figure 10 shows the correlation coefficient between the reconstructed and the exact POD mode for the first wall-normal eigenfunction. As could be expected, the temporal correlation between the POD modes roughly matches the spatial autocorrelation of the corresponding structures over the limited domain. It is high for wavenumbers, such that $k_z<k_0+2k_x$, and very low for wavenum-

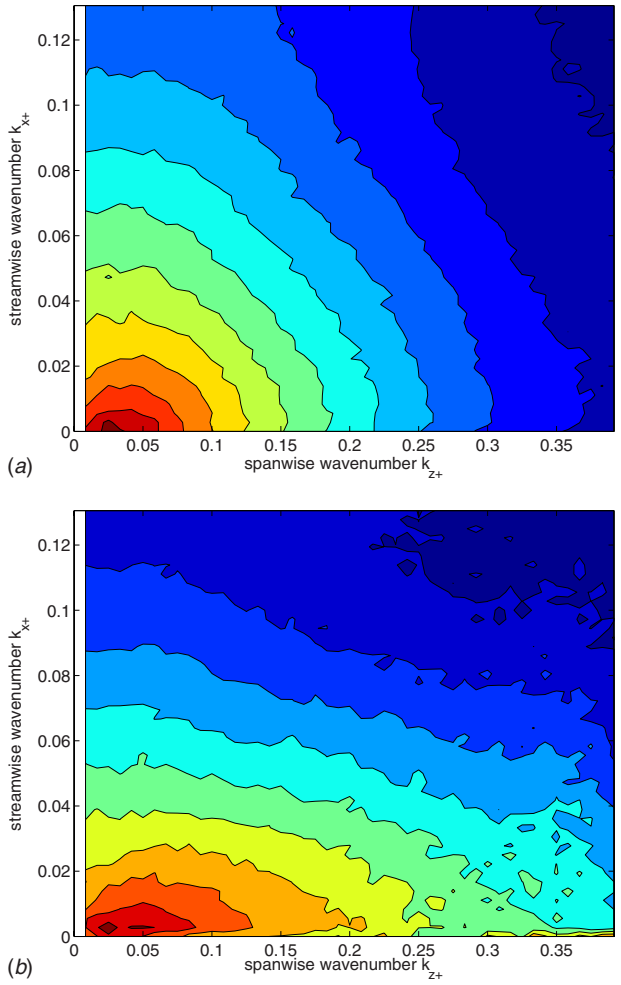

Fig. 9 Amount of energy in the first wall-normal mode-log scale representation: (*a*) real POD mode $|a_{lk}^1|^2$, and (*b*) reconstructed POD mode $|\hat{a}_{lk}^1|^2$

bers, such that $k_z > k_0 + 2k_x$. We note that the value of 2 found here is merely indicative. The physical significance of this ratio is still unclear to us, although we believe it could be related to the development of the streamwise instability as it is convected by the zero streamwise structures. Let us consider the zero streamwise

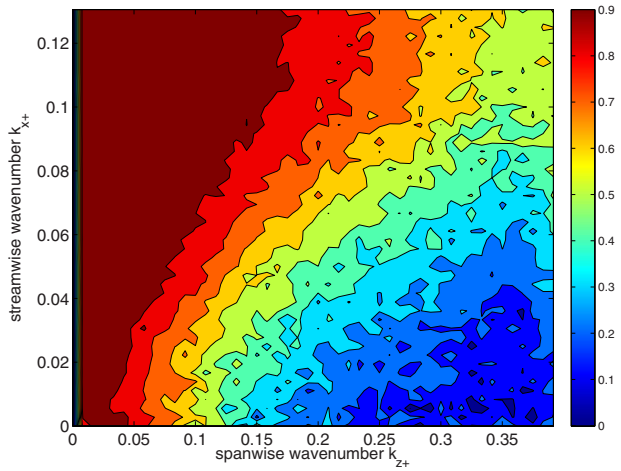

Fig. 10 Correlation coefficient between the real and the reconstructed first wall-normal POD mode a_{lk}^1

Table 2 Correlation coefficient between the components of the velocity field corresponding to Figs. 11 and 12

y+	u	v	w
40	0.67	0.80	0.68
10	0.44	0.41	0.52

field $U_{0k_0}^M = \underline{U}_{0k_0}^M(y,t)e^{2i\pi k_0 z}$. We consider perturbations of that mode of the form $u_{k_x k_z} = \underline{u}_{k_x k_z}(y,t)e^{2i\pi(k_x x + k_z z)}$. Let us assume that the rate of convection of the fluctuation by the zero streamwise modes is the same in the streamwise and the spanwise direction

$$\left|\frac{\partial}{\partial x_3}(U_3^M u_i u_i)\right| \sim \left|\frac{\partial}{\partial x_1}(U_1^M u_i u_i)\right| \tag{21}$$

Using the form of the perturbations to evaluate the partial derivatives, this means that

$$|\,2\pi k_x U_1^M u_i u_i)| \sim |(2\pi k_z U_3^M u_i u_i + 2\pi k_0 U_3^M u_i u_i\,| \tag{22}$$

or

$$|k_x U_1^M| \sim |(k_z + k_0)U_3^M| \tag{23}$$

It now remains to estimate the relative value of U_3^M and U_1^M. Following Hinze [44], the ratio of the streamwise and spanwise turbulent characteristic intensities is close to 3 at the wall, and falls down as one moves away from the wall. Over the distance of $0.4h$, from Fig. 7.17 in Ref. [44], this ratio is closer to 2.

Reconstruction of instantaneous flow fields was carried out on the planes $y+=40$ and $y+=10$. Table 2 shows average correlation coefficients for each component of the velocity field. The correlation for each velocity component is on the order of 0.7–0.8 at $y+=40$, which is quite satisfactory, and remains larger than 0.3 down to $y+=10$ for all three velocity components. The relative excess energy in the reconstruction, which was apparent in Fig. 9, is computed in Table 3 for each component of the velocity field. Only one wall-normal mode is considered. Overall, 30% excess is measured in the streamwise component, which is also the most energetic. The largest discrepancy (200%) is observed for the wall-normal component. As both Figs. 11 and 12 show, the larger-scale patterns are well recovered, while the error is entirely concentrated in the overprediction of intense, highly localized events. These events appear to correspond to the well-known ejections of low-speed fluid, associated with the bursting cycle and the production of turbulence, which originate very close to the wall [45]. The upper layer provides almost no information on the details of these ejections, in agreement with conventional views [46,47].

4.3 LES at $R_\tau = 550$

4.3.1 Flow Reconstruction at $R_\tau = 550$. Figure 13 shows the correlation coefficient between the estimated and the reconstructed POD modes a_{lk}^1 as a function of the streamwise and spanwise wavenumber for all three layer heights. The correlation naturally improves as y_1 is decreased. The general shape of the correlation coefficient is similar for all values of y_1, and is also similar to that found for the DNS at $R_\tau = 180$, namely, it is very high (over 0.9) for the largest, most energetic scales, but falls down rapidly for smaller scales elongated in the streamwise direc-

Table 3 Energy ratio between the reconstructed and the projected field for each component of the velocity field corresponding to Figs. 11 and 12

y+	u	v	w
40	1.42	2.07	1.6
10	1.24	1.74	1.95

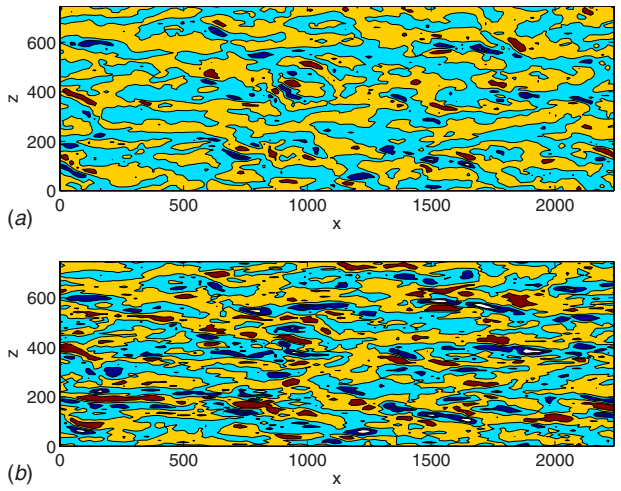

Fig. 11 Comparison of the reconstructed and projected wall-normal velocity at $y+=40$—contour lines are at $-0.08U$, $-0.04U, 0, 0.04U$, where U is the streamwise velocity at the center of the channel: (*a*) v^p and (*b*) v^R

tion. The drop is particularly sharp for the most energetic wavenumbers. As was also observed in Sec. 4.2, Fig. 14(*a*) shows that the abrupt decrease in the temporal correlation of the POD modes is associated with the low energy of the corresponding spatial structure over the information domain. In other words, all structures associated with wavenumbers (k_x, k_z), such that $k_z > 2k_x + k_0$, are confined to the lower wall region.

As in the case with $R_\tau = 180$, the correlation coefficient appeared to vary sharply for modes of the form $\alpha kx + k_0 < kz < \beta kx + k_0$, where k_0 depended on the height. We found $\alpha = 1.67$ and $\beta = 2.22$ along the frontier domain over which the partial correlation decreased suddenly. These values are close to the average spanwise to streamwise wavenumber ratio of about 2, found in Sec. 4.2, and matches the 1:2 ratio observed in the DNS of del Álamo et al. [9]. The respective values of k_0 were found to correspond to scales of 56, 87, and 155 wall units for values of y_1 of 50, 100, and 160 wall units. The limiting spanwise wavelength therefore appears to vary linearly with the layer height. This finding is in agreement with Morrison and Kronauer 's [7] observation of self-similar waves in the logarithmic layer, as well as in the

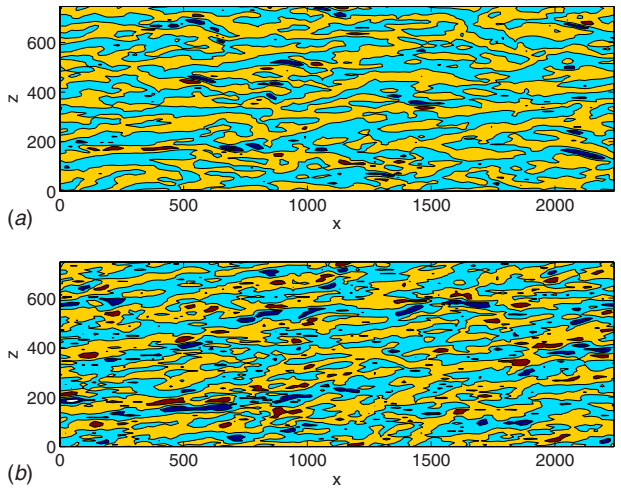

Fig. 12 Comparison of the reconstructed and projected wall-normal velocity at $y+=10$—contour lines are at $-4.10^{-5}U$, $-2.10^{-5}U, 0, 2.10^{-5}U$, where U is the streamwise velocity at the center of the channel: (*a*) v^p and (*b*) v^R

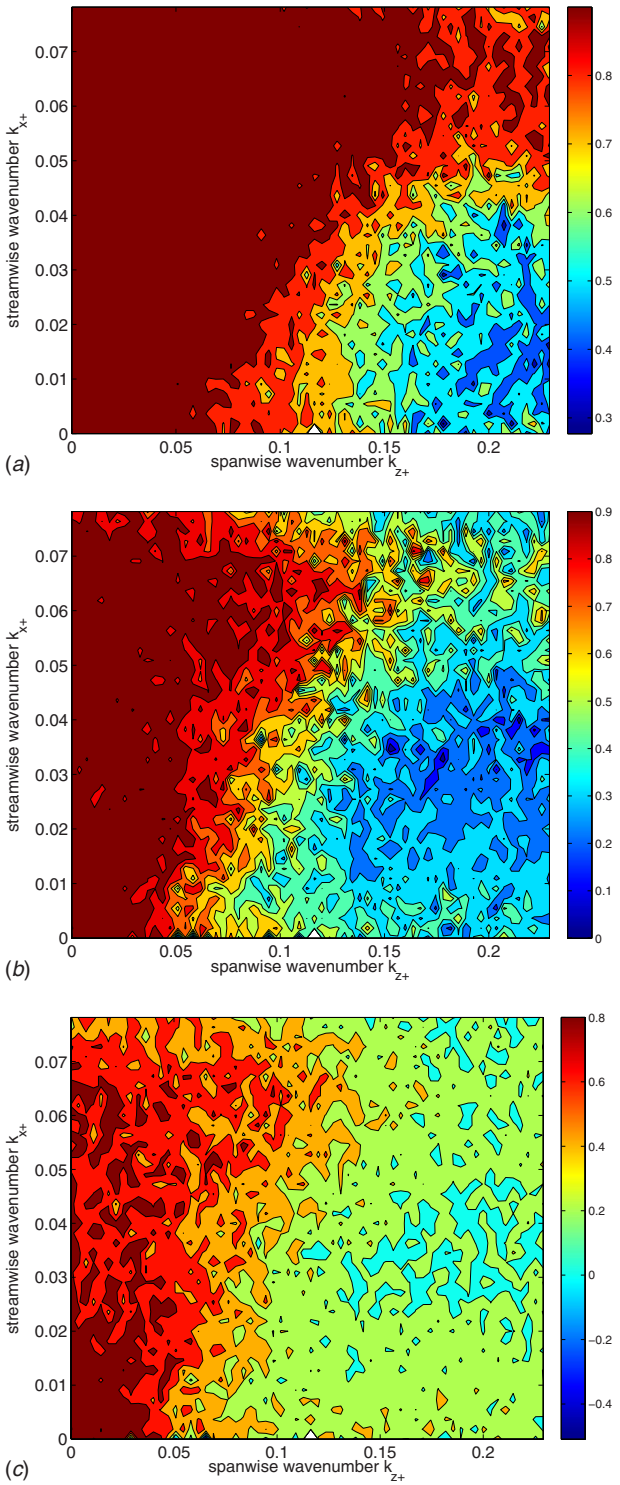

Fig. 13 Correlation coefficient between the real and the reconstructed first wall-normal mode a^1_{lk}: (*a*) $y_1 = 50$, (*b*) $y_1 = 100$, and (*c*) $y_1 = 160$

sublayer. They found that the intensity of these waves reached a peak at a height h_c, scaling with their wavelength, such that $h_c = 0.6/(k_x^2 + k_z^2)^{1/2}$. A rough estimate for the full extent of the waves can then be given by $2h_c$, which corresponds to the values for k_0 we observe for the autocorrelation.

Examination of the corresponding diagonal term for the second wall-normal mode in Fig. 14(*b*) reveals a picture similar to that obtained for the first mode. Modes such as $k_z < k_0' + 2k_x$ are con-

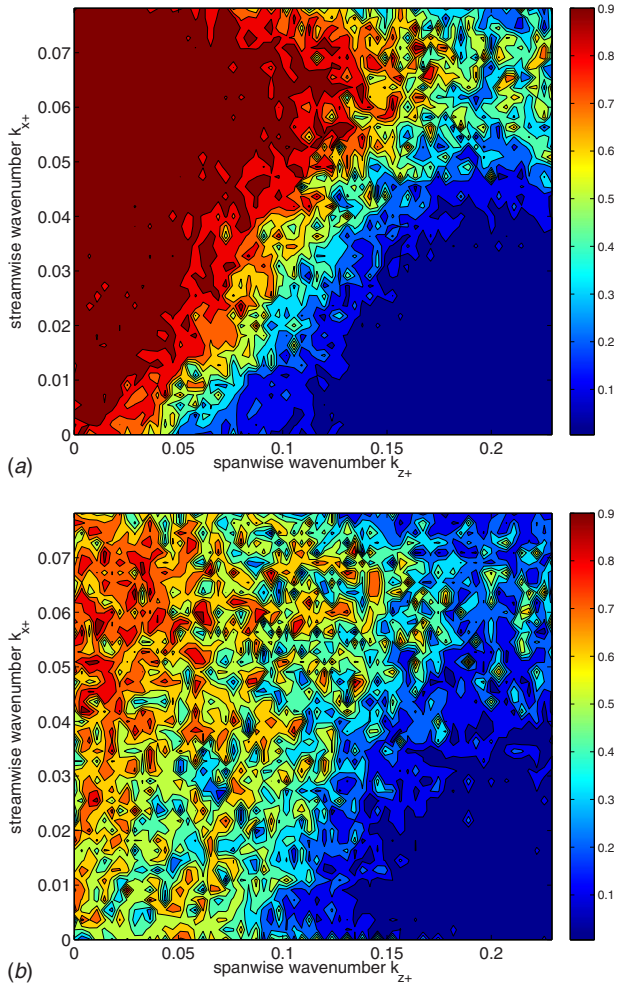

Fig. 14 Diagonal coefficient B_{lk}^{nn} when $y_1=100$—(*a*) $n=1$ and (*b*) $n=2$

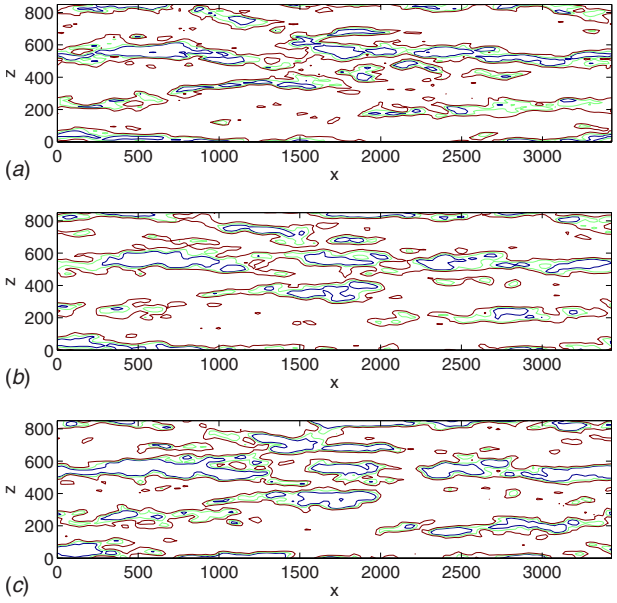

Fig. 15 Reconstruction of the streamwise velocity at $y+=90$ when $y_1=100$: (*a*) real field *u*, (*b*) projected field with 25 wall-normal modes u^p, and (*c*) reconstructed field u^R with 25 wall-normal modes-contours from $-0.15-0.1-0.05U$

fined to the inner layer, with $k_0' > k_0$, while modes invariant or quasi-invariant in the spanwise direction can be observed in the outer region. At a given wavenumber, second-order eigenmodes tend to be distributed over a larger, more diffuse portion of the wall region than the first-order ones, and are typically characterized by several peaks in the wall-normal direction.

Figure 15 compares the real and the reconstructed streamwise velocity on the plane $y+=90$ for the value of y_1 equal to 100. The position and intensity of the low-speed streaks is well recovered by the reconstruction procedure, although some slight discrepancies can be observed in the smallest scales. For all three values of y_1, we computed the correlation coefficient between the estimated field and the projection of the real field on the POD modes. The correlation coefficient was computed separately for each component of the velocity field. Results are displayed in Fig. 16. We first observe that each component is about equally well reconstructed with the reconstruction procedure, even though, as mentioned before, the POD is an energy-based extraction technique, and therefore, is expected to give more weight to the streamwise fluctuation. The correlation for the streamwise component is observed to be the highest in the information domain, but this is not true in the estimation domain. As should be expected, the correlation decreases with the size of the information domain. When $y_1=160$, the correlation between the reconstructed and the projected field is on the order of 0.7–0.8 for the streamwise and wall-normal components, and only 0.5–0.6 for the spanwise component within the information domain. This reflects that relatively energetic POD modes ϕ_{0kz} with a spanwise wavelength $\lambda_z < y_1$ cannot be well recovered, while there is nonetheless a significant amount of energy in larger scales $\lambda_z > y_1$, as observed by Tomkins and Adrian [24], which results in strongly positive values for the correlation.

The correlation for each velocity component also decreases with the distance to the wall in the reconstruction domain. The average rate of decrease appeared to be roughly the same for all three values of y_1: averaging over the three velocity components, the correlation fell by 0.15 over 40 wall units, 0.3 over 90 wall units, and 0.5 over 150 wall units. This is consistent with the idea that, as y decreases in the reconstruction domain, modes (k_x, k_z), such that $k_z \sim 2k_x + 2\pi/y$, suddenly become detectable and make up a new contribution to the estimation error. This extra contribution scales like the turbulent velocity at that height, which results in an approximately constant relative error. The lowest value of the correlation for all three components at $y+=10$ was still significant (0.35) for $y_1=160$. In this last case, we note that the correlation between the fields is still significant, despite evidence [48] that flow organization in the upper region $y+>160$ is markedly different from that in the lower region. However, our results are in agreement with Tuktun's [49], who identified persistent structures extending over the full layer height.

4.3.2 Improving the Estimation of Near-Wall Modes. Figure 17 shows the repartition of energy in the first wall-normal POD mode, and Fig. 18 compares the repartition of energy in the reconstructed fields for all layer heights. As was observed in Sec. 2, there is a clear overestimation of the energy at wavenumbers in the right-hand corner of the picture, which corresponds to structures of relatively long streamwise extent and short spanwise dimensions. The signature of these structures in the outer layer is very weak, which results in an ill-conditioned system. As the first line of Table 4 shows, assuming that the correlation matrix B_{lk} is diagonal, leads to an overprediction of the energy in the modes, an effect which increases with y_1.

A particularly efficient technique to solve ill-conditioned linear systems is based on singular value decomposition (SVD). We briefly summarize the technique here and refer the reader to Ref. [50] for more details. The idea is to use the singular value decomposition of the matrix B_{lk}, which can be written as the product

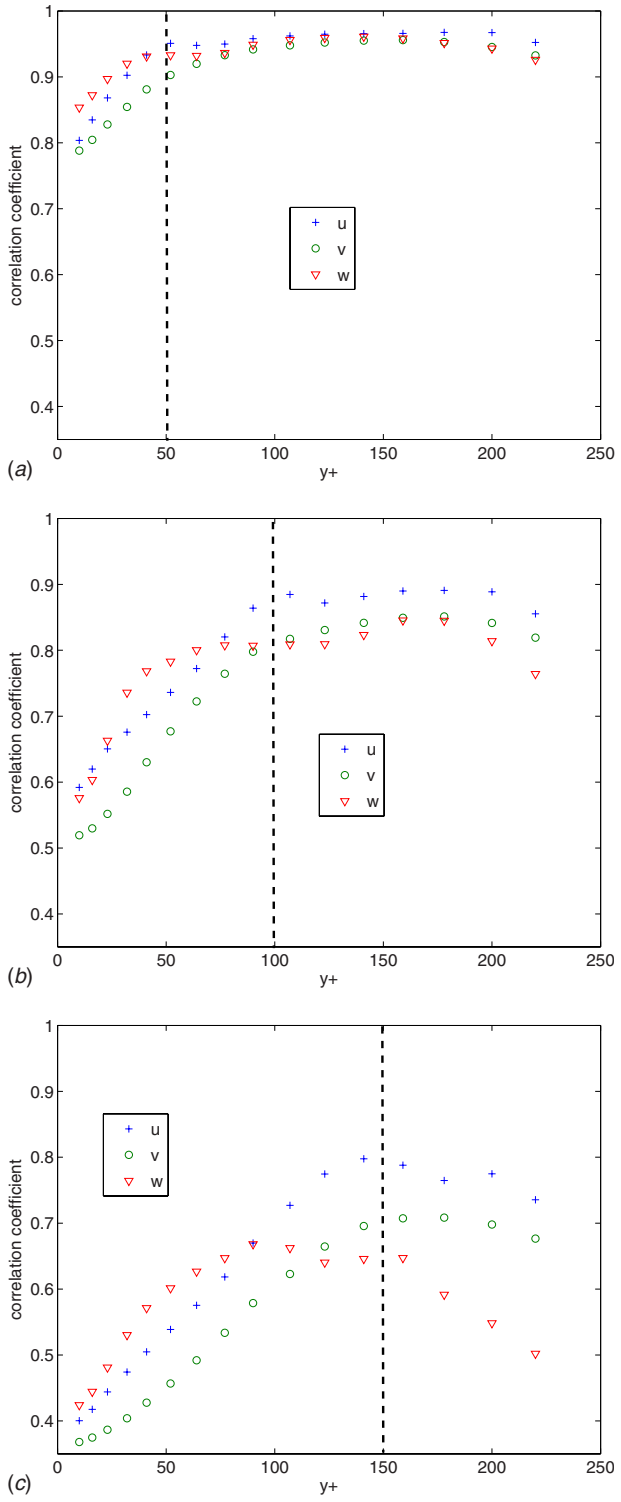

Fig. 16 Correlation coefficient between the reconstructed and the projected field for 25 modes: (*a*) $y_1=50$, (*b*) $y_1=100$, and (*c*) $y_1=160$—the dashed line represents the lower limit y_1 of the information domain

$$B_{lk} = UDV^T \tag{24}$$

where U and V are unitary, and D is diagonal

$$D = \mathrm{diag}[d_i]$$

where $d_i \geq 0$. Solving the system $Ba=b$ for a (the suffix lk has been dropped) can be obtained by computing $a=VD^{-1}U^Tb$, where

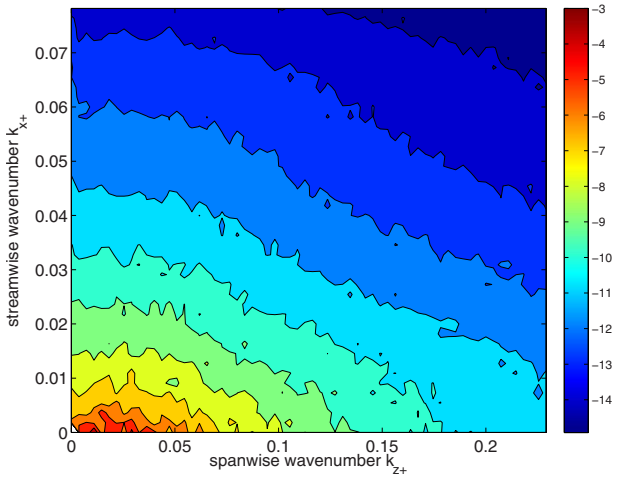

Fig. 17 Energy of the first wall-normal mode $\langle |a_{lk}^1|^2 \rangle$

$D^{-1}=[1/d_i]$. An ill-conditioned matrix B is characterized by a large ratio between the largest and the smallest of d_i. A small value of d_i corresponds to an almost singular direction for the matrix B, and may therefore be associated with spuriously large values in the vector a. The idea is therefore to construct a residual solution, which excludes this nearly singular direction by setting the ith diagonal term of D^{-1} equal to zero. The method is effective, but requires computing the SVD of a matrix at each wavenumber, which is cumbersome.

This motivated us to consider a simpler, physics-based rationale. However, as Fig. 14(*b*) shows, the partial autocorrelation of higher-order wall-normal modes remains non-negligible over a larger spectrum of wavenumbers. The idea was therefore to solve independently the higher-order modes with a non-negligible signature

$$\tilde{a}_{lk}^n = \frac{b_{lk}^n}{B_{lk}^n}, \quad n \geq 2$$

then to replace their estimations in the equation for the first wall-normal mode

$$\tilde{a}_{lk}^1 = \frac{b_{lk}^1 - \sum_{n>1} B_{lk}^m a_{lk}^m}{B_{lk}^n}$$

We compare our estimate with the one obtained by application of the SVD technique described above. Both estimates were closer to the real POD mode than the solution corresponding to the direct inversion of B_{lk}. Comparison of Fig. 18 with Fig. 19 shows that the energy in the first wall-normal mode is significantly reduced for wavenumbers (k_x,k_z) verifying $k_z > k_0 + 2k_x$ (lower-right corner of the picture) when the effect of higher-order modes is taken into account. Table 4 indicates that the total energy of the estimated POD modes $|a_{lk}^1|^2$ became comparable to that of the real ones when the correction term was applied. Although the phase information of the first-order modes was not completely recovered, we found that the correlation coefficient between the exact and the estimated POD mode remained essentially unchanged by the higher-order correction. This suggests the existence of a feedback for these high spanwise wavenumbers between the higher-order modes, which represents motions with several peaks in the wall-normal direction, and the first-order mode, which corresponds to a pair of streamwise rolls associated with longitudinal streaks. Higher-order eigenmodes thus appear to be involved in the regeneration of the streamwise invariant structures. The idea that the formation of longitudinal vortices is conditioned from "background" turbulence is consistent with the model of Hamilton et al.

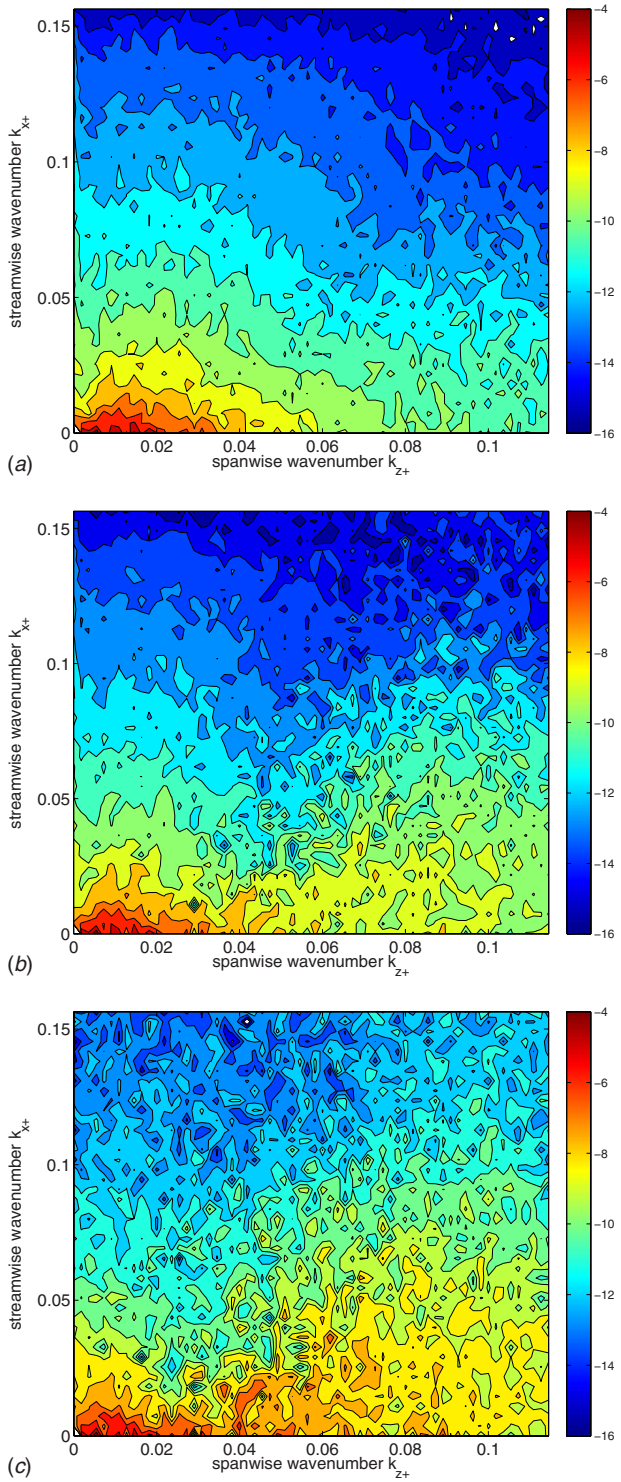

Fig. 18 Energy of the reconstructed POD mode $\langle|\tilde{a}^1_{lk}|^2\rangle$ when B_{lk} is approximated by its diagonal: (*a*) $y_1=50$, (*b*) $y_1=100$, and (*c*) $y_1=160$

[51], in which the streamwise invariant vortices are regenerated through nonlinear interaction of the streamwise modes, which themselves arise from an instability of the streamwise invariant streaks.

5 Conclusion

We have used a reconstruction technique to estimate the flow in the inner wall region based on measurements in the upper buffer layer (or information domain), with the goal to obtain insight about the organization of the flow. The reconstruction procedure is based on the relative energy or signature of the proper orthogonal decomposition eigenfunctions in the information domain. Different versions of the POD were used to compute an estimate for the velocity field. The quality of the reconstruction procedure was found to depend on the adequacy of the POD basis to represent the flow, and in particular on the correct representation of small scales. When the field lay outside the linear span of the snapshots used to compute the POD basis, the spectral energy content of the reconstructed structures was correctly predicted, but the phase information was lost and the reconstructed flow was no longer correlated with the real flow close to the wall.

Table 4 Energy ratio between the reconstructed and the real POD mode $\Sigma_{lk}|\tilde{a}^1_{lk}|^2/\Sigma_{lk}|a^1_{lk}|^2$

y_1	50	100	160
Diagonal form	1.24	2.03	3.70
Correction term	1.00	1.12	1.40

The estimation error was analyzed in the fully spectral POD space. The estimation of POD modes at a given wavenumber is found to depend on the signature of the corresponding spatial structures on the information domain. The same self-similar trends were observed for a DNS at $R_\tau=180$ and a LES at $R_\tau=550$, which gives us some confidence in their generality.

Our results appear to be an independent confirmation of Townsend's hypothesis, as formulated by Perry and Chong [3], that "the eddies that contribute strongly to the Reynolds shear stress at a given height scale with that height and are therefore … attached to the wall." For the first-order wall-normal mode in particular, we observe that elongated structures with short spanwise wavelengths were concentrated in the inner region, while those with shorter streamwise wavelengths and/or larger spanwise wavelengths were dominant in the outer region. The limiting set of wavenumbers (kx,kz) for which the partial autocorrelation varies sharply consists of a narrow region centered around wavenumbers of the form $kz\sim 2kx+k_0$, where k_0 roughly corresponds to the height of the inner layer y_1 for the range of y_1 considered. Energy transfers across the plane y_1 occur mostly between modes belonging to this narrow region.

It was also found that the first-order wall-normal POD modes corresponding to narrow, elongated structures (small k_x and large k_z) were best estimated if the effect of higher-order wall-normal structures was taken into account. This tends to support the existence at these wavenumbers of a feedback mechanism from higher-order modes to the lowest-order one, corresponding in physical space to the sweeping of diffuse, less organized motions toward the wall, and probably related to the regeneration of the streamwise vortices.

All the way down to the wall, the energy of the reconstructed field was found to be reasonably close to that of the real field, and each component of the reconstructed field was relatively well correlated with the projection of the full velocity field. For all the values of y_1 that were considered, the correlation was found to remain significant down to the near-wall. This to us constitutes evidence of organized coherent motions extending over the entire buffer layer. Further work is now required to determine if the global picture of wall layer turbulence provided here by POD is still valid in the full logarithmic layer (spanning several hundreds of wall units).

Acknowledgment

This work has been performed under the WALLTURB project. WALLTURB (A European synergy for the assessment of wall turbulence) is a collaboration between LML UMR CNRS 8107, ONERA, LEA UMR CNRS 6609, LIMSI UPR CNRS 3251,

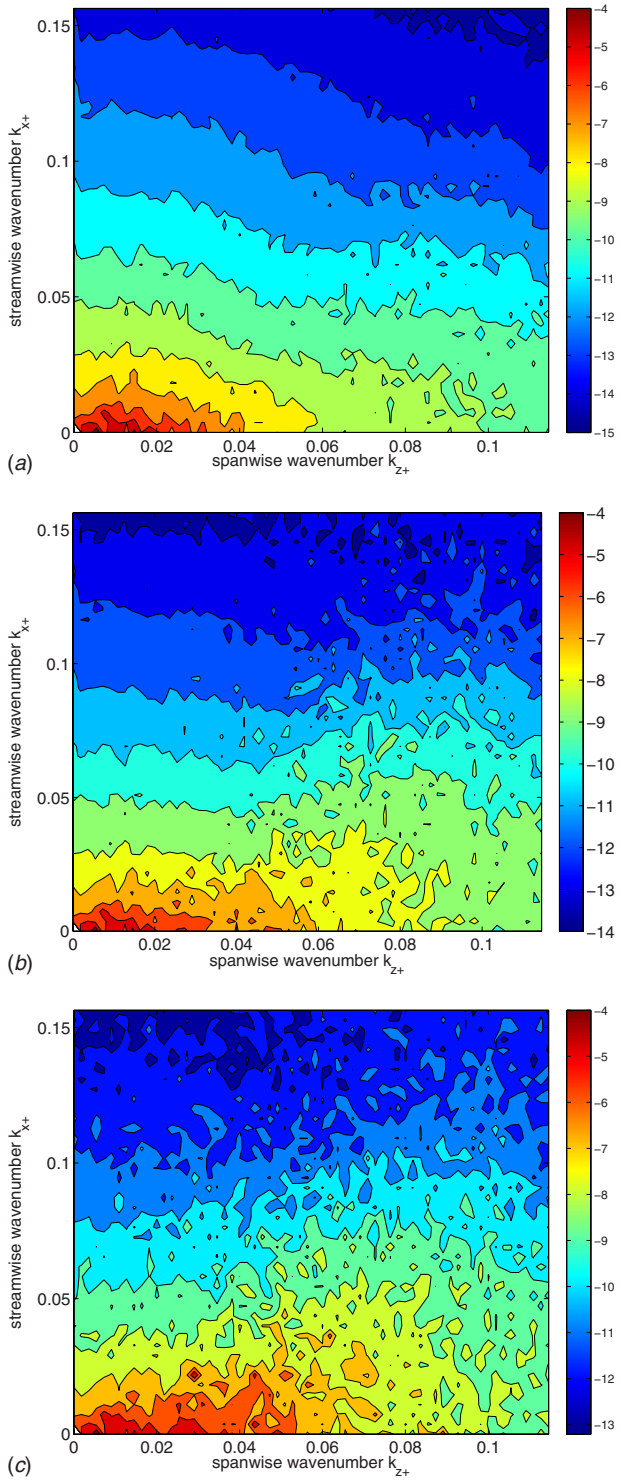

Fig. 19 Energy of the reconstructed POD mode $\langle|\tilde{a}^1_{lk}|^2\rangle$ taking into account the effect of higher-order wall-normal modes: (*a*) $y_1=50$, (*b*) $y_1=100$, and (*c*) $y_1=160$

Chalmers University of Technology, Ecole des Mines de Paris, CNRS groupe Instabilité et Turbulence Saclay, University of Cyprus, University of Rome La Sapienza, University of Surrey, Universidad Politécnica de Madrid, Technische Universität München, Czestochowa University of Technology, FFI, DASSAULT AVIATION, AIRBUS. The project is managed by LML UMR CNRS 8107 and is funded by the EC under the Sixth framework program (Contract No. AST4-CT-2005-516008). Some of the numerical computations were carried out at IDRIS. We are grateful to Professor W.K. George for many helpful suggestions. We are also deeply thankful to the referees for their valuable comments.

References

[1] Theodorsen, T., 1952, "Mechanism of Turbulence," *Proceedings of the Second Midwestern Conference on Fluid Mechanics*, Ohio State University.
[2] Head, M. R., and Bandyopdhyay, P., 1981, "New Aspects of Turbulent Boundary-Layer Structure," J. Fluid Mech., **107**, pp. 297–338.
[3] Perry, A. E., and Chong, M. S., 1982, "On the Mechanism of Wall Turbulence," J. Fluid Mech., **119**, pp. 173–217.
[4] Bakewell, H. P., and Lumley, J. L., 1967, "Viscous Sublayer and Adjacent Wall Region in Turbulent Pipe Flow," Phys. Fluids, **10**(9), pp. 1880–1889.
[5] Zhou, J., Adrian, R. J., Balachandar, S., and Kendall, T. M., 1999, "Mechanisms for Generating Coherent Packets of Hairpin Vortices in Channel Flow," J. Fluid Mech., **387**, pp. 353–396.
[6] Adrian, R. J., Meinhart, C. D., and Tomkins, C. D., 2000, "Vortex Organization in the Outer Region of the Turbulent Boundary Layer," J. Fluid Mech., **422**, pp. 1–54.
[7] Morrison, W. R. B., and Kronauer, R. E., 1969, "Structural Similarity for Fully Developed Turbulence in Smooth Tubes," J. Fluid Mech., **39**(1), pp. 117–141.
[8] Liu, Z., Adrian, R. J., and Hanratty, T. J., 2001, "Large-Scale Modes of Turbulent Channel Flow: Transport and Structure," J. Fluid Mech., **448**, pp. 53–80.
[9] del Álamo, J. C., Jiménez, J., Zandonade, P., and Moser, R. D., 2006, "Self-Similar Vortex Clusters in the Turbulent Logarithmic Region," J. Fluid Mech., **561**, pp. 329–358.
[10] Keating, A., and Piomelli, U., 2006, "A Dynamic Stochastic Forcing Method as a Wall-Layer Model for Large-Eddy Simulation," J. Turbul., **7**(12), pp. 1–24.
[11] Deardorff, J. W., 1970, "Numerical Study of Three Dimensional Turbulent Channel Flow at Large Reynolds Numbers," J. Fluid Mech., **41**, pp. 453–480.
[12] Piomelli, U., Ferziger, J., and Moin, P., 1989, "New Approximate Boundary Conditions for Large Eddy Simulations of Wall-Bounded Flows," Phys. Fluids A, **1**(6), pp. 1061–1068.
[13] Kalitzin, G., Medic, G., and Templeton, J. A., 2008, "Wall Modeling for LES of High Reynolds Number Channel Flows: What Turbulence Information Is Retained?," Comput. Fluids, **37**, pp. 809–815.
[14] Nicoud, F., Baggett, J. S., Moin, P., and Cabot, W., 2001, "Large Eddy Simulation Wall-Modeling Based on Suboptimal Control Theory and Linear Stochastic Estimation," Phys. Fluids, **13**(10), pp. 2968–2984.
[15] Templeton, J. A., Wang, M., and Moin, P., 2008, "A Predictive Wall Model for Large-Eddy Simulation Based on Optimal Control Techniques," Phys. Fluids, **20**, p. 065104.
[16] Cabot, W., 1996, "Near-All Models in Large Eddy Simulations of Flow Behind a Backward-Facing Step," Annual Research Briefs 1996, Center for Turbulance Research, NASA Ames/Stanford University, pp. 199–210.
[17] Townsend, A. A., 1976, *The Structure of Turbulent Shear Flow*, Cambridge University Press, Cambridge, England.
[18] Bradshaw, P., 1967, "'Inactive' Motion and Pressure Fluctuations in Turbulent Boundary Layers," J. Fluid Mech., **30**, pp. 241–258.
[19] Piomelli, U., and Balaras, E., 2002, "Wall-Layer Models for Large-Eddy Simulations," Annu. Rev. Fluid Mech., **34**, pp. 349–374.
[20] Metzger, M. M., and Klewicki, J. C., 2001, "A Comparative Study of Near-Wall Turbulence in High and Low Reynolds Number Boundary Layers," Phys. Fluids, **13**, pp. 692–701.
[21] Hutchins, N., and Marusic, I., 2007, "Evidence of Very Long Meandering Features in the Logarithmic Region of the Turbulent Boundary Layer," J. Fluid Mech., **579**, pp. 1–28.
[22] Mathis, R., Hutchins, N., and Marusic, I., 2009, "Large-Scale Amplitude Modulation of the Small-Scale Structures in Turbulent Boundary Layers," J. Fluid Mech., **628**, pp. 311–337.
[23] Lumley, J. L., 1967, "The Structure of Inhomogeneous Turbulent Flows," *Atmospheric Turbulence and Radio Wave Propagation*, A. M. Iaglom and V. I. Tatarski, eds., Nauka, Moscow, pp. 221–227.
[24] Tomkins, C. D., and Adrian, R. J., 2005, "Energetic Spanwise Modes in the Logarithmic Layer of a Turbulent Boundary Layer," J. Fluid Mech., **545**, pp. 141–162.
[25] Orlandi, P., and Jiménez, J., 1994, "On the Generation of Turbulent Wall Friction," Phys. Fluids, **6**(2), pp. 634–641.
[26] Moin, P., and Moser, R., 1989, "Characteristic-Eddy Decomposition of Turbulence in a Channel," J. Fluid Mech., **200**, pp. 471–509.
[27] Podvin, B., and Lumley, J. L., 1998, "Reconstructing the Flow in the Wall Region From Wall Sensors," Phys. Fluids, **10**(5), pp. 1182–1191.
[28] Podvin, B., Fraigneau, Y., Lusseyran, F., and Gougat, P., 2006, "A Reconstruction for the Flow Past an Open Cavity," ASME J. Fluids Eng., **128**(3), pp. 531–541.
[29] Holmes, P., Lumley, J. L., and Berkooz, G., 1996, *Turbulence, Coherent Structures, Dynamical Systems and Symmetry*, Cambridge University Press, Cambridge, England.
[30] Pope, S., 2000, *Turbulent flows*, Cambridge University Press, Cambridge, England.
[31] Gadoin, E., Le Quéré, P., and Daube, O., 2001, "A General Methodology for Investigating Flow Instability in Complex Geometries: Application to Natural Convection and Enclosures," Int. J. Numer. Methods Fluids, **37**, pp. 175–208.

[32] Hirsch, C., 2006, *Numerical Computation of External and Internal Flows: Introduction to the Fundamentals of CFD*, Butterworth, Washington, DC.
[33] Podvin, B., and Lumley, J. L., 1998, "A Low-Dimensional Approach for the Minimal Flow Unit," J. Fluid Mech., **362**, pp. 121–155.
[34] Podvin, B., 2001, "On the Adequacy of the Ten-Dimensional Model for the Wall Layer," Phys. Fluids, **13**, pp. 210–224.
[35] Podvin, B., 2009, "A Pod-Based Model for the Wall Layer of a Turbulent Channel Flow," Phys. Fluids, **21**(1), pp. 015111.
[36] Germano, M., Piomelli, U., Moin, P., and Cabot, W., 1991, "A Dynamic Subgrid-Scale Eddy-Viscosity Model," Phys. Fluids A, **3**, pp. 1760–1766.
[37] Lilly, D. K., 1992, "A Proposed Modification of the Germano Subgrid Scale Closure Method," Phys. Fluids A, **4**, pp. 633–636.
[38] Marquillie, M., Laval, J.-P., and Dolganov, R., 2008, "Direct Numerical Simulation of Separated Channel Flows With a Smooth Profile," J. Turbul., **9**(1), pp. 1–23.
[39] Aubry, N., Holmes, P., Lumley, J. L., and Stone, E., 1988, "The Dynamics of Coherent Structures in the Wall Region of the Wall Boundary Layer," J. Fluid Mech., **192**, pp. 115–173.
[40] Jiménez, J., and Pinelli, A., 1999, "The Autonomous Cycle of Near-Wall Turbulence," J. Fluid Mech., **389**, pp. 335–359.
[41] Jiménez, J., del Álamo, J. C., and Flores, O., 2004, "The Large-Scale Dynamics of Near-Wall Turbulence," J. Fluid Mech., **505**, pp. 179–199.
[42] Rajaee, M., Karlsson, S., and Sirovich, L., 1995, "On the Streak Spacing and Vortex Roll Size in a Turbulent Channel Flow," Phys. Fluids, **7**(10), pp. 2439–2443.
[43] del Álamo, J. C., and Jiménez, J., 2006, "Linear Energy Amplification in Turbulent Channels," J. Fluid Mech., **559**, pp. 205–213.
[44] Hinze, J. O., 1976, *Turbulence*, McGraw-Hill, New York.
[45] Corino, E. R., and Brodkey, R. S., 1969, "A Visual Investigation of the Wall Region in Turbulent Flow," J. Fluid Mech., **37**, pp. 1–30.
[46] Robinson, S. K., 1991, "Coherent Motions in the Turbulent Boundary Layer," Annu. Rev. Fluid Mech., **23**, pp. 601–639.
[47] Jiménez, J., 2007, "Recent Developments on Wall-Bounded Turbulence," Rev. R. Acad. Cien. Exactas Fis. Nat. Ser. A Mat., **101**(2), pp. 187–203.
[48] Stanislas, M., Perret, L., and Foucaut, J. M., 2008, "Vortical Structures in the Turbulent Boundary Layer: A Possible Route to a Universal Representation," J. Fluid Mech., **602**, pp. 327–382.
[49] Tuktun, M., 2008, "Structures of Zero Pressure Gradient High Reynolds Number Turbulent Boundary Layers," Ph.D. thesis, Chalmers University of Technology, Sweden.
[50] Press, W. H., Teukolsky, S. A., Vettering, W. T., and Flannery, B. P., 1992, *Numerical Recipes in Fortran*, Cambridge University Press, Cambridge, England.
[51] Hamilton, J. M., Kim, J., and Waleffe, F., 1995, "Regeneration Mechanisms of Near-Wall Turbulence Structures," J. Fluid Mech., **287**, pp. 317–348.

Review of Hydraulic Roughness Scales in the Fully Rough Regime

Karen A. Flack
Department of Mechanical Engineering,
United States Naval Academy,
Annapolis, MD 21402
e-mail: flack@usna.edu

Michael P. Schultz
Department of Naval Architecture and Ocean Engineering,
United States Naval Academy,
Annapolis, MD 21402
e-mail: mschultz@usna.edu

A review of predictive methods used to determine the frictional drag on a rough surface is presented. These methods utilize a wide range of roughness scales, including roughness height, pitch, density, and shape parameters. Most of these scales were developed for regular roughness, limiting their applicability to predict the drag for many engineering flows. A new correlation is proposed to estimate the frictional drag for a surface covered with three-dimensional, irregular roughness in the fully rough regime. The correlation relies solely on a measurement of the surface roughness profile and builds on previous work utilizing moments of the surface statistics. A relationship is given for the equivalent sandgrain roughness height as a function of the root-mean-square roughness height and the skewness of the roughness probability density function. Boundary layer similarity scaling then allows the overall frictional drag coefficient to be determined as a function of the ratio of the equivalent sandgrain roughness height to length of the surface.
[DOI: 10.1115/1.4001492]

1 Introduction

The most important unresolved issue regarding surface roughness in fluids engineering practice is how frictional drag (for external flows) or pressure drop (for internal flows) relates to the particular roughness topography. In other words, which roughness length scales best typify a surface hydraulically? Researchers have been working on this problem since the early experimental work of Nikuradse [1] and Colebrook [2]. However, most previously proposed roughness scales, discussed in detail later in this paper, are not sufficiently robust and are valid only for regular roughness or for a limited range of roughness types. What is needed in engineering practice is some means of relating the rough surface waveform to its frictional drag. In recent years, direct numerical simulations (DNS) have further elucidated the understanding of the underlying flow physics on rough walls (e.g., Refs. [3–5]). To date, however, DNS computations have been limited to idealized roughness types at a limited Reynolds number range, making them incapable of resolving issues regarding appropriate scaling for irregular three-dimensional roughness. Therefore, the need for accurate predictive correlations in engineering practice remains.

One of the most commonly employed fluids engineering tools is the Moody [6] diagram. This useful diagram relates the pressure drop in a pipe to the relative roughness (i.e., the ratio of the roughness height to the pipe diameter) and the Reynolds number. Moody developed the diagram to be used for naturally occurring roughness based on the results of Colebrook [2] for smooth and rough pipe flow. However, recent results by Allen et al. [7] and Langelandsvik et al. [8] show that the Moody diagram significantly overestimates the pressure drop in the transitionally rough flow regime for honed and commercial steel pipes, respectively. This clearly indicates that the Colebrook roughness function used in the formulation of the Moody diagram may not be applicable to a wide range of roughness of engineering interest. Fortunately, from an engineering standpoint, the Moody diagram likely gives a conservative estimate of pressure drop for a given roughness in the transitionally rough regime.

A more important issue regarding the Moody diagram is defining the appropriate roughness length scale to use as the roughness height. The diagram was developed using the equivalent sandgrain roughness height k_s [1]. However, k_s for a generic roughness cannot be accurately assigned a priori and must be determined experimentally. The roughness values listed on the diagram for copper, galvanized steel, etc., were determined from fitting a roughness height to match a measured pressure drop from an experiment, or in other words, determining k_s. The question then is how the height listed on the diagram relates to a physical roughness length scale measured from surface topography. This is especially pertinent since many of the manufactured surfaces listed on the Moody diagram do not have a consistent roughness. For example, some surfaces are listed with a roughness height that spans an order of magnitude. Additionally, the equivalent sandgrain roughness height is unknown for numerous other surfaces of engineering interest. As a result, one can only expect to obtain accurate results using the Moody diagram if k_s is known for the surface of interest and the flow is fully rough.

The naval architecture community includes the effects of surface roughness (e.g., paint, corrosion, and fouling) in an allowance coefficient, which is added to the smooth surface friction and residual (wave making) resistance coefficients when determining the overall drag of a full scale ship [9]. The International Towing Tank Committee [10] adopted the allowance coefficient of Bowden and Davison [11] to be used with the 1978 ITTC performance prediction line for ship resistance. This coefficient is a function of the mean hull roughness, the average peak-to-trough roughness height measured over 50 mm sampling lengths on the hull surface, as compared with the ship length. This equation, however, is not an accurate hull roughness penalty predictor since it includes additional residual components of resistance prediction, including model scale effects [12]. Townsin et al. [13] provided a formula for predicting the roughness penalty based on the mean hull roughness and the Reynolds number. While the inclusion of a Reynolds number dependence allows for calculations in the transitionally rough regime, the roughness parameter is still only based on a simple measure of the roughness height and does not account for other roughness texture characteristics. These considerations, along with a lack of accurate hull roughness measurements, led the ITTC Specialist Committee on Powering Performance Prediction [12] to conclude in 2005 that the methods used to correct for hull roughness and fouling are of doubtful accuracy.

Computational fluid dynamics (CFD) has generally represented rough surfaces by a smooth surface with modified boundary conditions or near wall equations. Discrete roughness models include

Contributed by the Fluids Engineering Division of ASME for publication in the JOURNAL OF FLUIDS ENGINEERING. Manuscript received July 3, 2009; final manuscript received March 12, 2010; published online April 20, 2010. Assoc. Editor: James A. Liburdy.

roughness as an additional drag term in the near wall momentum equations. Using this approach, the effect of roughness is confined to the near wall mean flow, not influencing the outer layer turbulence. Alternately, roughness can be accounted for in the turbulence by modifying the eddy viscosity models [14]. In this approach, a wall offset is included in the mixing length model that produces a nonzero eddy viscosity at the wall. The mean flow log region extends to this new origin. The amount of wall offset is a function of an empirically determined hydraulic roughness length. For the two layer approach, the wall layer model is patched to the outer layer model by modifying the k boundary condition in the $k-\varepsilon$ model, and the ω boundary condition in the $k-\omega$ model [15]. In the fully rough regime, the proposed $k-\varepsilon$ [16] and $k-\omega$ [17] models do not require a wall function since the log layer extends all the way to the wall. The common feature of all the models is an empirically determined term to accurately account for the roughness. Predictive correlations for a wide range of rough surfaces would provide computational models the necessary roughness length scale.

The development of more accurate predictive correlations relies on a robust database of experimental results that have accurate frictional loss data and detailed surface topography information. The approach taken in the present research is to expand on previous work that uses statistical moments of the surface profile, including a wider range of three-dimensional roughness. Successful correlation of the momentum deficit due to roughness with surface statistics will provide a method of drag prediction based solely on the surface roughness topography.

2 Background

The velocity deficit due to roughness has been represented in a variety of ways, based on the smooth wall log-law profile. Equation (1) represents the effect of roughness by the roughness function ΔU^+ or the downward shift in the log-law profile

$$U^+ = \frac{1}{\kappa}\ln y^+ + B - \Delta U^+ \tag{1}$$

where κ is the von Kármán constant and B is the intercept for a smooth wall. This can also be recast into a relative roughness form, Eq. (2), where k is a measure of the roughness height.

$$U^+ = \frac{1}{\kappa}\ln\frac{y}{k} + B - \Delta U^+ + \frac{1}{\kappa}\ln k^+ \tag{2}$$

Atmospheric boundary layer analyses generally represent roughness by a roughness length scale y_0, which matches the smooth wall log-law profile, as shown in Eq. (3). In this equation, d is the zero-plane displacement, or the distance below the top of the roughness where the mean flow is zero.

$$U^+ = \frac{1}{\kappa}\ln\left(\frac{y-d}{y_0}\right) \tag{3}$$

Equation (3) is only valid in the fully rough regime; thus y_0 is an alternate scale that is similar to the equivalent sandgrain roughness height k_s, forcing collapse to a single profile in the fully rough regime.

Figure 1 shows typical rough wall boundary layer profiles and the corresponding roughness functions. The results presented are from Flack et al. [18] for flows over sandgrain and mesh roughness. The roughness heights for these surfaces are a significant fraction of the boundary layer thickness, resulting in large roughness functions. Similar roughness functions are obtained for the mesh and sandgrain surfaces at approximately the same unit Reynolds number even though the roughness heights differ substantially. This indicates that the roughness height alone is not adequate to scale the momentum deficit resulting from surface roughness.

If the shapes of the mean profile in the overlap and outer region of the boundary layer are similar for smooth and rough walls, then

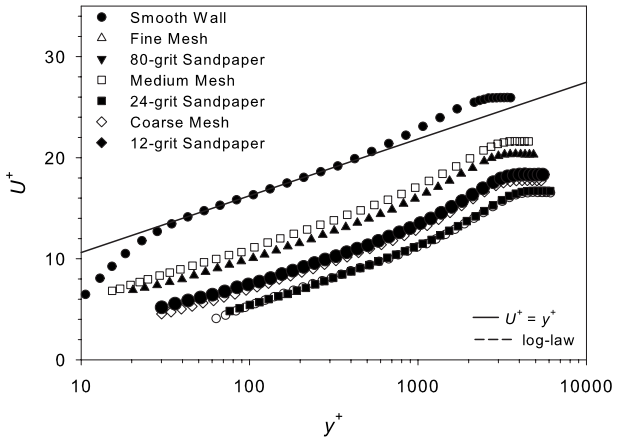

Fig. 1 Mean velocity profiles for mesh and sandpaper surfaces from Ref. [18]

the roughness function can also be expressed as the difference in skin friction for the smooth wall C_{fS} and the rough wall C_{fR}, at the same displacement thickness Reynolds number (Re_{δ^*}) as proposed by Hama [19] and shown in

$$\Delta U^+ = \left(\sqrt{\frac{2}{C_f}}\right)_S - \left(\sqrt{\frac{2}{C_f}}\right)_R = U^+_{eS} - U^+_{eR} \tag{4}$$

This allows roughness function results from rough surfaces obtained in the laboratory to be scaled up to full scale using the same outer layer similarity arguments. Mean flow similarity can be demonstrated through collapse of smooth and rough wall data when plotted in a velocity-defect form. Similarity has been experimentally verified by a number of researchers (e.g., Refs. [20–23]) including the present authors for a wide range of roughness types [18,24–28]. A representative velocity-defect plot from Flack et al. [18] for mesh and sandgrain roughness is shown in Fig. 2.

Ideally, the roughness function could be determined using a correlation based on a physical measure of the surface roughness instead of having to rely on laboratory hydrodynamic tests. The challenge is to determine the proper scales obtained from surface measurements that effectively correlate with the roughness function for a wide range of roughness types. Figure 3 shows the relationship between the roughness function and the roughness height for a variety of surfaces. For comparison, the uniform sandgrain roughness results of Nikuradse [1] are also presented. Three flow regimes are observed in Fig. 3. When the roughness Reynolds number k^+ is small, the flow is hydraulically smooth (i.e., $\Delta U^+=0$). In this case the perturbations generated by the roughness elements are completely damped out by the fluid vis-

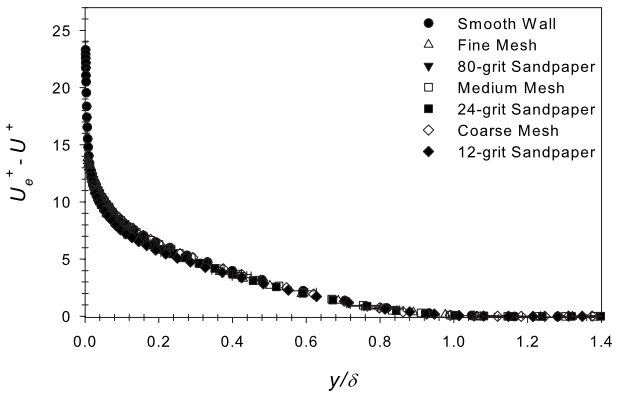

Fig. 2 Mean velocity profiles in velocity-defect form from Ref. [18]

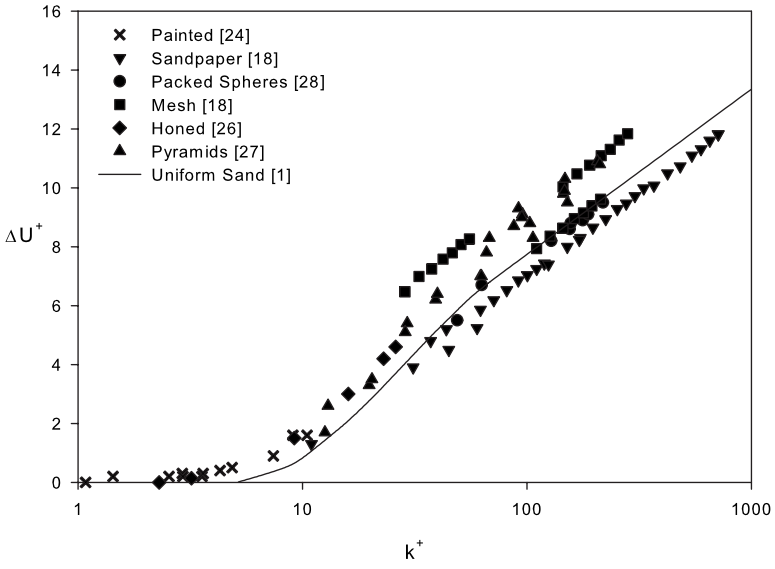

Fig. 3 Roughness function results for a variety of rough surfaces

cosity, creating no additional drag. As k^+ increases, the flow becomes transitionally rough. In the transitionally rough regime, viscosity is no longer able to damp out the turbulent eddies created by the roughness elements and form drag on the elements, as well as the viscous drag, contributes to the overall skin friction. As k^+ increases further, the roughness function reaches a linear asymptote. This asymptotic region at large values of k^+ is the fully rough regime. In this regime, the skin friction coefficient is independent of Reynolds number, and form drag on the roughness elements is the dominant mechanism responsible for the momentum deficit.

In Fig. 3, the peak-to-trough roughness height is used as the roughness scale. A common roughness scale in literature is the equivalent sandgrain roughness height k_s. This is the roughness height that produces the same roughness function as the uniform sandgrain of Nikuradse in the fully rough regime. Using the equivalent sandgrain roughness height as the roughness height in Eq. (2), and the log-law intercept for a uniform sandgrain surface in relative roughness form ≈ 8.5 (Eq. (2)), k_s can be determined for a given roughness from its roughness function ΔU^+ in the fully rough regime using the following relationship:

$$B - \Delta U^+ + \frac{1}{\kappa} \ln k_s^+ = 8.5 \tag{5}$$

The equivalent sandgrain roughness height is then used as the scale in Fig. 4. As expected, all surfaces asymptote to the same line in the fully rough regime. It should be noted, however, that k_s^+ is unable to collapse the surfaces in the transitionally rough regime. Figures 3 and 4 highlight the fact that a single measure of the roughness height, i.e., k, k_s, and k_{rms}, is not able to collapse the roughness function results in all regimes for a range of surfaces.

A number of questions remain regarding the relationship between the roughness Reynolds number and the roughness function for a generic roughness. The value of k^+ (or k_s^+) when the surface

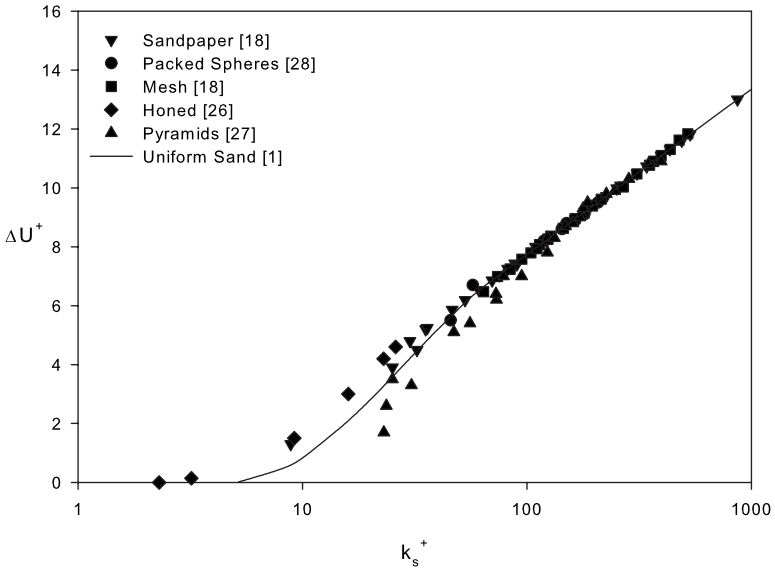

Fig. 4 Roughness function results for a variety of rough surfaces using k_s

roughness ceases to be hydraulically smooth has been shown to be a function of the roughness type. Second, the shape of the roughness function in the transitionally rough regime varies depending on the roughness type and is not known for most surfaces. Additionally, the value of k^+ that defines the onset of the fully rough regime is unknown for most roughness types. The transitionally rough regime has previously been defined as $5<k_s^+<70$, based on the uniform sandgrain results of Nikuradse [1]. However, a wide range of values has been reported in literature for other roughness types. Ligrani and Moffat [29] reported that the transitionally rough regime spans $15<k_s^+<50$ for a packed sphere bed. This range is reported as $3.5<k_s^+<30$ for honed pipe roughness by Shockling et al. [30] and is given by the present authors [26] as $2.5<k_s^+<25$ for a similar surface created by surface scratches. Langelandsvik et al. [8] indicated that the range of the transitionally rough regime is $1.4<k_s^+<18$ for a commercial steel pipe. Lewkowicz and Musker [31] found that the onset of the fully rough regime ranged from $k_{\mathrm{rms}}^+=17$ to 40 for ship-hull roughness. These disparate results for various roughness types clearly illustrate the difficulty of identifying scaling parameters that are applicable in both the transitionally and fully rough regimes. As illustrated in Fig. 4, collapse in the fully rough regime at high Reynolds numbers does not ensure that the transitionally rough regime has been properly captured. In fact, Clauser [32] discussed the difficulty of finding a roughness scale in the transitionally rough regime stating that some roughness types produce roughness functions with a monotonically changing slope while others have inflection points.

3 Previously Proposed Roughness Function Correlations

The development of correlations for the roughness function has been an area of active research for many years. Correlations range from simple models based on roughness height and pitch to more complicated relationships that include density and shape parameters, as detailed below.

Bettermann [33] proposed a functional relationship between the rough wall log-law intercept and a roughness spacing parameter λ, where λ=pitch/height of 2D transverse bars, as shown in Eq. (6), for the range of λ listed.

$$f(\lambda)=B-\Delta U^+ +\frac{1}{\kappa}\ln k^+ = 17.35(1.165\log_{10}\lambda-1), \quad 1\le\lambda\le 5 \tag{6}$$

Dvorak [34] modified this relationship, using a density parameter, λ=total surface area/total roughness area, which is equivalent to the spacing parameter of Bettermann for square bars. Dvorak added another relationship, which extends the range of applicability for more sparse roughness as follows:

$$f(\lambda)=17.35(1.165\log_{10}\lambda-1) \quad 1\le\lambda\le 4.68$$

$$f(\lambda)=-5.95(1.103\log_{10}\lambda-1) \quad \lambda>4.68 \tag{7}$$

These correlations were developed using sandgrain surfaces [1,35,36], mesh screens [19], staggered rows of spheres [37], and square bars [33]. Simpson [38] modified the parameter further using λ_k=total surface area/total roughness frontal area normal to the flow, showing reasonable agreement for spheres and cones [39], staggered hemispheres [40], and machined groves [41].

Dirling [42] introduced a combined density and shape parameter Λ. Roughness density is included as the ratio of the average element spacing d to roughness height k, whereas shape is accounted for in the frontal area of a single roughness element A_f and the windward wetted surface area of a single roughness element A_s.

$$\Lambda=\left(\frac{d}{k}\right)\left(\frac{A_f}{A_s}\right)^{-4/3} \tag{8}$$

Dirling provided correlations for the ratio of the equivalent sandgrain roughness height k_s, to roughness height k, for two-dimensional square rods, hemispheres, spheres, cones, right angles, as well as Nikuradse sand.

$$\frac{k_s}{k}=0.0164\Lambda^{3.78}, \quad \Lambda\le 4.93$$

$$\frac{k_s}{k}=139\Lambda^{-1.90}, \quad \Lambda>4.93 \tag{9}$$

Sigal and Danberg [43] introduced the effect of roughness density in a different manner, including S, the reference surface area before adding roughness, and S_f, the total frontal area of the roughness.

$$\Lambda_s=\left(\frac{S}{S_f}\right)\left(\frac{A_f}{A_s}\right)^{-1.6} \tag{10}$$

The following correlations were provided for two-dimensional transverse roughness including bars, rods, and ribs.

$$\frac{k_s}{k}=0.00321\Lambda_s^{4.925}, \quad 1.400\le\Lambda_s\le 4.890$$

$$\frac{k_s}{k}=8, \quad 4.890\le\Lambda_s\le 13.25$$

$$\frac{k_s}{k}=151.711\Lambda_s^{-1.1379}, \quad 13.25\le\Lambda_s\le 100 \tag{11}$$

van Rij et al. [44] expanded the use of this parameter to three-dimensional regular roughness, using the results of Schlichting [39] for staggered patterns of spheres, spherical segments, and cones. The data used incorporated the corrections given in Ref. [45]. The correlations for three-dimensional roughness are listed as follows:

$$\frac{k_s}{k}=1.583\times 10^{-5}\Lambda_s^{5.683}, \quad \Lambda_s<7.842$$

$$\frac{k_s}{k}=1.802\Lambda_s^{0.03038}, \quad 7.842\le\Lambda_s\le 28.12$$

$$\frac{k_s}{k}=255.5\Lambda_s^{-1.454}, \quad \Lambda_s>28.12 \tag{12}$$

van Rij et al. [44] also tested irregular, three-dimensional roughness and applied a modified version of the roughness parameter, defined as

$$\Lambda_s=\left(\frac{S}{S_f}\right)\left(\frac{S_f}{S_s}\right)^{-1.6} \tag{13}$$

where S, S_f (as defined by Sigal and Danberg [43]), and S_s, the total windward wetted surface area, are calculated numerically based on detailed surface profiles. The equivalent sandgrain roughness is determined from the correlations developed for three-dimensional regular roughness, Eq. (12), using this modified roughness parameter and k_{avg}, the average roughness height. Experimental results for two rough surfaces were used to test the correlation: one completely covered by the roughness and one where rough regions of the surface alternate with smooth regions. The predicted skin friction, using the calculated values of k_s, compared well to experimentally results obtained from the pressure drop in a channel.

Additional three-dimensional roughness predictive correlations were presented by Waigh and Kind [46]. Their relationships were based on the results for a variety of roughness element shapes

including cubes, blocks, flat plates, cylinders, rods, cones, spheres, and hemispheres. They expressed the effect of roughness as a log-law shift C (Eq. (14)), using a similar form of the law of the wall as Eq. (2).

$$U^+ = \frac{1}{\kappa}\ln\frac{y}{k} + B - \Delta U^+ + \frac{1}{\kappa}\ln k^+ = \frac{1}{\kappa}\ln\frac{y}{k} + B - C \tag{14}$$

The element distribution is characterized by a density parameter Λ_k, which modifies the density parameter of Simpson [38] λ_k, with the streamwise aspect ratio k/s_m, where k is the roughness height and s_m is the streamwise roughness length.

$$\Lambda_k = \lambda_k \frac{k}{s_m} \tag{15}$$

The following relationships were presented for two density regimes:

$$C = 10.56\log_{10}\left[\lambda_k\left(\frac{k}{b_m}\right)^{0.87}\left(\frac{A_w}{A_f}\right)^{0.44}\right] - 7.59, \quad \Lambda_k < 6$$

$$C = -5.75\log_{10}\left[\lambda_k\left(\frac{k}{b_m}\right)^{0.55}\left(\frac{A_w}{A_f}\right)^{1.38}\right] + 5.78, \quad \Lambda_k > 6 \tag{16}$$

where A_w is the roughness wetted area, A_f is the projected frontal area, and b_m is the spanwise roughness length. Waigh and Kind discussed the fact that the relationships were obtained for simple roughness element shapes in regular patterns and stressed the need to find ways to parametrize the geometry of natural roughness.

Turbine blade roughness that included surfaces with pitting, erosion, and deposits was studied by Bons [47]. Bons also adapted the Sigal and Danberg parameter for irregular roughness to calculate the equivalent sandgrain roughness for the surfaces as follows:

$$\log\left(\frac{k_s}{k}\right) = -1.31\log(\Lambda_s) + 2.15 \tag{17}$$

The surface parameters were determined numerically from detailed surface profiles, with the roughness height k, taken as the average of the local peak-to-trough roughness height for smaller subregions. The skin friction correlation using k_s proposed by Schlichting [39] fits the experimental data best.

Many of the proposed correlations are valid for two- and three-dimensional regular roughnesses, including bars, blocks, cones, hemispheres, etc. Determining the required shape and density parameters for an idealized roughness is a relatively straightforward procedure. Extending this work to naturally occurring, irregular roughness is more challenging due to potentially complex surface features. While it is possible to determine the required shape and density parameters for irregular, three-dimensional roughness [44,47], complex numerical fitting procedures are needed. A simpler method of utilizing the surface topography map would be useful for predicting frictional drag due to roughness in a wider range of engineering applications.

Correlations that relate the statistical moments of the surface profile with the frictional drag or roughness function have been offered by various investigators. Musker [48] proposed an effective roughness height to correlate the roughness function $\Delta U^+ = f(k^+)$, as shown in

$$k^+ = \frac{kU_\tau}{\nu} = \frac{k_{\text{rms}}U_\tau}{\nu}(1 + as_p)(1 + bs_k k_u) \tag{18}$$

where k_{rms} is the standard deviation, s_k is the skewness, k_u is the kurtosis of the surface elevation distribution, and s_p is the average slope of the roughness elements. The constants a and b were empirically chosen to collapse the data of naturally occurring surfaces. This effective roughness height was reasonably successful in collapsing the roughness function for pipes covered with positive replicas of ship-hull roughness. Musker cautioned that the cut-off wavelength used to characterize the surface should depend on the size of the roughness elements since the sizes of the turbulent eddies near the surface are a function of the longest surface wavelength. He proposed the use of the Taylor integral microscale [49] as the cut-off for the longest wavelength and two orders of magnitude lower for the smallest wavelengths.

Medhurst [50,51] reported correlations for painted ship roughness based on a parameter C_1h, which he called the hydrodynamic roughness number, having units of roughness height. Medhurst used the following form of the roughness function:

$$\Delta U^+ = \frac{1}{\kappa}\ln\left[\frac{C_1}{B_1}\frac{hU\tau}{\nu} + C_2\right] \tag{19}$$

where B_1 is found using an alternate form of the smooth wall log-law intercept

$$B = \frac{1}{\kappa}\ln[B_1] \tag{20}$$

Utilizing the linearized form of Eq. (20) along with experimental data, a regression analysis can be performed to determine C_1h and C_2.

$$B_1 e^{\kappa\Delta U^+} = (C_1h)\left(\frac{U_\tau}{\nu}\right) + B_1C_2 \tag{21}$$

If the surface is assumed to follow a Colebrook form of the roughness function (i.e., monotonic), then $C_2 = 1.0$ and ΔU^+ is only a function of C_1h. Medhurst presented different values of the hydrodynamic roughness number for three types of ablative paints. Medhurst also cautioned on the use of cut-off wavelengths and other filtering techniques, as well as spatial resolution issues that can bias results and reject important surface information.

Townsin and Dey [52] utilized the moments of the roughness amplitude energy spectral density, incorporating a variable long wavelength cut-off, to determine the roughness function for painted ship surfaces. The height of the roughness is represented by the spectral area m_0, the slope by the second moment m_2, and the range of frequencies composing the roughness profile by a bandwidth parameter $\alpha = m_0m_4/m_2^2$. Based on the results for 26 ship paint surfaces, the best correlation between the roughness function ΔU^+ and the roughness height k is shown in

$$k \propto \sqrt{\alpha m_0 m_2} = \sqrt{\frac{m_0^2 m_4}{m_2}} \tag{22}$$

While this technique shows promise, significant scatter was present using this correlation in the fully rough regime while the correlation did not collapse the data in the transitionally rough regime.

The correlations presented have demonstrated some utility in collapsing experimental data for a subset of rough surfaces, but they yield a high degree of variance when applied to a larger range of three-dimensional roughness types. Furthermore, many of the correlations are difficult to apply to irregular, three-dimensional roughness. The approach taken in the present research has been to expand on the previous work using statistical moments of the surface profile, including a wider range of three-dimensional roughness. Successful correlation of the roughness function with surface statistics will provide a method of drag prediction based solely on the surface roughness.

4 Full Scale Prediction Methods

Roughness function results for rough surfaces obtained in the laboratory can be scaled up to full scale using outer layer similarity arguments. Thus, knowing $\Delta U^+ = f(k^+)$ allows for the frictional drag of a full scale rough surface to be determined. If the equivalent sandgrain roughness k_s is taken as the roughness scale, then this functional relationship is valid for all roughness in the fully

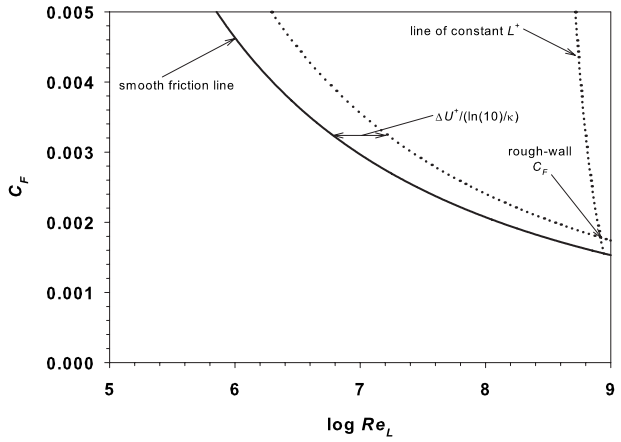

Fig. 5 Scaled-up procedure from $C_{F\ \text{smooth}}$ to $C_{F\ \text{rough}}$

rough regime provided k_s is properly specified. Schultz [53] detailed the similarity methods used to determine the overall frictional resistance coefficient C_F for rough wall boundary layer flow over a flat plate of length L if the roughness function ΔU^+ is known. The methodology incorporates the analysis of Granville [54,55] and relies on outer layer similarity in the mean flow for smooth and rough walls, as demonstrated in the velocity-defect profiles shown in Fig. 2. A graphical representation of the scaling procedure is shown in Fig. 5. Here, the smooth wall overall frictional drag coefficient C_F is plotted as a function of $\log_{10}(\mathrm{Re}_L)$ using the Karman–Schoenherr [56] friction line as follows:

$$\sqrt{\frac{2}{C_F}} = \frac{1}{\kappa}\ln(\mathrm{Re}_L\ C_F) \tag{23}$$

The rough surface overall frictional resistance coefficient for a known roughness function is determined by displacing the smooth friction line by a distance $\Delta U^+\kappa[\ln(10)]^{-1}$ in the positive $\log_{10}(\mathrm{Re}_L)$ direction. For a given plate length L, a line of constant $L^+=LU_\tau\nu^{-1}$, which satisfies the following relationship, is plotted:

$$\mathrm{Re}_L = \frac{L^+}{\sqrt{\frac{C_F}{2}}\left(1-\frac{1}{\kappa}\sqrt{\frac{C_F}{2}}\right)} \tag{24}$$

The intersection of this line and the rough surface line identifies C_F for the rough plate at a single value of Re_L for a given ΔU^+.

If this process is repeated for a range of ΔU^+ and L, the overall frictional resistance coefficient can be mapped out. If the relationship $\Delta U^+=f(k_s^+)$ is used to account for the roughness, then this diagram is valid for all roughness in the fully rough regime provided k_s is known. This is shown in Fig. 6, as a "Moody" type diagram, where the overall frictional drag coefficient is presented as function of the ratio of k_s to the overall length of the plate L. In the fully rough regime the relationship can be expressed as the following formula:

$$\sqrt{\frac{2}{C_F}} = -2.186\ln\left(\frac{k_s}{L}\right) + 0.495 \tag{25}$$

With an estimated 10% uncertainty in ΔU^+ at 95% confidence, the resulting uncertainty in the overall frictional drag coefficient C_F is 2% for $k_s/L=0.001$, decreasing to less than 1% for $k_s/L=0.00001$.

On the diagram, it is assumed that the onset of the fully rough regime occurs at $k_s^+=70$, based on the uniform sandgrain results of Nikuradse. As noted previously, the onset of the fully rough regime is highly dependent on the specific roughness and likely occurs at lower values of k_s^+ for many types engineering roughness. Additional measurements that span the transitionally rough regime are needed to determine the important scales for predicting when a surface becomes fully rough. With the relationship given in Eq. (25), the frictional drag on a planar surface can be determined by identifying roughness scales that accurately predict k_s. It should also be noted that the roughness function could also be incorporated in CFD models and used to calculate the frictional drag of an arbitrary body covered with the given roughness.

5 Development of a New Roughness Correlation

The development of a roughness function correlation is restricted here to flows in the fully rough regime. In this regime, a larger number of experimental results are available, and it is possible to collapse all roughness functions to a single line if the equivalent sandgrain roughness height k_s is used as the roughness

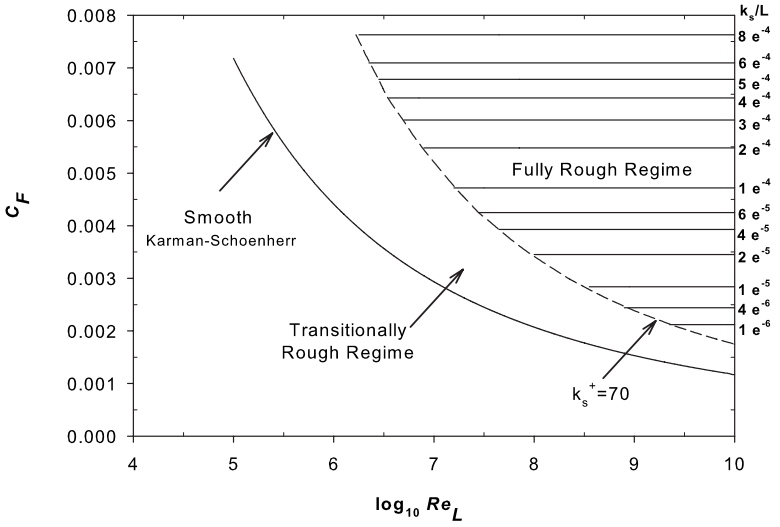

Fig. 6 Overall frictional drag coefficient in the fully rough regime

Table 1 Surfaces used in predictive correlation for k_s

Surface	Ref.	k_t (μm)	k_{rms} (μm)	s_k	k_u	k_s actual (μm)	k_s predicted (μm)	% diff
Sandpaper—80 grit	[18]	546	67.9	0.497	4.49	529	522	1.3
Sandpaper—24 grit	[18]	1291	167	0.719	4.06	2626	1954	25.6
Sandpaper—12 grit	[18]	2466	320	1.51	6.17	6354	6512	2.5
Packed spheres	[28]	824	199	0.212	1.90	876	1146	30.8
Packed spheres with grit	[28]	738	158	0.315	2.22	1097	1018	7.2
Honed (scratch)	[26]	193	26.4	−0.455	3.63	71.0	51.0	28.2
Honed pipe	[30]	15.96	2.5	0.31	4.05	7.5	16.0	113
Commercial pipe	[8]	27.27	5.0	−0.19	2.53	8.0	16.5	106
Gravel—medium	[23]	3079	605	0.618	3.43	5383	5167	4.0
Gravel—coarse	[23]	7350	1490	0.0305	2.46	6785	6875	1.3
Pyramid—A1	[27]	304.8	72.1	0.566	2.40	510	589	15.5
Pyramid—A2	[27]	457.2	108	0.566	2.40	706	883	25.1
Pyramid—A3	[27]	609.6	144	0.566	2.40	1301	1177	9.5
Pyramid—B1	[27]	304.8	72.1	0.566	2.40	540	589	9.1
Pyramid—B2	[27]	457.2	108	0.566	2.40	577	883	53.0
Pyramid—B3	[27]	609.6	144	0.566	2.40	1012	1177	16.3

scale. This scale understandably has its limitations since it is not intrinsically related to roughness topography. The advantage of k_s is that it provides a "common currency" among different roughness types as pointed out by Bradshaw [57]. Here an investigation is made into which physical roughness scales, if any, effectively correlate with k_s. This study was conducted using the results from a variety of three-dimensional rough surfaces, listed in Table 1. Numerous other researchers have measured the roughness function in the fully rough regime for other surfaces. However, only results that also report detailed surface topographical measurements have been included.

A sample three-dimensional topographical map for the honed surface of Schultz and Flack [26] is shown in Fig. 7. This surface was profiled using a CyberOptics laser diode point range sensor laser profilometer system. The vertical accuracy of the sensor is 1 μm with a laser spot diameter of 10 μm. The data were digitized at increments of 25 μm in the lateral directions, and the sampling area was 5×5 mm^2. The other surfaces of the present authors [18,24,27], as well as the surfaces of Castro [23], were profiled using the MicroPhotonics Nanavea ST300 white light chromatic aberration surface profilometer. The vertical accuracy of this system is 0.3 μm with a lateral resolution of 6 μm. Five replicate surface profiles were gathered on each of these surfaces as well as the surface shown in Fig. 7. The sampling interval was 25 μm, and the sampling length was 50 mm. The surface statistics and roughness parameters, listed in Table 1, were calculated as the mean value from the replicate profiles. The data were not filtered to remove short or long wavelength roughness components. However, long wavelength or "wavy" roughness has not been included in this study. Expanding on the work of Napoli et al. [58], Schultz and Flack [27] determined that roughness with an effective slope ES less than approximately 0.35 does not scale on the roughness height. The relationship for the effective slope is shown in

$$\mathrm{ES} = \frac{1}{L_s}\int_{L_s}\left|\frac{\partial r}{\partial x}\right| dx \tag{26}$$

Filtering, sampling interval, and sampling length can all have a significant effect on roughness statistics as pointed out by Medhurst [51] and Howell and Behrends [59]. This was not a primary focus in the present study. The practical difficulty in addressing the effect of these parameters is that not all surfaces were profiled using the same sampling interval and length. Specifying the most appropriate sampling interval, sampling length, and filtering length is quite complex and can be expected to depend at least to some extent on the inner and outer length scales of the flow in question. This point underlines the need for the adoption of a consistent method of measuring hydraulic surface roughness, as was highlighted by Howell and Behrends [59].

Common surface statistical parameters, as well as the wide

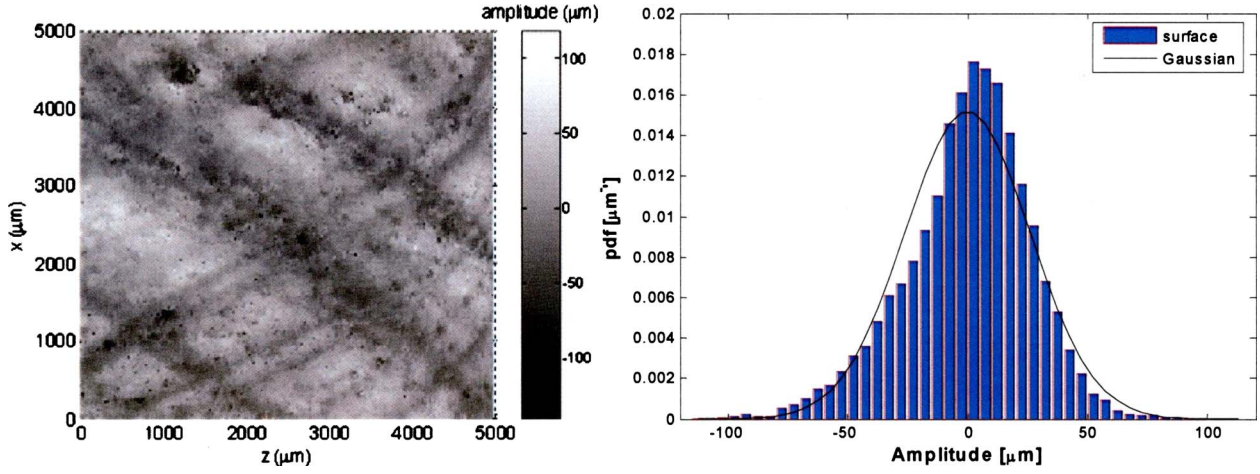

Fig. 7 Surface topography map and pdf of *r*, distance above the mean roughness elevation, for a honed surface

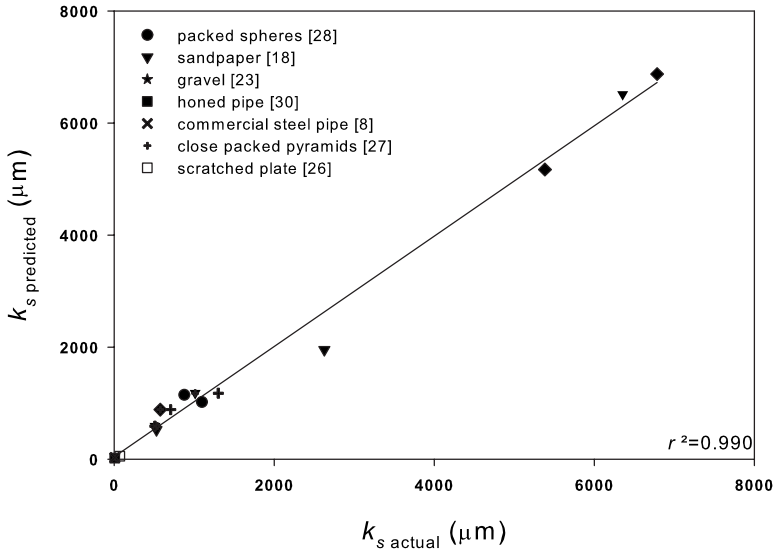

Fig. 8 Predicted k_s versus actual k_s using Eq. (27)

range of other roughness scaling parameters reviewed previously in this paper, were investigated as candidate hydraulic scales. This was done using a series of statistical correlations between the candidate hydraulic scales and the measured equivalent sandgrain roughness height k_s for the surface. This analysis indicated that the root-mean-square roughness height scale ($k_{\rm rms}$) and the skewness of the roughness surface elevation probability density function (pdf) (s_k) had the strongest correlations with k_s. Based on this observation, it was decided to develop a single length-scale correlation using both of these parameters. A number of different functional forms were considered. The function that best correlates the present data (Table 1) is given in Eq. (27) and graphically represented in Fig. 8.

$$k_s = f(k_{\rm rms}, s_k) \approx 4.43 k_{\rm rms}(1 + s_k)^{1.37} \tag{27}$$

In Fig. 8, k_s actual was determined using Eq. (8) for an experimentally determined value of ΔU^+ with $B=5.0$ and $\kappa=0.41$ in the fully rough regime. The surfaces used in this correlation along with some of their roughness statistics are shown in Table 1. The skewness is a quantitative way of describing whether the roughness has more peaks or valleys. A roughness with isolated large peaks will have a high positive skewness. Surfaces that have become rough due to deposits of roughness elements (i.e., exhaust particulates, biological fouling, etc.) will generally have positively skewed pdf's. A surface that is pitted (i.e., corrosion, surface wear, etc.) will have negatively skewed pdf's. It should be cautioned that only two surfaces used in the present correlation had a negative skewness, and both are relatively mild. The correlation, given in Eq. (27), has an additive constant of 1. This means that the present correlation would be undefined for $s_k \leq -1$. This constant was chosen in order to define a predictive correlation that is near the range of the parameter space that was investigated. It should be noted that using a larger additive constant would change the other constants in Eq. (27) but would not significantly reduce the goodness of fit. However, further data for surfaces with negative s_k are needed to validate and refine this correlation for a larger range of the parameter space. Nevertheless, Fig. 8 shows the linear correlation between the predicted value of k_s using the correlation and the measured k_s. The goodness of fit is excellent with $r^2=0.990$.

Table 1 also lists the difference between the measured and predicted values of the k_s. The correlation works very well for the sandgrain, sanspray (gravel), and packed spheres covered with grit. This indicates that the correlation would do an excellent job of predicting the equivalent sandgrain roughness height for large ($k_s > 500$ μm) naturally occurring type roughness. The only exception is the 24 grit sandpaper surface. However, even with a 26% difference in the predicted k_s from the measured value for the 24 grit sandpaper, the predicted overall drag coefficient $C_F=0.00773$ is only 6.5% in error from values measured in tow tank tests $C_F=0.00826$ [60].

Considering the percent error from the expected value, the correlation does not adequately predict the small values of k_s for the honed and commercial steel pipes. This is not surprising due to the nature of the fitting where the sum of the square of the residual is being minimized. This will bias the best fit toward the larger roughness where the absolute value of the difference is larger even though the relative difference is smaller. Using the results of Shockling et al. [30], a 113% difference in the predicted value of k_s yields an error in friction factor of approximately 30%. Therefore, the correlation presented may not be adequate for all the roughness considered. However, it appears that the important scales for better predictive correlations are the root-mean-square roughness height and the skewness of the surface elevation pdf. It should be noted that this is a sparse data set to base a predictive correlation. Unfortunately, experimentally obtaining the roughness function for a single roughness requires a large number of boundary layer profile measurements. While pressure drop data are easier to obtain in pipe flow, it is more difficult to coat/manufacture the pipe surface with a specific roughness. Recent advances in computing the flow over complicated surfaces, which can be easily parametrically changed, may be capable of providing a larger data set covering more of the sample space. This should allow for improvement in predictive capabilities.

6 Conclusions and Recommendations

An investigation has been carried out to identify hydraulically relevant roughness scales for three-dimensional roughness in the fully rough regime. A range of common surface statistical parameters, as well as a host of roughness parameters from literature, was considered. The results indicate that the root-mean-square roughness height ($k_{\rm rms}$) and the skewness of the surface elevation pdf (s_k) are the most effective parameters in describing a surface hydraulically. A correlation based on these parameters is offered, and it shows promising agreement with the measured equivalent sandgrain roughness height (k_s). However, further data are needed to validate and refine this correlation. Surfaces with negative s_k (i.e., pitted or eroded surfaces) would be especially helpful in this regard. Collapse of the roughness function in the fully rough re-

gime does not ensure collapse in the transitionally rough regime. In fact, the nonuniversal nature of the roughness function in the transitionally rough regime makes a universal scaling for this regime seem intractable. Therefore, the development of a Moody-type diagram that is applicable to a wide range of surfaces and is accurate in the transitionally rough regime appears highly unlikely.

Acknowledgment

The authors would like to thank the Office of Naval Research for financial support of this research. Thanks also go to Professor Ian Castro of the University of Southampton and Professor Lex Smits of Princeton University for providing surface samples, surface profiles, and data used in this research. Finally, the authors acknowledge the superior support given to this research by USNA Hydromechanics Laboratory and USNA Technical Support Branch.

Nomenclature

a = roughness function fitting constant
A_f = frontal area of a single roughness element
A_s = windward wetted area of a single roughness element
A_w = wetted area of a single roughness element
b = roughness function fitting constant
b_m = spanwise roughness length
B = smooth wall log-law intercept ≈ 5.0
C = log-law shift in a relative roughness form
C_f = skin friction coefficient $= \tau_w / \frac{1}{2}\rho U_e^2$
C_F = frictional resistance coefficient $= F_D / \frac{1}{2}\rho U_e^2 S$
$C_1 h$ = hydrodynamic roughness number
C_2 = roughness function constant
d = average roughness element spacing
ES = effective roughness slope
F_D = drag force
k = arbitrary measure of roughness height
k_{avg} = average roughness height
k_{rms} = root-mean-square roughness height $= \sqrt{1/N \Sigma_{i=1}^{N} r_i^2}$
k_s = equivalent sandgrain roughness height
k_t = maximum peak-to-trough height $= r_{\max} - r_{\min}$
k_u = kurtosis of the roughness elevation distribution $= (1/N)\Sigma_{i=1}^{N} r_i^4 / [(1/N)\Sigma_{i=1}^{N} r_i^2]^2$
k_x = wavenumber of the surface roughness
L = plate length
L_s = sampling length
m_0 = zeroth moment of the roughness amplitude energy spectra $= \int_0^\infty S_r dk_x$
m_2 = second moment of the roughness amplitude energy spectra $= \int_0^\infty k_x^2 S_r dk_x$
m_4 = fourth moment of the roughness amplitude energy spectra $= \int_0^\infty k_x^4 S_r dk_x$
N = number of samples
r = distance above the mean roughness elevation
Re_{δ^*} = displacement thickness Reynolds number $= U_e \delta^* / \nu$
Re_L = Reynolds number based on plate length $= U_e L / \nu$
Re_θ = momentum thickness Reynolds number $= U_e \theta / \nu$
s_k = skewness of the roughness elevation distribution $= (1/N)\Sigma_{i=1}^{N} r_i^3 / [(1/N)\Sigma_{i=1}^{N} r_i^2]^{3/2}$
s_m = streamwise roughness length
s_p = average roughness slope
S = wetted surface area without roughness
S_f = total frontal area of roughness
S_r = energy spectral density of roughness elevation
U = mean velocity
U_e = mean freestream velocity
U_τ = friction velocity $= \sqrt{\tau_o / \rho}$
y = normal distance from the wall or virtual origin
y_0 = effective roughness height
α = roughness bandwidth parameter $= m_0 m_4 / m_2^2$
δ = boundary layer thickness
δ^* = displacement thickness $= \int_0^\delta (1 - U/U_e) dy$
ΔU^+ = roughness function
κ = von Kármán constant ≈ 0.41
λ = roughness spacing or density parameter
λ_k = modified roughness density parameter
Λ = roughness density and shape parameter
Λ_k = modified roughness density parameter
Λ_s = modified roughness density and shape parameter
ν = kinematic viscosity of the fluid
θ = momentum thickness $= \int_0^\delta U/U_e (1 - U/U_e) dy$
τ_w = wall shear stress

Superscript

$+$ = inner variable (normalized with U_τ or U_τ / ν)

Subscript

min = minimum value
max = maximum value
R = rough surface
S = smooth surface

References

[1] Nikuradse, J., 1933, "Laws of Flow in Rough Pipes," NACA Technical Memorandum 1292.
[2] Colebrook, C. F., 1939, "Turbulent Flow in Pipes, With Particular Reference to the Transitional Region Between Smooth and Rough Wall Laws," J. Inst Civ. Eng., **11**, pp. 133–156.
[3] Flores, O., and Jiménez, J., 2006, "Effect of Wall-Boundary Disturbances on Turbulent Channel Flows," J. Fluid Mech., **566**, pp. 357–376.
[4] Lee, S. H., and Sung, H. J., 2007, "Direct Numerical Simulation of the Turbulent Boundary Layer Over a Rod-Roughened Wall," J. Fluid Mech., **584**, pp. 125–146.
[5] Orlandi, P., and Leonardi, S., 2008, "Direct Numerical Simulation of Three-Dimensional Turbulent Rough Channels: Parameterization and Flow Physics," J. Fluid Mech., **606**, pp. 399–415.
[6] Moody, L. F., 1944, "Friction Factors for Pipe Flow," Trans. ASME, **66**, pp. 671–684.
[7] Allen, J. J., Shockling, M. A., and Smits, A. J., 2005, "Evaluation of a Universal Transitional Resistance Diagram for Pipes With Honed Surfaces," Phys. Fluids, **17**, p. 121702.
[8] Langelandsvik, L. I., Kunkel, G. J., and Smits, A. J., 2008, "Flow in a Commercial Steel Pipe," J. Fluid Mech., **595**, pp. 323–339.
[9] 1988, *Principles of Naval Architecture*, Vol. II, E. V. Lewis, ed., Society of Naval Architects and Marine Engineers, Jersey City, NJ.
[10] International Towing Tank Conference (ITTC), 1978, "Report of the Powering Performance Committee," 15th ITTC, Hague.
[11] Bowden, B. S., and Davison, N. J., 1974, "Resistance Increments Due to Hull Roughness Associated With Form Factor Extrapolation Methods," National Physical Laboratory (NP) Ship Technical Manual 3800.
[12] International Towing Tank Conference (ITTC), 2005, "Report of the Powering Performance Committee," 24th ITTC, Edinburgh, Scotland, UK.
[13] Townsin, R. L., Byrne, D., Svensen, T. E., and Milne, A., 1981, "Estimating the Technical and Economic Penalties of Hull and Propeller Roughness," Trans. SNAME, **89**, pp. 295–318.
[14] Durbin, P. A., 2009, "Limiters and Wall Treatments in Applied Turbulence Modeling," Fluid Dyn. Res., **41**, p. 012203.
[15] Leighton, R. I., and Walker, D. T., 2007, "Reynolds Stress Modeling for Rough Wall Turbulence: An Invited Paper," 37th AIAA Fluid Dynamics Conference and Exhibit, AIAA Paper No. 2007-4615.
[16] Durbin, P. A., Medic, G., Seo, J. M., Eaton, J. K., and Song, S., 2001, "Rough Wall Modification of Two-Layer $k-\varepsilon$," ASME J. Fluids Eng., **123**, pp. 16–21.
[17] Seo, J. M., 2004, "Closure Modeling and Numerical Simulation for Turbulent Flows: Wall Roughness Model, Realizability and Turbine Blade Heat Transfer," Ph.D. thesis, Stanford University, Stanford, CA.
[18] Flack, K. A., Schultz, M. P., and Connelly, J. S., 2007, "Examination of a Critical Roughness Height for Boundary Layer Similarity," Phys. Fluids, **19**, p. 095104.
[19] Hama, F. R., 1954, "Boundary-Layer Characteristics for Smooth and Rough Surfaces," Trans. SNAME, **62**, pp. 333–351.

[20] Bandyopadhyay, P. R., 1987, "Rough Wall Turbulent Boundary Layers in the Transition Regime," J. Fluid Mech., **180**, pp. 231–266.
[21] Raupach, M. R., Antonia, R. A., and Rajagopalan, S., 1991, "Rough Wall Turbulent Boundary Layers," Appl. Mech. Rev., **44**, pp. 1–25.
[22] Antonia, R. A., and Krogstad, P. Å., 2001, "Turbulence Structure in Boundary Layers Over Different Types of Surface Roughness," Fluid Dyn. Res., **28**, pp. 139–157.
[23] Castro, I. P., 2007, "Rough-Wall Boundary Layers: Mean Flow Universality," J. Fluid Mech., **585**, pp. 469–485.
[24] Schultz, M. P., and Flack, K. A., 2003, "Turbulent Boundary Layers Over Surfaces Smoothed by Sanding," ASME J. Fluids Eng., **125**, pp. 863–870.
[25] Flack, K. A., Schultz, M. P., and Shapiro, T. A., 2005, "Experimental Support for Townsend's Reynolds Number Similarity Hypothesis on Rough Walls," Phys. Fluids, **17**, p. 035102.
[26] Schultz, M. P., and Flack, K. A., 2007, "The Rough-Wall Turbulent Boundary Layer From the Hydraulically Smooth to the Fully Rough Regime," J. Fluid Mech., **580**, pp. 381–405.
[27] Schultz, M. P., and Flack, K. A., 2009, "Turbulent Boundary Layers on a Systematically-Varied Rough Wall," Phys. Fluids, **21**, p. 015104.
[28] Schultz, M. P., and Flack, K. A., 2005, "Outer Layer Similarity in Fully Rough Turbulent Boundary Layers," Exp. Fluids, **38**, pp. 328–340.
[29] Ligrani, P. M., and Moffat, R. J., 1986, "Structure of Transitionally Rough and Fully Rough Turbulent Boundary Layers," J. Fluid Mech., **162**, pp. 69–98.
[30] Shockling, M. A., Allen, J. J., and Smits, A. J., 2006, "Roughness Effects in Turbulent Pipe Flow," J. Fluid Mech., **564**, pp. 267–285.
[31] Lewkowicz, A. K., and Musker, A. J., 1978, "The Surface Roughness on Ship Hulls: Interaction in the Viscous Sublayer," *Proceedings of the International Symposium on Ship Viscous Resistance-SSPA*, Goteborg, Sweden.
[32] Clauser, F. H., 1956, "The Turbulent Boundary Layer," Adv. Appl. Mech., **4**, pp. 1–51.
[33] Bettermann, D., 1965, "Contribtion a L'etude de la Couche Limite Turbulent le Long de Plaques Regueuses," Center National de la Recherche Scientifique, Report No. 65-6.
[34] Dvorak, F. A., 1969, "Calculation of Turbulent Boundary Layers on Rough Surfaces in Pressure Gradients," AIAA J., **7**, pp. 1752–1759.
[35] Granville, P. S., 1958, "The Frictional Resistance and Turbulent Boundary Layer of Rough Surfaces," J. Ship. Res., **2**, pp. 52–74.
[36] Lui, C. K., Kline, S. J., and Johnston, J. P., 1966, "An Experimental Study of Turbulent Boundary Layers on Rough Walls," Department of Mechanical Engineering, Stanford University, Report No. MD-15.
[37] Schlichting, H., 1937, "Experimental Investigation of the Problem of Surface Roughness," NACA Technical Memorandum 823.
[38] Simpson, R. L., 1973, "A Generalized Correlation of Roughness Density Effects on the Turbulent Boundary Layer," AIAA J., **11**, pp. 242–244.
[39] Schlichting, H., 1979, *Boundary-Layer Theory*, 7th ed., McGraw-Hill, New York.
[40] Chen, D. K., and Roberson, J. A., 1971, "The Structure of Turbulence in the Wakes of Roughness Elements," *ASCS Hydraulics Division Specialty Conference*, University of Iowa, Iowa City, IA.
[41] Streeter, V. L., 1936, "Frictional Resistance in Artificially Roughened Pipes," Proceedings of the ASCE, Vol. 101, pp. 681–713.
[42] Dirling, R. B., 1973, "A Method for Computing Rough Wall Heat Transfer Rates on Re-Entry Nosetips," AIAA Paper No. 73-763.
[43] Sigal, A., and Danberg, J. E., 1990, "New Correlation of Roughness Density Effects on the Turbulent Boundary Layer," AIAA J., **28**, pp. 554–556.
[44] van Rij, J. A., Belnap, B. J., and Ligrani, P. M., 2002, "Analysis and Experiments on Three-Dimensional, Irregular Surface Roughness," ASME J. Fluids Eng., **124**, pp. 671–677.
[45] Coleman, H. W., Hodges, B. K., and Taylor, R. P., 1984, "A Re-Evaluation of Schlichting's Surface Roughness Experiment," ASME J. Fluids Eng., **106**, pp. 60–65.
[46] Waigh, D. R., and Kind, R. J., 1998, "Improved Aerodynamic Characterization of Regular Three-Dimensional Roughness," AIAA J., **36**, pp. 1117–1119.
[47] Bons, J. P., 2002, "*St* and C_F Augmentation for Real Turbine Roughness With Elevated Freestream Turbulence," ASME Paper No. GT-2002-30198.
[48] Musker, A. J., 1980–1981, "Universal Roughness Functions for Naturally-Occurring Surfaces," Trans. Can. Soc. Mech. Eng., **1**, pp. 1–6.
[49] Taylor, G. I., 1938, "The Spectrum of Turbulence," Proc. R. Soc. London, Ser. A, **164**, pp. 476–490.
[50] Medhurst, J. S., 1989, "The Systematic Measurement and Correlation of the Frictional Resistance and Topography of Ship Hull Coatings, With Particular Reference to Ablative Antifoulings," Ph.D. thesis, University of Newcastle-upon-Tyne, Newcastle, UK.
[51] Medhurst, J. S., 1990, "Outline of a Draft International Standard for the Measurement and Characterisation of Roughness Topography in Fluid Flow," *Proceedings of the RINA International Workshop on Marine Roughness and Drag*, London, UK.
[52] Townsin, R. L., and Dey, S. K., 1990, "The Correlation of Roughness Drag With Surface Characteristics," *Proceedings of the RINA International Workshop on Marine Roughness and Drag*, London, UK.
[53] Schultz, M. P., 2007, "Effects of Coating Roughness and Biofouling on Ship Resistance and Powering," Biofouling, **23**, pp. 331–341.
[54] Granville, P. S., 1978, "Similarity-Law Characterization Methods for Arbitrary Hydrodynamic Roughness," David W. Taylor Naval Ship Research and Development Center, Report No. 78-SPD-815-01.
[55] Granville, P. S., 1987, "Three Indirect Methods for the Drag Characterization of Arbitrarily Rough Surfaces on Flat Plates," J. Ship. Res., **31**, pp. 70–77.
[56] Schoennerr, K. E., 1932, "Resistances of Flat Surfaces Moving Through a Fluid," Trans. SNAME, **40**, pp. 279–313.
[57] Bradshaw, P., 2000, "A Note on 'Critical Roughness Height' and 'Transitional Roughness'," Phys. Fluids, **12**, pp. 1611–1614.
[58] Napoli, E., Armenio, V., and DeMarchis, M., 2008, "The Effect of the Slope of Irregularly Distributed Roughness Elements on Turbulent Wall-Bounded Flows," J. Fluid Mech., **613**, pp. 385–394.
[59] Howell, D., and Behrends, B., 2006, "A Review of Surface Roughness in Antifouling Coatings Illustrating the Importance of Cutoff Length," Biofouling, **22**, pp. 401–410.
[60] Shapiro, T. A., Schultz, M. P., and Flack, K. A., 2004, "The Effect of Surface Roughness on Hydrodynamic Drag and Turbulence," USNA Trident Scholar, Report No. USNA-1531-2.

Seyyed Hossein Hosseini[1]
Department of Chemical Engineering,
Faculty of Engineering,
University of Ilam,
Ilam, Iran
e-mail: s.h.hosseini@mail.ilam.ac.ir

Wenqi Zhong
School of Energy and Environment,
Southeast University,
Nanjing 210096, People's Republic of China

Mohsen Nasr Esfahany
Department of Chemical Engineering,
Isfahan University of Technology,
Isfahan 8415683111, Iran

Leila Pourjafar
Department of Chemical Engineering,
University of Sistan and Baluchesta,
Zahedan 98164-161, Iran

Salar Azizi
Department of Chemical Engineering,
Faculty of Engineering,
Arak University,
Arak, Iran

CFD Simulation of the Bubbling and Slugging Gas-Solid Fluidized Beds

A two-dimensional transient Eulerian model integrating the kinetic theory for emulsion phase is used to simulate the bubbling and slugging gas-solid fluidized beds, including the Geldart B and D particles, respectively. CFD results show that utilizing an algebraic granular temperature equation, instead of a full granular temperature, one leads to a significant reduction in computational time without loosing accuracy. Different drag models have been examined in the current study. CFD results show that the Syamlal–O'Brien and Di Felice adjusted drag models, based on minimum fluidization velocity, are not suitable for the bed, including coarse particles (Geldart group B). The Gidaspow drag model displays better results in comparison with the others. A good agreement with the available experimental data and the researcher's findings has been reached quantitatively and qualitatively. The proposed model can reasonably be used for simulation of slugging fluidized beds. This study reduces the computational error compared with the previous works. [DOI: 10.1115/1.4001140]

Keywords: multiphase, fluidized bed, hydrodynamics, CFD, KTGF

1 Introduction

Gas-solid fluidized bed reactors have many applications in chemical, oil, medical, agricultural, biochemical, electronic, and power industries. Their widespread application is due to the suitable mixing characteristics and high surface contacting between the phases [1]. In order to increase the efficiency, hydrodynamic knowledge of these systems is essential. Besides much experimental studies using various optical probes, numerical simulation can be a useful technique for achieving more information about the flow pattern of the gas-solid fluidized beds in detail. One of the important numerical methods is computational fluid dynamics (CFD). CFD has shown that it can be a powerful tool for modeling of gas-solid flows, reducing design time and cost [2,3]. This technique is derived from the equations governing the fluid flow in the form of partial differential equations representing the conservation of mass, momentum, and energy. Before comparing CFD results with experimental data, it is necessary to undertake verification procedures, i.e., confirming the accuracy of the computational aspect of the model. Only after this stage can validation be performed. Validation requires objective consideration of computational and numerical errors, as well as comparison of model predictions and experimental data over broad ranges of conditions [4,5].

CFD divided the important approaches of Eulerian–Eulerian and Eulerian–Lagrangian into two. In this study, a Eulerian–Eulerian two-fluid model (TFM) is adopted. Each phase has an interpenetrating continuum behavior that leads to a suitable approach for large-scale fluidized bed systems. When solving the TFM, a set of physical or empirical models are required in order to close the system of equations. In TFM, the critical closure law is the particle phase stress, i.e., normal and tangential stresses of the emulsion phase. Two approaches are currently utilized for treating the emulsion phase stress in TFM. The first approach is the constant viscosity model (CVM), which is expressed in terms of a modulus of elasticity that is only based on local porosity. Various empirical correlations for the modulus of elasticity, based on the experimental results, have been reported in the literature [6]. The second approach is the kinetic theory of granular flow (KTGF). To describe solid shear stress, solid pressure, and solid viscosity in TFM, KTGF could be the best choice. Patil et al. [7,8], who simulated a gas-solid bubbling fluidized bed with a central jet and a uniform distributor, showed that KTGF, by the incorporation of frictional stresses, leads to the significantly better results in comparison with the CVM approach.

Analogous to the thermodynamic temperature for gases, the granular temperature, which is the basic parameter in KTGF, can be introduced as a measure of the particle velocity fluctuations ($\Theta_s=(1/3)\overline{\nu_s'^2}$). Numerous studies have shown the capability of KTGF for modeling the freely bubbling fluidized beds [9–13].

To have a successful simulation of a gas-solid fluidized bed, recognition of major forces such as gravity and drag are important. In dense fluidized bed simulations, frictional stress can also play an important role [14–16]. Several correlations for calculating the momentum exchange coefficient of gas-solid systems were reported in the literatures [17–19]. Hosseini et al. [20] simulated a freely bubbling fluidized bed including FCC particles. They achieved to the reasonable simulation results by utilizing a Eulerian–Eulerian approach, integrating the KTGF for the particulate phase and modified Gibilaro drag model as the interaction between the phases in terms of bed expansion and local time-averaged voidage. Hosseini et al. [21] simulated a fluidized bed of Geldart B particles at high gas velocities by the CFD code MFIX. They indicated the sensitivity of their system to the model parameters such as drag function, restitution coefficient, and solid maximum packing.

[1]Corresponding author.

Contributed by the Fluids Engineering Division of ASME for publication in the JOURNAL OF FLUIDS ENGINEERING. Manuscript received June 25, 2009; final manuscript received January 18, 2010; published online March 29, 2010. Assoc. Editor: Ian Eames.

Numerous CFD simulations have been carried out for studying hydrodynamic parameters of the bubbling bed such as the bed expansion height, time-averaged voidage, and pressure drop. McKeen and Pugsley [22] observed large errors for bed expansion between CFD results and experimental data. After applying modification in the Gibilaro drag model, their predicted result agreed with the experimental data only qualitatively. Taghipour et al. [23] studied the bed expansion ratio and bubbling behavior of the bed using different drag models. Their predicted that the results qualitatively agreed with the experimental data while they got large errors as much as 30–50% in voidage and pressure drop of the bed. Behjat et al. [24] obtained the numerical results using CFD code MFIX with error of 28.8% for a bubbling fluidized bed. Ahuja and Patwardhan [25] obtained the same trend of solid concentration profiles of CFD results and experimental data while they got large errors as much as 46–51% in the solid hold-up of the bed.

In this research, a Eulerian–Eulerian approach integrating the kinetic theory for the solid phase is used to simulate gas-solid fluidized beds at a wide range of operating conditions by considering a suitable model in terms of CPU time and simulation results. The algebraic granular temperature equation and the full granular temperature one are utilized for comparison between them in simulation of the gas-solid fluidized bed. Effects of different drag models and some adjusted drag models are studied in a bubbling gas-fluidized bed of Geldart B particles. The simulation results errors are reported in terms of time-averaged local voidage. Several hydrodynamics parameters are predicted by using the CFD software package, FLUENT 6.3. The model validation is also investigated for a slugging gas-solid fluidized bed.

2 CFD Model

The simulation of the gas-solid fluidized beds were carried out using a Eulerian–Eulerian approach, containing the set of momentum and continuity equations for each phase, which are linked through pressure and interphase exchange coefficients. The continuity equation for qth phase without any mass transfer between the phases is given by

$$\frac{\partial}{\partial t}(\alpha_q \rho_q) + \nabla \cdot (\alpha_q \rho_q \boldsymbol{\nu}_q) = 0 \tag{1}$$

where α_q, ρ_q, and $\boldsymbol{\nu}_q$ are the volume fraction, density, and velocity of the qth phase, respectively. Equations (2) and (3) give the conservation of momentum for the gas phase (g) and the solid phase, respectively

$$\frac{\partial}{\partial t}(\alpha_g \rho_g \boldsymbol{\nu}_g) + \nabla \cdot (\alpha_g \rho_g \boldsymbol{\nu}_g \cdot \boldsymbol{\nu}_g) = -\alpha_g \nabla P + \nabla \cdot \bar{\bar{\tau}}_g + \alpha_g \rho_g g - K_{gs}(\boldsymbol{\nu}_g - \boldsymbol{\nu}_s) \tag{2}$$

$$\frac{\partial}{\partial t}(\alpha_s \rho_s \boldsymbol{\nu}_s) + \nabla \cdot (\alpha_s \rho_s \boldsymbol{\nu}_s \cdot \boldsymbol{\nu}_s) = -\alpha_s \nabla P - \nabla P_s + \nabla \cdot \bar{\bar{\tau}}_s + \alpha_s \rho_s g + K_{gs}(\boldsymbol{\nu}_g - \boldsymbol{\nu}_s) \tag{3}$$

where $\alpha_s = 1 - \alpha_g$.

Conservation of the kinetic energy of the moving particles is described based on granular temperature Θ_s as

$$\frac{3}{2}\left[\frac{\partial}{\partial t}(\alpha_s \rho_s \Theta_s) + \nabla \cdot (\alpha_s \rho_s \boldsymbol{\nu}_s \Theta_s)\right] = (-p_s \bar{\bar{I}} + \bar{\bar{\tau}}_s) : \nabla \boldsymbol{\nu}_s + \nabla \cdot (k_{\Theta s} \nabla \Theta_s) - \gamma_{\Theta m} + \phi_{gs} \tag{4}$$

Assuming that the granular energy is in steady state and its dissipation occurs locally, then the convection and diffusive terms can be neglected [10,26,27]. With this assumption, Eq. (5) is expressed as

$$0 = (-p_s \bar{\bar{I}} + \bar{\bar{\tau}}_s) : \nabla \boldsymbol{\nu}_s - \gamma_s \tag{5}$$

Equations (6)–(21) represent the other constitutive correlations, which are used in the present work.

Solid phase stress tensor is expressed as

$$\bar{\bar{\tau}}_s = \alpha_s \mu_s (\nabla \boldsymbol{\nu}_s + \nabla \boldsymbol{\nu}_s^T) + \alpha_s \left(\lambda_s - \frac{2}{3}\mu_s\right) \nabla \cdot \boldsymbol{\nu}_s \bar{\bar{I}} \tag{6}$$

The radial distribution function is calculated by

$$g_0 = \frac{1 + 2.5\alpha_s + 4.5904\alpha_s^2 + 4.515439\alpha_s^3}{\left[1 - \left(\frac{\alpha_s}{\alpha_{s,\max}}\right)^3\right]^{0.67802}} \tag{7}$$

Collision dissipation of energy is given by

$$\gamma_s = \frac{12(1 - e_s^2) g_0}{d_s \sqrt{\pi}} \rho_s \alpha_s^2 \Theta_s^{3/2} \tag{8}$$

In this study, the value of restitution coefficient (e_s) of 0.9 is utilized [23,28].

Transfer of kinetic energy is expressed as

$$\phi_{gs} = -3 K_{gs} \Theta_s \tag{9}$$

Solid pressure is calculated by

$$P_s = \alpha_s \rho_s \Theta_s + 2\rho_s (1 + e_s) \alpha_s^2 g_0 \Theta_s \tag{10}$$

Solid shear viscosity is given by

$$\mu_s = \frac{4}{5}\alpha_s \rho_s d_s g_0 (1 + e_s)\left(\frac{\Theta_s}{\pi}\right)^{1/2} + \frac{10 d_s \rho_s \sqrt{\Theta_s \pi}}{96(1 + e_s) g_0}\left[1 + \frac{4}{5}\alpha_s g_0 (1 + e_s)\right]^2 + \frac{P_s \sin \phi}{2\sqrt{I_{2D}}} \tag{11}$$

The solid bulk viscosity is expressed as [29]

$$\lambda_s = \frac{4}{3}\alpha_s \rho_s d_s g_0 (1 + e_s)\left(\frac{\Theta_s}{\pi}\right)^2 \tag{12}$$

The drag functions that have been used in this study are as follows.

Drag model of Syamlal–O'Brien [16]

$$K_{gs} = \frac{3}{4}\frac{\alpha_s \alpha_g \rho_g}{\nu_{r,s}^2 d_s} C_D\left(\frac{\mathrm{Re}_s}{\nu_{r,s}}\right) |\boldsymbol{\nu}_s - \boldsymbol{\nu}_g| \tag{13}$$

where the drag coefficient C_D and the solids Reynolds number Re_s are written as

$$C_D = \left(0.63 + \frac{4.8}{\sqrt{\mathrm{Re}_s / \nu_{r,s}}}\right)^2, \quad \mathrm{Re}_s = \frac{\rho_g d_s |\boldsymbol{\nu}_s - \boldsymbol{\nu}_g|}{\mu_g} \tag{14}$$

The terminal velocity is written as

$$\nu_{r,s} = 0.5[A - 0.06\ \mathrm{Re}_s + \sqrt{(0.06\ \mathrm{Re}_s)^2 + 0.12\ \mathrm{Re}_s (2B - A) + A^2}] \tag{15}$$

where

$$A = \alpha_g^{4.14} \quad \text{and} \quad B = C_1 \alpha_g^{1.28} \quad \text{for} \quad \alpha_g \le 0.85$$

$$A = \alpha_g^{4.14} \quad \text{and} \quad B = \alpha_g^{C_2} \quad \text{for} \quad \alpha_g > 0.85 \tag{16}$$

where the default values for C_1 and C_2, respectively, are 0.8 and 2.65.

The Gidaspow drag model

$$K_{gs} = \frac{3}{4} C_D \frac{\alpha_s \alpha_g \rho_g |\boldsymbol{\nu}_s - \boldsymbol{\nu}_g|}{d_s} \alpha_g^{-2.65} \quad \text{for} \quad \alpha_g > 0.8$$

$$C_D = \begin{cases} \dfrac{24}{\alpha_g \mathrm{Re}_s}[1 + 0.15(\alpha_g \mathrm{Re}_s)^{0.687}] & \text{for} \quad \mathrm{Re} < 1000 \\ C_D = 0.44 & \text{for} \quad \mathrm{Re} > 1000 \end{cases}$$

Table 1 Parameter used for simulations

Parameters	Unit	Value case study (1)	Value case study (2)
Particle diameter range	μm	250–300	–
Mean particle diameter	μm	275	1899
Particle density	kg/m^3	2500	1102
Gas density	kg/m^3	1.18	1.18
Gas viscosity	kg/m s	1.8×10^{-5}	1.8×10^{-5}
Voidage at minimum fluidization condition (ε_{mf})	–	0.4	0.45
Minimum fluidization velocity	m/s	0.065	0.62
Sphericity (ϕ_S)	–	1	1
Superficial gas velocity	m/s	0.1–0.6	2.8
Static bed height ($H0$)	M	0.4	0.51
Height of the bed	M	1.0	4
Width of the bed	M	0.28	0.382

$$K_{gs} = 150\frac{\alpha_s^2\mu_g}{\alpha_g d_s^2} + 1.75\frac{\alpha_s\rho_g|\boldsymbol{\nu}_s - \boldsymbol{\nu}_g|}{d_s} \quad \text{for} \quad \alpha_g \le 0.8 \tag{17}$$

The Di Felice drag model

$$K_{gs} = \frac{3}{4}C_D\frac{\alpha_s\rho_g}{d_s}|\boldsymbol{\nu}_s - \boldsymbol{\nu}_g|f(\alpha_s), \quad \text{where} \quad f(\alpha_s) = (1-\alpha_s)^{-x} \tag{18}$$

The empirical coefficient of x is described as a function of the Reynolds number, following the relation

$$x = P - Q\exp\left[-\frac{(1.5-\beta)^2}{2}\right]$$

$$\beta = \log_{10}(\mathrm{Re}_s)$$

$$P = 3.7 \quad \text{and} \quad Q = 0.65 \tag{19}$$

The Zhang–Reese drag model

$$K_{gs} = \begin{cases} 150\dfrac{\alpha_s^2\mu_g}{\alpha_g d_s^2} + 1.75\dfrac{\alpha_s\rho_g}{d_s}U_r, & \alpha_g < 0.8 \\ \dfrac{3}{4}C_D\dfrac{\alpha_s\rho_g}{d_s}U_r\alpha_g^{-2.65}, & \alpha_g \ge 0.8 \end{cases}$$

$$U_r = \left[(U_s - U_g)^2 + \frac{8\Theta_s}{\pi}\right]^{1/2}, \quad C_D = \left(0.28 + \frac{6}{\sqrt{\mathrm{Re}_s}} + \frac{21}{\mathrm{Re}_s}\right),$$

$$\mathrm{Re}_s = \frac{\rho_g U_t d_s}{\mu_g} \tag{20}$$

The Ma and Ahmadi drag model

$$K_{gs} = \frac{18\mu_g\alpha_s}{d_s^2}\frac{[1+0.1(\mathrm{Re}_s)^{0.75}]}{\left(1-\dfrac{\alpha_s}{\alpha_{s,\max}}\right)^{2.5\alpha_{s,\max}}} \tag{21}$$

The parameter C_1 in Eq. (16) is related to the minimum fluidization velocity through the velocity voidage correlation and the terminal Reynolds number Re_t. C_1 is changed until the following criterion is met:

$$\left\{U_{\mathrm{mf}}^{\mathrm{experiment}} - \mathrm{Re}_t\cdot\frac{\alpha_g\mu_g}{d_s\rho_g}\right\} = 0 \tag{22}$$

where

$$\mathrm{Re}_t = \nu_{r,s}\mathrm{Re}_{ts}$$

$$\nu_{r,s} = (A + 0.06B\ \mathrm{Re}_{ts})/(1 + 0.06\ \mathrm{Re}_{ts})$$

$$\mathrm{Re}_{ts} = \left(\frac{\sqrt{23.04 + 2.52\sqrt{4Ar/3}} - 4.8}{1.26}\right)^2$$

$$Ar = \frac{(\rho_s - \rho_s)d_s^3\rho_g g}{\mu_g} \tag{23}$$

In addition, the parameter C_2 in Eq. (16) is adopted to guarantee the continuity of the velocity voidage correlation as follows:

$$C_2 = 1.28 + \frac{\log(C_1)}{\log(0.85)} \tag{24}$$

By considering Eqs. (22)–(24), the modified values for C_1 and C_2 are 0.376 and 7.29, respectively.

As another alternative, based on the same concept, the following method is adopted to adjust the Di Felice drag model. In the absence of gas-wall friction and solid stress transmitted by the particles, the momentum balance at minimum fluidization can be written as follows [18]:

$$\text{Buoyancy} = \text{Drag}$$

$$(1-\alpha_g)(\rho_s - \rho_g)g = \frac{K_{gs}}{\alpha_g}(\boldsymbol{\nu}_g - \boldsymbol{\nu}_s) \tag{25}$$

At the minimum fluidization velocity, considering that $\boldsymbol{\nu}_s = 0$, $\boldsymbol{\nu}_g = U_{\mathrm{mf}}$, Eq. (25) is rewritten as

$$(1-\alpha_{g,\mathrm{mf}})(\rho_s - \rho_g)g = \frac{K_{gs}}{\alpha_{g,\mathrm{mf}}}(U_{\mathrm{mf}}) \tag{26}$$

By replacing the Di Felice drag model into Eq. (26) and utilizing a nonlinear optimization algorithm, the drag model parameters of P and Q (Eq. (19)) can be adjusted for the system under study using experimental data at minimum fluidization velocity. However, when adjusting the drag models, it should be considered that the adjustment should not alter the behavior of the drag correlation when voidage approaches the value of 1. Therefore, the modified values for P and Q are 5.2 and 0.31, respectively.

3 Model Solution Procedure

In the present study, the experimental data in conventional gas-solid fluidized beds [23,30,31] are adopted to validate the model predictions. The operating conditions and solid properties are summarized in Table 1. In this work, the gas is air and the solids are glass beads and polystyrene for case studies (1) and (2), respectively. The simulations are carried out in two-dimensional frameworks. The grids, which have an independent solution, are dense near the wall where the velocity gradients increase, but they become dilute away from the wall. The governing equations in

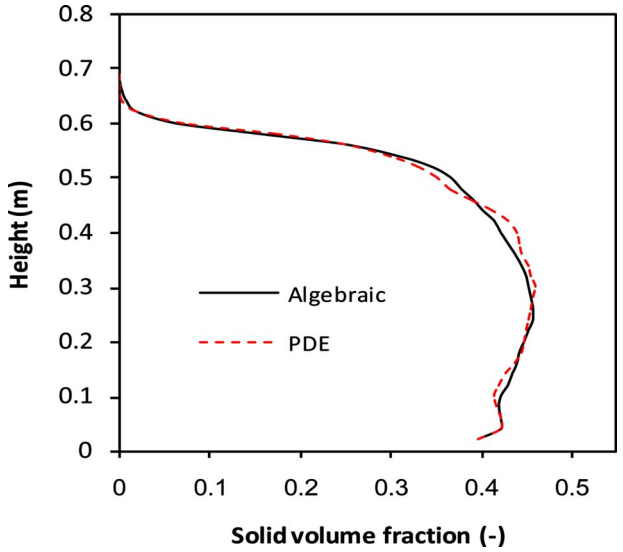

Fig. 1 Time-averaged solid volume fraction along the bed height using PDE and algebraic equation of granular temperature

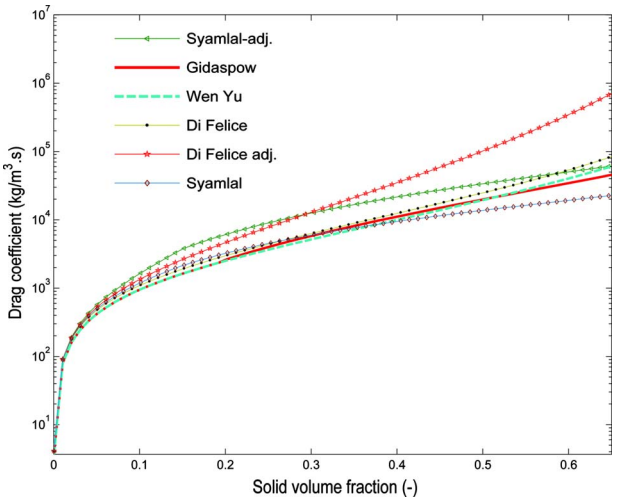

Fig. 2 Quantitatively comparison between different drag models at wide range of solid volume fraction

this system are solved by the finite volume approach. The first order upwind discretization scheme is used for discretizing all conservation equations. The phase-coupled PC–SIMPLE algorithm is used for the pressure-velocity coupling. The linearized equations are solved using a block algebraic multigrid method. The upper section of the simulated geometry, or freeboard, is considered to be occupied by gas only. The no-slip boundary condition is assumed for the two phases at the walls. The Dirichlet boundary condition is employed at the bottom of the bed to specify a uniform gas inlet velocity, and the pressure boundary condition is set to atmospheric at the top of the freeboard.

4 Results and Discussions

4.1 Case Study (1). The experimental data in Refs. [23,30] are utilized for validation of the model. The bed is 1 m in height and 0.28 m in width. Its thickness is negligible, as compared with the other dimensions. Therefore, the bed can be considered as two-dimensional. Glass beads with the average diameters of 275 μm and density of 2500 kg/m^3 are fluidized by air with density of 1.225 kg/m^3. The range of superficial gas velocities is 0.1–0.6 m/s.

4.1.1 Granular Temperature. The basic parameter of kinetic theory for emulsion phase is the granular temperature, which is utilized in several structural correlations of the Eulerian–Eulerian two-fluid model. The predicted result of the time-averaged solid volume fraction along the bed is displayed in Fig. 1 in order to compare the partial differential and algebraic granular temperature equations. It is observed that both methods show the same results with negligible discrepancy.

The computational time using the partial differential equation (PDE) of the granular temperature, Eq. (4), is more than the algebraic equation (AE) of the granular temperature, Eq. (5). In addition, the time step for achieving the convergence solution using the PDE method is 0.0001 s, while for the AE method, it is 0.0005 s. The most important is that the CPU time taken to complete a simulation increases as the time step decreases. Therefore, for saving the computational time without losing accuracy, the algebraic equation of the granular temperature can be utilized reasonably. This method is used in the rest of the simulations.

4.1.2 Comparison Between Different Drag Models Quantitatively. The drag coefficient values as a function of the solid volume fraction for different drag models are plotted in Fig. 2. The drag coefficient values are calculated at a constant Reynolds number equal to 10, using the solid properties of case study (1). All drag coefficients show a rising trend of drag coefficient values by increasing the solid volume fraction. Figure 2 indicates that, excluding the Syamlal–O'Brien and Di Felice adjusted models, which overestimate the drag coefficient values, remnant drag models represent almost the same value of drag coefficient. The Di Felice adjusted model precipitously separates from the others toward the higher values of the drag coefficient. This trend continues until it cross the Syamlal–O'Brien adjusted model at the values of solid volume fraction equal to 0.3. From this point on, the Di Felice adjusted model gives the highest drag force's values. Figure 2 also reveals that adjusted drag models, based on the minimum fluidization velocity, results in the prediction of higher values of drag coefficient through the whole range of solid volume fraction in case study (1).

4.1.3 Bed Expansion Ratio ($H/H0$). After the first 5 s, the quasisteady state is reached. Therefore, the time-averaged distributions of flow variables are computed from 5–25 s to avoid the start up effect. Figure 3 shows the experimental data and simulation results of the time-averaged bed expansion ratio. The figure demonstrates the different drag model effects on the prediction of the bed expansion. By increasing the superficial gas velocity, the bed expansion ratio increases. From Fig. 3, it is observed that the Syamlal–O'Brien adjusted model predicts a suitable bed expansion at a gas velocity of 0.1 m/s, while the original form of the Syamlal–O'Brien drag model does not predict the expansion of the bed at a corresponding gas velocity. In addition, the Syamlal–O'Brien adjusted model predicts the overestimation of the bed expansion at high gas velocities. The Di Felice adjusted model overestimates the bed expansion in the whole range of gas velocities. As a result, the Di Felice and Syamlal–O'Brien adjusted drag models predict the highest values of computational errors compared with the others in terms of the bed expansion ratio. Figure 3 also shows that the Ma–Ahmadi and Di Felice drag models predict appropriate results for a limited number of gas velocities. In Sec. 4.1.4, these drag models are investigated in terms of the time-averaged local voidage to choose the best one. The Syamlal–O'Brien, Gidaspow, and Zhang–Reese drag models underestimate the bed expansion ratio with appropriate values.

4.1.4 Time-Averaged Local Voidage. Figure 4 shows the influence of different drag models on the prediction of time-averaged

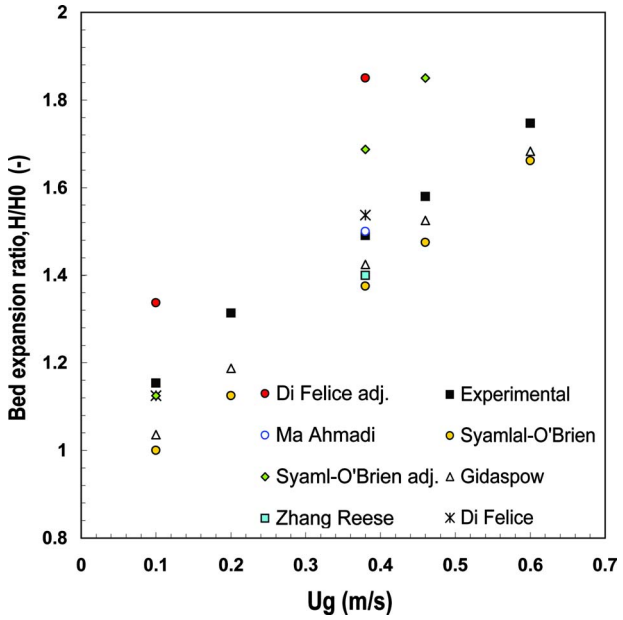

Fig. 3 Computed bed expansion ratio by using different drag models compared with experimental data

local voidage at $U_g=0.38$ m/s and the axial level (y) of 0.2 m just above the distributor. The drag models of the Ma–Ahmadi, Di Felice, Syamlal–O'Brien, and Di Felice adjusted models lead to the overestimation of time-averaged voidage, especially in the central region of the bed. However, the Gidaspow, Syamlal–O'Brien, and Zhang–Reese drag models predict suitable results at a corresponding position in terms of the gas volume fraction. Figure 5 shows the comparison between the two drag models of Gidaspow and Syamlal–O'Brien for $U_g=0.46$ m/s at $y=0.2$ m in terms of voidage profile. rms deviation of simulation results for both suitable drag models of Gidaspow and Syamlal–O'Brien have been reported in Table 2, based on

$$\delta_{\mathrm{rms}D}=\left[\frac{1}{N}\sum_{1}^{N}\left(\frac{X_{\mathrm{experimental}}-X_{\mathrm{computational}}}{X_{\mathrm{experimental}}}\right)^2\right]^{1/2}\times 100 \quad (27)$$

By considering Figs. 3–5, and Table 2, it is found that the Gidaspow drag model is a better choice to predict several hydrodynamic parameters of case study (1), in comparison with the others. Therefore, the Gidaspow drag function is used in the rest of the simulations. In Figs. 4 and 5, increasing the gas volume fraction in the central area of the bed is expected, due to the considerable bubbles passing in this area, since the solids tend to flow down near the wall. It is observed that the time-averaged local voidage is smoother and more symmetric for a higher gas velocity of 0.46 m/s, in comparison with a lower gas velocity of 0.38 m/s (Figs. 4 and 5).

4.1.5 Comparison Between Different Drag Models Qualitatively. The experimental observations display small bubbles near the distributor, and large bubbles at the top of the bed. The bubbles grow while they rise to the top of the bed with coalesces [8,10,22]. The reasons of this phenomenon are the wall effects and interaction between the bubbles. In addition, body, stress, and drag forces can influence on the bubble coalescence phenomenon in the gas-solid fluidized beds. The experimental result of the gas volume fraction, which is displayed in Fig. 6, indicates the small bubbles near the gas distributor and large bubbles in the top region of the bed. This behavior is also illustrated in Fig. 6 for drag functions, excluding the adjusted drag models. The adjusted drag models underestimate the effect of particle clustering. As can be seen in Fig. 6, the behavior of the fluidization in the bubbling fluidized bed containing Geldart B is similar for all drag models qualitatively, excluding the adjusted drag models, based on the minimum fluidization velocity.

4.1.6 Pressure Drop. In order to avoid the temporal fluctuations of pressure drop in the early seconds of the simulation, the time-averaged pressure drop is calculated after establishing a quasisteady state. Therefore, time averaging is calculated over a range of 5–25 s of real time simulation, similar to the previous sections. Figure 7(a) shows the time-averaged pressure drop inside the bed (between 2 axial levels of 0.03 m and 0.3 m) against the superficial gas velocity. The model predicts the declining trend by the increase in the superficial gas velocity that is in agreement with the experimental data qualitatively. Deviation from the experimental data is observed that may be explained by the influence of the gas distributor, which was not considered in the simulation. A comparison of the time-averaged overall pressure drop against gas velocity is plotted in Fig. 7(b), which is in good agreement with the experimental data. As can be seen, there is no significant difference in the prediction of the overall pressure drop for the range of the superficial gas velocity under study, except for the lower gas velocity. The discrepancy at low gas velocity may be attributed to the solids being fluidized hardly, due to dominant interparticle frictional forces, which are not predicted by the model reasonably.

4.1.7 Model Prediction for Case Study (1). Figure 8 shows the pressure drop versus time at three different gas inlet velocities of 0.2 m/s, 0.38 m/s, and 0.46 m/s. The total pressure drop has an oscillatory behavior in the bed. This figure indicates that the higher gas velocity, the higher the bubble size. Therefore, bubble breakup and coalescence rate will rise up by increasing the gas velocity, which leads to higher fluctuations in pressure drop. This prediction is inline with researchers' findings [32]

The predicted results of the time-average solid volume fraction are plotted in Fig. 9(a) for a gas velocity of 0.38 m/s in all sections of the bed. It is observed that in the middle of the bed, by increasing the bed height, the solid volume fraction is decreased, while this term is increased near the wall regions. Thus, two major regions of the solid distribution concentration can be estimated. The first region is the central part of the bed, where concentration of the particles is low, and the second region is near the wall that indicates high concentration of the solid particles, due to the accumulation of particles when they reverse.

In Fig. 9(b), the time-averaged axial solid velocity at $U_g=0.38$ m/s in all sections of the bed is shown. It is seen that the particles' velocity increases to the positive value of 0.574 m/s, and then decreases to the negative value of -0.203 m/s along the bed at the central parts. An experimental validation of this phenomenon, which is vital in heat and mass transfer studies, is required. Descending of the particles from the top of the bed is the mean reason for negative velocity.

4.2 Case Study (2). Experimental results reported in Ref. [31] were used for validation of the model in a slugging regime. The bed is 4 m in height and 0.382 m in diameter. The two-dimensional simulation has been done for the bed, including polystyrene particles with the average diameters of 1899 μm and density of 1102 kg/m^3. The bed is fluidized by air with density of 1.18 kg/m^3. The gas velocity is 2.8 m/s.

4.2.1 Time-Averaged Voidage. Figures 10(a) and 10(b) show the computational results and experimental data of radial distribution of the gas volume fraction at different axial locations of 0.517 m, 0.757 m, and 1.365 m, and gas velocity of 2.8 m/s. The figure displays that the gas volume fraction in the center of the bed increases by increasing axial locations of the bed. As seen in Figs. 10(a) and 10(b), axial distributions of the gas volume fractions are different. The average errors of the gas volume fraction between the CFD results and the experimental data for different axial

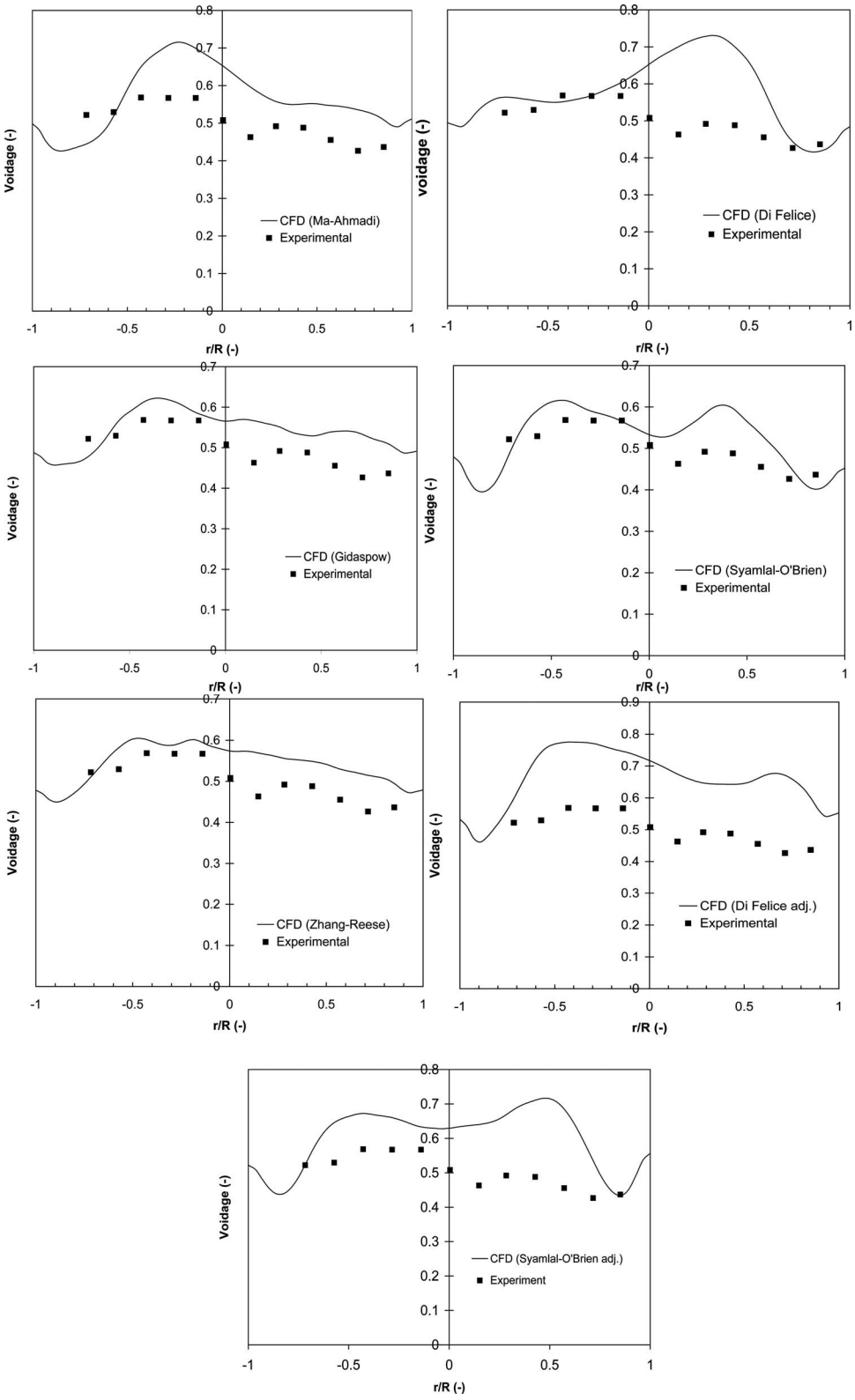

Fig. 4 Comparison of experimental and simulated time-averaged local voidage using different drag models at y=0.2 m and U_g=0.38 m/s

locations of 0.517 m, 0.757 m, and 1.365 m are 4.7%, 6.7%, and 1.1%, respectively. By considering the reported computational errors in the present work, it is found that the model represents better results, compared with the previous works [22–25].

4.2.2 Time-Averaged Solid Velocity Vector, and Contour Plot of Gas Volume Fraction. Figure 11 shows the time-averaged velocity vectors of the particles. This figure indicates that the particles move upward at the center of the bed and fall down near the

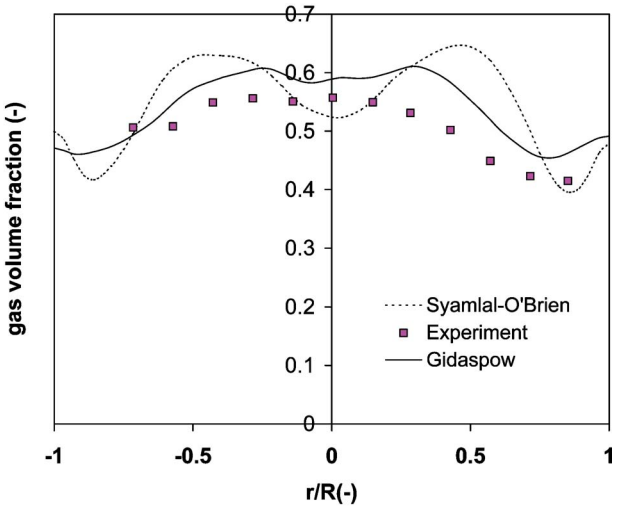

Fig. 5 Comparison of experimental and simulated time-averaged local voidage using drag models of Gidaspow and Syamlal–O'Brien at y=0.2 m and U_g=0.46 m/s

wall. This phenomenon is in accordance with the experimental data reported in the literature [33,34].

In general, slugging fluidization can occur in the beds of small diameter such as laboratory scale reactors and pilot-scale units, if three conditions are met: (1) the maximum bubble size greater than 0.6 times the diameter of the bed, (2) the superficial gas velocity sufficiently high, and (3) the sufficient depth of the bed [35]. Baeyens and Geldart [32] suggested a key correlation for the prediction of the slugging velocity limit

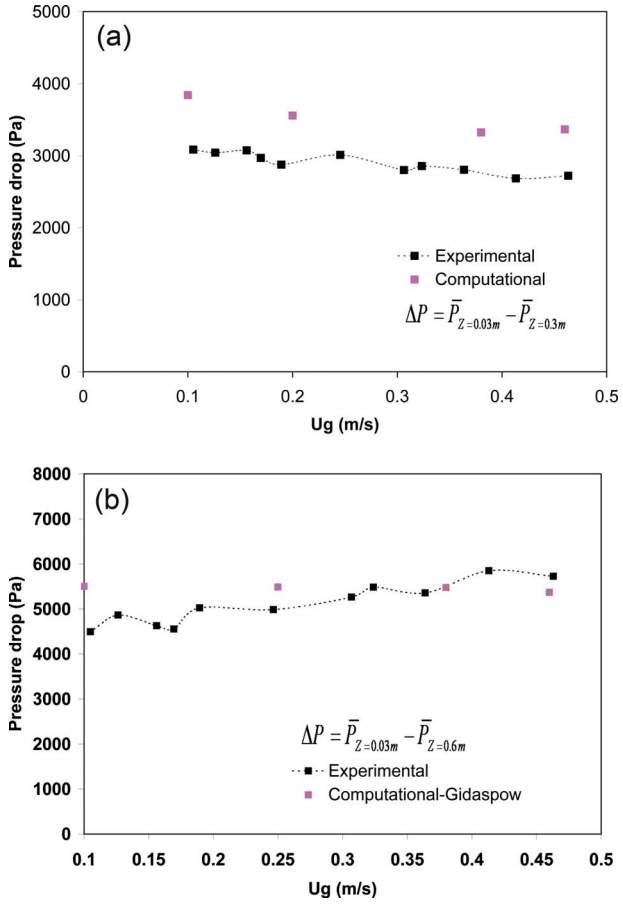

Fig. 7 Time-averaged pressure drop against superficial gas velocity (*a*) inside the bed and (*b*) overall the bed

Table 2 RMS deviation of numerical results

rms %	With Syamlal–O'Brien drag model	With Gidaspow drag model
Bed expansion ratio (H/H_0)	8.03	5.53
Local voidage at U_g=0.38 m/s	15.73	17.93
Local voidage at U_g=0.46 m/s	21.92	13.51

$$U_{ms} - U_{mf} = 0.07(gD)^{1/2} + 1.6 \times 10^{-3}(H_L - H_0)^2, \quad H_L = 60D^{0.175} \tag{28}$$

By considering U_{mf}=62 cm/s and Eq. (28), the minimum slugging velocity U_{ms} is equal to 81.8 cm/s. Therefore, in the case study (2), the bed operates in the slugging regime, which is confirmed by Fig. 12. This figure shows the snapshots of the gas

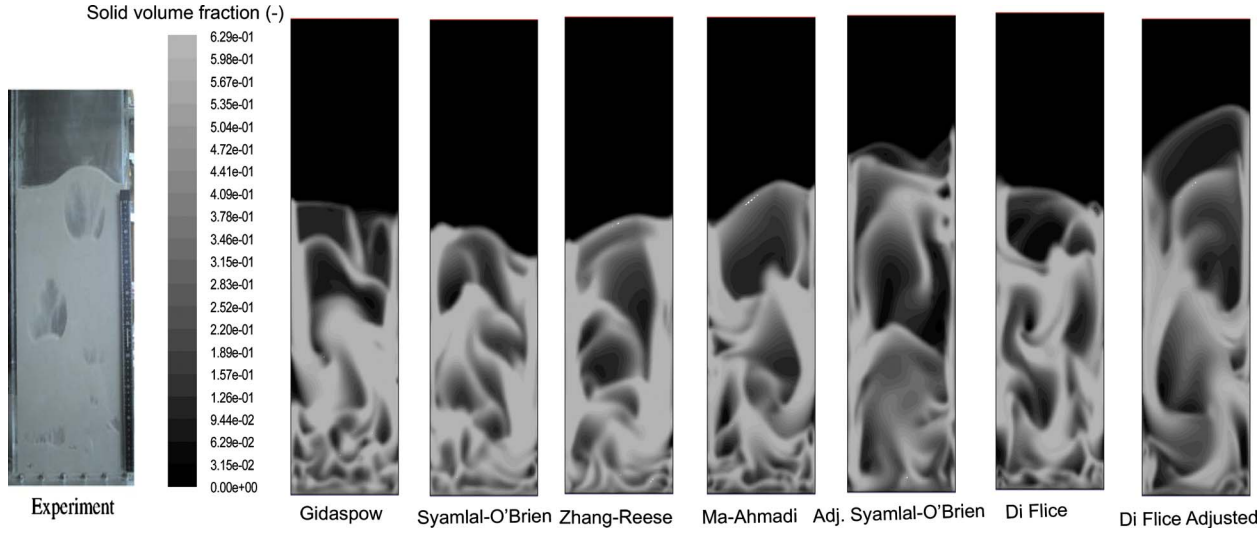

Fig. 6 Comparison of experiment and simulated bubbles for different drag models qualitatively (U_g=0.38 m/s)

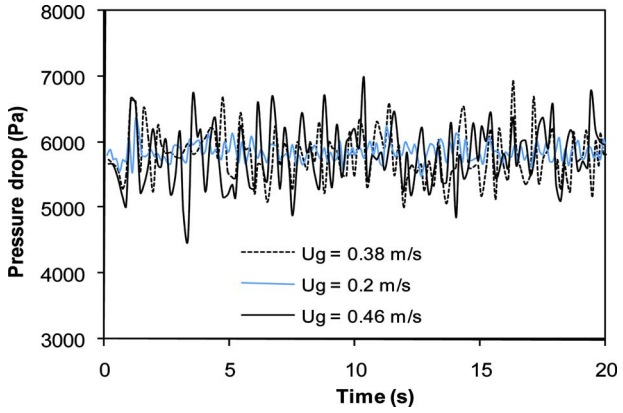

Fig. 8 Simulated bed pressure drop versus time at different gas velocities

volume fraction profile. Initially, the height of the solid in the bed increased until it leveled off at a quasisteady state bed height, although the apparent fluctuation in the bed height is due to bubble growth and coalescence. The slug is reached at $t=9$ s (Fig. 12).

By considering U_{ms}, Figs. 10(*a*) and 12, it can be concluded that the present model is suitable for simulation of the slugging fluidized beds. However, fluidized beds are chaotic systems and changes in geometry of the system; parameters of the solid phase and gas velocities lead to different results and conclusions. The current work showed that the model could be used for the wide range of gas velocity and different types of solid particles such as Geldart B and D.

5 Conclusion

The algebraic granular equation could be used for simulation of the dense gas-solid fluidized beds instead of the full granular temperature equation to reduce the computational time without loosing accuracy.

Predicted results showed that the Gidaspow's drag model had a better agreement with the experimental data, in comparison with the other drag models for the conventional BFB. The bubbling fluidization is occurred using all drag models excluding the adjusted models. Researchers reported that using the Syamlal–O'Brien adjusted drag model for BFB and circulating fluidized beds of FCC particles leads to reasonable results [36–38], while the present study showed that the adjusted drag functions, based on the minimum fluidization velocity, were not suitable for simulation of BFB of Geldart B particles.

The proposed model predicted the overall time-averaged pressure drop of the bed reasonably, especially when the bubbling regime was established. The model overpredicted the time-averaged pressure drop inside the bed. Besides, for the gas velocity in the range of the slugging regime, the simulation results not only predicted the good results in terms of the voidage profile in several levels of the bed and suitable solid velocity vector, but also showed the slug formation in the bed.

Predicted results also determined two major regions of the solid concentrations: the central part of the bed with dilute solid con-

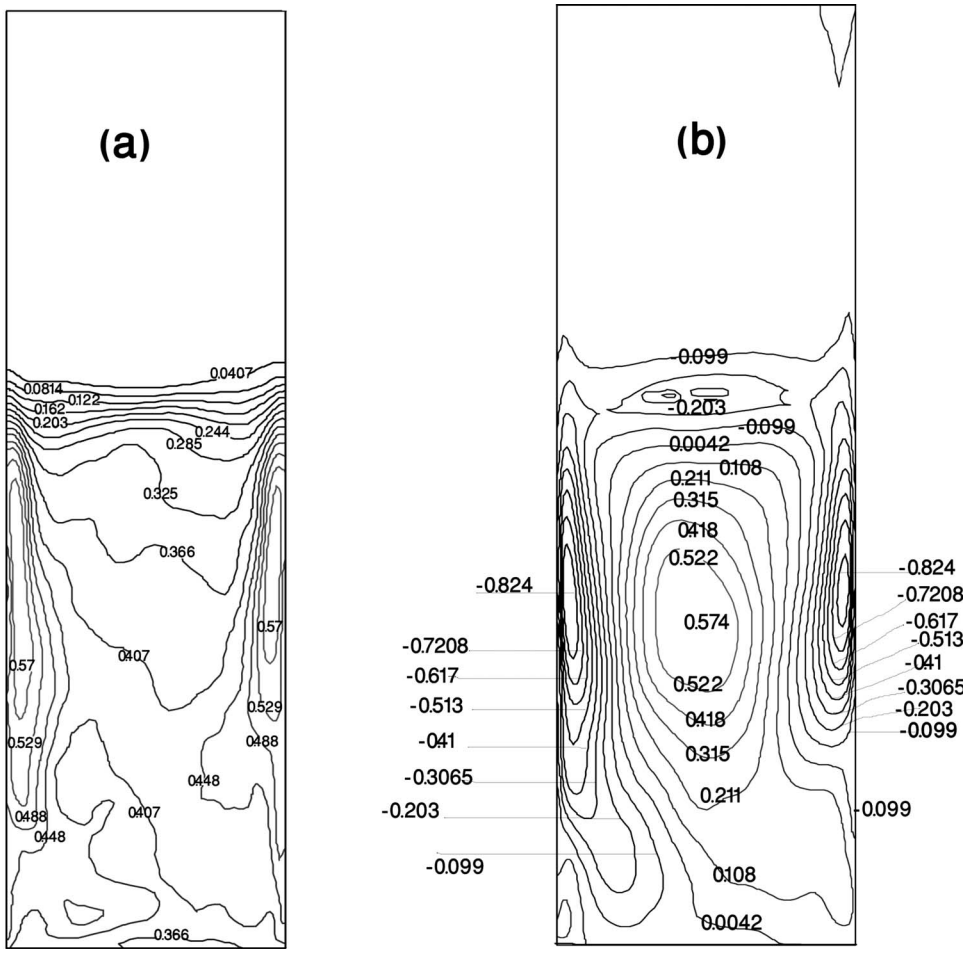

Fig. 9 Computed time-averaged (*a*) solid volume fraction and (*b*) solid axial velocity (m/s)

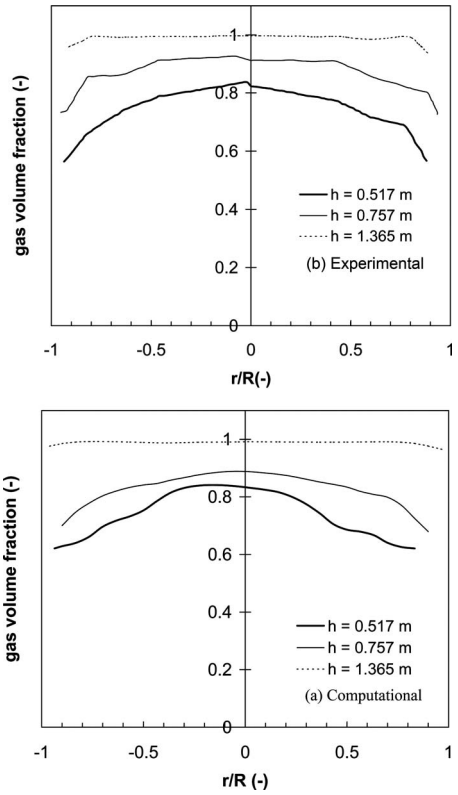

Fig. 10 Comparison between simulation results and experimental data in terms of radial distribution of gas volume fraction at various axial locations of the bed and U_g=2.8 m/s: (*a*) computational and (*b*) experimental

centration and near the wall with dense solid concentration. This model predicted more information about the time-averaged solid particles velocity at the whole part of the bed, which are helpful in the heat and mass transfer studies for future works.

Nomenclature

C_D = drag coefficient, dimensionless
d_i = diameter (m)
e_s = restitution coefficient, dimensionless
g = acceleration due to gravity (m/s^2)
g_0 = radial distribution coefficient, dimensionless
H = expanded bed height (m)
H_0 = static bed height (m)
$\bar{\bar{I}}$ = stress tensor, dimensionless
I_{2D} = second invariant of the deviatoric stress tensor, dimensionless
$k_{\Theta s}$ = diffusion coefficient for granular energy (kg/s m)
K_{gs} = gas/solid momentum exchange coefficient, dimensionless
P = pressure (Pa)
r = radial coordinate (m)
R = radius (m)
Re_s = Reynolds number, Eqs. (15) and (16), dimensionless
t = time (s)
U = superficial gas velocity (m/s)
v_i = velocity (m/s)
z = height coordinate measured from distributor (m)
v_s' = fluctuating particle velocity of the particulate phase

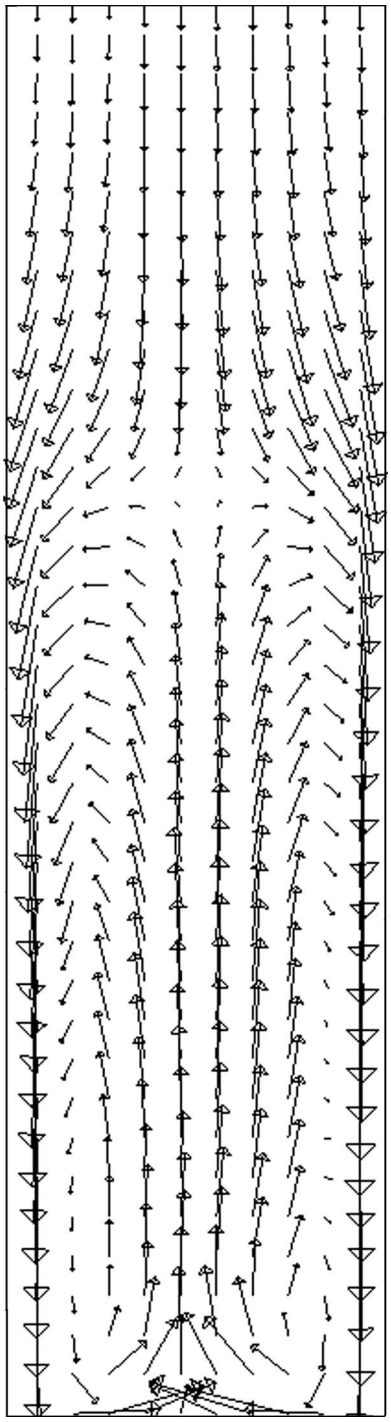

Fig. 11 Time-averaged velocity vectors of particles at U_g =2.8 m/s

$\langle v_s' \rangle$ = ensemble averaging of fluctuating particle velocity

Greek Letters

α_i = volume fraction
γ_s = the collisional dissipation of energy
Θ_s = granular temperature
λ_i = bulk viscosity (kg/(s m))
μ_i = shear viscosity (kg/(s m))
ρ_i = density (kg/m^3)
$\bar{\bar{\tau}}_i$ = stress tensor (Pa)

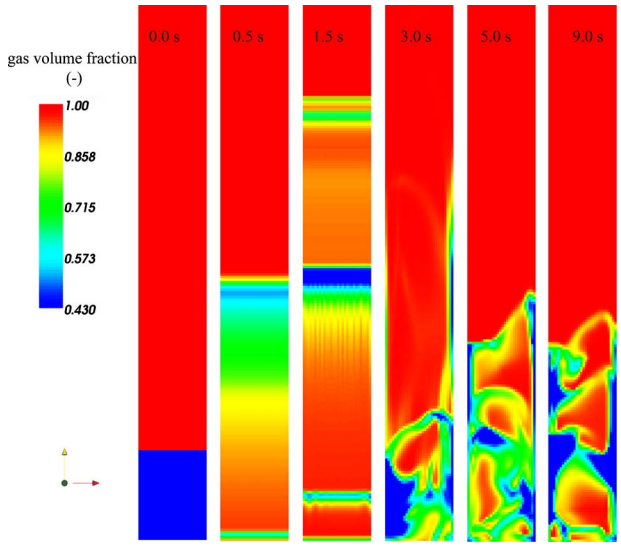

Fig. 12 Contour plot of gas volume fraction at U_g=2.8 m/s

ϕ = angle of internal friction
ϕ_{gs} = transfer rate of kinetic energy (kg/(s^3 m))

Subscripts

col = collision
fr = friction
g = gas
i = general index
kin = kinetic
mf = minimum fluidization
q = phase type (solid or gas)
s = solids
t = terminal
T = stress tensor

References

[1] Kunii, D., and Levenspiel, O., 1991, *Fluidization Engineering*, 2nd ed., Butterworths, London.
[2] Versteeg, H. K., and Malalsekera, W., 1995, *An Introduction to Computational Fluid Dynamics: The Finite Volume Method*, Longmans, London.
[3] Hosseini, S. H., Rahimi, R., Zivdar, M., and Samimi, A., 2009, "The Effect of Ring Baffles on Hydrodynamics of a Gas-Solid Bubbling Fluidized Bed by Using Computational Fluid Dynamics," Proc. Inst. Mech. Eng., Part C: J. Mech. Eng. Sci., **223**, pp. 2281–2289.
[4] Oberkampf, W. L., and Trucano, T. G., 2002, "Verification and validation in computational fluid dynamics," Prog. Aerosp. Sci., **38**(3), pp. 209–272.
[5] Grace, J. R., and Taghipour, F., 2004, "Verification and Validation of CFD Models and Dynamic Similarity for Fluidized Beds," Powder Technol., **139**, pp. 99–110.
[6] Rietema, K., and Mutsers, S. M. P., 1973, "The Effect of Inter-Particle Forces on the Expansions of a Homogeneous Gas-Fluidized Bed," *Proceedings of the International Symposium on Fluidization*, Toulouse, pp. 28.
[7] Patil, D. J., van Sint Annaland, M., and Kuipers, J. A. M., 2005, "Critical Comparison of Hydrodynamic Models for Gas-Solid Fluidized Beds—Part I: Bubbling Gas-Solid Fluidized Beds Operated With a Jet," Chem. Eng. Sci., **60**, pp. 57–72.
[8] Patil, D. J., van Sint Annaland, M., and Kuipers, J. A. M., 2005, "Critical Comparison of Hydrodynamic Models for Gas-Solid Fluidized Beds—Part II: Freely Bubbling Gas-Solid Fluidized Beds," Chem. Eng. Sci., **60**, pp. 73–84.
[9] Pain, C. C., Mansoorzadeh, S., and de Oliveira, C. R. E., 2001, "A Study of Bubbling and Slugging Fluidised Beds Using the Two-Fluid Granular Temperature Model," Int. J. Multiphase Flow, **27**, pp. 527–551.
[10] van Wachem, B. G. M., Schouten, J. C., Krishna, R., and van den Bleek, C. M., 1998, "Eulerian Simulations of Bubbling Behaviour in Gas-Solid Fluidised Beds," Comput. Chem. Eng., **22**, pp. S299–S306.
[11] Ding, J., and Gidaspow, D., 1990, "A Bubbling Fluidization Model Using Kinetic Theory of Granular Flow," AIChE J., **36**, pp. 523–538.
[12] Ding, J. M., and Lyczkowski, R. W., 1992, "Three-Dimensional Kinetic-Theory Modeling of Hydrodynamics and Erosion in Fluidized-Beds," Powder Technol., **73**, pp. 127–138.
[13] Enwald, H., and Almstedt, A. E., 1999, "Fluid Dynamics of a Pressurized Fluidized Bed: Comparison Between Numerical Solutions From Two-Fluid Models and Experimental Results," Chem. Eng. Sci., **54**, pp. 329–342.
[14] van Wachem, B. G. M., Schouten, J. C., Krishna, R., van den Bleek, C. M., and Sinclair, J. L., 2001, "Comparative Analysis of CFD Models of Dense Gas-Solid Systems," AIChE J., **47**(5), pp. 1035–1051.
[15] Huilin, L., Yurong, H., Wentie, L., Jianmin, D., Gidaspow, D., and Bouillard, J., 2004, "Computer Simulations of Gas-Solid Flow in Spouted Beds Using Kinetic-Frictional Stress Model of Granular Flow," Chem. Eng. Sci., **59**(4), pp. 865–878.
[16] Du, W., Bao, X. J., Xu, J., and Wei, W. S., 2006, "Computational Fluid Dynamics (CFD) Modeling of Spouted Bed: Influence of Frictional Stress, Maximum Packing Limit and Coefficient of Restitution of Particles," Chem. Eng. Sci., **61**(14), pp. 4558–4570.
[17] Syamlal, M., and O'Brien, T., 1989, "Computer Simulation of Bubbles in a Fluidized Bed," AIChE Symp. Ser., **85**, pp. 22–31.
[18] Gidaspow, D., 1994, *Multiphase Flow and Fluidization: Continuum and Kinetic Theory Descriptions*, Academic, San Diego.
[19] Wen, C.-Y., and Yu, Y. H., 1966, "Mechanics of Fluidization," Chem. Eng. Prog., **62**(2), pp. 100–111.
[20] Hosseini, S. H., Rahimi, R., Zivdar, M., and Samimi, A., 2009, "CFD Simulation of Gas-Solid Bubbling Fluidized Bed Containing FCC Particles," Korean J. Chem. Eng., **26**(5), pp. 1405–1413.
[21] Hosseini, S.H., Zivdar, M., Rahimi, R., and Samimi, A., 2009, "CFD Simulation of Solid Hold-Up in Gas-Solid Fluidized Bed at High Gas Velocities," Chemical Product and Process Modeling, **4**(1), Article 19, pp. 1–24.
[22] McKeen, T. R., and Pugsley, T. S., 2003, "Simulation and Experimental Validation of a Freely Bubbling Bed of FCC Catalyst," Powder Technol., **129**, pp. 139–152.
[23] Taghipour, F., Ellis, N., and Wong, C., 2005, "Experimental and Computational Study of Gas-Solid flUidized Bed Hydrodynamics," Chem. Eng. Sci., **60**, pp. 6857–6867.
[24] Behjat, Y., Shahhosseini, S., and Hashemabadi, S. H., 2008, "CFD Modeling of Hydrodynamic and Heat Transfer in Fluidized Bed Reactors," Int. Commun. Heat Mass Transfer, **35**, pp. 357–368.
[25] Ahuja, G. N., and Patwardhan, A. W., 2008, "CFD and Experimental Studies of Solids Hold-Up Distribution and Circulation Patterns in Gas-Solid Fluidized Beds," Chem. Eng. J., **143**, pp. 147–160.
[26] Syamlal, M., Rogers, W., and O'Brien, T.J., 1993, MFIX Documentation: Theory Guide, Technical Paper No. DOE/METC-94/1004.
[27] Boemer, A., Qi, H., Renz, U., Vasquez, S., and Boysan, F., 1995, "Eulerian Computation of Fluidized Bed Hydrodynamics—A Comparison of Physical Model," *Proceedings of the International Conference on FBC*, Orlando, FL, pp. 775.
[28] Esfahani, M. N., Rahimi, R., and Hosseini, S. H., 2006, "Hydrodynamics of a Gas-Fluidized Bed by CFD," *Proceedings of the 11th Iranian National Chemical Engineering Congress*, Tarbiat Modarres University, Tehran.
[29] 2006, FLUENT 6.3, User's Guide, 23.5 Eulerian Model, Fluent Inc.
[30] Vejahat, F., 2006, "CFD Simulation of Gas-Solid Bubbling Fluidized Bed," MS thesis, University of Regina, Canada.
[31] Pain, C. C., Mansoorzadeh, S., de Oliveira, C. R. E., and Goddard, A. J. H., 2001, "Numerical Modelling of Gas-Solid Fluidized Beds Using the Two-Fluid Approach," Int. J. Numer. Methods Fluids, **36**, pp. 91–124.
[32] Baeyens, J., and Geldart, D., 1974, "An Investigation Into Slugging Fluidized Beds," Chem. Eng. Sci., **29**, pp. 255–265.
[33] Laverman, J. A., Roghair, I., and van Sint Annaland, M., 2008, "Investigation Into the Hydrodynamics of Gas-Solid Fluidized Beds Using Particle Image Velocimetry Coupled With Digital Image Analysis," Can. J. Chem. Eng., **86**, pp. 523–535.
[34] Lin, J. S., Chen, M. M., and Chao, B. T., 1985, "A Novel Radioactive Particle Tracking Facility for Measurement of Solids Motion in Gas Fluidized Beds," AIChE J., **31**, pp. 465–473.
[35] Lettieri, P., Cammarata, L., Micale, G. D. M., and Yates, J., 2003, "CFD Simulations of Gas Fluidized Beds Using Alternative Eulerian-Eulerian Modelling Approaches," International Journal of Chemical Reactor Engineering, **1**, Article A5, pp. 1–19.
[36] Syamlal, M., and O'Brien, T. J., 2003, "Fluid Dynamic Simulation of O_3 Decomposition in a Bubbling Fluidized Bed," AIChE J., **49**(11), pp. 2793–2801.
[37] Zimmermann, S., and Taghipour, F., 2005, "CFD Modeling of the Hydrodynamics and Reaction Kinetics of FCC Fluidized-Bed Reactors," Ind. Eng. Chem. Res., **44**, pp. 9818–9827.
[38] Almuttahar, A., and Taghipour, F., 2008, "Computational Fluid Dynamics of High Density Circulating Fluidized Bed Riser: Study of Modeling Parameters," Powder Technol., **185**, pp. 11–23.

Implicit LES Predictions of the Cavitating Flow on a Propeller

Rickard E. Bensow

Göran Bark

Shipping and Marine Technology,
Chalmers University of Technology,
412 96 Gothenburg, Sweden

We describe an approach to simulate dynamic cavitation behavior based on large eddy simulation of the governing flow, using an implicit approach for the subgrid terms together with a wall model and a single fluid, two-phase mixture description of the cavitation combined with a finite rate mass transfer model. The pressure-velocity coupling is handled using a PISO algorithm with a modified pressure equation for improved stability when the mass transfer terms are active. The computational model is first applied to a propeller flow in homogeneous inflow in both wetted and cavitating conditions and then tested in an artificial wake condition yielding a dynamic cavitation behavior. Although the predicted cavity extent shows discrepancy with the experimental data, the most important cavitation mechanisms are present in the simulation, including internal jets and leading edge desinence. Based on the ability of the model to predict these mechanisms, we believe that numerical assessment of the risk of cavitation nuisance, such as erosion or noise, is tangible in the near future. [DOI: 10.1115/1.4001342]

1 Introduction

Cavitation is responsible for most major constraints in propeller design, related to noise, vibration, and erosion but is a complex phenomenon not yet neither reliably assessable nor fully understood. Standard design tools typically include potential flow solvers, lifting surface or boundary element approaches, with strict theoretical limits on cavitation modeling that only in the hands of an experienced designer may give satisfactory propeller designs. This situation, together with fairly short design cycles, makes it difficult to advance the design toward smaller safety margins to cavitation nuisance and thus hinder efficiency improvements. There is thus a need both for better understanding of the physical mechanisms leading to cavitation nuisance as well as for improved prediction and analysis tools.

Experimental observations alone can show many of the phenomena occurring but suffers from limitations in the measurement techniques. One example is in measuring reentrant jets and internal flow, flow features hidden for optical measurement techniques by the cavity itself but often important to study in the development of erosive cavitation [1]. The access to the complete flow field through a numerical simulation would thus be a welcome complement to experimental data. The numerical simulation of cavitation does, however, include many complications since some of the physics of the fluid and the mass transfer are unknown. Moreover, the cavitation dynamics is governed by medium to small flow scales, both in time and space [1], necessitating large computational grids and small time steps.

In this paper, we study the feasibility to use incompressible large eddy simulation (LES) techniques, using an implicit modeling approach for the subgrid term, for the prediction of cavitation on a propeller, based on considering the flow as a single fluid, two-phase mixture. A model transport equation for the local volume fraction of vapor is solved together with the LES equations and a finite rate mass transfer model is used for the vaporization and condensation processes.

The propeller we use is the four-bladed INSEAN E779A. Although an old design, the experimental database is extensive, including both PIV and LDV wake measurements [2–4] and cavitation observation in homogeneous [5] and inhomogeneous [6] flow conditions, which makes it a good validation case. The conditions studied computationally in this work is (i) uniform inflow at an advance number $J=0.71$ and cavitation number $\sigma=1.76$ and (ii) nonuniform inflow, formed by an artificial wake inflow, at $J=0.71$ and $\sigma=4.455$. Bensow and Liefvendahl [7] previously reported a validation study for this propeller in noncavitating conditions, using the same LES technique as in this work.

We start by describing the modeling approaches in some detail and discuss the basic validation of the computational model both for noncavitating as well as for cavitating flows. We then continue by summarizing the results of Bensow and Liefvendahl [7] for the noncavitating conditions at $J=0.88$ as a validation for wetted propeller flow. Next, follows an analysis of the simulations results for the cavitating flow, starting in uniform inflow followed by the propeller in the artificial wake. Finally, we summarize our findings and give some outlooks for future work.

2 Modeling Techniques

The simulations presented in this paper are based on applying an incompressible LES approach, based on cell-centered, unstructured finite volume (FV) technique, solved using a segregated pressure implicit with splitting of operators (PISO) algorithm for the velocity-pressure coupling with a modified pressure equation to increase the stability for cavitation simulations. To model the cavitating flow, we adopt a two-phase mixture assumption by introducing the vapor volume fraction and solving an additional transport equation, incorporating finite rate mass transfer models for the vaporization and condensation processes. Before giving some details of the different modeling components listed above, we start by discussing and motivating our choices. References are given to recent work that complement or support our ideas but are not intended as a review of the current status of the research field. For comparisons between different mass transfer modeling approaches based on a transport equation we refer to, e.g., Refs. [8] or 9, where the latter also gives a brief outlook on other approaches.

In LES, the large, energy-containing structures are resolved on the computational grid, whereas the smaller, more isotropic, subgrid structures are modeled; this separation of scales within the flow is accomplished by a (implicit) low-pass filtering of the Navier–Stokes equations, see, e.g., the book by Sagaut [10]. In contrast with RANS approaches (e.g., Wilcox [11]), which are based on the average flow description, LES naturally and consistently allows for medium- to small-scale, transient flow structures. When simulating unsteady, cavitating flows, we believe this is an important property in order to be able to capture the mechanisms

Contributed by the Fluids Engineering Division of ASME for publication in the JOURNAL OF FLUIDS ENGINEERING. Manuscript received July 1, 2009; final manuscript received February 9, 2010; published online April 13, 2010. Assoc. Editor: Olivier Coutier-Delgosha.

governing the dynamics of the formation and shedding of the cavity. An alternative approach that also takes these scales into account is to solve the Euler equations, thus neglecting viscous effects. However, we believe that viscosity plays a small but important role in the generation of secondary cavities that can be of very erosive character. Moreover, the long-term goal is to study propeller and rudder cavitation and it's erosive and noise generating nature in a correctly simulated ship hull wake, thus including boundary layers and appendage wakes, which are due to viscous action.

It is often considered that compressibility effects can be neglected unless pressure pulse generation and propagation is of particular interest, and this was also our starting point for this work. We have however noted, both in this study and from experiences from Huuva [12], that there seems to be a possibility for improvement in the flow physics representation if compressibility is accounted for. This relates to rebounds and interaction phenomena between different cavities as well as the pressure field development. The coupling between the pressure and the density in a PISO based approach is further discussed by Senocak and Shyy [13], where different approximations of the speed of sound are tested and greatly affects the unsteady behavior of an attached sheet cavity. Furthermore, good results were recently obtained using a fully compressible solver by, e.g., Schnerr et al. [14] and Koop [15], although at a tough penalty having the time step limited by the acoustics, or by Qin et al. [16], where a weakly compressible approach is used.

The two-phase mixture assumption, as compared with a two fluid modeling, is well in line with the filtering in LES; small bubbles that are not possible to resolve are seen as a mixture through the LES filter. This will hold also for larger bubbles unless the grid is aligned with the interface, which is not a reasonable approach. The imposed approximation with this approach is that it does not easily include the slip between the velocities in the liquid and vapor phases, which may occur for large bubbles. We do however believe this to have a very small influence of the dynamics being governed by the heavier phase.

The finite rate mass transfer modeling follows the work of Kunz et al. [17] with one vaporization source, active in regions, where the pressure is below vaporization pressure and a condensation source active in the interface regions, both entering the vapor volume fraction transport equation and the velocity divergence constraint. In our experience, as well as in literature [8,18,19], different phase change modeling approaches yield similar results and the choice of one or another seem not to be crucial in cavitation simulation.

One important effect not included in our model, is the presence of noncondensable gases dissolved in the liquid water. During the vaporization, this gas content will be transferred to a gaseous state and remain in gaseous form for some time after the condensation and leaves a clear trace of previous cavitation in the water, affecting its strength and thus it's cavitation dynamics if passing into a low-pressure region once more. This would be of great importance when simulating, e.g., rudder cavitation in behind conditions or flows where ventilation is important. Noncondensable gas effects are included in Ref. [17] but in the present efforts to simulate the primary occurring cavities on the propeller blade, we believe this is not of a significant importance. However, in the continued work toward more complex configurations or looking more into details of secondary cavitation and rebounds, noncondensable gases certainly needs to be taken into account.

2.1 Large Eddy Simulation. Starting from the incompressible Navier–Stokes equations, the governing flow equations consist of the balance equations of mass and momentum,

$$\partial_t(\rho\mathbf{v}) + \nabla\cdot(\rho\mathbf{v}\otimes\mathbf{v}) = -\nabla p + \nabla\cdot\mathbf{S}$$
$$\nabla\cdot(\rho\mathbf{v}) = 0 \tag{1}$$

where $\mathbf{v}$ is the velocity, p is the pressure, $\mathbf{S}=2\mu\mathbf{D}$ is the viscous stress tensor, where the rate-of-strain tensor is expressed as $\mathbf{D}=1/2(\nabla\mathbf{v}+\nabla\mathbf{v}^T)$, and μ is the viscosity. The LES equations are derived, following, e.g., Sagaut [10], from Eq. (1) by applying low-pass filtering, using a predefined filter kernel function $G=G(\mathbf{x},\boldsymbol{\Delta})$, such that

$$\partial_t(\rho\bar{\mathbf{v}}) + \nabla\cdot(\rho\bar{\mathbf{v}}\otimes\bar{\mathbf{v}}) = -\nabla\bar{p} + \nabla\cdot(\bar{\mathbf{S}}-\mathbf{B})$$
$$\nabla\cdot(\rho\bar{\mathbf{v}}) = 0 \tag{2}$$

where overbars denote filtered quantities and commutation errors have been neglected. Equation (2) introduces one new term when compared with the unfiltered Eq. (1): the unresolved transport term, where $\mathbf{B}=\rho(\overline{\mathbf{v}\otimes\mathbf{v}}-\bar{\mathbf{v}}\otimes\bar{\mathbf{v}})$ is the subgrid stress tensor. Following Bensow and Fureby [20], $\mathbf{B}$ can be exactly decomposed as

$$\mathbf{B} = \rho(\overline{\bar{\mathbf{v}}\otimes\bar{\mathbf{v}}} - \bar{\bar{\mathbf{v}}}\otimes\bar{\bar{\mathbf{v}}} + \widetilde{\mathbf{B}}) \tag{3}$$

where now only $\widetilde{\mathbf{B}}$ needs to be modeled. We remark that the first term on the right hand side in Eq. (3) is identical to the scale similarity term of Bardina et al. [21]. We will here employ an implicit LES (ILES) approach, meaning that no explicit model is applied for $\widetilde{\mathbf{B}}$. Instead the numerical dissipation is considered enough to mimic the action of $\widetilde{\mathbf{B}}$, see Ref. [22] and the references therein and Bensow and Liefvendahl [7] for an application to propeller flows.

In LES, the grid in the near wall region needs refinement in all three directions compared with the free-stream resolution in order to resolve the energetic structures. In particularly, the resolution in the spanwise direction is important, as opposed to RANS where the wall normal resolution is in focus. However, for flows of engineering interest, the computational cost for a wall resolved LES, capturing the anisotropic flow structures such as streaky structures, hairpin vortices and ejection events, is too high. Instead, we apply a wall model based on the logarithmic law of the wall, implemented through an adjustment of the viscosity in the cells adjacent to the wall. We thus add a subgrid wall-viscosity ν_{WM} to $\nu=\mu/\rho$ on the wall so that the effective viscosity $\nu+\nu_{WM}$ becomes $\nu+\nu_{WM}=\tau_w/(\partial v_y/\partial y)_p=u_\tau y_{y,p}/v^+_{y,p}$, where the subscript P denotes evaluation at the first grid point away from the wall, see Ref. [23] for more details. Although a very simple approach, it was successfully applied to a wide range of flows, including the ILES modeling we use in this paper, see, e.g., Refs. [7,24,25].

2.2 Multiphase Modeling. To simulate cavitating flows, the two phases, liquid and vapor, need to be represented in the problem, as well as the phase transition mechanism between the two. Here, we consider a one fluid, two-phase mixture approach, where density and viscosity varies linearly as a function of the local vapor volume fraction. The spatial and temporal variation in the vapor fraction is described by a transport equation including source terms for the mass transfer rate between the phases.

Adding this transport equation to the filtered equations of continuity and momentum, Eq. (2), we get

$$\partial_t(\rho\bar{\mathbf{v}}) + \nabla\cdot(\rho\bar{\mathbf{v}}\otimes\bar{\mathbf{v}}) = -\nabla\bar{p} + \nabla\cdot(\bar{\mathbf{S}}-\mathbf{B}) \tag{4a}$$

$$\partial_t\rho + \nabla\cdot(\rho\bar{\mathbf{v}}) = 0 \tag{4b}$$

$$\partial_t\alpha + \nabla\cdot(\alpha\bar{\mathbf{v}}) = \dot{m}/\rho_v \tag{4c}$$

where $\dot{m}$ is the mass transfer rate from liquid to vapor, ρ_v the density of the vapor, and α is the vapor volume fraction, where $\alpha=1$ corresponds to pure vapor and $\alpha=0$ to pure liquid. Of course, alternatively, the liquid volume fraction could be used with the corresponding definition and transport equation.

As mentioned above, the vapor volume fraction is used to scale the physical properties of vapor and liquid as

$$\rho = \alpha\rho_v + (1-\alpha)\rho_l \tag{5a}$$

$$\mu = \alpha\mu_v + (1-\alpha)\mu_l \tag{5b}$$

where the bulk densities, ρ_l and ρ_v and viscosities μ_l and μ_v for liquid and vapor are kept constant throughout the computation. Inserting the density according to Eq. (5*a*) into the continuity Eq. (4*b*) and using the vapor transport Eq. (4*c*), we find the well known inhomogeneous velocity divergence for the cavitating flow,

$$\nabla \cdot \mathbf{v} = \left(\frac{1}{\rho_v} - \frac{1}{\rho_v}\right)\dot{m} \tag{6}$$

which indicates that the mass transfer rate needs to be incorporated also in the pressure equation in the PISO algorithm we use.

2.3 Kunz *et al.* [17] Mass Transfer Model. The mass transfer model used in this study is based on the ideas of Kunz et al. [17], that in turn originates from the work of Merkle et al. [26]. The final form of the model can however be considered as based on fairly intuitive, ad hoc arguments. The mass transfer in this model is based on different strategies for vaporization and condensation, compared with most similar models that only rely on a single expression for both creation and destruction of vapor. The vaporization $\dot{m}^+$ is modeled to be proportional to the amount by which the pressure is below the vapor pressure and the amount of liquid present while the condensation $\dot{m}^-$ is based on a third order polynomial function of the vapor volume fraction,

$$\dot{m}^+ = A^+\rho_v(1-\alpha)\frac{\min[0,\bar{p}-p_v]}{1/2\rho_l U_\infty^2} \tag{7a}$$

$$\dot{m}^- = A^-\rho_v(1-\alpha)\alpha^2 \tag{7b}$$

and the specific mass transfer rate is computed as $\dot{m}=\dot{m}^+-\dot{m}^-$. Here, $\bar{p}$ is the filtered pressure, p_v is the vaporization pressure and A^+ and A^- are empirical constants (of dimension $[s^{-1}]$); the values used and their impact on the results will be discussed below in connection with the simulation results. Thus, vaporization occurs when the pressure is below the vapor pressure and there exist some liquid to vaporize while condensation is restricted to the interface region of the cavity, independent of the pressure with a maximum at $\alpha=1/3$ and going to zero in the pure vapor region and the pure liquid region. The properties of $\dot{m}$ are thus such that the vapor fraction should stay in the interval $\alpha \in [0,1]$ but in the numerical solution procedure this is however not guaranteed. In our simulations, this has not been a problem and no limiting procedure on α has been applied.

2.4 Discretization and Solver Procedure. The computational model described above has been implemented using the OpenFOAM libraries [27]. The spatial discretization is performed using a cell-centered colocated FV method for unstructured meshes with arbitrary cell-shapes, and a multistep scheme is used for the time derivatives. To complete the FV-discretization the face fluxes need to be reconstructed from grid variables at adjacent cells, requiring interpolation of the convective fluxes and difference approximations for the inner derivatives of the diffusive fluxes; see Refs. [28,29] for more details on the discretization and the numerics used in OpenFOAM. For the simulations presented in this paper, a second order implicit time scheme is used combined with second order linear interpolation in space, except for the convective terms discussed in the next paragraph. The time step is set small enough to ensure a maximum Courant number (Co) of less than 0.5 everywhere in the computational domain. The iterative solvers are considered converged when the residuals have been reduced by a factor of 10^{-10}.

Since the present methodology is based on implicit modeling of the modified subgrid stress tensor $\tilde{\mathbf{B}}$, a slightly diffusive scheme is needed to make the leading order truncation error act as the dissipative action of the subgrid stress tensor. This can be performed using different kind of limiters and schemes, and in the present simulations a simple form is used via a TVD limited linear interpolation scheme. Several different discretization schemes were tested and it is shown in Bensow and Liefvendahl [7] that this approach does not cause excessive numerical diffusion and yields results that are comparable to the ones achieved with a pure second order scheme together with an explicit subgrid model.

The pressure-velocity coupling is handled via a PISO procedure [30] based on a Rhie–Chow-like interpolation for cell-centered data [31]. Before entering the PISO-loop, the vapor volume fraction transport equation is solved as well as a momentum predictor step. The mass transfer terms are incorporated into the pressure Poisson equation through Eq. (6) as a split source term with the part including the pressure treated implicitly, whereas the rest is treated explicitly, similar to what was done in Ref. [17],

$$\nabla \cdot \left(\frac{1}{\mathbf{A}}\nabla[\bar{p}]\right) - (\rho_v^{-1}-\rho_l^{-1})M^+[\bar{p}] = \nabla \cdot [\mathbf{U}^*] + (\rho_v^{-1}-\rho_l^{-1})(\dot{m}^- - M^+ p_v) \tag{8}$$

where $\mathbf{A}$ is the discretized operator decomposed from the momentum equations, $\mathbf{U}^*$ is the intermediate velocity prediction, and M^+ is the pressure independent part of Eq. (7*a*),

$$M^+ = -A^+\rho_v(1-\alpha)\frac{\text{neg}[\bar{p}^{k-1}-p_v]}{1/2\rho_l U_\infty^2} \tag{9}$$

where is $\bar{p}^{k-1}$ the pressure solution in the previous iteration. This split is introduced to increase the stability of the solution procedure, since the mass transfer terms can reach very large values in certain regions of the computational domain.

The current solver implementation does not support relative motion between different parts in the domain. Thus, the propeller rotation is created by rotating the complete mesh in space, updating the grid points in each time step. The solver is modified as described in Ref. [32] to implement the mesh motion while respecting the so-called discrete space conservation law, which is particularly important for incompressible flow simulations. The alternative approach of using a rotating frame of reference yields, according to our experience, degraded accuracy, possibly due to the introduction of large centrifugal and Coriolis forces into the momentum equations. In particular the case with the propeller in nonuniform inflow would benefit from the possibility of keeping the major part of the domain fixed in space and only rotate a part surrounding the propeller. This is since a large amount of control volumes are wasted in resolving the artificial wake when the complete mesh is rotated. Relative motion is of course a necessary solver development to be performed before a hull/propeller/rudder simulation can be performed.

2.5 Validation of Computational Model. The modeling techniques and their implementation described above were used extensively for noncavitating flows, ranging from more basic validation cases such as channel flow [24] and the flow past a circular cylinder [33] to more advanced cases such as the Darpa SubOFF [24] and the propeller simulations reviewed below from Ref. [7]. This last reference includes a discussion of, e.g., subgrid model sensitivity, and a comparison between ILES and the use of an explicit subgrid model.

For the cavitation modeling we here briefly report simulations of the cavitation on a hemispherical head shape at 0 deg angle of attack at $\text{Re}=1.36\times10^5$, experimentally investigated by Rouse and McNown [34]. This was one of the cases used by Kunz et al. [17] and it was repeated in the investigations by, e.g., Vaidyanathan et al. [35], Senocak and Shyy [9], and Ahuja et al. [36]. Our simulations were performed transiently in a fully three-dimensional domain in order to mimic the configurations used for the propeller simulations and for wetted flow and cavitating flow at $\sigma=0.40$. The grid used contained 2.2×10^6 hexahedral cells

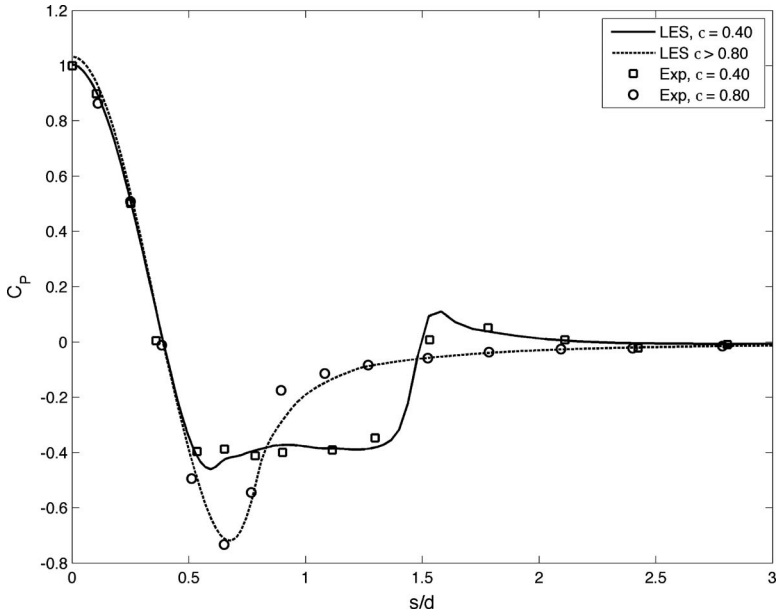

Fig. 1 Pressure distribution on the hemispherical head shape for noncavitating and cavitating conditions

with the parameters $A^+=2\times10^4$, $A^-=10^3$, and $\rho_l/\rho_v=1000$, same as we use for the propeller simulations. As can be seen in Fig. 1 the pressure distribution agrees well with experimental data for both the wetted and the cavitating flow. We noted some minor unsteadiness of the cavity in the simulations, as can be expected, and we here report average values.

3 The INSEAN E779A Propeller

The propeller INSEAN E779A is a four-bladed propeller, originally designed in the 1950:s for a ferry but was never built in full scale. Although being an outdated design, an extensive experimental database has been built by the research team at the Italian ship model basin, INSEAN, and it can be considered as one of the most completely mapped conventional propellers in open literature. Moreover, the propeller was selected as a validation case for multiphase flow developments within the EU-project VIRTUE and comparisons between several different simulation approaches, including potential flow solvers, RANS, and LES, were reported in Refs. [18,19]. The data set covers the propeller in both homogeneous inflow as well as in an artificial wake for both noncavitating and cavitating conditions. Among the published data are PIV and LDV of the propeller wake [2,3], cavitation pattern [6], and pressure-velocity correlations [4].

The propeller geometry has been obtained through a three-dimensional mapping using a digital topometry technique. The propeller diameter is $D_P=0.227$ m and is displayed in Fig. 2. The cavitation tunnel, where the experiments were performed has a square cross section with fillets in the corners. The propeller blocking is reported to be less than 10%. The experimental conditions were a water density of $\rho=1000$ kg/m^3 and viscosity $\nu=1.11\times10^{-6}$ m^2/s.

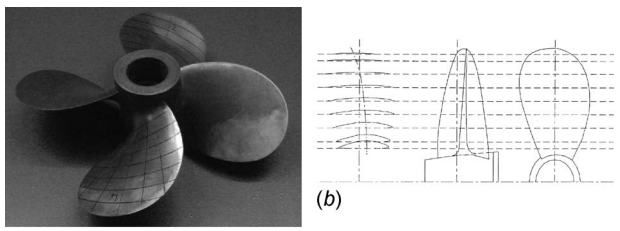

Fig. 2 The INSEAN E779A propeller

4 Simulation Results

4.1 Computational Domain and Grids. In order to avoid the need for relative motion between the propeller and the external domain, the computational domain was simplified to a cylinder extending one D_P upstream the propeller and 3.75 D_P downstream with a radius of 0.334 m, yielding the same cross-sectional area as the cavitation tunnel. The computational grids have approximately 4.5×10^6 cells composed of tetrahedrals with prisms in the boundary layer and manually refined in the tip vortex region, the region of expected cavitation and the blade wakes, see Fig. 3. For the nonuniform inflow case, the refinement in the blade wake was sacrificed in order to increase the resolution upstream of the propeller to be able to transport the artificial wake, defined as an inlet

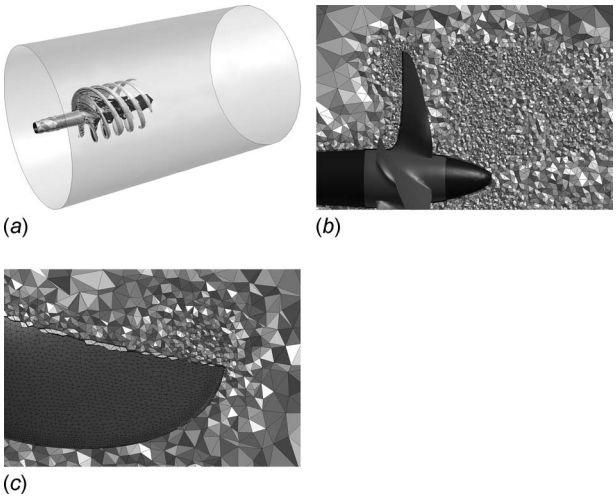

Fig. 3 The computational domain and the grid for the uniform inflow case. In (a), the flow is visualized with two isosurfaces of the helicity.

Table 1 Computed open water coefficients at $J=0.88$ and $J=0.71$ in noncavitating conditions

J		K_T	$10K_Q$	η
0.88	Exp	0.157	0.306	0.719
	LES	0.159	0.307	0.725
0.71	Exp	0.256	0.464	0.623
	LES	0.256	0.453	0.639

boundary condition, up to the propeller. On the blades, the cell sizes in the wall normal direction are such that $y^+ \leq 10$ except near the leading edge, where higher velocities lead to slightly higher values. For the surface mesh, a typical triangle base length of $x^+ \approx 300$ is encountered in the middle of the blade with considerably smaller triangles used toward the edges. This near wall resolution is deemed sufficient for reliable wall-modeled LES based on our experiences with the applied wall model. In order to reach a high accuracy in time, we allow for 20 time steps per degree rotation thus satisfying the $\mathrm{Co} < 0.5$ limit mentioned above.

The computational time for this set up is approximately two days for one revolution on 21 Intel Xeon 5160, 3 GHz dual core CPUs once the flow is fully developed, which is attainable within two weeks of computing. Reaching a statistically converged mean flow thus indicates a running time of several weeks, even if the computational resources are scaled up. However, when it comes to a cavitating flow in a prescribed wake, the simulation yields useful data already during the first blade passage in the developed flow and sampling statistical data seems necessary primarily when an unsteady wake is used in the simulation.

5 Noncavitating Flow Conditions

This section constitutes a summary of the results in Bensow and Liefvendahl [7]. It is included here to demonstrate the capabilities of the described LES approach for propeller flows, the accuracy of the chosen discretization scheme and that the grid resolution is deemed sufficient. The experimental data for this condition are reported in Stella and co-workers [2,37], Di Florio et al. [3], and Di Felice et al. [4].

5.1 Open Water Characteristics. We start with a quantitative comparison of the measured thrust coefficient $K_T = T/(\rho n^2 D_P^4)$, where T is the thrust, n is the rate of revolution, and torque coefficient $K_Q = Q/(\rho n^2 D_P^5)$, where Q is the torque. The forces and moments are here computed for the blades only, in order to compare with the measurements, where T_0 and Q_0 measured without the propeller mounted in the tunnel are deducted from the total values. Comparisons have been made for two advance numbers, $J=0.88$ and 0.71, and the agreement is excellent in both cases, see Table 1. These two conditions have been chosen since the experiments are focused on $J=0.88$ for the wetted flow

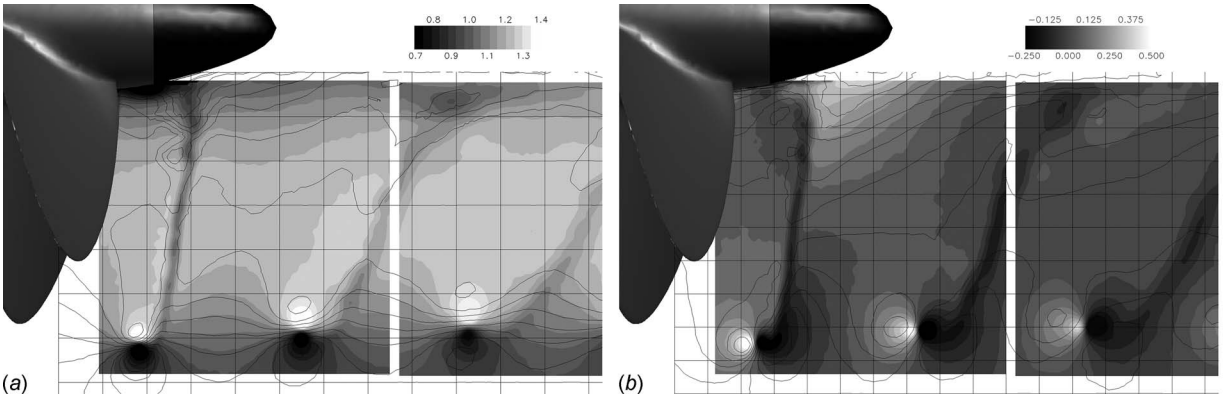

Fig. 4 Contours of the inplane velocity components: (*a*) U/U_∞ and (*b*) V/U_∞. The background contour plane indicates the experimental data and the lines the computational results.

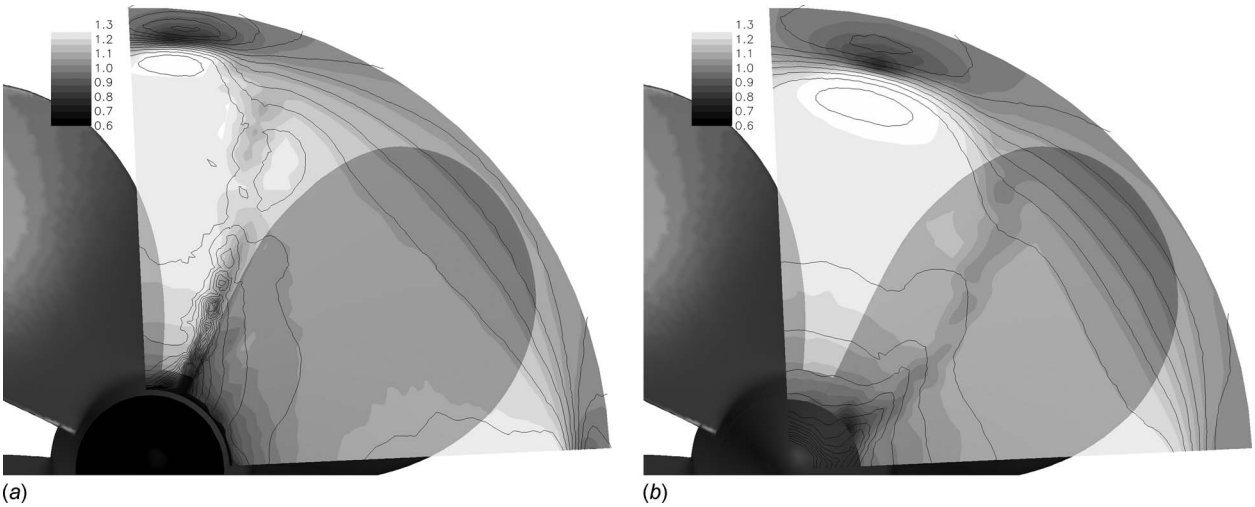

Fig. 5 Contours of the axial velocity U/U_∞: (*a*) $x/R_P=0.2$ and (*b*) $x/R_P=0.2$. The background contour plane indicates the experimental data and the lines the computational results.

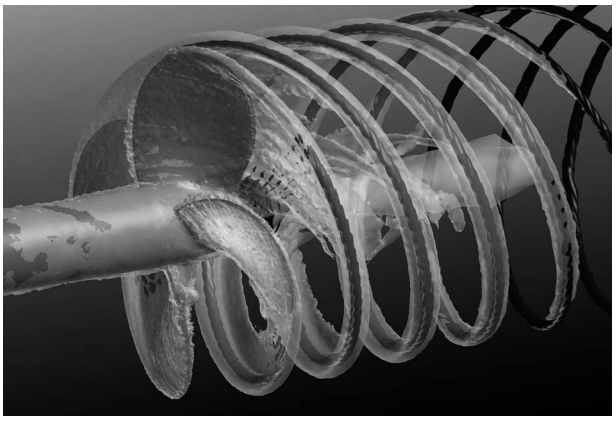

Fig. 6 Isosurfaces of the magnitude of the vorticity $||\nabla \times \mathbf{v}|| = 100\ s^{-1}$ for the experiments (in black) and the computation (in light gray)

conditions and $J=0.71$ for the steady cavitating conditions. The cost to perform these computations using LES prohibits the evaluation of a full propeller characteristics curve.

5.2 Wake Flow Validation at $J=0.88$. This is the flow case in the experimental database with best wake flow measurements, and was thus used to validate the computational model for propeller flows. In this setup, $n=25$ rps and $U_\infty=5$ m/s, and the Reynolds number, based on the propeller tip velocity, is $\mathrm{Re}=2.9\times10^5$. From Figs. 4–6, in combination with the agreement of K_T and K_Q from Table 1, we conclude that the flow is correctly predicted within the limits of the mesh resolution. The tip vortex location, including the slipstream contraction, as well as the blade wake deformation is in good agreement with the experimental data. However, the sharpness of the structures is lost and the tip vortex fades after approximately one revolution. Considering the mesh resolution this is not surprising, since there are only four to five cells across the vortex core and even less in the thin blade wake. It thus seems very clear that an automatic mesh refinement algorithm needs to be applied for a propeller flow in order to get the best possible cell distribution, probably combined with a vortex preservation method, such as vorticity confinement [38] or vorticity-strain VMS [39], to be able to predict the tip vortex evolution.

6 Cavitating Flow Conditions

We have simulated the cavitating flow on the propeller for two conditions. In the first case the inflow is undisturbed and thus constitutes a steady condition, comparing with the experimental results of Pereira et al. [5] while in the second case an artificial wake field was created causing a dynamic loading of the blades and thus forming an unsteady cavity, experimental results are reported in Pereira et al. [6]. In both cases the cavitation phenomena are reasonably well predicted, displaying the main controlling mechanisms, although the cavity extent is not satisfactory. For the steady case a parametric study regarding the parameters A^+ and A^- has been performed in order to establish any sensitivity on cavity extent related to the model settings. The conclusion is that within certain parameter ranges, no significant differences on the simulation results could be detected.

6.1 Uniform inflow at $J=0.71$ and $\sigma_n=1.76$

6.1.1 Comparison With Experiments. For this flow, the rate of revolution was $n=36$ rps and the inlet velocity $U_\infty=5.808$ m/s and the pressure was adjusted to reflect the cavitating condition at $\sigma_n=1.76$ with p_∞-$p_v=58{,}900$ Pa. As can be seen in Figs. 7 and 8, displaying a snapshot from the simulation, the simulated cavity is too large and extends to a smaller propeller radius than in the experiments. This behavior was however noted in most computations, using a variety of simulation techniques and models, reported in Ref. [18] and could thus be due to geometrical modeling problems, related to, e.g., turbulence triggering or similar effects. We note that the flow is clearly deflected by the cavity and a jet is formed, which rolls up into the tip vortex, visible via the surface streamlines displayed in Fig. 7(*a*). This jet also seems to be the main cause of instabilities in the simulation since the flow gets quite strongly accelerated when passing between the blade and the tip vortex. It is also worth noting that this deflection is effective mainly for higher levels of vapor fraction, say above $\alpha=0.75$, and the simulated flow and pressure distribution seem to "see" a smaller cavity, more similar to the one in the experiments. This is also indicated by the location of the tip vortex, which seems to be in good agreement with the experimental picture. If this behavior is due to that the interface is not sharp enough, particularly in the downstream edge of the cavity, insufficient mesh resolution, mass transfer model deficiencies, or a combination, needs to be further investigated. Looking at the thrust and torque (Table 2), the trends from the experiments are correctly captured although slightly exaggerated but consistent with the overpredicted cavity extent.

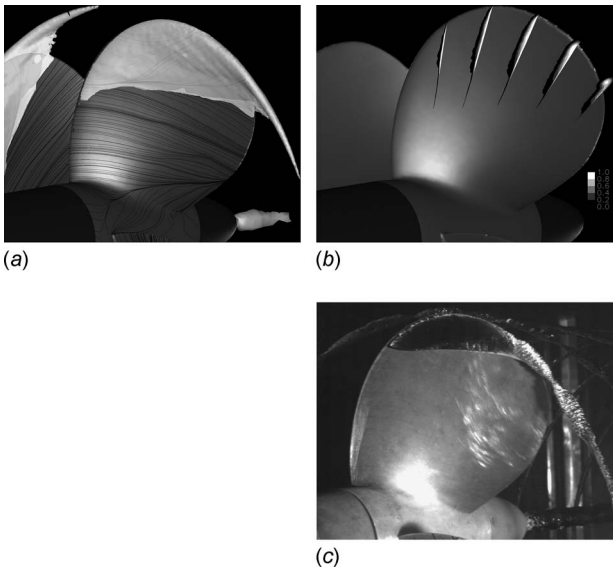

Fig. 7 Cavity extent in steady conditions in (*a*) and (*b*) computations and in (*c*) experiments; (*a*) shows the isosurface of vapor fraction $\alpha=0.5$ and in (*b*) planes with contours of α

6.1.2 Parameter Sensitivity. Due to the discrepancies in cavity extent between simulations and experiments, we performed several simulations varying the parameters controlling the mass transfer modeling, A^+, A^-, and ρ_l/ρ_v. The simulations displayed above was performed using $A^+=2\times10^4$, $A^-=10^3$, and $\rho_l/\rho_v=1000$. These choices are based on previous experience that best results

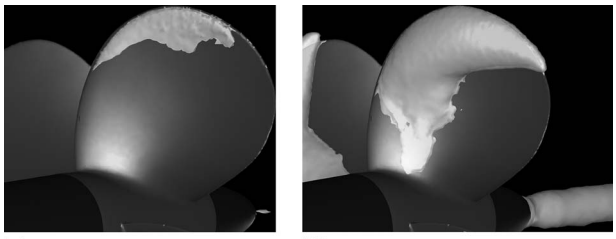

Fig. 8 Isosurfaces of pressure in (*a*) $C_P=1.76$ and in (*b*) $C_P=1.0$

Table 2 Computed open water coefficients at $J=0.71$ in non-cavitating and cavitating conditions

J	σ_n		K_T	$10K_Q$
0.71	1.763	Exp	0.255	0.460
		LES	0.252	0.450
	∞	Exp	0.256	0.464
		LES	0.256	0.453

are achieved setting these values as high as possible without endangering numerical stability [12]. In order to detect if the over predicted cavity extent was influenced by these ad hoc choices simulations were performed varying the values according to Table 3.

The influence of density ratio was studied by Kunz et al. [17] with the conclusion that $\rho_l/\rho_v=1000$ is sufficiently high and there is no need to use the correct vapor density, $\rho_v=0.022$. This has been confirmed for this case as well.

The vaporization and condensation parameters, A^+ and A^-, are more difficult to say something definite about. In the original work by Kunz et al. [17], A^+ and A^- were identical and set to $100t_\infty$, where t_∞ represents a mean flow time scale. Estimating t_∞, not given in the paper, yields an A^+ of the same order of magnitude as used in this work while A^- is approximately one order of magnitude higher. The simulations presented by Huuva et al. [40] used a considerably lower A^- than used in this work without degraded performance. In Vaidyanathan et al. [35] a sensitivity analysis is performed for this particular mass transfer model. Their results showed that the case with highest values A^+ and A^- yields best agreement with experimental data, thus supporting our impression, although the actual values appear to be lower than what we have used in this work. It thus seems that the choices are implementation dependant and possibly also to some extent case dependant. The overall impression from this study is that this cavitating flow is surprisingly insensitive to the parameter values. As long as the condensation parameter A^- is above 500, no significant difference between the simulations could be detected. Using A^- greater than 2500 yielded numerical instabilities while a too low value yield a very smeared cavity with the trailing edge diffused over the blade.

Table 3 Tested parameter ranges for the mass transfer modeling

A^+	A^-	ρ_v	ρ_l/ρ_v
2×10^2–2×10^5	5–5000	0.022–1	10^3–4.5×10^4

6.2 Artificial Wake Inflow at $J=0.90$ and $\sigma_n=4.455$

6.2.1 Definition of the Wake Inflow. In this case, the inflow to the propeller is disturbed by five vertical plates, creating a region of velocity deficit in order to emulate a ship wake. The resulting velocity field was measured using LDV both without the propeller mounted to achieve the nominal wake distribution, as well as during operating conditions of the propeller, giving the total artificial wake propeller inflow. The measurement plane was located 0.52 propeller radii upstream of the propeller origin.

In order to compute this flow without modeling the actual plates and the tunnel, it was recommended for the VIRTUE, Second WP4 workshop, Rome, October 2008, as reported in Salvatore et al. [19] to use the nominal wake distribution as inflow conditions to the computational domain. However, in our implementation, this resulted in several unphysical pressure peaks forming at the inlet; the reason is presently unknown. Instead an analytical expression was derived to mimic the wake.

$$\mathbf{U}_{\text{Inflow}} = \mathbf{U}_0(f_1 f_2 + f_3)$$
$$\text{where} \begin{cases} f_1 = u_{\max} + h/2(\tanh(\mathrm{C_S}(z - \mathrm{C_W}R_P))) - \tanh(\mathrm{C_S}(z + \mathrm{C_W}R_P)) \\ f_2 = 0.5 + 0.5\tanh(\mathrm{C_S}(y - \mathrm{C_{VD}}R_P)) \\ f_3 = u_{\max}(0.5 + 0.5(1 - \tanh(\mathrm{C_S}(y - \mathrm{C_{VD}}R_P)))) \end{cases} \tag{10}$$

where $u_{\max}=1.02$ is the maximum relative velocity, $\mathrm{C_S}=150$ defines the sharpness of the edges of the wake, $\mathrm{C_{WD}}=0.4$ and $\mathrm{C_{VD}}=0.25$ is the width of the wake and its distance from the center axis (both normalized by the propeller diameter, R_P), $u_{\text{diff}}=u_{\max}-u_{\min}$, where $u_{\min}$ is the minimum relative velocity and y and z are the inplane coordinates at the inflow. The expression is formed using the "smooth step"-function property of the tanh, and combine several steps to create the rectangular shape of the experimental wake.

As can be seen in Fig. 9, the resemblance between the simulated total wake and the measured one is fair. There are four noticeable differences that most likely affect the comparison between computational and experimental results: the velocity deficit at 0 deg (twelve o'clock) is larger in the computational wake, the wake is sharper in the experiments, the flow outside the wake is more accelerated in the experiments, and the flow field is more regular in the computations. The last one is probably less important while the others may have a significant impact on the results.

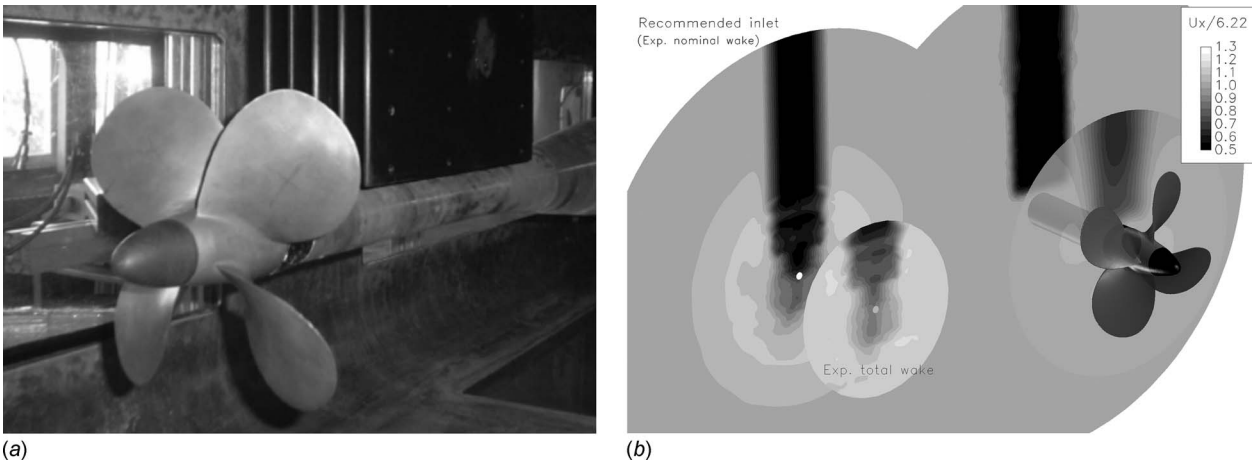

(*a*) (*b*)

Fig. 9 The five wake generator plates in the experiments, seen behind the propeller in (*a*), is in the computations replaced by a inflow velocity deficit. Figure (*b*) shows a comparison between measured propeller inflow (to the left) and the inflow in the simulation (to the right).

Computations done at INSEAN also show that the analytical wake yields a higher loading of the propeller blade compared with the measured wake [19]. The exact impact of these differences has not yet been thoroughly investigated but is commented in the following section when comparing the simulation with experimental data.

6.2.2 Features of the Cavitating Flow and Comparison With Experimental Data. The experimental data available consist of a series of photographs, measures of cavity extent, and cavity-pressure correlations. Some features, crucial in the generation of higher order pressure pulses, noise, and erosion, can be detected in the experiments as well as in the simulated flow. The three most important mechanisms noted are the occurrence of the following:

(i) internal jets, and hence shedding
(ii) upstream desinence
(iii) leading edge vortices influenced by the internal jet

In Fig. 10, we can identify the above flow features both in the simulation data and in the photographs from the experiments; the left column displays snapshots from the simulation corresponding to the experimental photos in the right column.

Examining the photographs, we see that the sheet cavity starts to grow directly as the blade enters the wake. In Fig. 10(*d*), the sheet is fully developed with side-entrant jets along the larger part of the cavity rolling up into the tip vortex. We note that the trailing part of the cavity is fairly distant from the blade surface due to the internal jet and transformed into a partly cloudy character. Moreover, there is no cavitating tip vortex in this frame, instead shed cloud cavity is drawn into the vortex flow extending the cavitating region behind the blade. In Fig. 10(*f*), the blade has started to exit the velocity deficit of the wake, and the cavity is more or less detached from the leading edge; there is however still some detectable cavitation on the edge. Now, the whole cavity is relatively distant from the blade and the rotational motion of the cavity, extending into the tip vortex region, is visible. The only difference in the last frame, Fig. 10(*g*), is that the cavity has shrunk further, and now seems fully transformed into a cloud. The latest part of the cavity development is unfortunately not registered in the experiments and it is not clear whether the cavity collapses on the blade or not.

The simulated dynamics, shown in the left column of Fig. 10 via an isosurface of the vapor fraction $\alpha=0.5$, display the same qualitative behavior as the experiments. The cavity starts to develop earlier and already in frame (a) a fully developed sheet cavity has developed with distinct internal jets. If this is due to differences in the inflow or indicates a problematic behavior of the mass transfer model is subject to further studies. The development until Fig. 10(*c*) has not changed the cavity dramatically in the simulation although the side-entrant jets are even more clearly visible jets, which bring water between the cavity and the blade surface and rolling up into the tip vortex. At this instant the quality of the simulation is comparable to what was described for the steady cavitating condition: The cavity volume is exaggerated, the cavity extends to a smaller propeller radii but the internal structure seems well captured as well as the location of the tip vortex. In frame (e), we note that leading edge desinence is present in the simulation, correctly responding to the change in load as the blade exits the wake. In Fig. 10(*g*), the cavity now seems to be smaller than in the experiments but both shed cavities, one cloud shed into the tip vortex and one from the leading edge, are present and predicted at the correct location. The contradictable behavior regarding the cavity extent, i.e., that the vapor region is overpredicted in the early stages but underpredicted in the later stage, might partly be explained by the uncertainty in what value of vapor fraction α to compare: For a sheet cavity this is not crucial as the interface is thin but the amount of vapor in the clouds in frame (h) might be lower while still being registered by the camera (Fig. 11).

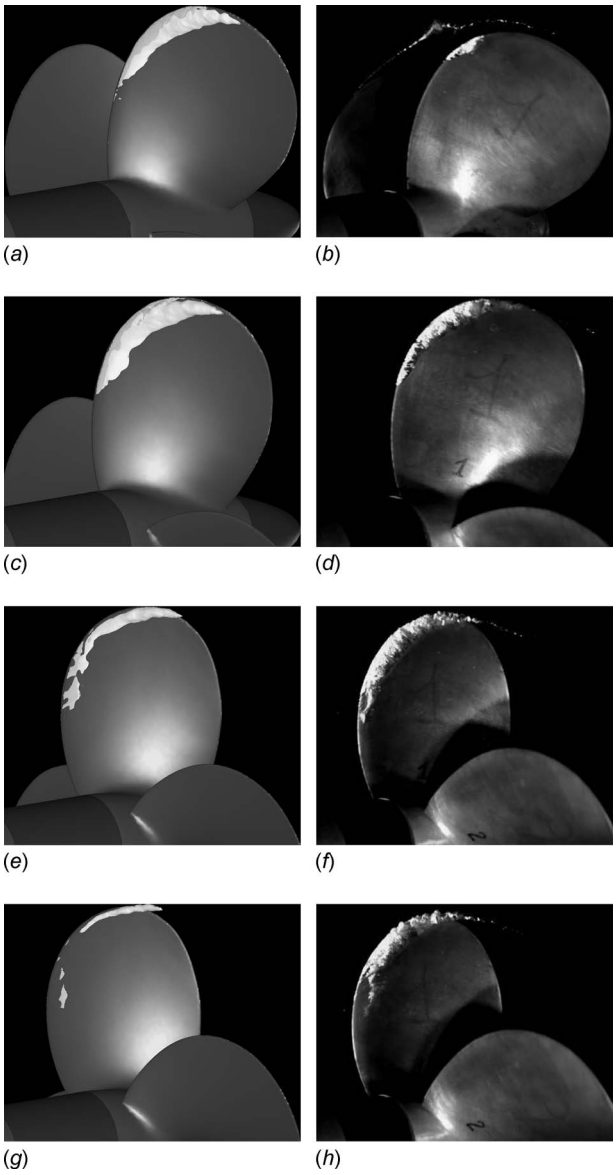

Fig. 10 The left column shows the simulation (isosurface of vapor fraction $\alpha=0.5$) and the right column the experimental photographs [6]. The series of pictures are for propeller angles –30 deg (frames (*a*) and (*b*)), –10 deg (frames (*c*) and (*d*)), 10 deg (frames (*e*) and (*f*)) and 15 deg (frames (*g*) and (*h*)).

The development of the leading edge vortex is more closely studied in Fig. 12. In the first figure, the sheet is fully developed and the leading edge detachment has not yet started. The cavity is showed as well as the secondary velocity field around the blade tip. We can see that once the internal jets develop, a vortex core is created that greatly influences the dynamics of the trailing part of the cavity. Such a vortex core is not unusual on modern, skewed propellers, and possibly the very sharp wake in the present case is responsible for the occurrence of this phenomena here. Looking at an earlier instance, Fig. 12(*b*), we show proof that this vortex is not a consequence of an in-blade tip vortex. Here, the vortical structure develops around the edge of the cavity due to the side-entrant jet while the propeller tip vortex starts just at the tip due to the overflow from the pressure to the suction side of the blade; at this instant the cavity has still not reached the tip. Moreover, in Bensow and Liefvendahl [7] it was demonstrated that in noncavitating conditions, the tip vortex can be generated further in on the blade but only at lower advance numbers and still considerably

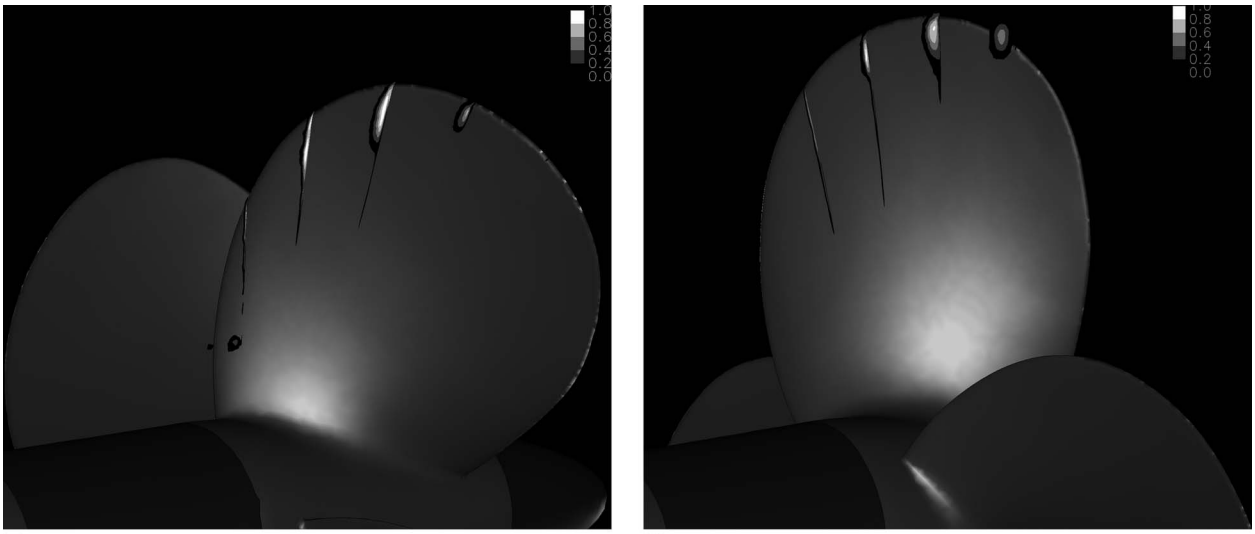

(*a*) (*b*)

Fig. 11 Planes with contours of vapor fraction: (*a*) corresponds to Figs. 10(*a*) and 10(*b*) to Fig. 10(*e*)

closer to the edge than in the present case. Although the generated vorticity is not sufficiently high to sustain the cavity toward its collapse dynamics, the presence of this flow feature in the simulation is a promising indication of the potential in the technique. Describing and understanding vortex dynamics, as is to some extent shown in this simulation, is an important step toward improved propeller designs.

7 Concluding Remarks

We have demonstrated that the wall-modeled, implicit LES described above have the ability to capture large to medium-small-scale flow structures that are deemed not only necessary for the prediction of cavitation nuisance such as erosion or noise but also that further work is needed to reach this predictive capability. We argue that it is important that the main cavitation mechanisms, such as internal jets and leading edge desinence, are captured by the simulation in order to advance toward reliable predictive tools and this is clearly the case for the present modeling approach. One necessary ingredient is a high resolution in both space and time.

The main discrepancy when comparing the simulated results with the experimental data is the cavity extent that is not satisfactory to be useful for, e.g., noise prediction. We have here shown that this problem is insensitive to parameter variations in the mass transfer model, and other studies have shown that different mass transfer modeling techniques behave similarly. The two most probable causes of this discrepancy are thus believed to be related to either the resolution or the incompressible segregated solver approach.

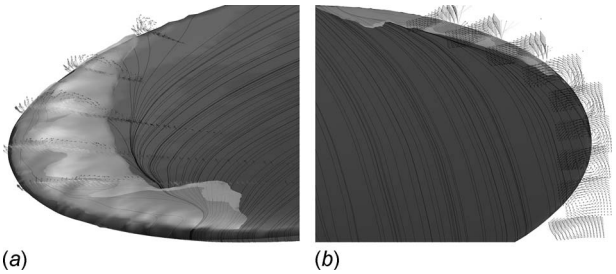

(*a*) (*b*)

Fig. 12 The cavity is indicated by an isosurface of vapor fraction α=0.5, complemented by vectors, colored with α, of the secondary flow around the cavity and blade tip: (*a*) shows an instant, where the cavity is fully developed and (*b*) an earlier instant, where a side-entrant jet has just developed

To conclude, we believe that for studying the details of a cavitating flow field, LES has a great potential to become a useful and reliable tool. Although not part of the short-term design cycle, the improved understanding of governing mechanisms that can be achieved using high-end LES will help in interpreting the results from faster tools, as well as guiding the actual development of the design tools and principles. LES can also be part of the validation of a final design, as experiments are sometimes used today, and on the same time scale as the experiments. Such studies can preferably be done using both experimental and computational techniques, yielding complementary databases. Even though it is not yet possible to numerically predict the final collapses of cavities, the general, large-scale behavior toward the state generating approximate initial conditions for the final collapse can be studied to evaluate the risk of destructive collapses, i.e., erosion. Reliable prediction of this kind of early development, and its relation to design parameters, is clearly within reach using present cavitation modeling techniques.

Acknowledgment

We thank Francesco Salvatore and his colleagues at INSEAN for their assistance with the experimental data. The presented research has been financed through the European VIRTUE in the Sixth EC framework program, Grant No. TIP5-CT-2005-516201, and by Rolls-Royce Plc through the University Technology Centre in Computational Hydrodynamics at Chalmers. Computational resources were in part provided by Chalmers Centre for Computational Science and Engineering, C3SE.

References

[1] Bark, G., Grekula, M., Bensow, R., and Berchiche, N., 2009, "On Some Physics to Consider in Numerical Simulation of Erosive Cavitation," Proceedings of the Seventh International Symposium on Cavitation, Ann-Arbor, MI.
[2] Stella, A., Guj, G., Di Felice, F., and Elefante, M., 2000, "Experimental Investigation of Propeller Wake Evolution by Means of LDV and Flow Visualizations," J. Ship Research, **44**(3), pp. 155–169.
[3] Di Florio, D., Di Felice, F., Romano, G. P., and Elefante, M., 2001, "Propeller Wake Structure at Different Advance Coefficients by Means of PIV," Proceedings of PSFVIP-3, Maui, HI.
[4] Di Felice, F., Felli, M., Giordano, G., and Soave, M., 2003, "Pressure and Velocity Correlation in the Wake of a Propeller," Proceedings of Propeller Shafting, Virginia Beach, Norfolk, VA.
[5] Pereira, F., Salvatore, F., and Di Felice, F., 2004, "Measurement and Modeling

of Propeller Cavitation in Uniform Inflow," ASME J. Fluids Eng., **126**, pp. 671–679.
[6] Pereira, F., Salvatore, F., Di Felice, F., and Soave, M., 2004, "Experimental Investigation of a Cavitating Propeller in Non-Uniform Inflow," Proceedings of the 25th ONR Symposium on Naval Hydrodynamics, St. John's, Canada.
[7] Bensow, R. E., and Liefvendahl, M., 2008, "Implicit and Explicit Subgrid Modeling in Les Applied to a Marine Propeller," Paper No. AIAA-2008-4144.
[8] Frikha, S., Coutier-Delgosha, O., and Astolfi, J. A., 2008, "Influence of the Cavitation Model on the Simulation of Cloud Cavitation on a 2D Foil Section," Int. J. Rotating Mach., **2008**, Article ID 146234.
[9] Senocak, I., and Shyy, W., 2004, "Interfacial Dynamics-Based Modelling of Turbulent Cavitating Flows, Part-1: Model Development and Steady-State Computations," Int. J. Numer. Methods Fluids, **44**(9), pp. 975–995.
[10] Sagaut, P., 2006, *Large Eddy Simulation for Incompressible Flows*, 3rd ed., Springer, New York.
[11] Wilcox, D. C., 1998, *Turbulence Modeling for CFD*, DCW, La Canada, CA.
[12] Huuva, T., 2008, "Large Eddy Simulation of Cavitating and Non-Cavitating Flow," Ph.D. thesis, Chalmers University of Technology, Göteborg, Sweden.
[13] Senocak, I., and Shyy, W., 2004, "Interfacial Dynamics-Based Modelling of Turbulent Cavitating Flows, Part-2: Time-Dependent Computations," Int. J. Numer. Methods Fluids, **44**(9), pp. 997–1016.
[14] Schnerr, G. H., Sezal, I. H., and Schmidt, S. J., 2008, "Numerical Investigation of Three-Dimensional Cloud Cavitation With Special Emphasis on Collapse Induced Shock Dynamics," Phys. Fluids, **20**, p. 040703.
[15] Koop, A., 2008, "Numerical Simulation of Unsteady Three-Dimensional Sheet Cavitation," Ph.D. thesis, Twente University, Netherlands.
[16] Qin, Q., Song, C. S. S., and Arndt, R. E. A., 2003, "A Numerical Study of Unsteady Turbulent Wake Behind a Cavitating Hydrofoil," Proceedings of the Fifth International Symposium on Cavitation, Osaka, Japan.
[17] Kunz, R. F., Boger, D. A., Stinebring, D. R., Chyczewski, T. S., Lindau, J. W., Gibeling, H. J., Venkateswaran, S., and Govindan, T. R., 2000, "A Preconditioned Navier-Stokes Method for Two-Phase Flows With Application to Cavitation Prediction," Comput. Fluids, **29**(8), pp. 849–875.
[18] Streckwall, H., and Salvatore, F., 2008, "Results of the Wageningen 2007 Workshop on Propeller Open Water Calculations Including Cavitation," Proceedings of the RINA CFD 2008, Southhampton, UK.
[19] Salvatore, F., Streckwall, H., and Terwisga, T. V., 2009, "Propeller Cavitation Modelling by CFD–Results From the VIRTUW 2008 Rome Workshop," Proceedings of the First International Symposium on Marine Propulsors, Trondheim, Norway.
[20] Bensow, R. E., and Fureby, C., 2007, "On the Justification and Extension of Mixed Methods in LES," J. Turbul., **8**, p. N54.
[21] Bardina, J., Ferziger, J. H., and Reynolds, W. C., 1980, "Improved Subgrid Scale Models for Large Eddy Simulations," Paper No. AIAA-80-1357.
[22] Grinstein, F. F., Margolin, L., and Rider, W., eds., 2007, *Implicit Large Eddy Simulation: Computing Turbulent Fluid Dynamics*, Cambridge University Press, Cambridge, England.
[23] Fureby, C., Alin, N., Wikström, N., Menon, S., Persson, L., and Svanstedt, N., 2004, "On Large Eddy Simulations of High Re-Number Wall Bounded Flows," AIAA J., **42**, pp. 457–468.
[24] Fureby, C., 2007, "ILES and LES of Complex Engineering Flows," ASME J. Fluids Eng., **129**, pp. 1514–1523.
[25] Fureby, C., and Karlsson, A., 2009, "LES of the Flow Past a 6:1 Prolate Spheroid," Proceedings of the 47th AIAA Aerospace Sciences Meeting, Paper No. AIAA-2009-1616.
[26] Merkle, C. L., Feng, J., and Buelow, P. E. O., 1998, "Computation Modeling of the Dynamics of Sheet Cavitation," Proceedings of the Third International Symposium on Cavitation, Grenoble, France.
[27] OpenFOAM Web Site, 2008, www.openfoam.com.
[28] Weller, H. G., Tabor, G., Jasak, H., and Fureby, C., 1998, "A Tensorial Approach to CFD Using Object Oriented Techniques," Comput. Phys., **12**, pp. 620–631.
[29] Jasak, H., 1996, "Error Analysis and Estimation for the Finite Volume Method With Applications to Fluid Flows," Ph.D. thesis, Imperial College, London, UK.
[30] Issa, R. I., 1986, "Solution of the Implicitly Discretised Fluid Flow Equations by Operator-Splitting," J. Comput. Phys., **62**(1), pp. 40–65.
[31] Rhie, C. M., and Chow, W. L., 1983, "Numerical Study of the Turbulent Flow Past an Airfoil With Trailing Edge Separation," AIAA J., **21**(11), pp. 1525–1532.
[32] Demirdzic, I., and Peric, M., 1990, "Finite Volume Method for Prediction of Fluid Flow in Arbitrarily Shaped Domains With Moving Boundaries," Int. J. Num. Methods Fluids, **10**(7), pp. 771–790.
[33] Persson, T., Fureby, C., and Bensow, R. E., 2005, "Large Eddy Simulation and Detached Eddy Simulation Around a Circular Cylinder," Chalmers Report No 05:98, ISSN 1652-9189.
[34] Rouse, H., and McNown, J. S., 1948, "Cavitation and Pressure Distribution, Head Forms at Zero Angle of Yaw," Studies in Engineering, Bulletin 32, State University of Iowa.
[35] Vaidyanathan, R., Senocak, I., Jiongyang, W., and Shyy, W., 2003, "Sensitivity Evaluation of a Transport Based Turbulent Cavitation Model," ASME J. Fluids Eng., **125**, pp. 447–458.
[36] Ahuja, V., Hosangadi, A., and Arunajatesan, S., 2001, "Simulations of Cavitating Flows Using Hybrid Unstructured Meshes," ASME J. Fluids Eng., **123**, pp. 331–340.
[37] Stella, A., Guj, G., and Di Felice, F., 2000, "Propeller Wake Flowfield Analysis by Means of LDV Phase Sampling Technique," Exp. Fluids, **28**, pp. 1–10.
[38] Steinhoff, J., 1994, "Vorticity Confinement: A New Technique for Computing Vortex Dominated Flows," *Frontiers of Computational Fluid Dynamics*, Wiley, New York.
[39] Bensow, R. E., and Larson, M. G., 2010, "Residual Based VMS Subgrid Modeling for Vortex Flows," Comput. Methods Appl. Mech. Eng., **199**, pp. 802–809.
[40] Huuva, T., Bark, G., Cure, A., and Nilsson, H., 2007, "Computations of Unsteady Cavitating Flow on Wing Profiles Using a Volume Fraction Method and Mass Transfer Models," Proceedings of the Second IAHR International Meeting of the Workgroup on Cavitation and Dynamic Problems in Hydraulic Machinery and Systems, Timisoara, Romania.

An Examination of Trapped Bubbles for Viscous Drag Reduction on Submerged Surfaces

Kelly A. Stephani
e-mail: kelly.stephani@mail.utexas.edu

David B. Goldstein
e-mail: david@cfdlab.ae.utexas.edu

Department of Aerospace Engineering and Engineering Mechanics,
University of Texas at Austin,
1 University Station,
C0600 Austin, TX 78712-0235

Viscous drag reduction on a submerged surface can be obtained both in the limit of an unbroken gas film coating the solid and in the nanobubble or perhaps microbubble coating regime when an air layer is created with superhydrophobic coatings. We examine an intermediate bubble size regime with a trapped-bubble array (TBA) formed in a tap water environment using electrolysis to grow and maintain bubbles in thousands of millimeter-sized holes on a solid surface. We show that even though surface tension is sufficient to stabilize bubbles in a TBA against hydrostatic and shear forces beneath a turbulent boundary layer, no drag reduction is obtained. Drag measurements were acquired over Reynolds numbers based on plate length ranging from $7.2\times10^4<Re_L<3.1\times10^5$ *using either a force balance for plates mounted in a vertical orientation, or by performing a momentum integral balance using a wake survey for a flat plate mounted in either vertical or horizontal orientation. In that the drag forces were small, emphasis was placed on minimizing experimental uncertainty. For comparison, the flow over a flat plate covered on one side by a large uninterrupted gas film was examined and found to produce large drag reductions of up to 32%.* [DOI: 10.1115/1.4001273]

1 Introduction

1.1 Motivation and Background. The efficiency of a system involving submerged surfaces is often dependent on its ability to overcome viscous drag effects that are inherent to solid surface-liquid interaction. Drag reduction methods involving changes to the near-wall boundary condition have been investigated over a wide range of applications, from Poiseuille-flow and Stokes-flow problems (e.g., "lab-on-a-chip" technology) to high-speed underwater projectiles where Reynolds numbers are large and flow cavitation is possible. Implementation of these drag reduction methods also varies from passive surface textures to active systems, which require continuous energy expenditure to provide drag reduction.

The idea of using air injection to create an air film along the bottom of ship hulls and similar submerged surfaces has been of interest since the late 1800s. Successful implementation of this technique requires the generation of a stable air film on the hull bottom using a low air injection rate, which can be difficult to achieve without a thorough understanding of the physical mechanisms involved. Matveev [1] discusses some of the limiting parameters involved in artificial cavitation for air cavity ships. Latorre [2] provides a brief review examining the effectiveness of this application for high-speed planning craft as well as barges and cargo ships. While integration of the air injector system into the hull bottom creates appendage drag, using an appropriate air injection rate leads to a net decrease in the original base hull drag of 15–18% in model tests and 10–12% for full-scale applications. Overall, this drag reduction technique has demonstrated a reduction in the vehicle's net power requirement.

Drag reduction schemes involving microbubble injection into turbulent boundary layers by Madavan et al. [3,4], Pal et al. [5] and more recent work by Sanders et al. [6] have been shown to reduce friction. It is thought that although the addition of bubbles to a liquid effectively increases its viscosity, the bubbles act to reduce the liquid density and modify turbulence in the boundary layer so as to reduce skin friction. Sanders et al. [6] emphasize that microbubbles should be sized on the order of the smallest turbulent flow scales and remain within 300 wall units of the surface to be most effective. They also determined, in agreement with prior work, that for bubbles injected into the flow on the bottom side of the model surface, an increase in flow speed reduces the amount of drag reduction observed, with the maximum drag reduction occurring at the lowest test speed. This group was, in particular, able to demonstrate a sustained drag reduction over the length of the test plate for the lowest flow speeds studied ($6\ \mathrm{m\ s^{-1}}$). At these flow speeds, the bubbles injected into the flow through the upstream injector coalesced at the plate surface to form a quasi-continuous gas film, particularly at high gas injection rates, and reductions in local shear stress of up to nearly 100% were indicated on the bottom surface of the test plate. Similar to the microbubble injection drag reduction method, the method described in the present paper also utilizes tiny bubbles to reduce viscous drag; however, it is important to note that the drag reduction mechanism pursued here is quite different from bubble injection.

Some passive drag reduction methods (in which the flow conditions at the wall are modified using microfabrication techniques) have been investigated and show promising results. Balasubramanian et al. [7] investigated water flow over submerged hydrophobic surfaces and were able to demonstrate 10–20% viscous drag reduction. This benefit, however, diminished over time due to water infiltration of the air layer between the nanostructures on the surface. Velocity slip has been clearly measured over superhydrophobic or ultrahydrophobic surfaces at a microscale. Joseph et al. [8] measured slip in a water flow over a carbon nanotube forest on one wall of a microchannel. Gas between the nanotubes presumably kept the water confined to the forest canopy. Several microns of slip length were possible in distilled water provided the water did not infiltrate between the nanotubes. Ou et al. [9] used microparticle image velocimetry to measure large velocity slip in water

Contributed by the Fluids Engineering Division of ASME for publication in the JOURNAL OF FLUIDS ENGINEERING. Manuscript received June 27, 2008; final manuscript received February 9, 2010; published online April 20, 2010. Assoc. Editor: Steven Ceccio.

flow over a slotted silicon surface treated with a hydrophobic coating that prevented the liquid from penetrating into the slots. Laminar computational simulations of the arrangement were used as validation for the velocity measurements and showed good agreement with the gas bubble slip model. Pressure drop measurements through a channel demonstrated reduced viscous drag. Larger scale grooves containing gas have been examined [10] but the bubble films were found to be unstable in a shear flow and required continuous gas injection.

Hydrophobic surfaces show promise as a method for reducing drag on submerged surfaces. However, the limitations of the hydrophobic surface drag reduction methods, particularly loss of hydrophobicity over time or the small slip lengths obtained, suggest the need for a drag reduction method, which can produce a slip surface similar to that of a hydrophobic surface, but maintain a gas layer at the wall for extended periods of time. The method examined in this investigation accomplishes this by using electrolysis to form a layer of air on the submerged surface. Doing so could provide continuous drag reduction over perhaps any length of time desired with only small energy expenditures required to replace occasional bubble loss.

Ideally, an entire submerged surface would be covered in one large continuous bubble film, forming a near-slip surface and providing a drastic reduction in viscous drag. This, however, is not practical as a large bubble is easily torn away from the surface when subjected to high shear and buoyancy effects. As an alternative, it is suggested that covering the surface with millions of tiny, densely packed bubbles, which form a trapped-bubble array may provide nearly the same drag-reducing effects as one large, continuous bubble, while keeping the bubbles sufficiently small to remain attached to the submerged surface. Thus, in forming a TBA on a submerged surface, the bubble surface effectively replaces the solid surface it forms on, and therefore, the net shear stress on the entire surface should be reduced.

The bubbles in our TBA are produced by means of electrolysis. The TBA surface is selected as the cathode, so hydrogen gas is collected to form the trapped bubbles. Drag measurements are obtained over a range of Reynolds numbers for flow over a flat plate surface, a flat plate with a large trapped bubble, and a flat plate covered with the TBA using either a calibrated force balance system or by performing a momentum integral balance with a wake survey.

The remainder of this paper is divided as follows: Implementation of the bubble formation process as well as a description of the experimental facilities and apparatus follows directly from previous work by Stephani and co-workers [11,12] and will be discussed in the next section (Sec. 2). Results are presented and discussed in Sec. 3, followed by conclusions in Sec. 4. The objectives of this paper are to determine the effects of trapped bubbles on viscous drag by examining the net change in drag produced by the bubbles, as well as the mechanisms by which the bubbles may reduce drag. Since it is difficult to observe physical phenomena on the tiny trapped bubbles, we examine a single, large trapped bubble to investigate effects of contamination on bubble drag reduction, which we expect to apply to the tiny trapped bubbles. The large trapped bubble also demonstrates the maximum drag reduction that we may expect to obtain if the entire solid surface were covered with trapped bubbles. We emphasize that this research aims to investigate a potentially practical approach to drag reduction using the TBA [13]. The experiments are designed to emulate, in part, the environment in which this drag reduction method may be used, rather than study a computationally perfect model or a physical model that is useful only in near-pristine laboratory environments; the intention was to demonstrate an efficient drag reduction method. Thus, the bubbles are formed beneath a turbulent boundary layer developing over a flat plate with a vertical orientation such that the bubbles are not hydrostatically stabilized, and the experiments are performed in ordinary tap water that has received algicidal chemical treatment.

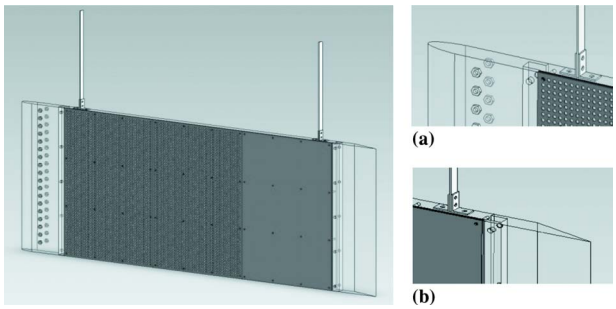

Fig. 1 Schematic of flat acrylic test plate assembly in vertical orientation with dark gray bubble plate inserts and thin flexures: (*a*) detailed view of the elliptical leading edge and (*b*) detailed view of the tapered trailing edge

2 Experimental Facilities and Apparatus

2.1 Water Channel Facility. All experiments in this study were conducted in an Eidetics model 1520 closed-loop water channel containing tap water. Flow velocity measurements are taken with a Dantec Dynamics BSA F50 two-component laser Doppler anemometer (LDA). Flow uniformity, even at the maximum speed of 0.4 m s^{-1}, is excellent. Horizontal and vertical velocity profiles were acquired throughout the test section with the LDA. Spanwise and vertical variation in the mean flow velocity was found to be less than 1% everywhere outside of the boundary layers, and variation in the centerline flow velocity along the length of the empty test section was at most 1%. LDA velocity measurements across the span of the test plate indicate that disturbances due to plate end effects start at the front of the plate and spread toward the plate centerline at a streamwise spreading angle of approximately 11 deg. Maximum freestream turbulence levels (represented as U'/U_∞) were found to be between 1–1.5% of the freestream velocity value anywhere in the test section outside the boundary layers over the entire useful range of water tunnel speeds. Water temperatures in the channel during experiments were observed to remain within $20.9\,^\circ\mathrm{C} \pm 0.3\,^\circ\mathrm{C}$, which corresponds to a nominal viscosity of 0.98 mPa s $\pm 0.75\%$.

2.2 Force Balance, Test Plate, and Components. The test plate used in this study is an adaptation of an earlier design [11,12] with several changes made to improve the plate's structural integrity and versatility. The 1.016 m $\times$ 0.381 m $\times$ 2.3 cm test plate is assembled from three interlocking pieces (Figs. 1(*a*) and 1(*b*)). The leading edge (Fig. 1(*a*)) has a 4:1 elliptical shape to promote flow attachment over the front of the plate, while the trailing edge has a single-sided taper (Fig. 1(*b*)). The taper is oriented to force flow separation on the side opposite the bubbles to ensure the flow remains attached on the side of the plate with the bubbles, and that measured changes in drag are due to changes in shear stress, not movement of a separation point. A row of boundary layer trips is adhered approximately 64 mm from the leading edge on both sides of the plate to generate turbulent boundary layer flow over the surface.

The plate may be mounted in either a horizontal or vertical configuration. The plate is suspended horizontally in the test section by four thin struts. In order to examine flow over large bubbles, thin strips of styrene are adhered to the sides of the bottom of the flat plate surface to form a large, shallow cavity. The plate is positioned cavity-side down in the middle of the test section, and air is injected into the cavity forming a large hydrostatically stabilized bubble on the bottom surface (Fig. 2). To instead examine flow over a solid flat plate, three flat aluminum plate inserts are screwed into the main-plate cavity to form a smooth solid flat plate surface.

Surface tension forces hold the tiny bubbles fixed to the TBA surface regardless of plate orientation. Thus, flow over tiny

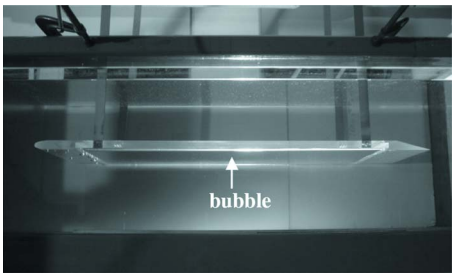

Fig. 2 Acrylic plate with large trapped bubble mounted horizontally in the test section

trapped bubbles is examined for a plate suspended vertically. The plate is suspended vertically by two flexures within fairings (Fig. 3). The remaining exposed flexure contributes a small drag; this additional drag as well as drag due to the boundary layer trips is included in the predicted one-seventh power law drag values presented in Sec. 3.3. Specifically, the analytic one-seventh power law profile represents a calculation of the drag assuming friction drag in the laminar flow up to the trips (D_{laminar}), a one-seventh power law velocity profile aft of the trips ($D_{\text{turbulent}}$), a profile drag contribution from the trips themselves (D_{trips}), and a profile drag contribution from the small area of the flexures exposed to the flow (D_{flexure}). The sum of these four drag contributions provide the drag estimate referred to as the analytic one-seventh power law for the flat plate. In particular, drag on the leading edge portion of the plate up to the trips is calculated assuming a Blasius solution

$$D_{\text{laminar}} = 2b\left(\frac{1}{2}\rho U_\infty^2\right)\frac{2 * 0.664 x_{\text{trips}}}{\sqrt{\frac{\rho U_\infty x_{\text{trips}}}{\mu}}} = 0.1514 U_\infty^{3/2} \tag{1}$$

where b is the plate span, x_{trips} is the streamwise location of the trips from the plate leading edge, ρ and μ are water density and dynamic viscosity, respectively, and U_∞ is the freestream flow speed. The drag on the turbulent flow region of the plate is given by

$$D_{\text{turbulent}} = 2\int_{x_{\text{trips}}}^{L} 0.0576\left(\frac{U_\infty x}{v}\right)^{-1/5}\left(\frac{1}{2}\rho U_\infty^2\right) b dx = 1.56 U_\infty^{9/5} \tag{2}$$

The drag due to the 60 boundary layer trips may be roughly approximated by

$$D_{\text{trips}} = 60 * C_D \tfrac{1}{2}\rho U_\infty^2 A = 0.15 U_\infty^2 \tag{3}$$

where A is the frontal area of each trip and $C_D \approx 0.5$ [16]. Finally, the majority of each flexure is shielded from the flow by the fairings, except for a 15-mm section. The drag on the exposed area is approximated by

$$D_{\text{flexures}} = 2 * C_D\left(\tfrac{1}{2}\rho U_\infty^2\right) A = 0.177 U_\infty^2 \tag{4}$$

where $C_D \approx 0.5$ [16] and $A \approx 1.5 \times 10^{-4}$ m^2 is the frontal area of each exposed flexure. The total analytic drag (in Newtons) is then

$$D_{\text{total}} = 0.1514 U_\infty^{3/2} + 0.327 U_\infty^2 + 1.56 U_\infty^{9/5} \tag{5}$$

The TBA is made of two 0.254 m $\times$ 0.381 m $\times$ 1.5875 mm aluminum plate inserts screwed into the acrylic plate cavity. These plate inserts are 6061 aluminum, polished with a Scotch Brite pad, degreased with acetone and treated with Metal Ready® primer, then airbrushed with a waterproof, nonconductive POR-15® Hardnose two-component epoxy coating. Small nonthru holes are drilled into the painted plates, comprising the cavities in which the trapped bubbles are formed. The drilling process exposes the conductive aluminum surface beneath, resulting in a flat plate surface with 367,000 holes m^{-2}. The holes are 1.143 mm in diameter and are drilled 0.762 mm into the aluminum plate in a staggered pattern. The bubble array begins at a location $x=0.127$ m, with $x=0$ being the location of the acrylic flat plate leading edge. At the highest Reynolds numbers examined, these holes are small; the hole diameter is about 21 viscous length scales (k^+) near the leading edge of the bubble region and 19 k^+ at the trailing edge. Since approximately 70% of the drag occurs over the leading 50% of the plate length, the two drilled plates are mounted closest to the leading edge, and a third simple painted plate is positioned downstream of them. Bubbles are produced in the drilled holes via electrolysis (Fig. 4). The conductive bubble plates are connected to the negative terminal of a power supply and thus work as the cathode and a nearby submerged stainless steel mesh is connected to the positive terminal and serves as the anode.

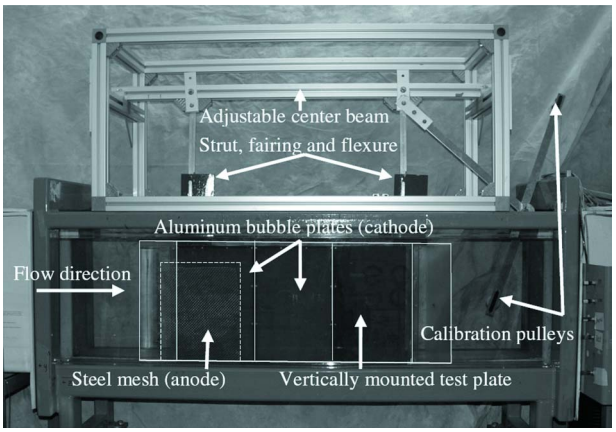

Fig. 3 Vertically mounted plate in the water tunnel test section. Test plate, cathodes, and anode are outlined for clarity.

2.3 Drag Measurement Systems. Drag measurements on the flat plate are obtained using either a proximity sensor/force balance system or by using a laser Doppler anemometer wake survey and momentum balance approach. Both measurement techniques may be used to obtain data for a vertically oriented plate, but drag on the horizontally mounted plate must be acquired using the LDA system. Bench tests of the proximity sensor, which measures the deflection of the aft support flexure (Fig. 5) showed repeatability of measurements to within 0.5% and negligible drift in voltage output over time.

The sensor signal is related to drag by a simple calibration

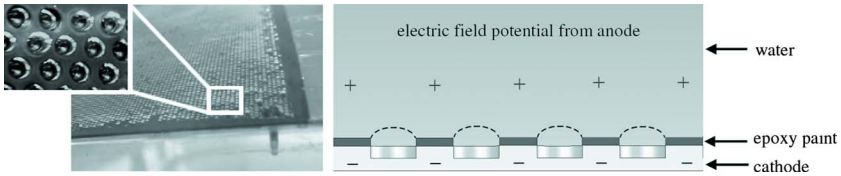

Fig. 4 Photograph of TBA during electrolysis (left). Schematic of the electrolysis process for trapped-bubble formation (right).

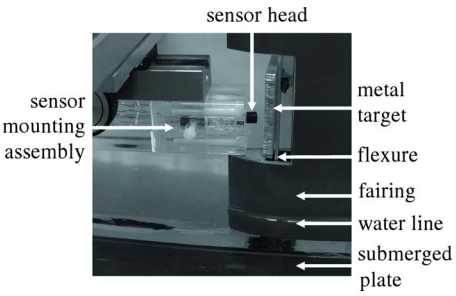

Fig. 5 Proximity sensor setup used in force balance measurements

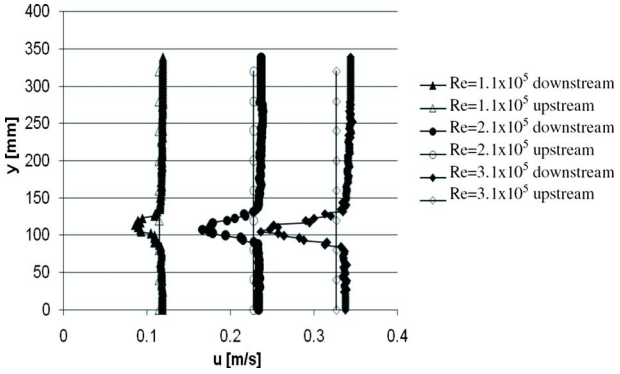

Fig. 6 Sample velocity profiles acquired at upstream and downstream stations of a horizontally mounted plate

technique as follows: the sensor head is positioned at its neutral value (which is equivalent to an output of 1.0 V $\pm$ 0.05 V) so that it is nearly touching the target. Six weights (0.016 kg each) are then hung in succession on a calibration fiber that is attached to the plate through a pair of pulleys shown in Fig. 3. The sensor is mounted such that the full load of calibration weights produces a deflection corresponding to the full-scale voltage output of the sensor, or approximately 11.0 V $\pm$ 0.05 V. The flexure deflection corresponding to this full-scale output is more than the maximum deflection occurring during the experiments. As the plate is displaced, the sensor output is sent to the computer and a LABVIEW virtual instrument (VI). The calibration curve fits were determined to be repeatable to within 10% (due to friction within the pulley system), which for a direct comparison of bubbles/no bubbles configurations is too large of a variation to be useful, as this trapped-bubble drag reduction method being tested is anticipated to produce up to a 10% drag reduction. Since the pulley system introduced additional error in the system that is not present during the experiments, one single calibration curve is instead acquired at the beginning of each set of experiments (one set consists of drag measurements taken over a range of Reynolds numbers with and without bubbles) and is used to compute an absolute drag for the entire set of experiments. Prior to each individual experiment, the vertical plate is prepared and the system is allowed to come to rest completely. Then the proximity sensor is set to its neutral value, and the voltage output by the proximity sensor during the experiments are converted to a force via the calibration curve.

Each drag value obtained using the proximity sensor is an average of ten individual measurements acquired in two sets of five in-test repeated measurements. The experimental procedure to obtain these measurements is as follows:

(1) Flat plate is prepared for experiment. If measuring drag without bubbles, all bubbles are removed from holes (by brushing over holes repeatedly with a small brush); if measuring drag with bubbles, bubbles are grown in holes via electrolysis, as described in Sec. 2.2 (holes are "full" when bubbles are protruding, as illustrated in Fig. 4).
(2) System is brought to rest and proximity sensor is set to its neutral value.
(3) Water tunnel is brought up to test speed and one drag measurement is then acquired every minute for 5 min. Each drag measurement is an average of 1000 samples acquired over 10 s at a sampling rate of 100 Hz, which yields approximately four statistically independent data points per acquisition. Freestream velocity measurements are also obtained during each experiment using the LDA.
(4) Water tunnel is turned off and system is brought to rest. The results from the experiment are accepted if the neutral value to which the sensor returns has not changed by more than 2% ($\pm$0.02 V) and rejected otherwise.
(5) Steps (3) and (4) are repeated a second time for the second set of in-test measurements.

The final goal of the experiments is to determine a relative change in drag produced by the TBA with and without bubbles. Error bars are calculated for the uncertainty in measured drag from the proximity sensor and also for the uncertainty in the corresponding Reynolds number.

The uncertainty in the sensor system is determined by measuring the variation in the proximity sensor neutral value before and after the experiment. The student's t-distribution is then used to calculate the contribution of this error to the overall uncertainty in the measured drag. The relative uncertainty in the sensor neutral value varied among experiments but is always equal to or less than 2.1% of the proximity sensor neutral value. Uncertainty is also dependent upon the random error in the experiments, which is calculated from the variation in the ten individual measurements using the student's t-distribution; uncertainty due to randomness in the experiments is always less than 4.1%. These two uncertainties added together determine the overall uncertainty in the drag measurements. These total uncertainties are generally around 2–3% of the measured drag value with the largest relative uncertainty being 6.64% of the drag value at the lowest Reynolds number tested. Since we are concerned with the relative change in drag between the two cases (flat plate drag with bubbles versus without bubbles), it is assumed that obtaining a sufficiently small uncertainty (using a 95% confidence level) in the sensor's neutral value plus random experimental uncertainty provides a standard through which we may compare the two drag values. As can be seen from Sec. 3.3, these measures of uncertainty are sufficient for determining whether we obtain the expected drag reduction using the TBA. A complete description of the uncertainty analysis is provided in Appendix C of Ref. [19].

Flat plate drag measurements for a vertically or horizontally mounted plate may be independently obtained by integrating the momentum equation over a control volume surrounding the test plate. When the plate is mounted horizontally in the test section, LDA velocity profiles must be obtained in the vertical y-direction to capture the wake profile. The upstream and downstream velocity profiles (Figs. 6 and 7) were obtained at the plate midspan and were numerically integrated assuming spanwise uniformity to obtain the total drag on the plate.

Comparison of the upstream and downstream velocity profiles shows a small streamwise flow speed increase along the plate due to solid blockage from the plate itself as well as wake blockage. This flow speed increase acts to slightly "pull" the model downstream. Corrections may be made for both types of blockage and are outlined according to Barlow et al. [14] below.

The correction for solid blockage is given by

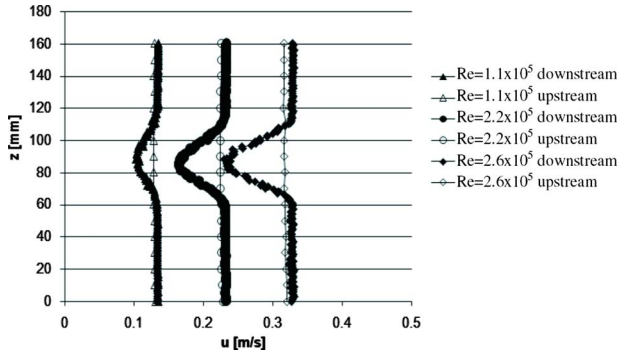

Fig. 7 Sample velocity profiles acquired at upstream and downstream stations of a vertically mounted plate

$$\varepsilon_{sb} = \frac{K_1 V_{model}}{C^{3/2}} \tag{6}$$

A parameter value of $K_1=0.74$ is suggested for the plate in the horizontal orientation and $K_1=0.52$ for the plate in the vertical orientation [14]. The variables V and C are plate volume and test section cross-sectional area, respectively. The solid blockage correction term was found to be approximately $\varepsilon_{sb}=0.077$.

The correction for wake blockage is given in Ref. [14] as

$$\varepsilon_{wb} = \frac{c}{4h} C_{du} \tag{7}$$

The parameter c represents the plate chord length, h is the water height (or channel span, as appropriate), and C_{du} is the uncorrected drag coefficient. The wake blockage correction was found to be approximately $\varepsilon_{wb}=0.011$ at the highest flow speeds. The uncorrected drag coefficient is determined by applying Eq. (8) to the control volumes. The wake width $Y_w=y_2-y_1$ is determined from the downstream velocity profile, and q and q_o are the dynamic pressures determined from the wake and downstream freestream velocity, respectively. Note that extending the numerical integration from Eq. (8) outside of the wake provides little to no contribution to the drag coefficient (since $q(y)$ is equal to q_o outside the wake); thus, the drag coefficient may be determined by numerically integrating Eq. (8) across the wake only

$$C_{du} = \frac{Y_w}{c} - \frac{1}{q_o c}\int_{y_1}^{y_2} q(y)dy \tag{8}$$

The solid and wake blockage corrections are applied to the uncorrected drag coefficient to yield the final drag coefficient value

$$C_d = C_{du}(1 - 3\varepsilon_{sb} - 2\varepsilon_{wb}) \tag{9}$$

from which we may obtain the drag. Note that the largest wake and solid body correction made to any of the drag coefficients was $C_d/C_{du}=0.74$ or about 26%.

3 Trapped-Bubble Results

3.1 Overview. We first examine the drag reduction produced by a large trapped bubble on the bottom of the horizontally mounted flat plate. Results from these large trapped-bubble experiments provide some perspective on the characteristics of the tiny trapped bubbles, which are significantly more difficult to study to the extent of that done for the large bubble. In particular, bubble surface contamination observed on the large trapped bubble is found to correspond to the amount of drag reduction obtained, and it is expected that this observation will apply for the tiny trapped bubbles. Drag results from this study also provide insight into the magnitude of maximum drag reduction attainable by a trapped-bubble drag reduction method.

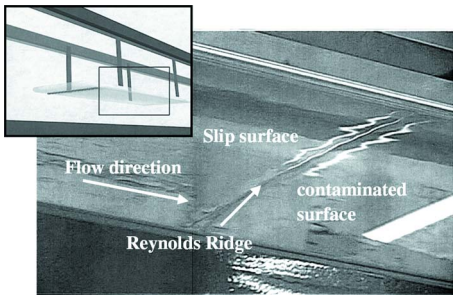

Fig. 8 Reynolds ridge formation on the surface of a large trapped bubble. Note that the Reynolds ridge is nearly straight and spans virtually the entire bubble width. View taken from an oblique angle below bubble (see schematic).

3.2 Large Trapped-Bubble Results. Several interesting bubble surface phenomena were observed on the large bubble. After forming the large bubble in the cavity, contaminants in the water accumulate onto the clean bubble surface over time. When the flow is turned on, shear forces strip away some of these contaminants while the rest are pushed toward the back of the bubble, resulting in a bubble, which has a clean surface in front and a contaminated surface further downstream.

A crease in the surface separating these two regions of clean and contaminated bubble surface is known as the Reynolds ridge (Fig. 8). These regions were examined by using the LDA to acquire streamwise mean and rms velocity profiles near the surface of the bubble (Fig. 9). The mean velocity profile acquired at the surface of the contaminated region (at a location $x=0.323$ m downstream of the leading edge) shows a large velocity gradient at the bubble surface with only a small slip velocity, which is approximately 10% of the freestream value.

It is believed that the relatively large velocity gradient at the interface is caused by the build-up of contaminants at the surface. A small amount of velocity slip is observed, which may be a result of the movement of the contaminants on the bubble surface. The

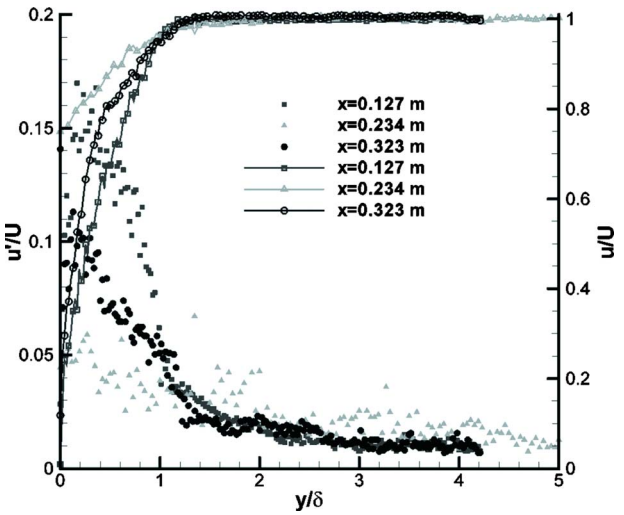

Fig. 9 Streamwise mean (line with open symbols) and rms (filled symbols) velocity profiles acquired over a large trapped bubble at three streamwise locations from $y/\delta=0$ ($y=0$ mm, on the surface) to $y/\delta=5$ ($y=20$ mm) with $U_\infty=0.17$ m/s, where δ is based on $0.95U_\infty$. Measurements taken at $x=0.127$ m from the leading edge correspond to the solid flat plate surface, $x=0.234$ m corresponds to the clean portion of the trapped bubble, and $x=0.323$ m corresponds to the contaminated portion of the trapped bubble (approximately 3 cm downstream of the Reynolds ridge).

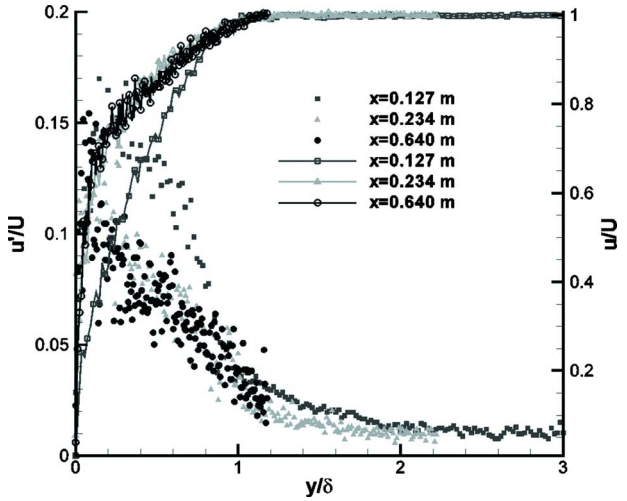

Fig. 10 Streamwise mean (line with symbols) and rms (filled symbols) velocity profiles acquired over a solid flat plate surface at three streamwise locations from $y/\delta=0$ (surface) to $y/\delta=3$ with $U_\infty=0.17$ m/s, where δ is based on $0.95U_\infty$. Measurements taken at $x=0.127$ m are identical to the data set presented in Fig. 9. Measurements at $x=0.234$ m correspond to the second measurement location in Fig. 9, $x=0.640$ m corresponds to the end of the trapped-bubble array.

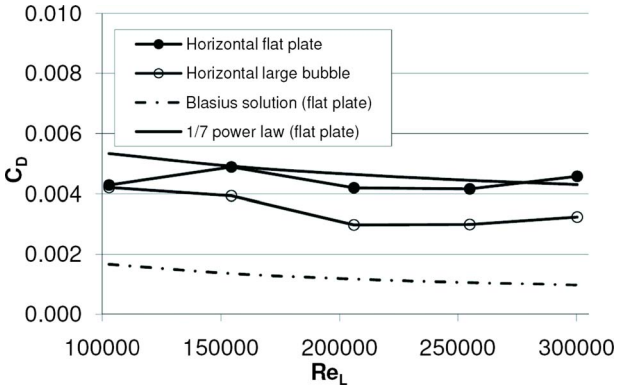

Fig. 11 Drag profiles obtained by the LDA wake survey over a range of Reynolds numbers based on plate length ($1.1\times10^5<\mathrm{Re}_L<3.1\times10^5$) for a horizontal flat plate and a horizontal plate with a large trapped bubble. The one-seventh power law solution accounts for laminar flow up to the boundary layer trips, drag due to the trips and turbulent flow downstream of trips.

streamwise rms velocity does not go to zero at the surface of the contaminated bubble region, shown by the circle symbols in Fig. 9, perhaps because this surface is not rigid and the air allows for compliance at the interface. The contaminants formed a visible crust on the bubble surface that exhibited slow, large-scale convection within the contaminated layer like that discussed previously by Phongikaroon et al. [15]. However, the mean velocity profile at $x=0.234$ m shows that the clean portion of the bubble exhibits near-slip at the surface; the clean bubble surface velocity was approximately 85% of the freestream value, thus the velocity gradient (and therefore shear stress) at the bubble surface was relatively small. Similar to the contaminated bubble surface, we observe from the triangle symbols in Fig. 9 that the rms velocity reaches its peak value at the clean bubble surface. It is interesting to compare this peak rms velocity value on the clean bubble surface to what we observe for the peak rms velocity at the same x-location, but on a solid surface (Fig. 10); the peak rms velocity on the clean bubble surface is approximately one-half the peak rms velocity value of a tripped boundary layer developed over a solid surface. At the lowest Reynolds number tested, the Reynolds ridge was noted to be located 0.27 m behind the leading edge of the bubble. As flow speed increased and shear at the bubble surface became greater, the fraction of the contaminated region of the bubble became progressively smaller; high shear pushed the surface contaminants further back on the bubble surface, resulting in a larger region of slip surface on the front of the bubble (Table 1). This is consistent with the observations in Ref. [6]. In their study, continuous air injection was used to form a presumably uncontaminated air layer on the bottom surface of the flat plate, resulting in 100% drag reduction on the solid surface shielded by the air layer. The uncontaminated region of the bubble in the current experiments indicate the same level of drag reduction as achieved in the high Reynolds number experiments of Sanders et al. [6].

Table 1 Reynolds ridge location and corresponding drag reduction for large trapped bubble

Re_L	Reynolds ridge location (m)	Percent slip on plate surface (%)	Percent drag reduction (%)
1.1×10^5	0.27	13	−3
1.6×10^5	0.47	23	19
2.1×10^5	0.58	29	29
2.6×10^5	0.68	34	27
3.1×10^5	0.71	35	32

Figure 10 shows similar mean and fluctuating velocity profiles taken at three streamwise (x) locations on the solid top side of the plate for comparison. The profiles on the top solid surface clearly indicate a turbulent boundary layer that is not fully developed at these Reynolds numbers. The first streamwise mean velocity profile at $x=0.127$ m (shown by a line with square symbols) in Fig. 10 reflects the wake of the boundary layer trips. A fully developed canonical turbulent boundary layer is, of course, not expected in such a regime and so close to the trips, but for our purposes it is not required either as we are simply running a side-by-side direct comparison to determine if a large bubble or TBA can reduce viscous drag. Farther downstream at $x=0.234$ m and $x=0.640$ m, we see the boundary layer thickening and the normalized streamwise rms velocity peak values approaching 0.11–0.12, which is approximately what we would expect to see in a canonical turbulent boundary layer [16].

The values for the drag coefficient obtained from both a simple solid horizontal flat plate and horizontal plate with a large trapped bubble are shown in Fig. 11. Note that the values agree closely with the analytic flat plate drag coefficient value for turbulent flow aft of the trips, rather than the laminar Blasius solution. In drag coefficient values presented, blockage effects are accounted for as indicated above in Sec. 2.3, but no accommodation is made for the edge effects of the plate near the sidewalls or the free surface. Introducing a large trapped bubble on the bottom surface of the plate significantly reduces the drag on the flat plate. Moreover, the percent drag reduction improves with increasing Reynolds number (Table 1), which corresponds to the movement of the Reynolds ridge further aft along the bubble surface and the increase in percent of slip on the plate surface. In fact, there is good agreement between the percent slip on the bubble surface and the percent drag reduction obtained. In Table 1, the ridge location refers to the downstream distance from the leading edge of the bubble. The percentage of slip is calculated as the ratio of the plate surface covered by clean bubble to the total wetted surface area of the flat plate. The percent drag reduction refers to the percent change in total drag per unit span of the flat plate with a large trapped bubble compared with the simple flat plate case. It should be mentioned that the difference in drag measured at the lowest Reynolds number for the flat plate and large trapped-bubble case is expected to be within the experimental uncertainty of the measurement; thus,

the drag reduction calculated at this particular Reynolds number is not considered to be reliable. We have observed that the plate with the large bubble, when left in the flow for several hours, builds up contamination on the surface and the Reynolds ridge moves forward, but we have not measured drag changes over long times. Presumably, the drag would increase as the amount of clean bubble is reduced.

While the use of a large bubble for drag reduction in a practical case seems unlikely, the bubble did generate some remarkable flows. Dye was injected with a needle into the flow just upstream of the bubble, and some of the dye became entrained in the air-water interface. It was rapidly swept off of the clean region and accumulated on the contaminated surface, forming streamwise streaks. The dye, along with the visible surface contaminants, highlights both large and small scale secondary flows on the bubble surface. These flows appear reminiscent of those observed by Phongikaroon et al. [15] in which a pair of recirculation cells was seen in a much smaller apparatus. The Reynolds ridge on our relatively large bubble spanned straight across the bubble surface. Spanwise-periodic fingerlike recirculation regions appeared in the surface contaminants reflecting both upstream- and downstream-moving flow on the interface. Hence, it appears that Phongikaroon et al. [15] were observing a single mode viscous instability of the contaminated interface while in our larger channel we obtain a multimode recirculating flow. That is, the small slip condition on the contaminated interface (Fig. 9) is a result of a time average over these up/downstream moving recirculation regions.

The drag reduction from the large trapped bubble presented in this paper should be comparable to the near 100% drag reduction obtained from the quasi-continuous bubble film by Sanders et al. [6]; however, it must be emphasized that the measurement technique used herein is different. Sanders et al. [6] considered only drag reduction on the bottom portion of the flat plate, and drag reduction was obtained by acquiring six local skin friction measurements along the length of the plate. In the present study, the total drag on the plate is measured using an LDA wake survey momentum integration technique, which obtains a measurement of total drag per unit span. The technique used in Ref. [6] was sensitive to the location of the gas film on the plate surface, particularly when the film was quasi-continuous. For example, a quasi-continuous bubble forming around (not over) the strain gage sensors may indicate a smaller drag reduction than actually exists on the bottom of the plate, while a gas film forming over only the sensors may indicate a larger drag reduction than actually exists. Thus, the large trapped-bubble drag reduction measurements reported in the present paper may not correspond to those obtained by Sanders et al. [6].

The observations, measuring techniques and drag reduction results obtained from the large bubble study offer both encouraging and useful information leading up to the drag reduction study using a TBA. However, it is not obvious how a Reynolds ridge applies to tiny bubbles. It is expected that contaminants found in the water will accumulate on the tiny bubble surfaces but may be stripped away or pushed to the back of the bubble surface similar to the large bubble. We do not expect that there would be any complex viscous recirculating flows on such tiny bubbles; one might expect at most a simple pair of recirculation cells. However, we did not directly observe this phenomenon on the tiny bubbles; it would be difficult to see due to their small size.

3.3 Trapped-Bubble Array Results. The tiny trapped bubbles offer more versatility than large bubbles in the experimental process and perhaps in applications in the sense that, due to a relatively greater influence of surface tension, tiny bubbles are more hydrodynamically stable than the large bubble. To demonstrate this, the test plate was mounted vertically in the test section in anticipation of demonstrating the drag-reducing capabilities of this method. For the flow speeds examined in these experiments, the largest bubbles in the trapped-bubble array have capillary and Reynolds numbers on the order of 10^{-3} and 10^{2}, respectively, which are defined as

$$\mathrm{Ca}_d \equiv \mu_{\mathrm{liquid}} \left.\frac{\partial u}{\partial y}\right|_{\mathrm{wall}} \frac{d}{\sigma} \tag{10}$$

$$\mathrm{Re}_d \equiv \frac{\rho \left.\frac{\partial u}{\partial y}\right|_{\mathrm{wall}} d^2}{\mu_{\mathrm{liquid}}} \tag{11}$$

Here, d is the bubble diameter and σ is the surface tension. Numerical studies by Feng and Basaran [17] on two-dimensional cylindrical bubbles indicate that the bubbles sizes used in our experiments are within the critical Reynolds number limit: full-profile bubbles at the bubble plate leading edge and highest test speeds have a Reynolds number and capillary number of $\mathrm{Re}_{d,\mathrm{turbulent}} \cong 239$ and $\mathrm{Ca}_{d,\mathrm{turbulent}} \cong 0.0043$, while Ref. [17] report that $\mathrm{Re}_c = 243.7$ for $\mathrm{Ca} = 0.005$ corresponds to neutral stability of the two-dimensional bubble surfaces. The product of the capillary and Reynolds numbers would yield a Weber number that, in this case, is approximately unity suggesting only small bubble deformations. Presumably in higher speed, higher shear stress flows, the bubble diameter would have to be reduced appropriately to maintain bubble stability.

It was noted during the experiments using the TBA that high shear at the plate surface tended to tear away the larger bubbles protruding from the surface at higher Reynolds numbers. The largest protruding bubbles were stripped away at the highest Reynolds number tested, resulting in a TBA with approximately 75% bubble coverage. This suggests that drag reduction, if it could be obtained, may diminish at higher flow speeds unless lost bubbles are actually replaced by electrolysis. We note that drag measurements were obtained with electrolysis power off: the bubbles were created before the test only in order to avoid having the stainless steel anode mesh in the test section during the experiments as it produced a large displacement thickness and increased the measured drag on the plate.

Drag measurements were obtained over a range of Reynolds numbers based on plate length, L ($7.2 \times 10^4 < \mathrm{Re}_L < 3.1 \times 10^5$) for both a vertical plate without trapped bubbles and a vertical plate filled with trapped bubbles. The drag on the vertically mounted plate is measured using both the proximity sensor measurement system and by a wake survey for the two cases examined. In both cases, the same three plate inserts remained in the cavity: two drilled bubble plate inserts in the front and one simple flat plate insert in the back. At the highest Reynolds numbers examined, the hole diameter is about 21 viscous length scales k^+ near the leading edge of the bubble region and 19 k^+ at the trailing edge. Although the holes themselves do not protrude into the flow, the surface is expected to be transitionally rough [16,18]. While we could have compared the drag of a TBA plate to a simple smooth plate it is reasonable to believe that (1) the holes in the bubble plates were sufficiently small so as to have only minor effects on the plate drag and (2) as seen below, the presence of bubbles in the holes hardly affected the drag so it did not matter. The drag results for each case are plotted in Fig. 12; open square and closed triangle symbols correspond to the proximity sensor measurements with and without bubbles, respectively, and are observed to be higher than the analytic (one-seventh power law) turbulent solution.

This difference in drag as measured by the proximity sensor and the wake survey may be a result of the uncertainty in the calibration curve fit discussed in Sec. 2.3, but it is also important to note that the drag values are obtained using two fundamentally distinct measurement techniques on a finite span plate. Measurements using the proximity sensor are obtained from a resultant displacement of the plate due to the total physical drag force on the plate, which presumably includes additional drag due to plate end effects. LDA velocity measurements across the span of the

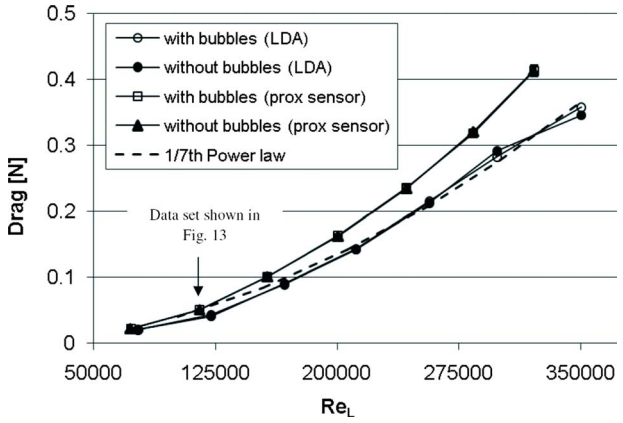

Fig. 12 Drag measurements obtained for a vertical flat plate ($7.2\times10^4<Re_L<3.1\times10^5$) with and without trapped bubbles using LDA and proximity sensor measurement systems. The one-seventh power law solution accounts for laminar flow up to the boundary layer trips, drag due to the trips and turbulent flow downstream of trips, and drag contributions from flexures (for vertical plate case). Error bars (based on a 95% level of confidence) are included for the proximity sensor data but are very small.

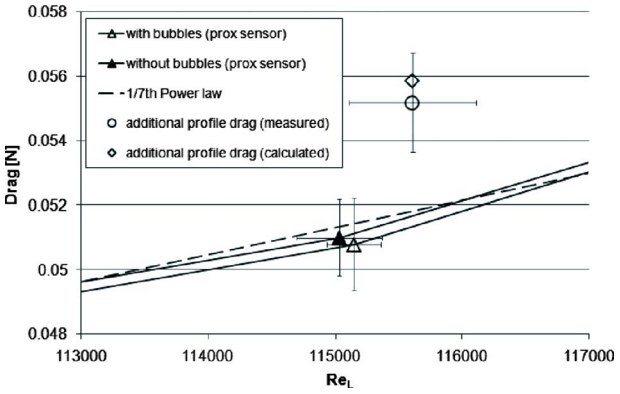

Fig. 13 Detailed plot of proximity sensor drag measurements (triangle symbols) corresponding to $Re_L=1.15\times10^5$ from Fig. 12. Error bars are based on a 95% level of confidence. Circle symbol shows 7.8% increase in drag due to an additional roughness element affixed to the plate in comparison to a calculated 9.8% drag increase seen with the open diamond symbol.

plate indicate that disturbances due to plate end effects spread toward the plate centerline at a streamwise spreading angle of approximately 11 deg. Drag measurements using the wake survey are obtained from velocity profiles taken at the plate midspan location, which should not reflect strong plate end effects, resulting in a lower measured drag compared with the force balance measurements. The disturbances and perhaps weak vortices forming in between the plate, channel floor, and free surface or weak free surface wave drag should be expected to lead to a higher drag than would occur for an infinite span flat plate.

The area of the flat plate covered with tiny trapped bubbles accounts for only 8.66% of the total wetted surface of the plate, so the effect of the trapped bubbles on the measured drag is expected to be small. Uncertainties in measured drag values ranged from approximately 1.1% to 6.6%, and uncertainties in measured Reynolds numbers were all within 0.5%. These uncertainty error bars are included on the proximity sensor data in Fig. 12, but are small compared with the symbols shown. Drag measurements (with and without bubbles) obtained from the proximity sensor at $Re_L=1.1\times10^5$ are shown in detail in Fig. 13.

Over the range of Reynolds numbers examined, all drag measurements with and without bubbles lie within the experimental uncertainty, so no substantial drag reduction was observed with the TBA. To demonstrate that the proximity sensor system is in fact able to measure a small change in drag (particularly at the low Reynolds numbers where we are trying to measure small changes in small drag values), three roughness elements were attached to the side of the plate in a separate experiment. Each roughness element was a simple rectangular aluminum shim. The elements were inserted lengthwise in the narrow gap between the first and second bubbles plates such that they were protruding from the plate surface, with 2.0 cm $\times$ 0.5 cm wetted frontal areas. The expected drag due to these three roughness elements was calculated based on the drag on a rectangular plate (with a drag coefficient, $C_D=2$) in freestream flow for $Re_L=1.15\times10^5$. The calculated percent drag increment due to this added roughness element is approximately 9.8%. The actual measured drag value is expected to be slightly smaller than this value since a significant portion of the roughness element is within the boundary layer of the plate. The drag measurements obtained from this study are shown in Fig. 13. It can be seen in the figure that the roughness elements increase the drag measured on the flat plate by approximately 0.004 N, which corresponds to a 7.8% drag increase in close agreement with the calculated 9.8%.

Drag measurements were also obtained using the numerical integration of the LDA wake survey and are shown in Fig. 12 as well. The open circle symbol corresponds to flat plate drag with bubbles, and the closed circle corresponds to a flat plate without bubbles. Both of the trends obtained from the LDA measurements agree remarkably well with the predicted (analytical) drag curve for a solid flat plate. Uncertainty analysis was not performed on the data obtained from the LDA as only one full velocity profile was obtained for each test case at each Reynolds number, but the percent changes in drag obtained from the LDA measurements again indicate negligible drag reduction from the TBA.

4 Summary and Conclusions

The principle objective of this experimental program was to demonstrate the drag-reducing capabilities of the TBA drag reduction approach, although no drag reduction was found. A baseline set of experiments involving a large trapped bubble provided a source of comparison and observations to examine the underlying principles of the TBA drag reduction approach, and provided insight as to the maximum drag reduction one could hope for with the trapped-bubble method.

Drag results for the trapped-bubble experiments were obtained using two independent measurement techniques: a proximity sensor, which measured plate deflection of the aft supporting flexure, and a wake survey using a LDA system. Drag measurements were acquired for a horizontally oriented solid flat plate and a horizontally mounted plate with a large trapped bubble on the bottom surface. Drag measurements were also acquired for a vertically oriented plate with bubble plate inserts that were either bare or filled with bubbles.

The large trapped bubble produced a maximum drag reduction of 32%, corresponding to a slip area, which occupied 35% of the wetted plate surface. The large trapped bubble indicated an improved drag reduction with increasing Reynolds number, which is believed to be a result of the slip surface increase associated with the receding Reynolds ridge on the bubble surface. Thus, it is reasonable to suggest that a clean bubble surface provides a drag reduction roughly proportional to the wetted surface area, which it occupies. This may also provide insight as to why no drag reduction was observed using the TBA; the means of bubble formation in each of the two experiments are significantly different. Recall that air is injected into the bottom-facing cavity of the plate to form the large trapped bubble, while electrolysis is used to form the TBA. It was observed during experiments that a white precipi-

tate (presumably a by-product of electrolysis) formed and collected inside the tiny bubble cavities over time. It is possible that this precipitate, although difficult to see due to the small size of the bubbles, collects on the surfaces of the tiny bubbles, effectively forming a no-slip bubble surface and inhibiting slip.

The tiny trapped bubbles that constituted the TBA surface covered only 8.66% of the wetted plate surface. The uncertainty analysis revealed that the change in drag observed from TBA measurements was within the experimental uncertainty and was not close to 8.66%. Thus, no appreciable drag reduction was obtained using the current trapped-bubble array method. No uncertainty analysis was performed for the LDA measurements, but the percent changes in drag generally agreed with the results obtained using the proximity sensor measurement system. Hence, it is not possible to make a claim of drag reduction using the TBA with any reasonable certainty and a cost/benefit analysis for use of a TBA is inappropriate.

Future work on the TBA concept should examine in greater detail flow over the tiny bubble surfaces in order to determine to what extent surface contaminants (either from the tap water or from the electrolysis process) affect slip on the bubble surface. It is possible that the tiny bubble surface behaves differently (in comparison to the large trapped bubble) when contaminated, and it is not clear whether a Reynolds ridge forms on the tiny bubble surfaces. Nonetheless, if the tiny bubbles provide clean slip surfaces, it would be important to investigate in detail the flow field over the TBA to determine if mean velocity slip occurs. In addition, bubble parameters including size and configuration should be investigated, and means of producing smaller holes should be sought. The Computer Numerical Control (CNC) machining process used here required approximately 2 s of drilling time for each hole, which is approaching the tolerable manufacturing limit to produce an entire surface of these holes.

Acknowledgment

The authors would like to thank Dr. David Bogard from the Mechanical Engineering Department at the University of Texas at Austin for his suggestions. Also thanks to Rick Maldonado, Travis Crooks, Frank Wise, Pablo Cortez, and their supporting staff for their contributions to the design and manufacturing of hardware used in this research. This research was sponsored by the Texas Advanced Technology Program.

References

[1] Matveev, K. I., 2003, "On the Limiting Parameters of Artificial Cavitation," Ocean Eng., **30**(9), pp. 1179–1190.
[2] Latorre, R., 1997, "Ship Hull Drag Reduction Using Bottom Air Injection," Ocean Eng., **24**(2), pp. 161–175.
[3] Madavan, N. K., Deutsch, S., and Merkle, C. L., 1984, "Reduction of Turbulent Skin Friction by Microbubbles," Phys. Fluids, **27**(2), pp. 356–363.
[4] Madavan, N. K., Deutsch, S., and Merkle, C. L., 1985, "Measurements of Local Skin Friction in a Microbubble-Modified Turbulent Boundary Layer," J. Fluid Mech., **156**, pp. 237–256.
[5] Pal, S., Deutsch, S., and Merkle, C. L., 1988, "Bubble Characteristics and Trajectories in a Microbubble Boundary Layer," Phys. Fluids, **31**(4), pp. 744–751.
[6] Sanders, W., Winkel, E., Dowling, D., Perlin, M., and Ceccio, S., 2006, "Bubble Friction Drag Reduction in a High-Reynolds-Number Flat-Plate Turbulent Boundary Layer," J. Fluid Mech., **552**, pp. 353–380.
[7] Balasubramanian, A., Miller, A. C., and Rediniotis, O. K., 2004, "Microstructured Hydrophobic Skin for Hydrodynamic Drag Reduction," AIAA J., **42**(2), pp. 411–414.
[8] Joseph, P., Cottin-Bizone, C., Benoît, J. M., Ybert, C., Journet, C., Tabeling, P., and Bocquet, L., 2006, "Slippage of Water Past Superhydrophobic Carbon Nanotube Forests in Microchannels," Phys. Rev. Lett., **97**(15), p. 156104.
[9] Ou, J., Perot, B., and Rothstein, J. P., 2004, "Laminar Drag Reduction in Microchannels Using Ultrahydrophobic Surfaces," Phys. Fluids, **16**(12), pp. 4635–4643.
[10] Reed, J. C., Bushnell, D. M., and Weinstein, L. M., 1991, "U.S. Patent for Hydrodynamic Skin-Friction Reduction," U.S. Patent No. 5,05,412.
[11] Stephani, K., and Goldstein, D., 2007, "The Effects of Trapped Bubbles on Viscous Drag Reduction for Submerged Surfaces," AIAA Paper No. 2007-4101.
[12] Stephani, K., Marr, K., Doctor, R. and Goldstein, D., 2006, "Drag Reduction Using Trapped Bubbles on a Flat Plate Surface," AIAA Paper No. 2006-3193.
[13] Goldstein, D., 2006, "U.S. Patent for Methods for Reducing the Viscous Drag on a Surface and Drag Reducing Device," U.S. Patent No. 7,044,073 B2.
[14] Barlow, J. B., Rae, W. H., and Pope, A., 1999, *Low Speed Wind Tunnel Testing*, 3rd ed., Wiley-Interscience, New York.
[15] Phongikaroon, S., Peter, J. K., Smith, G., and Handler, R., 2004, "The Thermal Structure of a Wind-Driven Reynolds Ridge," Exp. Fluids, **37**(2), pp. 153–158.
[16] White, F. M., 2006, *Viscous Fluid Flow*, 3rd ed., McGraw-Hill, New York.
[17] Feng, J. Q., and Basaran, O. A., 1994, "Shear Flow Over a Translationally Symmetric Cylindrical Bubble Pinned on a Slot in a Plane Wall," J. Fluid Mech., **275**, pp. 351–378.
[18] Schlichting, H., 1987, *Boundary-Layer Theory*, 7th ed., McGraw-Hill, New York.
[19] Stephani, K., 2006, "Drag Reduction Using Trapped Bubbles on a Submerged Flat Plate Surface," MS thesis, Department of Aerospace Engineering and Engineering Mechanics, University of Texas at Austin, Austin, TX.

On the Suppression of Vortex Shedding From Circular Cylinders Using Detached Short Splitter-Plates

Behzad Ghadiri Dehkordi
e-mail: ghadirib@modares.ac.ir

Hamed Houri Jafari[1]
e-mail: hhjafari@gmail.com

Department of Mechanical Engineering,
School of Engineering,
Tarbiat Modares University,
Tehran, Iran

Flow over a circular cylinder with detached short splitter-plates is numerically simulated in order to assess the suppression of periodic vortex shedding. A finite-volume solver based on the Cartesian-staggered grid is implemented, and the ghost-cell method in conjunction with Great-Source-Term technique is employed in order to enforce directly the no-slip condition on the cylinder boundary. The accuracy of the solver is validated by simulation of the flow around a single circular cylinder. The results are in good agreement with the experimental data reported in the literature. Finally, the flows over a circular cylinder with splitter-plate in its downstream (off and on the centerline) are computed in Re=40 as a nonvortex shedding case and in Re=100 and 150 as cases with vortex shedding effects. The same simulations are also performed for the case where dual splitter-plates are in a parallel arrangement embedded in the downstream of the cylinder. The optimum location of the splitter-plate to achieve maximum reduction in the lift and drag forces is determined. [DOI: 10.1115/1.4001384]

Keywords: vortex shedding, flow induced forces, circular cylinders, splitter-plate

1 Introduction

Suppression of vortex shedding from circular cylinders using splitter-plates in order to reduce flow induced forces on the structure is a matter of great importance, especially in deep water marine structures.

Rathakrishnan [1], Anderson and Szewczyk [2], and Kwon and Choi [3] comprehensively studied the vortex shedding suppression using the splitter-plates attached to the end of the cylinder. Ozono [4] initially developed the idea of using the detached splitter-plates. He experimentally analyzed the flow behavior in Re=6700, 17,000, and 25,000 by embedding a detached short splitter-plate (the length of the splitter-plate is the same as the cylinder diameter) at different distances from the cylinder. He showed that in a given Z/D, with decreasing G/D, (where D is the cylinder diameter, and G and Z are the horizontal and vertical distances, respectively, between leading edge of the splitter-plate and the cylinder base) in a certain value of G/D, which is called "critical value," the cylinder base pressure and the Strouhal number would change suddenly. Ozono [5] also carried out a similar investigation on the detached long splitter-plates (the length of splitter-plate was six times longer than the cylinder diameter). Hwang et al. [6] numerically studied the effect of using the detached short splitter-plates on the centerline of the cylinder ($Z/D=0$) and found the critical value of $G/D=2.6$ in Re=100 and 160. Hwang and Yang [7] numerated the drag reduction resulted from the use of dual short splitter-plates, one in the upstream and another in the downstream of the cylinder. They achieved 38.6% reduction in the drag coefficient in the situation of Re=100, $G1/D=1.5$, and $G2/D=2.4$ ($G1$ and $G2$ are the distances between the trailing and leading edges of the upstream and downstream splitter-plates, respectively, from the cylinder).

As it can be seen, the performed numerical investigations are limited to the replacement of the splitter-plates on the centerline of the cylinder or to attach it to the end of the cylinder. In the present paper, flow over a circular cylinder with detached short splitter-plate on and off the centerline of the cylinder has been numerically simulated. The flow field was computed for Re=40 as a nonvortex shedding case and for Re=100 and 150 as cases with vortex shedding effects. The numerical method is based on the finite-volume method and the Cartesian-staggered grid. A Ghost-cell method in conjunction with Great-Source-Term technique was employed to enforce the no-slip condition on the embedded boundaries [8]. The numerical procedure is based on the semi-implicit method for pressure-linked equations (SIMPLE) algorithm [9].

Section 2 of the present article outlines the numerical simulation procedure of the problem. Section 3 validates the approach for the flow around a single circular cylinder. In Sec. 4, the results are presented and analyzed for the flow around the circular cylinder with detached short splitter-plate in its downstream. Finally, the conclusions are drawn in Sec. 5.

2 Numerical Simulation Procedure

2.1 Flow Field Formulation. The governing equations on the flow field are the continuity and momentum equations (Navier–Stokes equations), which can be written as follows:

$$\frac{\partial \rho}{\partial t} + \mathrm{div}(\rho \boldsymbol{u}) = 0 \tag{1}$$

$$\frac{\partial}{\partial t}(\rho u) + \mathrm{div}(\rho \boldsymbol{u} u) = -\frac{\partial P}{\partial x} + \mathrm{div}(\mu\ \mathrm{grad}\ u) + \beta_x \tag{2}$$

$$\frac{\partial}{\partial t}(\rho v) + \mathrm{div}(\rho \boldsymbol{u} v) = -\frac{\partial P}{\partial y} + \mathrm{div}(\mu\ \mathrm{grad}\ v) + \beta_y \tag{3}$$

where ρ is the fluid density, μ is the fluid viscosity, $\boldsymbol{u}$ is the velocity vector of the flow field, P is the pressure, and u and v are the velocity components in the x- and y-directions, respectively. β_x and β_y are also the body forces per unit volume, which are negligible in the present study. The fluid has been assumed to be incompressible, and its properties has been taken as $\rho=10^3$ kg/m^3 and $\mu=10^{-3}$ kg/m s.

2.2 Limits of the Problem. A rectangular domain was used with a length of $40D$ and a width of $20D$, where $D=0.04$ m is the cylinder diameter. The cylinder center had the coordinates $x=10D$ and $y=10D$. The position of the splitter-plate is specified by Z and G, denoting the vertical and horizontal distances, respectively, between the leading edge of the splitter-plate and the base suction point of the cylinder. The splitter length and thickness are D and $1/20D$, respectively.

The boundary conditions were imposed in a way that the fluid flows uniformly (with velocity profile U) from left to right into the downstream of the domain. Boundary conditions should be also enforced at the outlet and the lateral boundaries of the computational domain, as well as on the surfaces of the embedded bodies.

[1]Corresponding author.

Contributed by the Fluids Engineering Division of ASME for publication in the JOURNAL OF FLUIDS ENGINEERING. Manuscript received July 12, 2009; final manuscript received February 25, 2010; published online April 16, 2010. Assoc. Editor: Mark Stremler.

A symmetry boundary condition has been used at the lateral boundaries of the computational domain. Whereas, the Dirichlet and Neumann boundary conditions have been employed for the inlet and outlet, respectively.

2.3 Discretization Method. The governing equations have been discretized using the finite-volume method on a fixed Cartesian-staggered grid with nonuniform grid spacing. The grids in the region of the embedded boundaries are sufficiently fine in order to achieve the reasonable accuracy. The temporal discretization has been done in conformity with the fully implicit scheme. For the spatial discretization, the Hybrid scheme has been employed. The SIMPLE procedure was applied to calculate the flow field [10].

2.4 The No-Slip Condition. The no-slip condition on the splitter-plate has been applied by setting the velocity components at zero for the grid points sitting on the surface of that. Because of the rectangular shape of the splitter-plate and Cartesian grid type of the mesh system, the application has been simply done. But applying the no-slip condition to the cylinder was the main difficulty of the method, which was applied using the ghost-cell method. The amounts of the flow field variables have been arranged to be the answers at the embedded boundaries (i.e., cylinder and splitter-plate) grid points using the Great-Source-Term technique. The implemented ghost-cell method and Great-Source-Term technique have been presented in detail in Ref. [8].

3 Verification of the Solver

In this section, the accuracy of the solver is validated by simulation of the flow around a single circular cylinder. In order to present the results, various parameters such as the Reynolds number $\mathrm{Re}=\rho UD/\mu$, drag coefficient $Cd=F_D/0.5\rho U^2D$, lift coefficient $Cl=F_L/0.5\rho U^2D$, pressure coefficient $Cp=P/0.5\rho U^2$, Strouhal number $\mathrm{St}=fD/U$, and dimensionless time $T=tU/D$ have been used.

Dehkordi and Houri Jafari [8] proved the grid-independency of the solver and showed that the results are not sensitive to the grid size. Hereinafter, all presented results have been obtained by the fine grid with 200×200 cells, assuming that this grid provides a sufficient grid-independency for all Reynolds numbers considered. The simulations were carried out as an unsteady state with a time step of $\Delta t=10^{-3}$ s.

The results of the flow around single circular cylinders were also comprehensively verified and analyzed in Ref. [8], using the dimensionless parameters defined above. Anyway, as evidence, Fig. 1 demonstrates the pressure distribution for Reynolds numbers of 40 and 100. Good agreement exists between the results of the present work and the other studies. Our simulations generally show that for Reynolds number equal to 40, the flow field is fully symmetric and steady, and consequently the lift coefficient is zero. For a Reynolds number of 47 and above, the Von Karman street is formed behind the cylinder, and the flow field is unsteady and asymmetric [11]. Thus, the lift and drag coefficients in Reynolds numbers of 100 and 150 oscillate due to the shedding of vortices. Moreover, the drag coefficient oscillates at twice the frequency of the lift coefficient [12].

In order to show variation patterns of the drag and lift coefficients, Dehkordi and Houri Jafari [8] graphed the drag and lift coefficients as a function of the dimensionless time for different values of the Reynolds number. Evidently, results drawn in their figures are in good agreement with the same graphs presented by other researchers [12,13]. For Re=40, the drag coefficient is high at the beginning and asymptotically decay to 1.52. The maximum amplitudes of the lift coefficients in Re=100 and 150 were also calculated as 0.27, and 0.39, respectively. In these Reynolds numbers the frequency of the oscillating lift is similar to the vortex shedding frequency. The Strouhal numbers for these Reynolds numbers are 0.163 and 0.179, respectively, which are in excellent agreement with the literature (the results of Refs. [11,14]).

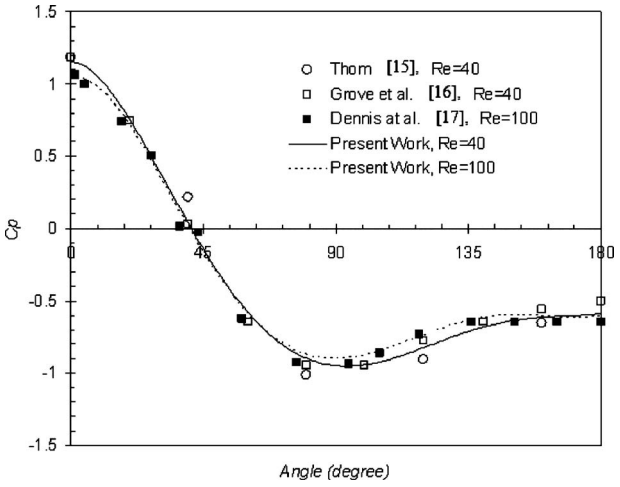

Fig. 1 Pressure distribution obtained by the present work in comparison with some experimental and numerical data reported in the literature (Re=40 and 100)

4 Results and Discussion

In the present section, the results are demonstrated and analyzed for Reynolds numbers of 40 and 100 [15–17]. Note that there is no vortex street in Re=40. The goal of the simulations in this Reynolds number is identifying the effect of the splitter-plate in flow pattern and drag reduction. Also, the performed simulations in Re=150 have shown that the key parameters of the flow have similar variation trend (with respect to the G and Z values) to the Re=100. Thus, the results of Re=100 are just presented and discussed as the case study of vortex shedding suppression. In addition, a similar investigation was performed where dual splitter-plates are placed in a parallel arrangement in the downstream of the cylinder in order to achieve further drag reduction. All the simulations (except Re=40) have been performed for configurations of $G/D=0$, 0.6, 1, 2, 2.1, 2.2, 2.3, 2.4, 2.5, 2.6, 2.7, 2.8, 2.9, 3, 4, 5, 7, and 10, for each $Z/D=0$, 0.25, 0.5, 0.75, 1, and 1.25. The case of Re=40 did not require high resolution variation in $2\leq G/D\leq3$. In order to compare the results, in Secs. 4.1 and 4.2, we nominated a case of the circular cylinder without splitter-plate as the "reference case."

4.1 Nonvortex Shedding Case (Re=40). Evaluation of the drag coefficient, as a function of G/D and Z/D, in Re=40, shows that the splitter-plate has not significantly changed the drag coefficient. In some cases, the resulted drag coefficients were more than the reference case, unexpectedly. Drag reduction has been observed more considerable in $Z/D=0.5$ and 0.75 configurations. The largest and smallest drag coefficients were obtained at ($Z/D=1.25$ and $G/D=0$) and ($Z/D=0.75$ and $G/D=0$), which were 4.2% and 2.6% more and less than the reference case, respectively.

4.2 Periodic Vortex Shedding Case (Re=100). The drag coefficient and absolute amplitude of the lift coefficient have been graphed in Fig. 2 for Re=100 and different Z/D and G/D values. As it is evident, embedding the splitter-plate in the downstream of a cylinder causes drag reduction by mechanism of vortex shedding interrupting. The splitter-plate limits the formation space of the vortices and suppresses vortex shedding, especially in low gaps. This effect also reduced the lift coefficient and confined its oscillations. In a constant Z/D, as G/D increases, the drag and lift coefficients will decrease continuously to their minimum amounts. After that in a certain value of G/D called "critical value" the drag and lift coefficients will suddenly increase. Over critical values, both the drag and lift coefficients reach the amounts near to

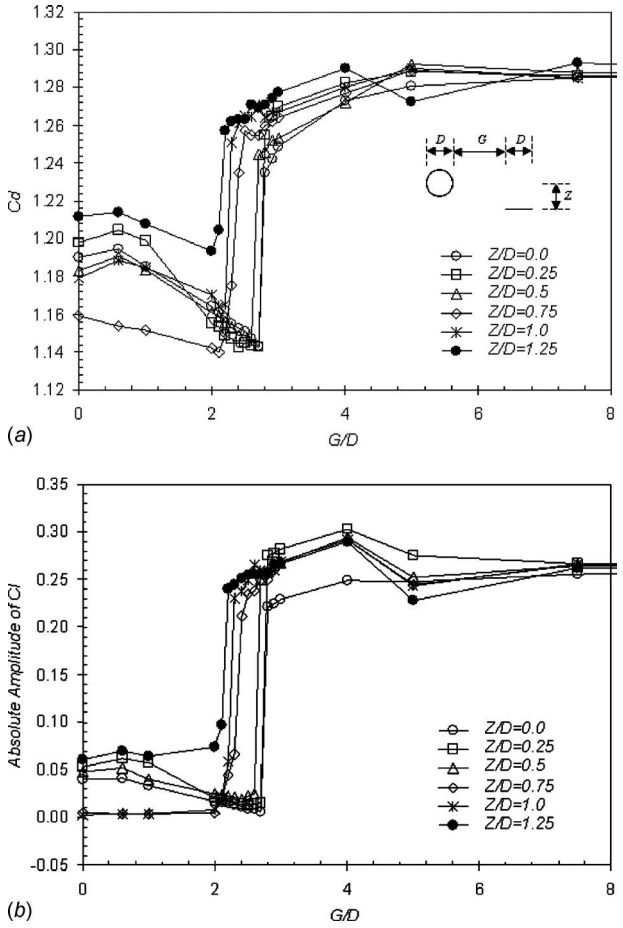

Fig. 2 Variation in the drag and lift coefficients in Re=100 and different *Z/D* and *G/D* values: (*a*) drag coefficient and (*b*) absolute amplitude of the lift coefficient

the reference case. This fashion was identically reiterated for all Z/D values. Our simulations have also shown that the critical values are significantly dependent on Z/D. The critical values for $Z/D=0$, 0.25, 0.5, 0.75, 1, and 1.25 are obtained as 2.7, 2.7, 2.6, 2.3, 2.2, and 2.1, respectively.

It is noteworthy to mention that, the most reduction in drag and lift coefficients occurred in $Z/D=0.75$. In this condition, the vortex shedding is fully suppressed, and absolute amplitude of the lift coefficient oscillations is nearly zero. This negligible lift is attributed to the change in the pressure distribution pattern from asymmetric to symmetric.

In Fig. 3, the Strouhal variations, with different G/D and Z/D values, are shown for Re=100. The trend of the Strouhal changes with G/D is similar for most Z/D values except $Z/D=1$ and 1.25. This matter is completely compatible with the experiments [4]. Over the critical points, the Strouhal numbers were also converged to the reference case amount.

Generally, using the splitter-plate off the centerline of the cylinder prevents high strength vortex shedding and finally leads to drag and lift coefficient reductions. Since pressure distribution gets asymmetric, the time-averaged lift coefficient has a slight variance in comparison with the reference case.

It seems that we can achieve twice reduction in flow induced forces using two splitter-plates in parallel arrangement relative to the centerline of the cylinder. In order to examine this idea, the drag coefficient was calculated for $Z1/D=Z2/D=0.75$ ($Z1$ and $Z2$ are vertical distances between the cylinder and first and second splitter-plates, respectively) and figured in Fig. 4. This figure shows more drag reduction but not necessarily twice trend. The

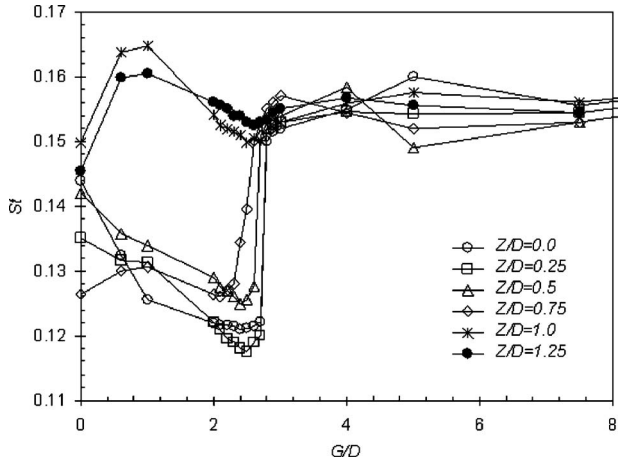

Fig. 3 Variation in the Strouhal number in Re=100 and different *Z/D* and *G/D* values

maximum reduction occurred in $G/D=0$ with 20% diminution compared with the reference case. However, this value is still smaller than 38.6%, which was achieved by dual splitter-plates, one upstream and another downstream of the cylinder [7].

5 Conclusions

The major conclusions are drawn as follows:

(1) The splitter-plate slightly changed the drag force in Re =40. In some cases, the obtained drag coefficient was more than the reference case, unexpectedly.
(2) In the case of vortex shedding, which is observed Re =100 and 150, the flow induced forces on the cylinder are greatly dependent on the position of the splitter-plate related to the cylinder. The critical values of G/D are also significantly dependent on Z/D, in these low Reynolds numbers.
(3) Interrupting regular vortex shedding is the major mechanism of detached splitter-plates in order to suppress the vortex shedding and reduce the flow induced forces.
(4) The best configuration to achieve maximum reduction in the lift and drag forces is $Z/D=0.75$ for Reynolds numbers of 100 and 150.
(5) A diminution of 20% in the drag force was obtained by embedding twin splitter-plates downstream of the cylinder at ($Z1/D=Z2/D=0.75$ and $G/D=0$).

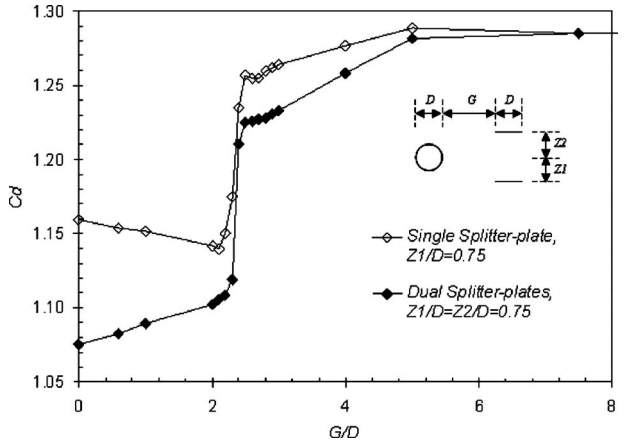

Fig. 4 Variation in the drag coefficient in Re=100 and different *G/D* values for both single and dual splitter-plate cases

References

[1] Rathakrishnan, E., 1999, "Effect of Splitter-Plate on Bluff Body Drag," AIAA J., **37**(9), pp. 1125–1126.

[2] Anderson, E. A., and Szewczyk, A. A., 1997, "Effect of a Splitter on the Near Wake of a Circular Cylinder in Two and Three Dimensional Flow Configurations," Exp. Fluids, **23**, pp. 161–174.

[3] Kwon, K., and Choi, H., 1996, "Control of Laminar Vortex Shedding Behind a Circular Cylinder Using Splitter-Plates," Phys. Fluids, **8**, pp. 479–486.

[4] Ozono, S., 1999, "Flow Control of Vortex Shedding by a Short Splitter-Plate Asymmetrically Arranged Downstream of a Circular Cylinder," Phys. Fluids, **11**(10), pp. 2928–2934.

[5] Ozono, S., 2000, "Flow Control of Vortex Shedding by Asymmetrically Arranged Plates," Theor. Appl. Mech., **49**, pp. 191–196.

[6] Hwang, J. Y., Yang, K. S., and Sun, S. H., 2003, "Reduction of Flow-Induced Forces on a Circular Cylinder Using a Detached Splitter-Plate," Phys. Fluids, **15**(8), pp. 2433–2436.

[7] Hwang, J. Y., and Yang, K. S., 2007, "Drag Reduction on a Circular Cylinder Using Dual Detached Splitter-Plates," J. Wind Eng. Ind. Aerodyn., **95**, pp. 551–564.

[8] Dehkordi, B. G., and Houri Jafari, H., 2009, "Numerical Simulation of Flow Through Tube Bundles in In-Line Square and General Staggered Arrangements," Int. J. Numer. Methods Heat Fluid Flow, **19**(8), pp. 1038–1062.

[9] Patankar, S. V., and Spalding, D. B., 1972, "A Calculation Procedure for Heat, Mass and Momentum Transfer in Three-Dimensional Parabolic Flows," Int. J. Heat Mass Transfer, **15**, pp. 1787–1806.

[10] Patankar, S. V., 1980, *Numerical Heat Transfer and Fluid Flow*, Hemisphere, New York.

[11] Williamson, C. H. K., 1996, "Vortex Dynamics in the Cylinder Wake," Annu. Rev. Fluid Mech., **28**, pp. 477–539.

[12] Wanderley, J. B. V., and Levi, C. A., 2002, "Validation of a Finite Difference Method for the Simulation of Vortex-Induced Vibrations on a Circular Cylinder," Ocean Eng., **29**, pp. 445–460.

[13] Lima E Silva, A. L. F., Silveira-Neto, A., and Damasceno, J. J. R., 2003, "Numerical Simulation of Two-Dimensional Flows Over a Circular Cylinder Using the Immersed Boundary Method," J. Comput. Phys., **189**, pp. 351–370.

[14] Roshko, A., 1955, "On the Wake and Drag of Bluff Bodies," J. Aeronaut. Sci., **22**, pp. 124–132.

[15] Thom, A., 1933, "Numerical Solution for the Flow Around a Cylinder at Reynolds Numbers of 40, 200 and 500," J. Proc. R. Soc. A, **141**, pp. 651–669.

[16] Grove, A. S., Shair, F. H., Petersen, E. E., and Acrivos, A., 1964, "An Experimental Investigation of the Steady Separated Flow Past a Circular Cylinder," J. Fluid Mech., **19**, pp. 60–80.

[17] Dennis, S. C. R., and Chang, G., 1970, "Numerical Solutions for Steady Flow Past a Circular Cylinder at Reynolds Numbers up to 100," J. Fluid Mech., **42**, pp. 471–489.

Buoyancy Effects on Thermal Boundary Layer Over a Vertical Plate With a Convective Surface Boundary Condition

O. D. Makinde[1]
Senior Professor and Chair of Postgraduate Studies
e-mail: makinded@cput.ac.za

P. O. Olanrewaju
e-mail: oldapo_anu@yahoo.ie

Faculty of Engineering,
Cape Peninsula University of Technology,
P.O. Box 1906,
Bellville 7535, South Africa

This study aims to analyze the effects of thermal buoyancy on the laminar boundary layer about a vertical plate in a uniform stream of fluid under a convective surface boundary condition. Using a similarity variable, the governing nonlinear partial differential equations have been transformed into a set of coupled nonlinear ordinary differential equations, which are solved numerically by applying shooting iteration technique together with fourth-order Runge–Kutta integration scheme. The variations in dimensionless surface temperature and fluid-solid interface characteristics for different values of Prandtl number (Pr), local Grashof number Gr_x, and local convective heat transfer parameter Bi_x are graphed and tabulated. A comparison with previously published results on special case of the problem shows excellent agreement.
[DOI: 10.1115/1.4001386]

Keywords: vertical plate, boundary layer flow, heat transfer, local Grashof number, convective parameter

1 Introduction

Convective heat transfer studies are very important in processes involving high temperatures such as gas turbines, nuclear plants, thermal energy storage, etc. The classical problem (i.e., fluid flow along a horizontal, stationary surface located in a uniform freestream) was solved for the first time in 1908 by Blasius [1]; it is still a subject of current research [2,3] and, moreover, further study regarding this subject can be seen in most recent papers [4,5]. Moreover, Bataller [6] presented a numerical solution for the combined effects of thermal radiation and convective surface heat transfer on the laminar boundary layer about a flat-plate in a uniform stream of fluid (Blasius flow) and about a moving plate in a quiescent ambient fluid (Sakiadis flow). Recently, Aziz [7] investigated a similarity solution for laminar thermal boundary layer over a flat-plate with a convective surface boundary condition. Numerous studies such as Refs. [8–10] considered different variations in temperature and heat flux at the plate; no study appeared to have considered the combined effects of buoyancy force and a convective heat exchange at the plate surface on the boundary layer flow, which is the focus of this paper.

In this present paper, the recent work of Aziz [7] is extended to include the effect of buoyancy force. The numerical solutions of the resulting momentum and the thermal similarity equations are reported for representative values of thermophysical parameters characterizing the fluid convection process.

2 Mathematical Analysis

We consider a two-dimensional steady incompressible fluid flow coupled with heat transfer by convection over a vertical plate. A stream of cold fluid at temperature T_∞ moving over the right surface of the plate with a uniform velocity U_∞ while the left surface of the plate is heated by convection from a hot fluid at temperature T_f, which provides a heat transfer coefficient h_f (see Fig. 1). The density variation due to buoyancy effects is taken into account in the momentum equation (Boussinesq approximation). The continuity, momentum, and energy equations describing the flow can be written as

$$\frac{\partial u}{\partial x}+\frac{\partial v}{\partial y}=0 \tag{1}$$

$$u\frac{\partial u}{\partial x}+v\frac{\partial u}{\partial y}=\upsilon\frac{\partial^2 u}{\partial y^2}+g\beta(T-T_\infty) \tag{2}$$

$$u\frac{\partial T}{\partial x}+v\frac{\partial T}{\partial y}=\alpha\frac{\partial^2 T}{\partial y^2} \tag{3}$$

where u and v are the x (along the plate) and the y (normal to the plate) components of the velocities, respectively, T is the temperature, υ is the kinematics viscosity of the fluid, and α is the thermal diffusivity of the fluid and β is the thermal expansion coefficient. The velocity boundary conditions can be expressed as

$$u(x,0)=v(x,0)=0 \tag{4}$$

$$u(x,\infty)=U_\infty \tag{5}$$

The boundary conditions at the plate surface and far into the cold fluid may be written as

$$-k\frac{\partial T}{\partial y}(x,0)=h_f[T_f-T(x,0)] \tag{6}$$

$$T(x,\infty)=T_\infty \tag{7}$$

Introducing a similarity variable η and a dimensionless stream function $f(\eta)$ and temperature $\theta(\eta)$ as

$$\eta=y\sqrt{\frac{U_\infty}{\upsilon x}}=\frac{y}{x}\sqrt{\mathrm{Re}_x},\quad \frac{u}{U_\infty}=f',\quad v=\frac{1}{2}\sqrt{\frac{U_\infty\upsilon}{x}}(\eta f'-f),$$

$$\theta=\frac{T-T_\infty}{T_f-T_\infty} \tag{8}$$

where prime symbol denotes differentiation with respect to η and $\mathrm{Re}_x=U_\infty x/\upsilon$ is the local Reynolds number. Equations (1)–(7) reduces to

$$f'''+\frac{1}{2}ff''+\mathrm{Gr}_x\theta=0 \tag{9}$$

$$\theta''+\frac{1}{2}\mathrm{Pr}\,f\theta'=0 \tag{10}$$

$$f(0)=f'(0)=0,\quad \theta'(0)=-\mathrm{Bi}_x[1-\theta(0)] \tag{11}$$

$$f'(\infty)=1,\quad \theta(\infty)=0 \tag{12}$$

where

[1]Corresponding author.

Contributed by the Fluids Engineering Division of ASME for publication in the JOURNAL OF FLUIDS ENGINEERING. Manuscript received December 23, 2009; final manuscript received January 30, 2010; published online April 16, 2010. Assoc. Editor: Paul Durbin.

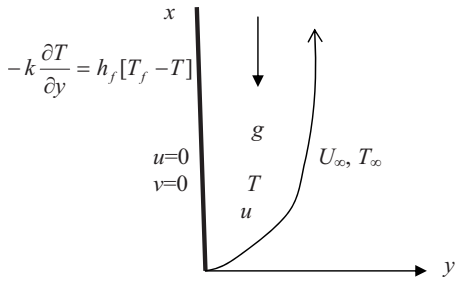

Fig. 1 Flow configuration and coordinate system

$$\mathrm{Bi}_x = \frac{h_f}{k}\sqrt{\frac{\upsilon x}{U_\infty}}, \quad \mathrm{Pr} = \frac{\upsilon}{\alpha}, \quad \mathrm{Gr}_x = \frac{\upsilon x g\beta(T_f - T_\infty)}{U_\infty^2} \tag{13}$$

For the momentum and energy equations to have a similarity solution, the parameters Gr_x and Bi_x must be constants and not functions of x as in Eq. (13). This condition can be met if the heat transfer coefficient h_f is proportional to $x^{-1/2}$ and the thermal expansion coefficient β is proportional to x^{-1}. We therefore assume

$$h_f = cx^{-1/2}, \quad \beta = mx^{-1} \tag{14}$$

where c and m are constants. Substituting Eq. (14) into Eq. (13), we have

$$\mathrm{Bi} = \frac{c}{k}\sqrt{\frac{\upsilon}{U_\infty}}, \quad \mathrm{Gr} = \frac{\upsilon m g(T_f - T_\infty)}{U_\infty^2} \tag{15}$$

With Bi and Gr defined by Eq. (15), the solutions of Eqs. (9)–(12) yield the similarity solutions, however, the solutions generated are the local similarity solutions whenever Bi_x and Gr_x are defined as in Eq. (13).

3 Numerical Solutions

The coupled nonlinear Eqs. (9) and (10) with the boundary conditions in Eqs. (11) and (12) are solved numerically using the fourth-order Runge–Kutta method with a shooting technique and implemented on Maple [11]. The step size 0.001 is used to obtain the numerical solution with seven-decimal place accuracy as the criterion of convergence.

4 Results and Discussion

Numerical calculations have carried out for different values of the thermophysical parameters controlling the fluid dynamics in the flow regime. The Prandtl number used are 0.72, 1, 3, and 7.1; the convective parameter Bi_x used are 0.05, 0.10, 0.20, 0.40, 0.60, 0.80, 1, 5, 10, and 20; and the Grashof number (Grashof number Gr_x) used are $\mathrm{Gr} > 0$ (which corresponds to the cooling problem). The cooling problem is often encountered in engineering applications; for example, in the cooling of electronic components and nuclear reactors. Comparisons of the present results with previously work is performed and excellent agreement has been obtained. We obtained the results as shown in Tables 1 and 2 and Figs. 2–6 below.

Table 1 shows the comparison of Aziz [7] work with the present work for Prandtl number (Pr=0.72) and it is noteworthy that there is a perfect agreement in the absence of Grashof number. Table 2, illustrates the values of the skin-friction coefficient and the local Nusselt number in terms of $f''(0)$ and $-\theta'(0)$, respectively, for various values of embedded parameters. From Table 2, it is understood that the skin-friction and the rate of heat transfer at the plate surface increases with an increase in local Grashof number and convective surface heat transfer parameter. However, an increase in the fluid Prandtl number decreases the skin-friction but increases the rate of heat transfer at the plate surface. Figures 2 and 3 depict the fluid velocity profiles. Generally, the fluid velocity is zero at the plate surface and increases gradually away from the plate toward the freestream value satisfying the boundary conditions. It is interesting to note that an increase in the intensity of convective surface heat transfer (Bi_x) produces a slight increase in the fluid velocity within the boundary layer. Similar trend is observed with an increase in local Grashof number due to buoyancy effects. Moreover, the effect of local Grashof number on the velocity profiles (see Fig. 3) is more pronounced than the effect of convection parameter (Bi_x) (see Fig. 2). Figures 4–6 illustrate the fluid temperature profiles within the boundary layer. The fluid temperature is maximum at the plate surface and decreases exponentially to zero value far away from the plate satisfying the boundary conditions. From this figures, it is noteworthy that the thermal boundary layer thickness increases with an increase in Bi_x and decreases with and increase in the values of Gr_x and Pr. Hence, convective surface heat transfer enhances thermal diffu-

Table 1 Computations showing comparison with Aziz [7] results for $\mathrm{Gr}_x=0$ and Pr=0.72

Bi_x	$\theta(0)$ Aziz [7]	$-\theta'(0)$ Aziz [7]	$\theta(0)$ Present	$-\theta'(0)$ Present
0.05	0.1447	0.0428	0.1447	0.0428
0.10	0.2528	0.0747	0.2528	0.0747
0.20	0.4035	0.1193	0.4035	0.1193
0.40	0.5750	0.1700	0.5750	0.1700
0.60	0.6699	0.1981	0.6699	0.1981
0.80	0.7302	0.2159	0.7302	0.2159
1.00	0.7718	0.2282	0.7718	0.2282
5.00	0.9441	0.2791	0.9442	0.2791
10.00	0.9713	0.2871	0.9713	0.2871
20.00	0.9854	0.2913	0.9854	0.2913

Table 2 Computation showing $f''(0)$, $\theta(0)$, and $\theta'(0)$ for different parameter values

Bi_x	Gr_x	Pr	$f''(0)$	$-\theta'(0)$	$\theta(0)$
0.1	0.1	0.72	0.36881	0.07507	0.24922
1.0	0.1	0.72	0.44036	0.23750	0.76249
10	0.1	0.72	0.46792	0.30559	0.96944
0.1	0.5	0.72	0.49702	0.07613	0.23862
0.1	1.0	0.72	0.63200	0.07704	0.22955
0.1	0.1	3.00	0.34939	0.08304	0.16954
0.1	0.1	7.10	0.34270	0.08672	0.13278

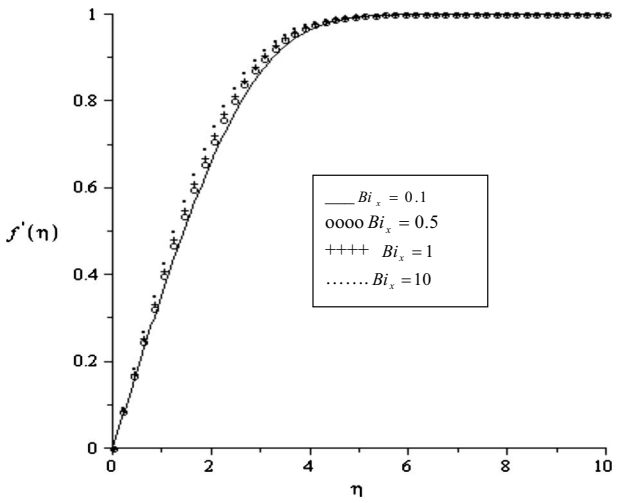

Fig. 2 Velocity profiles for Pr=0.72, $\mathrm{Gr}_x=0.1$

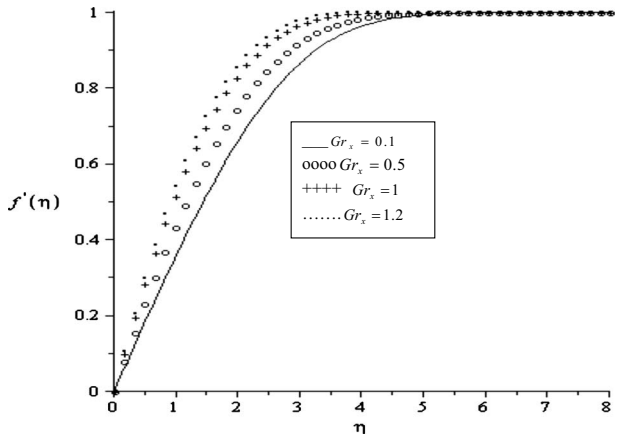

Fig. 3 Velocity profiles for Pr=0.72, Bi_x=0.1

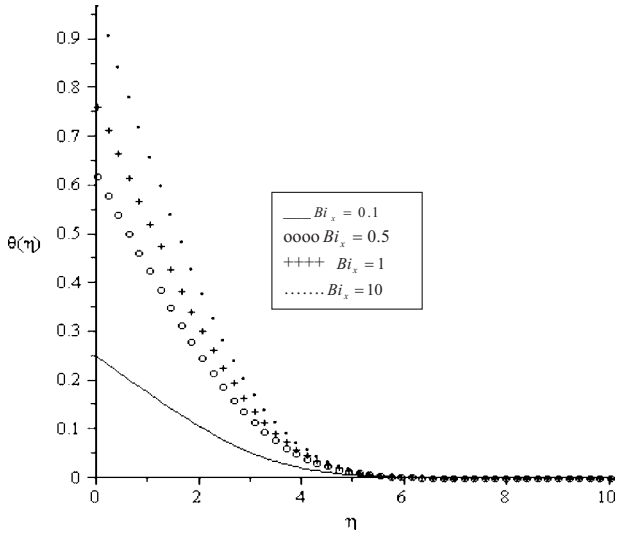

Fig. 4 Temperature profiles for Pr=0.72, Gr_x=0.1

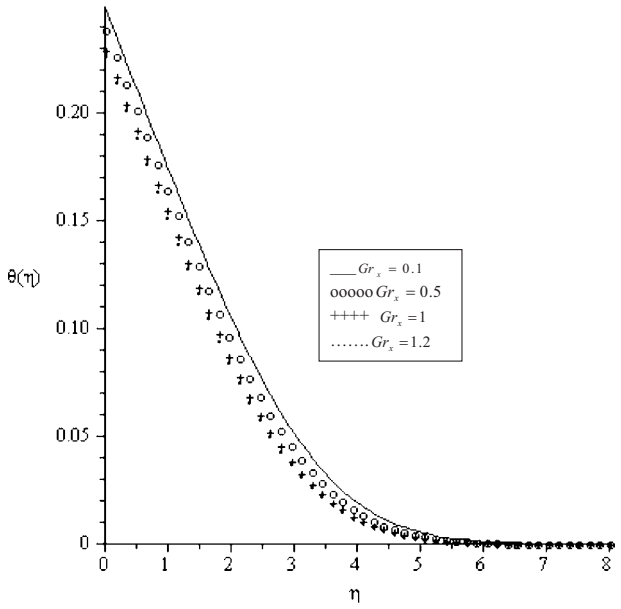

Fig. 5 Temperature profiles for Pr=0.72 and Bi_x=0.1

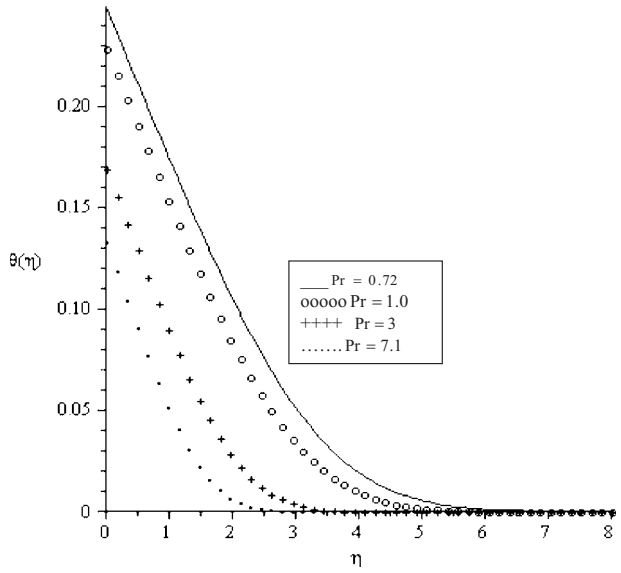

Fig. 6 Temperature profiles for Gr_x=0.1 and Bi_x=0.1

sion while an increase in the Prandtl number and the intensity of buoyancy force slows down the rate of thermal diffusion within the boundary layer.

5 Conclusion

Analysis has been carried out to study the boundary layer flow over a vertical plate with a convective surface boundary condition. A similarity solution for the momentum and the thermal boundary layer equations is possible if the convective heat transfer of the fluid heating the plate on its left surface is proportional to $x^{-1/2}$ and the thermal expansion coefficient β is proportional to x^{-1}. The numerical solutions of the similarity equations were reported for the various parameters embedded in the problem. The combined effects of increasing the Prandtl number and the Grashof number tends to reduce the thermal boundary layer thickness along the plate.

Acknowledgment

O.D.M. would like to thank the National Research Foundation (NRF) Thuthuka program for financial support. Dr. Olanrewaju of Convent University, Nigeria visited CPUT South Africa on Post-doctoral studies.

Nomenclature

(x,y) = Cartesian coordinates
(u,v) = velocity components
T_∞ = freestream temperature
T_f = hot fluid temperature
g = gravitational acceleration
T = fluid temperature
Pr = Prandtl number
U_∞ = freestream velocity
Gr_x = local Grashof number
Bi_x = local convective heat transfer parameter
k = thermal conductivity

Greek Symbols

α = thermal diffusivity of the fluid
β = thermal expansion coefficient
ν = kinematic viscosity

References

[1] Blasius, H., 1908, "Grenzschichten in Flussigkeiten mit kleiner reibung," Z. Math Phys., **56**, pp. 1–37.

[2] Weyl, H., 1942, "On the Differential Equations of the Simplest Boundary-Layer Problem," Ann. Math., **43**, pp. 381–407.

[3] Magyari, E., 2008, "The Moving Plate Thermometer," Int. J. Therm. Sci., **47**, pp. 1436–1441.

[4] Cortell, R., 2005, "Numerical Solutions of the Classical Blasius Flat-Plate Problem," Appl. Math. Comput., **170**, pp. 706–710.

[5] He, J. H., 2003, "A Simple Perturbation Approach to Blasius Equation," Appl. Math. Comput., **140**, pp. 217–222.

[6] Bataller, R. C., 2008, "Radiation Effects for the Blasius and Sakiadis Flows With a Convective Surface Boundary Condition," Appl. Math. Comput., **206**, pp. 832–840.

[7] Aziz, A., 2009, "A Similarity Solution for Laminar Thermal Boundary Layer Over a Flat Plate With a Convective Surface Boundary Condition," Commun. Nonlinear Sci. Numer. Simul., **14**, pp. 1064–1068.

[8] Makinde, O. D., and Sibanda, P., 2008, "Magnetohydrodynamic Mixed Convective Flow and Heat and Mass Transfer Past a Vertical Plate in a Porous Medium With Constant Wall Suction," ASME J. Heat Transfer, **130**, p. 112602.

[9] Makinde, O. D., 2009, "Analysis of Non-Newtonian Reactive Flow in a Cylindrical Pipe," ASME J. Appl. Mech., **76**, p. 034502.

[10] Cortell, R., 2008, "Similarity Solutions for Flow and Heat Transfer of a Quiescent Fluid Over a Nonlinearly Stretching Surface," J. Mater. Process. Technol., **2003**, pp. 176–183.

[11] Heck, A., 2003, *Introduction to Maple*, 3rd ed., Springer-Verlag, New York.